EMBRY-RIDDLE Aeronautical University
DAYTONA BEACH, FLORIDA

FDOT

Final Report

BRIDGE GIRDER ALTERNATIVES FOR EXTREMELY AGGRESSIVE ENVIRONMENTS

Florida Department of Transportation – BDV22-977-01

Prepared by:

Dr. Jeff Brown, Civil Engineering
Dr. Daewon Kim, Aerospace Engineering
Dr. Ali Tamijani, Aerospace Engineering

Graduate Research Assistants:

Vasileios Papapetrou
Abdellah Azeez
Satyagajen Arunasalam Rajenthiran

Embry-Riddle Aeronautical University
Daytona Beach, FL

January 2018

Disclaimer

The opinions, findings, and conclusions expressed in this publication are those of the author(s) and not necessarily those of the Florida Department of Transportation or the U.S. Department of Transportation.

Metric Conversion Chart

SYMBOL	WHEN YOU KNOW	MULTIPLY BY	TO FIND	SYMBOL
LENGTH				
in	inches	25.4	millimeters	mm
ft	feet	0.305	meters	m
yd	yards	0.914	meters	m
mi	miles	1.61	kilometers	km
mil	$1/1000^{th}$ of an inch	0.025	millimeters	mm
AREA				
in^2	square inches	645.2	square millimeters	mm^2
ft^2	square feet	0.093	square meters	m^2
yd^2	square yards	0.836	square meters	m^2
ac	acres	0.405	hectares	ha
mi^2	square miles	2.59	square kilometers	km^2
VOLUME				
fl oz	fluid ounces	29.57	milliliters	mL
gal	gallons	3.785	liters	L
ft^3	cubic feet	0.028	cubic meters	m^3
yd^3	cubic yards	0.765	cubic meters	m^3
NOTE: volumes greater than 1000 L shall be shown in m^3				
MASS				
oz	ounces	28.35	grams	g
lb	pounds	0.454	kilograms	kg
T	short tons (2000 lb)	0.907	metric ton	Mg (or "t")
TEMPERATURE (exact degrees)				
°F	Fahrenheit		Celsius	°C
ILLUMINATION				
fc	foot-candles	10.76	lux	lx
fl	foot-lamberts	3.426	candela/m^2	cd/m^2
FORCE and PRESSURE or STRESS				
kip	1000 pound force	4.45	kilonewtons	kN
lbf	pound force	4.45	newtons	N
lbf/in^2	pound force per square inch	6.89	kilopascals	kPa
ksi	kip per square inch	6.89	megapascals	MPa
ksf	kip per square foot	47.88	kilopascals	kPa
Msi	million pounds per square inch	6.89	gigapascals	GPa

SYMBOL	WHEN YOU KNOW	MULTIPLY BY	TO FIND	SYMBOL
LENGTH				
mm	millimeters	0.039	inches	in
m	meters	3.28	feet	ft
m	meters	1.09	yards	yd
km	kilometers	0.621	miles	mi
AREA				
mm^2	square millimeters	0.0016	square inches	in^2
m^2	square meters	10.764	square feet	ft^2
m^2	square meters	1.195	square yards	yd^2
ha	hectares	2.47	acres	ac
km^2	square kilometers	0.386	square miles	mi^2
VOLUME				
mL	milliliters	0.034	fluid ounces	fl oz
L	liters	0.264	gallons	gal
m^3	cubic meters	35.314	cubic feet	ft^3
m^3	cubic meters	1.307	cubic yards	yd^3
MASS				
g	grams	0.035	ounces	oz
kg	kilograms	2.202	pounds	Ib
Mg (or "t")	megagrams (or "metric	1.103	short tons (2000 Ib)	T
TEMPERATURE (exact degrees)				
°C	Celsius	1.8C+32	Fahrenheit	°F
ILLUMINATION				
Ix	lux	0.0929	foot-candles	fc
cd/m^2	candela/m^2	0.2919	foot-lamberts	fl
FORCE and PRESSURE or STRESS				
kN	kilonewtons	0.225	1000 pound force	kip
N	newtons	0.225	pound force	Ibf
kPa	kilopascals	0.145	pound force per square inch	Ibf/in^2

Technical Report Documentation Page

1. Report No.	**2. Government Accession No.**	**3. Recipient Catalog No.**
4 Title and Subtitle Bridge Girder Alternatives for Extremely Aggressive Environments		**5 Report Date** January 2018 **6 Performing Organization Code**
7. Author(s) Jeff R. Brown, Daewon Kim, Ali Tamijani, and Vasileios Papapetrou		**8 Performing Organization Report No.**
9 Performing Organization Name and Address Embry-Riddle Aeronautical University 600 S. Clyde Morris Blvd. Daytona Beach, FL 32114		**10 Work Unit No. (TRAIS)** **11 Contract or Grant No.** BDV22-977-01
12 Sponsoring Agency Name and Address Florida Department of Transportation Research Center, MS 30 605 Suwannee St Tallahassee, FL 32399-0450		**13 Type of Report and Period Covered** Final Report June 2015-January 2018 **14 Sponsoring Agency Code**
15 Supplementary Notes		

16 Abstract

The primary objective of this study was to identify viable alternatives for fiber-reinforced polymer (FRP) bridge girders and evaluate their potential for use in extremely aggressive environments in Florida. The first phase of the study included a comprehensive survey of in-service FRP-girder bridges in the U.S. along with several projects in Europe. Four distinct girder types were identified ((1) pultruded sections, (2) U-girders, (3) concrete-filled FRP tubes, and (4) Hillman Composite Beams (HCBs)) and the current status of existing bridges for each type was verified. Fiber-reinforced polymer flat-panel slab bridges were also investigated. Three general girder geometries were chosen for further investigation and evaluation: (1) hybrid FRP/concrete-filled U-girder, (2) hybrid FRP/concrete-filled tube, and a (3) pultruded double-web I-beam (DWB). Tthe required amount of FRP material and associated manufacturing costs were determined for a range of span lengths between 30 ft and 75 ft. All three options were assumed to develop full composite action with an 8-in-thick cast-in-place reinforced concrete deck. The number of girders per span was also treated as a variable. Two unique design methodologies were investigated for the FRP U-girders. The first method relied on AASHTO distribution factors to determine the single-girder structural demand. The second method involved finite element analysis of the entire bridge combined with structural optimization techniques to determine the most efficient girder geometry. The CFFTs were exclusively using the AASHTO distribution factor method, and the DWB alternative was evaluated using finite element analysis. Results indicate that the hybrid FRP/concrete U-girder is the most efficient and cost-effective alternative. The girder cost per square foot for the U-girder alternative ranges from just over $40 per square foot of bridge deck for a 30-ft span to $140 per square foot for the 75-ft span. These estimates include the costs for materials and manufacturing of the FRP U-girder and the cast-in-place concrete required to fill the girder on-site. Additional costs associated with placing the girders and the cast-in-place reinforced concrete deck are not included.

17 Key Words Fiber-reinforced polymer composites, bridge girders, extremely aggressive environments		**18 Distribution Statement** No restrictions. This document is available to the public through the National Technical Information Service, Springfield, Virginia 22161	
19 Security Classification (of this report) Unclassified	**20 Security Classification (of this page)** Unclassified	**21 No. of pages** 283	**22 Price**

Acknowledgements

The authors would like to thank Mr. Will Potter, PE, from the Florida DOT Structures Research Center, and Mr. Rick Vallier, PE, and Mr. Steve Nolan, PE, from the Florida DOT Structures Design Office, for their insight and thoughtful review of the work described in this final report. We would also like to thank Mr. Stanislav Sykulskyi for his contributions in the early phase of this study.

Executive Summary

There are four primary objectives in the current study:

1. Investigate the performance of previously implemented fiber-reinforced polymer (FRP) vehicle bridges and FRP bridge girders.
2. Identify three viable, non-proprietary, bridge girder alternatives for further analysis and development for use in extremely aggressive environments.
3. Evaluate and apply existing design criteria as described in AASHTO LRFD-7 and LRFD-FRP for each alternative for simply supported bridge spans ranging from 30 ft to 75 ft.
4. Perform a comprehensive alternatives analysis which considers cost, design methodology, materials, manufacturing, constructability, maintenance, and service life.

A total of five vehicle bridges in the U.S. were identified that utilize all-FRP girders as the primary flexural element to resist shear and bending along the span length. Two bridges in Virginia, constructed in 1997 and 2001, rely on pultruded double-web I-beams (DWBs) produced by the Strongwell Corporation to support a laminated timber deck with an asphalt overlay. The first bridge spans 18 ft and uses 8-in-deep DWBs spaced at 12 in on center. The second bridge spans 39 ft and uses 36-in-deep DWBs spaced at 42 in on center. The Texas DOT completed two demonstration bridges in 2005 and 2007 that utilize glass FRP U-girders with span lengths of 30 ft (x two spans) and 50 ft, respectively. Both of these bridges incorporated a cast-in-place reinforced concrete deck with cast-in-place barriers. Finally, the Kings Stormwater Channel bridge near the Salton Sea in California utilized concrete-filled FRP tubes (CFFTs) to support a pultruded FRP bridge deck. This bridge was completed in 2001 and then replaced in 2013 due to durability concerns with the FRP bridge deck. The CFFT girders did not present any maintenance or durability concerns during 12 years of service.

Three different FRP manufacturing methods were identified as potentially viable for FRP bridge girders in the current study: (1) vacuum-assisted resin transfer molding (VARTM)/vacuum infusion processing (VIP), (2) pultrusion, and (3) filament winding. VARTM/VIP allows the greatest flexibility with regards to U-shaped girder dimensions and laminate architecture (i.e., thickness and fiber orientation angle). The primary disadvantage associated with VARTM/VIP is that producing an individual girder is labor intensive. Pultrusion is a highly mechanized process that is capable of producing high volumes of structural shapes, but a major disadvantage is the high cost of tooling required for a specific girder geometry. Another disadvantage is that the fiber orientation angle is constrained to the primary axis direction of the girder. Some off-axis strength can be obtained, but this is usually limited. Filament winding can be used for the production of CFFT girders. The main advantages of this method are a relatively high fiber volume fraction and a low percentage of voids in finished parts. Disadvantages include the fact that fiber orientation angles typically limited to ~10 degrees by the winding angle capabilities of the filament winder. Higher winding angles result in CFFTs capable of providing high levels of confinement, but the strength and stiffness in the primary direction of the girder is relatively low compared to pultruded or VIP/VARTM produced girders.

Three general girder geometries were chosen for further investigation and evaluation: (1) hybrid FRP/concrete-filled U-girder, (2) hybrid FRP/concrete-filled tube, and a (3) pultruded double-web I-beam. The objective of this phase of the study was to determine the required amount of FRP material and associated costs for each alternative over a range of span lengths between 30 ft and 75 ft. All three options were assumed to develop full composite action with an 8-in-thick cast-in-place reinforced

concrete deck. A generic 32-ft clear-width (two 12-ft lanes with 4-ft shoulders) roadway cross-section was adopted and simply-supported span lengths of 30 ft, 40 ft, 50 ft, 60 ft, and 75 ft were evaluated for each alternative. The number of girders per span was varied from between four and 12.

For the FRP U-girders, two design methods were investigated. The first method relied on AASHTO distribution factors to determine the single-girder structural demand. The second method involved finite element analysis of the entire bridge, combined with structural optimization techniques to determine the most efficient girder geometry. The CFFTs were evaluated exclusively using the AASHTO distribution factor method, and the DWB alternative was evaluated using finite element analysis. Results indicate that the hybrid FRP/concrete U-girder is the most efficient and cost-effective alternative. The girder cost per square foot for the U-girder alternative ranges from just over $40 per square foot of bridge deck for a 30-ft span to $140 per square foot for the 75-ft span. These estimates include the costs for materials and manufacturing of the FRP U-girder and the cast-in-place concrete required to fill the girder on-site. Additional costs associated with placing the girders and the cast-in-place reinforced concrete deck are not included.

Existing AASHTO, ACI, and ASCE design guidelines ensure the long-term durability of FRP components by requiring vinylester resins with a final glass transition temperature ranging between 180°F – 212°F. Strength reduction factors for glass FRP (GFRP) ranging from 0.5 for aggressive environments to 0.65 for normal environments are also used to limit the maximum stress the material can experience at the strength limit state. The long-term effects of fatigue and creep rupture of GFRP are further mitigated by applying an additional strength reduction factor of 0.2. These two reduction factors combine to effectively limit the maximum tensile stress experienced by GFRP under service load conditions in an extremely aggressive environment to 10% of the manufacturer's specified tensile strength. A comprehensive review of previous research on the durability of FRP materials for civil infrastructure completed by the Advanced Structures and Composites Center at the University of Maine indicates that the actual strength reduction factor for a 100-year service life in a South Florida environment ranges from 0.71 to 0.98. The primary long-term durability concerns for GFRP exposed to ambient environmental conditions are related to fading and chalking of the outer surface. As long as a sacrificial gelcoat or polyamide epoxy paint is applied to protect the underlying glass reinforcement, the required service life of 75 years should be achieved with existing GFRP systems.

Contents

List of Figures

List of Tables

1. Introduction

Fiber-reinforced polymers (FRP) have a well-established history in the bridge industry. The most prominent applications of FRP to date have focused on pultruded bridge deck panels, internal reinforcement for concrete elements (e.g., FRP rebar), and externally bonded FRP strengthening systems for existing structures. Beginning in the mid 1990s, flat-panel FRP bridge systems were developed for short-span applications (less than 20-ft span length). These units consisted of top and bottom panel plates connected by a honeycomb core. Contact with several state and local transportation agencies indicated that many of these bridges were still in service as of 2016. The primary concerns or maintenance issues for these short-span FRP bridge systems involved minor damage due to guard rail impact and the durability of the bond between the FRP top panel and the polymer concrete overlay that serves as a friction course and wearing surface.

The objective of the current study was to investigate existing alternatives for FRP bridge girders in extremely aggressive environments—essentially saltwater marine environments in coastal areas—around the state of Florida. The span length of interest ranged from 30 ft to 75 ft (medium span bridges), and the most common anticipated application includes bridges with limited freeboard that are subject to high levels of saltwater spray. The low-rise relief bridge over the Halifax River (Intracoastal Waterway) in Port Orange, Florida, is an excellent example of where FRP composite bridge girders are potentially useful (Figure 1). This cast-in-place reinforced concrete slab bridge superstructure is currently performing very well, but past experience suggests that as chlorides diffuse through the concrete cover or flexural cracks begin to provide direct access for saltwater, the reinforcing steel will begin to corrode. The likelihood of achieving the desired 75-year service life for bridge structures like this one is generally low.

Figure 1. Low-rise relief bridge on Dunlawton Causeway in Port Orange, FL.

The advantages of FRP composite materials in extremely aggressive environments are well-documented. The primary motivation for incorporating these materials is their high resistance to corrosion combined with a relatively high tensile strength compared to steel. Current FDOT FRP guidelines[1] allow for the use of carbon and/or glass FRP (CFRP/GFRP) reinforcing bars in bridge decks, flat-slab superstructures, and other bridge pier elements not in direct contact with water. Prestressed CFRP strands can also be used in round and square piles. At present, however, the use of pultruded FRP elements or vacuum infusion-processed (VIP) FRP elements is limited to pedestrian bridge applications or bridge fender systems. The current study seeks to evaluate and extend existing AASHTO, ACI, and ASCE guidelines to incorporate FRP structural shapes for use as bridge girders.

Another major goal of the current study is to evaluate the short and long-term economic viability of different FRP bridge girder alternatives. It is generally accepted that incorporating large quantities of FRP in any bridge project will increase the initial cost of the structure, but there is currently little information available on the expected initial costs of FRP bridge girder for 30-ft to 75-ft span lengths. While this research stops short of a full life-cycle analysis that compares the total design, fabrication, construction, operations, maintenance, and decommissioning costs for FRP bridge girders compared to traditional materials (e.g. steel and reinforced concrete), it does seek to lay a solid foundation for determining the materials and manufacturing costs associated with FRP bridge girders for medium-span bridges.

Chapter 2 provides a comprehensive review of existing AASHTO design guidelines for the use of FRP materials in bridge applications. The focus of this chapter is on establishing the relevant limit states and evaluation criteria from LRFD-7 [2] and the AASHTO LRFD Design Specifications for Concrete-Filled FRP Tubes for Flexural and Axial Members (LRFD-FRP [3]). Other relevant documents from ACI and ASCE are also highlighted. Chapter 3 provides an overview of FRP materials characteristics and manufacturing methods that are applicable to bridge girder applications.

Chapter 4 includes a survey of existing vehicle bridges in the US that have incorporated FRP materials as the primary elements for resisting flexure and shear. This includes a number of short span bridges (< 20 ft) that are 100% FRP as well as five medium span bridges that utilize FRP girders with different deck materials (laminated timber, reinforced concrete, and FRP deck panels). A simple survey was developed to assess the performance of these FRP bridges from the perspective of the entity that is currently responsible for operations and maintenance. The only major problems identified for the short span bridges related to impact damage resulting from vehicle collisions with the guardrail and debonding of the polymer concrete overlay that serves as a wearing surface and friction course. Girders on the medium span bridges have performed very well since construction. Four of the five bridges are still in service after more than 10 years, and the one bridge that was removed from service was experiencing maintenance and durability issues with the FRP deck. In spite of the problems with the FRP deck, the concrete-filled FRP tube (CFFTs) girders were never a concern. Chapter 4 also includes a brief discussion of the Hillman Composite Beam (HCB), the Concrete Arch Bridge System (CABS)—formerly known as “Bridge-in-a-Backpack”—and several examples of FRP bridges from Europe.

Chapter 5 provides a brief glimpse into current research and development work related to composites in the aerospace industry. The disadvantages associated with composites for bridge applications (e.g. low modulus of elasticity, essentially non-ductile failure modes, interlaminar delaminations, and high initial fabrication costs) are also concerns for aircraft structures. One of the major goals in the aerospace industry is to transition from parts produced in an autoclave to parts produced using vacuum infusion processing (VIP) or vacuum assisted resin transfer molding (VARTM). To accommodate the reduction in material properties for VIP/VARTM parts compared to autoclaved parts, researchers are investigating 3-D stitching and integrating pultruded rods into structural panels.

Chapter 6 summarizes the three alternatives chosen for further analysis and refinement based on the findings from the literature review and survey of current FRP bridge owners. The three alternatives selected include:

- Hybrid FRP/concrete U-girder
- Concrete-filled FRP tube
- Pultruded double-web I-beam (Strongwell DWB 36)

Chapter 7 describes the design space variables included in the current study to determine the FRP material requirements for medium span bridges. Chapter 8 takes a closer look at the four limit states used to evaluate the suitability of a proposed FRP cross-section. The limit states investigated include maximum concrete compressive stresses, maximum deflection criteria, fatigue and creep rupture, and ultimate strength (flexural and shear). Several proposed models for evaluating the shear strength of a hybrid FRP/concrete cross-section were evaluated to determine the influence of different laminate architectures. A new model for determining the strength contribution of the FRP section that is based on the ultimate shear strength of the FRP laminate is also proposed.

Chapter 8, Chapter 9, and Chapter 10 describe the structural analysis and optimization performed for each alternative girder type. Two unique design methodologies were investigated for the FRP U-girder. The first involves AASHTO distribution factors for determining the structural demands imposed on a single girder. The second method involves developing a finite element model of the entire bridge structure and relying on structural optimization techniques to determine the most efficient girder geometry required to satisfy the limit state criteria. The CFFT option was evaluated exclusively using the AASHTO distribution factor method. Finite element modeling was used to capture the effects of shear deformations for the DWB alternative and determine the number of girders required to meet the deflection criteria for a given span length.

Chapter 11 provides a side-by-side comparison and alternatives analysis for each of the three options. Factors evaluated include: design methodology, materials and manufacturing methods, constructability, maintenance, and service life. Finally, Chapter 12 provides conclusions and recommendations for future research.

2. Existing Standards, Specifications, and Guidelines

The literature review completed in Task 1 involved identifying existing standards, specifications, and guidelines that are relevant to FRP in civil infrastructure. The objective of this review was to summarize the general design philosophy, applicable limit states, and basic material strength requirements for each organization. The primary focal point is the collection of guide specifications produced by AASHTO. Existing documents from the American Concrete Institute (ACI) and the American Society of Civil Engineers are also discussed. Finally, existing guidelines from the FRP pultrusion industry and the aerospace industry are highlighted.

2.1 AASHTO

Five AASHTO documents were identified and reviewed during Task 1:

- AASHTO LRFD Bridge Design Specifications, 7th Edition, 2014
- AASHTO LRFD Guide Specifications for Design of Concrete-Filled FRP Tubes, 1st Edition, 2012
- AASHTO LRFD Bridge Design Guide Specifications for GFRP-Reinforced Concrete Bridge Decks and Traffic Railings, 1st Edition, 2009
- Guide Specifications for Design of FRP Pedestrian Bridges, 1st Edition, 2008
- AASHTO Guide Specifications for Design of Bonded FRP Systems for Repair and Strengthening of Concrete Bridge Elements, 1st Edition, 2012

2.1.1 LRFD Bridge Design Specifications

The general design philosophy, limit states, and loading requirements defined in the LRFD Bridge Design Specifications (LRFD-7) provided the general framework for evaluating FRP bridge girder alternatives in the current study. The governing design equation for the LRFD method ensures that the factored force effects that develop in a structural element for specified limit states are less than or equal to the factored resistance provided by the structural element:

$$\sum \eta_i \cdot \gamma_i \cdot Q_i \leq \Phi \cdot R_n = R_r \quad \text{(Eq. 2-1)}$$

where

η_i = load modifier to account for combined ductility, redundancy, and importance factors (note: η_i varies between 0.95 and 1.0. For the current study, this value will be taken as 1.0 (conservative) for all cases).
γ_i = load factor applied to different force effects
Q_i = force effect (e.g. shear, moment, or axial load that develops at a specified location for the structural element)
Φ = resistance factor applied to nominal resistance (varies depending on force effect type and material used in structural element)
R_n = fominal resistance of structural element
R_r = factored resistance of structural element

2.1.1.1 *Limit States*

LRFD-7 identifies the following limit states that must be considered in design:

- **Service Limit State**: Restrictions or limitations imposed on stress, deflections, and crack widths under regular service conditions.
- **Fatigue and Fracture Limit State**: Fatigue limit is a limit on stress range that results from a standard design truck. The fracture limit state is defined for different materials in the AASHTO Materials Specification.
- **Strength Limit State**: Ensures that adequate strength and stability are provided throughout the service life of the structure.
- **Extreme Event Limit State**: Ensures the survival of a bridge during an extreme event (e.g. earthquake, vessel or vehicle impact, or ice flows). This limit state will not be considered in the current study.

Depending on the material under consideration for a particular structural element, different criteria are established for each limit state. The differences are most pronounced in the Service and Fatigue/Fracture Limit States. Different Φ factors are also applied in Equation 1 for different limit states depending on the material of the element being evaluated. The AASHTO LRFD Guide Specifications for Design of Concrete-Filled FRP Tubes (LRFD-FRP) relies on LRFD-7 to establish the criteria for determining force effects, Q_i, and load factors, γ_i, in Equation 1.

2.1.1.2 *Ductility*

The AASHTO requirements on ductility for structural elements pose the greatest challenge for incorporating FRP composite girders in highway bridges:

The structural system of a bridge shall be proportioned and detailed to ensure the development of significant and visible inelastic deformations at the strength and extreme limit states before failure.

For FRP composite structures, the deformations experienced under service loads typically control the design and proportioning of structural elements. The resulting stresses that develop at strength limit states are considered to be sufficiently low and concerns of failure by sudden rupture of FRP composites are minimized. The primary mechanism used to ensure that sudden, non-ductile failures do not occur in FRP composite elements involves manipulating the strength reduction factor, Φ. For steel-reinforced concrete beams that exhibit ductile behavior (i.e., tension-controlled), a strength reduction factor of 0.9 is used. For tension-controlled prestressed concrete beams, the strength reduction factor increases to 1.0. For FRP-reinforced sections, the strength reduction factor is reduced to between 0.55 and 0.65, depending on the degree to which concrete crushing occurs at the strength limit state.

2.1.1.3 *Deflection Control*

Section 2.5.2.6.2 of LRFD-7 establishes criteria for deflections due to live load. These criteria are intended to limit undesirable psychological effects that occur when users experience vibrations or other load-induced motion of the structure. The live load portion of the Service 1 Load Combination (including the dynamic impact factor, IM) is used to calculate the live load deflection. LRFD provides the following limitations on live load deflection if no additional criteria are provided by the owner:

- L/800 (vehicular traffic only)
- L/1000 (vehicular and pedestrian traffic)

2.1.1.4 *Other General Criteria*

Additional factors from LRFD-7 that will be included in the current study include:

- **Durability** – The ultimate goal is to achieve a 75-year design life in extremely aggressive marine environments.
- **Inspectability** – Any significant damage that occurs to structural elements due to overloading or other durability-related issues should be visible to inspectors under typical bridge maintenance operations.
- **Maintainability** – FRP composites are susceptible to damage from UV radiation. This is typically mitigated through external coatings. Careful consideration will be given to painting requirements throughout the service-life for FRP elements depending on their level of exposure to UV radiation. LRFD-7 also discusses the need to accommodate future deck overlays and/or deck replacement. Depending on the level of composite action that is achieved between the deck and the FRP girders, special consideration may be needed to prevent damage during deck removal.

LRFD-7 also discusses vessel collisions, but impact forces due to vessel collisions were not considered in the current design study.

2.1.1.5 *Design Loads and Load Cases*

Section 3.3.2 of LRFD-7 provides a comprehensive list of different load types that must be accounted for in bridge design. In the current study, the load types under consideration will be limited to those described in Table 1. The assumed unit weights for common bridge construction materials are summarized in Table 2. In accordance with the FDOT Structural Design Guidelines, a future wearing surface of 15 lbf/in^2 is assumed.

Table 1. Load types from LRFD-7 considered in current study

Load Description	Abbreviation
Permanent Loads	
Dead load of structural components and non-structural attachments	DC
Dead load of wearing surfaces and utilities	DW
Transient Loads	
Vehicular live load	LL
Vehicular dynamic live load	IM

Table 2. Assumed unit weights for traditional bridge materials from LRFD-7

Material	Unit Weight (kip/ft^3)
Asphalt/bituminous wearing surfaces	0.140
Lightweight concrete	0.110
Normal weight concrete	0.145
High strength concrete	0.140 + .001 f'_c

The AASHTO HL-93 design live load includes two fundamental sources:

- Design truck **or** design tandem load
- Design lane load

The design truck/tandem loading is provided in Figure 2. Only one design truck is required for each lane on the bridge. The location of the truck must be varied in the longitudinal direction (direction of traffic flow) and the rear axle spacing must also be allowed to vary between 14 feet and 30 feet to produce the maximum effect. The design lane load is a uniform distributed load with a magnitude of 0.64 kips/ft in the longitudinal direction of the bridge. This lane load is assumed to act over a 10 foot transverse width.

Design traffic lanes are 12 feet wide. The designer is required to investigate all possible combinations of simultaneous loading in multiple lanes of the bridge to produce the maximum effects due to vehicle live load. To account for the decreased probability that the bridge will experience simultaneous loading of multiple lanes, a *multiple presence factor* is applied the force effects obtained from a specific loading scenario that is dependent on the number of loaded lanes. These multiple presence effects are not considered in the case of fatigue loading or when the approximate load distribution factors specified in LRFD-7 Sections 4.6.2.2 and 4.6.2.3 are used to obtain the maximum moments and shears for single girders.

Table 3. Multiple presence factors from LRFD-7

Number of Loaded Lanes	Multiple Presence Factor
1	1.2
2	1.0
3	0.85
>3	0.65

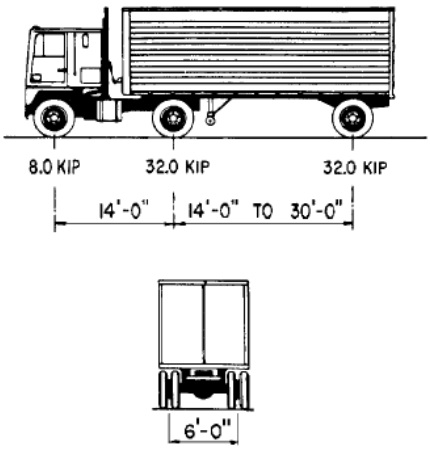

Design Truck (Figure 3.6.1.2.2-1)

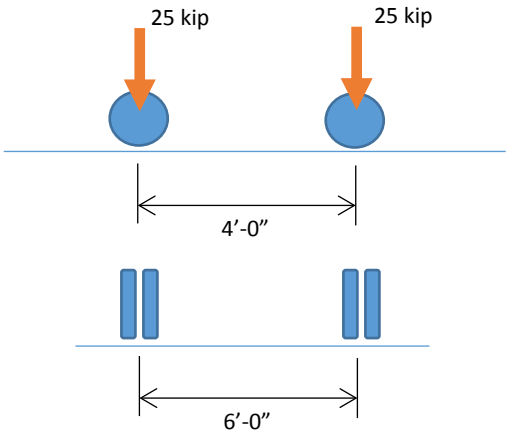

Design Tandem (Section 3.6.1.2.3)

Figure 2. AASHTO HL-93 design truck/tandem loading

When evaluating the bridge to meet the deflection criteria specified in LRFD-7 Section 2.5.2.6.2, the deflection should be calculated using the larger of the following:

- That resulting from the design truck alone
- That resulting from 25% of the design truck taken together with the design lane load

For fatigue loading, the force effects are calculated using one design truck with a constant rear axle spacing of 30 feet.

Section 3.6.2 of LRFD-7 also establishes provisions for a dynamic load allowance (IM) that is applied to the effects generated by a static analysis of the vehicular live loading. The dynamic load allowance is computed as (1 + IM/100), where IM is obtained from the following table:

Table 4. Dynamic load allowance from LRFD-7.

Component	IM
Deck joints	75%
All other components: • Fatigue and Fracture Limit State • All other limit states	 15% 33%

2.1.1.6 *Load Cases*

The primary load cases considered in the current study include:

- Strength I – Basic load combination relating to normal vehicular use of the bridge without wind
- Service I – Load combination related to normal use of the bridge with 55 MPH wind and all loads taken at their nominal values.
- Fatigue I – Fatigue and fracture load combination related to infinite load-induced fatigue life.

The relevant load combination factors specified in LRFD-7 are summarized Table 5. Some additional considerations that apply to the current study include the following:

- LRFD-7 provides recommended maximum and minimum values for certain permanent load types acting in various load combination limit states. For the current study, the maximum recommended load factors will be used (1.25 for DC and 1.5 for DW).
- Only the live load portion of the Service I case is used to evaluate deflections.
- The fatigue limit state in LRFD-7 is based on the effects generated by a single design truck with a constant rear axle spacing of 30 feet. The LRFD Guide Specifications for Design of Concrete-Filled FRP Tubes for Flexural and Axial Members (LRFD-FRP) requires that a combined Fatigue and Creep Rupture limit state must be considered. The load factors for this limit state are as follows:
    - DC and DW = 1.0
    - Truck LL for fatigue vehicle + Impact = 0.75

Table 5. Load combinations and load factors from LRFD-7

	Load Factors		
Load combination	DC	DW	LL
Strength I	1.25	1.5	1.75
Service I	1.0	1.0	1.0
Fatigue I	0	0	1.5

2.1.1.7 *Structural Analysis*

LRFD-7 provides guidance on acceptable methods for structural analysis in bridge design. The following methodologies was utilized in the current study:

- Finite element method applied to the entire single-span bridge
- Finite element method applied to a single girder
- Approximate methods based on moment and shear distribution factors

For all-FRP girders, a linear-elastic material model was used for FRP materials based on assumed properties for a proposed laminate architecture. For hybrid sections—all-FRP sections where composite action is developed with the reinforced concrete deck—a linear-elastic model was used for concrete as long as the concrete remained in compression. For cases where concrete was present in tension zones of the girder, a strain compatibility method was used to generate the moment-curvature diagram for a given FRP/concrete cross-section.

The moment and shear distribution factors outlined in Section 4.6.2 should be applicable to FRP girder designs assuming that the members provide sufficient torsional stiffness and resistance to strong-axis bending. Section 9.3 in the current study compares the AASHTO distribution factors for a 50-ft span bridge with distribution factors obtained using a finite element model.

2.1.2 LRFD Guide Specifications for Design of Concrete-Filled FRP Tubes (LRFD-FRP)

The 2012 AASHTO LRFD Guide Specifications for Design of Concrete-Filled FRP Tubes (LRFD-FRP) provides an excellent starting point for introducing FRP materials as primary structural elements in bridges. The role of LRFD-FRP is to establish the appropriate Φ factors and nominal resistances for FRP materials under different limit state conditions. A major focal point of this document is the concrete arch bridge system (CABS), formerly known as “Bridge-in-a-Backpack”, which utilizes concrete-filled FRP as arches with transverse FRP corrugated panels. This document also describes the design of concrete-filled FRP tubes as flexural beam/girder elements. This system was used in the King’s Stormwater Channel bridge in California. The specific details surrounding the CABS and King’s Stormwater Channel bridges will be discussed in Section 4.4 of this report. The main objectives of the current section are:

- Better understand the AASHTO code provisions for using FRP as a primary load-bearing material in highway bridges
- Identify the significant limit states and design philosophy that govern FRP flexural elements and how they might differ from the limit states specified in LRFD-7
- Identify appropriate resistance factors for FRP materials for different limit states

2.1.2.1 *Design Philosophy*

LRFD-FRP is also based on a limit-state design philosophy. Specific limit states identified in LRFD-FRP include:

- Service
- Fatigue and creep rupture (differs from LRFD-7, which is fatigue and *fracture*)
- Strength
- Extreme events

The document identifies serviceability (deflection control) and fatigue and creep rupture as limit states that will frequently control the design.

2.1.2.2 *Limitations*

LRFD-FRP identifies the following limitations:

- Concrete-filled FRP tubes (CFFTs) are not to be used as ductile earthquake resisting elements
- The design provisions in LRFD-FRP should not be applied to FRP tubes with fibers running only in the longitudinal direction
- The unconfined compressive strength, f'_c, of concrete used in CFFTs should not exceed 10 ksi
- The document is intended to apply only to concrete-filled FRP tubes (CFFT) where composite action is maintained between the FRP and the internal concrete.

To verify that composite action is maintained between the FRP and concrete for flexural members, LRFD-FRP requires the following testing:

- Three full-scale static tests to failure.
- Fatigue tests to 2 x 10^6 cycles using anticipated service loads and appropriate load ratio. The specimens are then loaded to failure after the fatigue tests.
- Specimens must not exhibit slip between FRP and concrete through specimen failure and the fatigued specimens must retain 90% of the static strength.

2.1.2.3 *Material Properties*

The design strength of composite materials is based on the material strength provided by the manufacturer and an environmental reduction factor that accounts for the specific fiber type and the anticipated service environments. Distinctions are also made between the design strengths in tension and compression as well as in the longitudinal and hoop directions. The following relationships are provided in LRFD-FRP:

$$f_{ful} = C_E \cdot f¤_{ful} \quad \text{Eq. 2-2}$$
$$f_{fuh} = C_E \cdot f¤_{fuh} \quad \text{Eq. 2-3}$$
$$f_{fcu} = C_E \cdot f¤_{fcu} \quad \text{Eq. 2-4}$$

where

f_{ful} = design tensile strength (longitudinal direction)
f_{fuh} = design tensile strength (hoop direction)
f_{fcu} = design compressive strength (longitudinal direction)
C_E = environmental knockdown factor
$f¤_{ful}$ = manufacturers specified tensile strength (long.)
$f¤_{fuh}$ = manufacturers specified tensile strength (hoop)
$f¤_{fcu}$ = manufacturers specified compressive strength (long.)

The design ultimate strains are given as:

$$\varepsilon_{ful} = C_E \cdot \varepsilon¤_{ful} \quad \text{Eq. 2-4}$$
$$\varepsilon_{fuh} = C_E \cdot \varepsilon¤_{fuh} \quad \text{Eq. 2-5}$$
$$\varepsilon_{fcu} = C_E \cdot \varepsilon¤_{fcu} \quad \text{Eq. 2-6}$$

where

ε_{ful} = design tensile strength (longitudinal direction)
ε_{fuh} = design tensile strength (hoop direction)
ε_{fcu} = design compressive strength (longitudinal direction)
$\varepsilon¤_{ful}$ = manufacturers specified tensile strength (long.)
$\varepsilon¤_{fuh}$ = manufacturers specified tensile strength (hoop)
$\varepsilon¤_{fcu}$ = manufacturers specified compressive strength (long.)

The moduli of elasticity of the material in the hoop and longitudinal directions are given as:

$$E_{fl} = \frac{f_{ful}}{\varepsilon_{ful}} \quad \text{Eq. 2-7}$$
$$E_{fh} = \frac{f_{fuh}}{\varepsilon_{fuh}} \quad \text{Eq. 2-8}$$

where

E_{fl} = modulus of elasticity in the longitudinal direction
E_{fh} = modulus of elasticity in the hoop direction

The strength reduction factor, C_E , is only used to determine the baseline design strengths for a specific FRP system. These design strengths are further reduced by the Φ-factor in the basic LRFD design equation for a specific limit-state.

Table 6. Environmental strength reduction factors from LRFD-FRP

	C_E	
Fiber Material	Normal Environment	Aggressive Environment
Carbon	.85	.85
Glass	.65	.5
Aramid	.75	.7

Section 3 of LRFD-FRP provides additional guidance related to material properties and testing for FRP. Important considerations include:

- Commercial grades of vinyl ester and epoxy resins are permitted
- Styrene may be added during composite processing, but it must be less than 10% by mass. Styrene is typically added to reduce viscosity and enhance wet-out of the fibers. It should also be noted that vinylester resins already contain a considerable amount of styrene (typically ~40% by mass). The material strength properties of vinylesters tend to degrade once the styrene content exceeds 50%.
- Certain inorganic fillers or other processing aids may be added to the resin, but these may not exceed 20% by mass.
- There are no limitations on the composite manufacturing method for the FRP tube.
- The glass transition temperature of the resin must not be less than 212 °F.
- The FRP material is required to have adequate resistance to moisture absorption and alkaline environments. Details are provided in Section 3.7.1 and 3.7.2 of LRFD-FRP for moisture and alkalinity, respectively.

2.1.2.4 *Limit States for CFFT Flexural Members*

Service Limit State: The service limit state identifies three basic criteria that must be satisfied:

- Deformations
- Cracking
- Concrete compressive stresses

Deformation/deflection control criteria are based on the limitations outlined in LRFD-7. Control of cracking is achieved by limiting the tensile stress in accordance with the fatigue and creep rupture limit state. Finally, concrete compressive stresses must be less than 0.45 f'_c under the Service I load combination defined in LRFD-7.

Fatigue and Creep Rupture Limit State: This limit state defines the maximum longitudinal tensile stress that is allowed to develop in the FRP due to all sustained loading plus fatigue loading, $f_{fl,s}$. For the current study, this includes the dead loads DC and DW and the fatigue load from Section 3.6.1.4 (a single design truck with rear axle spacing fixed at 30 feet). The load factors for this limit state are:

- DC and DW = 1.0
- Truck LL for fatigue vehicle + Impact = 0.75

The stress limits, $f_{fl,s}$,.for different FRP material types are given as:

- 0.55 f_{ful} for carbon-based FRP
- 0.20 f_{ful} for glass-based FRP
- 0.30 f_{ful} for aramid-based FRP

The hoop stresses must also be checked if the FRP tube is required for confinement of concrete in compression and the concrete compressive stress is greater than 0.65 f'_c under sustained and fatigue loading.

Strength Limit State: LRFD-FRP provides guidance on determining the nominal resistance of CFFTs and corresponding Φ-factors for the strength limit state. The Φ-factor is based on the relative proportion of FRP material in the tube to the concrete area, ρ. The balanced reinforcement ratio, ρ_b, is defined as the reinforcement ratio at which the concrete fails in compression at the same time the FRP material fails in tension (similar to the balanced reinforcement ratio in reinforced concrete where the concrete fails in compression at the same time the reinforcing steel yields). The Φ-factor for flexural elements is determined as follows:

$\Phi = 0.55$ if $\rho \leq \rho_b$ Eq. 2-9

$\Phi = 0.65$ if $\rho \geq \rho_b$ Eq. 2-10

$$\Phi = 0.3 + 0.25 \cdot \frac{\rho}{\rho_b} \text{ if } \rho_b \leq \rho \leq 1.48\ \rho_b \quad \text{Eq. 2-11}$$

where

ρ = reinforcement ratio
ρ_b = balanced reinforcement ratio resulting in simultaneous concrete crushing and FRP rupture

The nominal flexural resistance, M_n, for the strength limit state may be computed using a "rigorous cross-section analysis that satisfies equilibrium and strain compatibility" or a simplified method using the following formula:

$$M_n = 0.0045 \cdot {D_o}^3 \cdot f'_c \cdot \left(100 \cdot \left(\frac{4\ t}{D_o}\right) \cdot \left(\frac{f_{ful}}{f'c}\right)\right)^{0.815} \quad \text{Eq. 2-12}$$

where

M_n = nominal flexural resistance (kip-in)
D_o = outer tube diameter (in)
t = wall thickness of FRP tube (in)
f'_c = unconfined compressive (ksi)

This relationship for flexural capacity only applies to the concrete filled FRP tube. In the current study, the assumption is always made that the cast-in-place reinforced concrete deck develops full composite action with the FRP bridge girder beneath it. Therefore, the relationship described in LRFD-FRP is of limited use. A detailed description of how the moment capacity for an FRP U-girder is obtained

using strain compatibility is provided in Section 9.1.3.1. A similar procedure is adopted for CFFTs that develop full composite action with the deck.

2.1.3 LRFD Bridge Design Guide Specifications for GFRP-Reinforced Concrete Bridge Decks and Traffic Railings

The LRFD Bridge Design Guide Specifications for GFRP-Reinforced Concrete Bridge Decks and Traffic Railings (LRFD-GFRPD) addresses glass FRP bars that are used as an alternative to traditional steel reinforcements for concrete. Bond between the bars and concrete is provided either through deformations formed during bar manufacturing or a sand coating.

2.1.3.1 *Design Philosophy*

LRFD-GFRPD is also based on a limit-state design philosophy. The language describing design philosophy is identical to what is provided in LRFD-FRP. Specific limit states identified by LRFD-GFRPD include:

- Service
- Fatigue and creep rupture (differs from LRFD-7, which is fatigue and *fracture*)
- Strength
- Extreme events

The document identifies serviceability (deflection control) and fatigue and creep rupture as limit states that will frequently control the design.

2.1.3.2 *Limitations*

The LRFD-GFRPD document does not address the following:

- Prestressed concrete is not addressed
- The use of GFRP in combination with steel is not addressed
- Bars made from carbon or aramid fibers

Other limitations include:

- The failure mechanism for GFRP reinforced flexural members is not based on the formation of a plastic hinge (GFRP bars are non-ductile)
- The strength of GFRP bars in compression shall be ignored in design
- Lightweight concrete shall not be used with GFRP bars
- The empirical design process described in Section 9.7.2 of LRFD-7 is not applicable to GFRP bridge decks

2.1.3.3 *Material Properties*

The design tensile strength, f_{fd}, and design tensile strain, ε_{fd}, for GFRP bars is based on an environmental reduction factor, C_E, that is applied to the tensile strength reported from the manufacturer. The C_E value for GFRP bars embedded in concrete exposed to earth and weather is 0.7. This is slightly higher than the C_E values prescribed for CFFT elements subjected to normal environmental conditions, 0.65, and extreme environmental conditions, 0.5. The C_E value for GFRP bars not exposed to earth and weather is 0.8.

Section 4 of LRFD-GFRPD provides additional guidance related to material properties and testing for GFRP bars. Many of the material requirements previously listed in the discussion on LRFD-FRP are repeated. Items noted with an asterisk (*) indicate a divergence between the two documents:

- *Fibers shall consist of unidirectional rovings.
- Commercial grades of vinyl ester and epoxy resins are permitted. *The base polymer of the resin shall not contain polyester.
- Styrene may be added during composite processing, but it must be less than 10% by mass. Styrene is typically added to reduce viscosity and enhance wet-out of the fibers.
- Certain inorganic fillers or other processing aids may be added to the resin, but these may not exceed 20% by mass.
- *GFRP bars shall be manufactured using any variation of the pultrusion process.
- The glass transition temperature of the resin must not be less than 212 °F.
- *Only GFRP bars of round or elliptical cross-section are allowed
- *Minimum tensile strength properties for different size GFRP bars are provided in Table 4.6.1-1
- *The modulus of elasticity for a bar, regardless of size, shall not be less than 5.7×10^6 psi
- *The transverse shear strength for a bar should not be less than 18,000 psi
- *The tensile strain at rupture for GFRP bars shall be at least 1.2%
- *The bond strength of GFRP bars, as determined by ACI 440.3R Test Method B.3 shall not be less than 1,400 psi
- The FRP material is required to have adequate resistance to moisture absorption and alkaline environments. Moisture absorption, as determined by ASTM D570 at 122 °F shall be less than 1%. Details are provided in Section 4.7.1 and 4.7.2 of LRFD-GFRPD for moisture and alkalinity, respectively. *Requirements for longitudinal wicking are provided in Section 4.7.3.
- *Specifications related to GFRP bars with bends that form during curing of thermoset resins are provided in Section 4.8.1.

2.1.3.4 *Limit States for GFRP Bridge Decks*

Service Limit State: The service limit state identifies three basic criteria that must be satisfied:

- Cracking – If the aesthetics of the structure are a concern, the crack width should be limited to 0.02 in.
- Deformations – A slightly more conservative limitation of L/1200 is imposed for bridge decks subjected to a large volume of pedestrian loading
- Concrete stresses – Under the Service I load combination from LRFD-7, the maximum allowable stress in the concrete is 0.45 f'_c.

Fatigue and Creep Rupture Limit State:

The stress range, $f_{f,s}$, resulting from the Fatigue 1 load combination in LRFD-7 is limited to 20% of the design tensile strength.

Strength Limit State: LRFD-GFRPD provides guidance on determining the strength reduction factor, Φ, and the nominal resistance of GFRP reinforced concrete bridge decks. The approach to determining Φ is identical to the approach described for LRFD-FRP (Section 2.1.2.4)

The nominal resistances for moment and shear are detailed extensively in Section 2.9 and 2.10, respectively. ACI 440.1R15 provides guidance for GFRP reinforced concrete that is not necessarily limited to bridge decks.

2.1.4 Guide Specifications for Design of FRP Pedestrian Bridges

The AASHTO Guide Specifications for Design of FRP Pedestrian Bridges is a much shorter document (~16 pages) than LRFD-7, LRFD-FRP, and LRFD-GFRPD. This document describes the required design live load for pedestrian traffic (85 lbf/in^2) as well as provisions for a single design vehicle that the pedestrian bridge is required to accommodate.

Section 3 includes several relevant design details for FRP pedestrian bridges:

- Deflection due to the pedestrian live load shall not exceed L/500
- The fundamental frequencies in the vertical and horizontal directions shall be greater than 5 Hz and 3 Hz, respectively
- Allowable stress values shall be limited to 25% of the ultimate stress values for the FRP material (as determined by ASTM D7290 – Standard Practice for Evaluating Material Property Characteristic Values for Polymeric Composites for Civil Engineering Structural Applications)
- The minimum thicknesses for different FRP element types are as follows:
    - 0.25 in for closed structural tubular members
    - 0.375 in for open structural members and plate connections

2.1.5 AASHTO Guide Specifications for Design of Bonded FRP Systems for Repair and Strengthening of Concrete Bridge Elements

Repair of existing structures using FRP composites has been gaining popularity since the late 1990's. The design objectives for strengthening reinforced concrete structures with FRP composites are significantly different from the current study. Nonetheless, a review of this document is included to ensure that any assumptions made for the allowable and ultimate stress for FRP materials are within the realm of standard practice. This review will also emphasize material properties and other durability related concerns addressed in this guide specification (referred to as FRP-Repair).

2.1.5.1 *Material Properties*

One immediate difference in the material requirements for FRP strengthening relates to the glass transition temperature, T_g, for the matrix material. The glass transition temperature is defined as the temperature above which the matrix material (resin) begins to soften and lose its strength and stiffness properties. As long as the temperature of the cured resin remains below the glass transition temperature, the material is assumed to retain all of its strength and stiffness properties and exhibits brittle, glass-like behavior at failure.

The FRP-Repair document specifies a minimum T_g of 40 °F above the maximum design temperature for the bridge ($T_{MaxDesign}$ from Section 3.12.2.2 of LRFD-7). For the case of bridges in Florida, where the $T_{MaxDesign}$ is on the order of 105 °F, the required T_g for the composite would be 145 °F. The Tyfo SCH—41

is a common carbon-epoxy FRP repair system used to strengthen reinforced concrete structures. The T_g for the epoxy associated with the system is 180 °F, which is considerably lower than the 212 °F required by LRFD-FRP and LRFD-GFRPD.

The actual glass transition temperature that a resin achieves is a function of the temperature that is obtained during the curing cycle. For example, the glass transition temperature of resins in composites that are cured at elevated temperatures in an autoclave might exceed 500 °F. For composites that are cured at room temperature, the amount of exothermic heat generated by the composite during curing will affect the T_g of the cured composite. If the composite is relatively thick, there will be more exothermic heat generated and the resulting T_g will be higher. If the laminate is relatively thin, the exothermic heat generated will be low and result in a lower T_g. For externally applied strengthening systems, there is an added complication in that the large thermal mass of concrete can readily absorb the small amount of exothermic heat generated by the relatively thin laminates during curing. This explains why it is difficult to achieve high T_g values in externally applied strengthening systems. For composites that are cured in a factory setting, the desired T_g value is obtained by carefully controlling the amount of exothermic heat generated during curing. If there is not enough composite mass to generate the required exothermic heat, the part can be post-cured in an oven to raise the final glass transition temperature of the composite.

Additional limitations for FRP composite systems described in FRP-Repair include:

- The moisture equilibrium content, as determined by ASTM D5229, shall not be greater than 2%. The limit established in LRFD-FRP and LRFD-GFRPD is 1%.
- Specifications are also provided for other durability-related material properties. LRFD-Repair requires that specimens must retain 85% of their mechanical properties after being subjected to the following environmental conditional protocols:
    - Water – Specimens shall be submersed in distilled water at 100 °F and tested after 1,000, 3,000, and 10,000 hours of exposure
    - Alternating UV and Humidity – Samples are conditioned under Cycle 1-UV conditions per ASTM G154
    - Alkali – Similar to water conditioning, except samples are placed in a saturated calcium hydroxide solution (pH~11) at 73 °F.
    - Freeze-Thaw – Samples are subjected to 100 cycles of freeze-thaw

2.1.5.2 *Limit States*

The strength limit state described in FRP-Repair is not necessarily applicable to the current study because the majority of the overall strength is derived from the element being strengthened. The fatigue limit state described in FRP-Repair for flexural elements does place relevant limits on the strain experienced by the FRP due to the fatigue load combination established in LRFD-7. For glass FRP, the strain is limited to 20% of the manufacturer's specified ultimate tensile strain. The limits for carbon and aramid FRP are 55% and 30%, respectively. It should be noted that this strain limit does not include an environmental reduction factor, C_E, like the limits prescribed for CFFTs and GFRP reinforced bridge decks.

Creep-rupture due to dead loads is not a concern for FRP strengthening systems because the composite is normally applied while the dead loads are acting on the structure.

2.1.6 Summary of AASHTO Design Guidelines

The five AASHTO documents reviewed for this section establish critical design-space boundaries for the current study. The loading demands for highway bridges, load combinations for predetermined limit states, and guidelines for structural analysis are well-documented in LRFD-7. Specific considerations for FRP materials are provided in LRFD-FRP and LRFD-GFRPD. These documents also provide modified limit-states for different FRP materials to account for their unique properties related to durability, fatigue, and creep-rupture.

While these AASHTO documents provide an important foundation for developing and evaluating new concepts for FRP bridge girders, there are important issues not addressed by these specifications:

- **Developing composite action between FRP girders and reinforced concrete bridge decks**. A particular concern involves the case where a reinforced concrete deck requires replacement. Significant damage may occur to FRP elements during deck removal and reconstruction.
- **Laminate architecture**. The FRP-related design specifications provide allowable stress values based on material properties obtained from testing by the manufacturer. Specific details regarding laminate architecture and fiber orientation requirements for CFFTs are absent. This may lead to concerns surrounding the overall system performance at different limit states.

Current FHWA sponsored research with the Virginia DOT is investigating Carbon FRP pre-stressing strands for highway bridge girders. In addition to this work, NCHRP 12-97, Guide Specification for the Design of Concrete Bridge Beams Prestressed with CFRP Systems, is nearing completion (expected completion is December 2017) and will provide design guidelines in AASHTO LRFD format.

2.2 ACI

The American Concrete Institute (ACI) released their first guidelines for the design of structural concrete reinforced with FRP bars in 2001. The focus of the current study is not directed towards designing rectangular bridge girders that replace traditional steel reinforcement with FRP composite reinforcement. In the future, there may be interest in open-top FRP-reinforced concrete box girders. The ACI documents listed in Table 7 are relevant references for the current study.

Table 7. Relevant ACI publications related to FRP composites for bridges

440.1R-15: Guide for the Design and Construction of Structural Concrete Reinforced with Fiber-Reinforced Polymer (FRP) Bars
440.2R-08: Guide for the Design and Construction of Externally Bonded FRP Systems for Strengthening Concrete Structures
440.4R-04: Prestressing Concrete Structures with FRP Tendons (Reapproved 2011)
440.6-08: Specification for Carbon and Glass Fiber-Reinforced Polymer Bar Materials for Concrete Reinforcement
SP-245: Case Histories and Use of FRP for Prestressing Applications
549.4R-13: Guide to Design and Construction of Externally Bonded Fabric-Reinforced Cementitious Matrix (FRCM) Systems

2.3 ASCE LRFD Pre-Standard

In 2010, an ASCE project team finalized a document for the American Composites Manufacturing Association (ACMA) entitled *Pre-Standard for Load and Resistance Factor Design (LRFD) of Pultruded Fiber Reinforced Polymer Structures* [4]. This pre-standard describes its intended use as supporting "the design of new buildings and other structures," but the document is clearly not intended to encompass the design of bridge superstructure elements (i.e. FRP bridge girders). The commentary section on loads and load combinations (C1.5) limits the applicability of the pre-standard to building construction and excludes vehicle loads on bridges.

2.4 Florida Department of Transportation

The FDOT establishes criteria for the use of FRP composites through two primary documents. First, the FDOT Structures Manual, Volume 4 [1], describes the types of FRP products and different manufacturing methods that are suitable for specific structural applications. For example, Section 6.1A permits the use of vacuum infusion processed (VIP) structural shapes for bridge fender systems as long as they meet the criteria established in Section 3.14 of the FDOT structural design guidelines. Section 6.1B indicates that VIP shapes can will be considered for use in the following applications:

1. Decks for pedestrian bridges
2. Single sign support posts
3. Light poles
4. Sheet piles
5. Stay-in-place formwork
6. Concrete-filled tubes used as arch beams for culverts

Second, the current *FDOT Standard Specifications for Road and Bridge Construction*[*5*] (Section 973) provides detailed requirements for FRP material properties that will be used in FDOT projects. Requirements for pultruded shapes reference the ASCE *Pre-Standard for Load and Resistance Factor Design (LRFD) of Pultruded Fiber Reinforced Polymer Structures*. Specific properties for vacuum infusion processed (VIP) structural elements are listed directly in the FDOT Standard Specifications document. The requirements for VIP structural shapes are identical to the ASCE Pre-Standard, but slightly lower values are specified for VIP FRP plates. A sample of the requirements for pultruded and VIP shapes is provided in Table 8.

Table 8. Minimum physical property requirements for pultruded and VIP structural shapes.

Physical Property	Minimum Required Value	Test Method
Long. tensile strength	30,000 psi	ASTM D638 (pultruded)/ D3039 (VIP)
Transverse tensile strength	7,000 psi	
Long. tensile modulus	3×10^6 psi	
Transverse tensile modulus	0.8×10^6 psi	
Interlaminar shear strength	3,500 psi	ASTM D2344
Glass transition temperature	> 180 °F	ASTM D4065
Coefficient of thermal expansion	$< 7.5 \times 10^{-6}$	ASTM D696

Note: Property requirements for pultruded shapes and VIP shapes are identical unless noted.

The FDOT currently permits the use of carbon FRP (CFRP) strands for prestressed piles. The size and strength requirements are provided in Section 933-1.3 of the FDOT Standards and Specifications for

Bridge Construction. Single strands range in size from 0.20 in diameter to 0.5 in diameter. Larger diameters are achieved by combining 7, 19, or 37 strands together. Information on select cable sizes is provided in

Table 9. Typical sizes and loads of FRP prestressing strands and bars [5]

Cable type	Nominal diameter (in)	Nominal x-section area (in^2)	Nominal ultimate load (kips)	Nominal ultimate stress (ksi)
1- strand – 5 mm	0.2	0.03	9	300
7-strand – 10.5 mm	0.41	0.09	32	356
1-strand – 9.5 mm	0.38	0.11	35	318
19-strand – 25.5 mm	1.0	0.472	105	222
37-strand – 40 mm	1.57	1.24	270	218

2.5 Aerospace Industry

There are generally two types of standards and specifications used in the aerospace industry. The first type are standards that are developed by specific institutions, such as the Society for Aerospace Engineering's (SAE) Aerospace Materials Specifications, the US Department of Defense Composite Materials Handbook, and numerous standards developed by the American Society of Testing and Materials (ASTM) Committee D30. The second major type are proprietary specifications that each manufacturer has developed and owns. Common examples include DMS (McDonnell Douglas), BMS (Boeing), STP (Lockheed Martin), CMMP (Cessna) [6], and GAMPS (Gulfstream). These specifications typically are used to ensure that only approved materials from pre-approved suppliers are used in the production of components for a particular aerospace structure. Requirements for manufacturing and materials handling are also included in these proprietary specifications.

Due to the complexity of composites manufacturing and structural design, there is not a common specification for fabrication in use by the entire aerospace industry. At each company, each individual material system has its own processing specification. This has been a major concern for the airlines. For instance, it is common to see DMS, BMS, and Rockwell specifications on the same drawings issued for manufacturing. According to Alex Velicki from Boeing, there is incredible complexity surrounding the specifications for their PRSEUS stitched composite panels (described in Chapter 5): "Each material has its own spec that lays out the requirements for purchasing the material. Then, each process will have its own spec that details how the material is to be handled and manufactured. There's probably about a dozen specs needed to buy the materials [and] process a PRSEUS panel" (A. Velicki, private communication, October 29, 2015).

3. Material Systems and Manufacturing Methods

The use of composite materials has grown steadily during the last 50 years. Numerous applications can be found in aviation and aerospace engineering, the automotive industry, civil infrastructure, marine engineering, sporting goods and electrical components [7,8,9,10]. Commonly cited advantages of composites compared to conventional materials like aluminum and steel include:

- light weight
- high strength and stiffness to weight ratio
- tailorable strength and stiffness properties
- resistance to corrosion and fatigue
- tailorable thermal and electrical conductivity

At the same time, these materials also possess some inherent disadvantages:

- high cost of base materials and fabrication
- weak transverse properties that may lead to delamination and failure
- analysis and simulation can be complex
- difficult to detect internal damage
- matrix materials may be subject to environmental degradation
- reuse and disposal concerns

3.1 Properties of Composites

A composite material is broadly defined as a combination of two or more different materials. This combination generally results in better mechanical properties than when the individual components are used alone. The two constituents are typically a fiber and a matrix. Common types of fibers include glass, aramid, and carbon, while matrices can be polymers, metals, or ceramics [11,12].

Composites offer several advantages over steel, which is often limited by its high weight and susceptibility to corrosion that ultimately result in high transportation and maintenance costs. For instance, while a cubic foot of steel could weigh around 500 pounds, replacing that volume of steel with composites can save 60% to 80% in weight [13]. Composites also have high strength-to-weight and stiffness-to-weight ratios, high corrosion and fatigue resistance, and low thermal expansion. Glass and aramid fibers have the added advantage of being non-conductive. The properties of composites are determined by fiber and matrix properties, which can be summarized as follows[14,15]:

- **High strength and stiffness**: Individual carbon fibers (without matrix material) have strengths on the order of 530 ksi to 800 ksi with a stiffness modulus of 80 Msi. The corresponding unit weight of the fiber material is only 112 lbf/ft^3. The resulting strength-to-weight and stiffness-to-weight ratios are fundamental to the primary advantages of composites [16].

- **Corrosion and Chemical Resistance**: Composites offer high corrosion and chemical resistance. Steels and aluminums corrode in the presence of water and require surface coatings. Because the outer surface is formed by plastic polymers, composites have very good corrosion and chemical resistance [13].

- **Fatigue Resistance**: While most metals have fatigue strengths of about 40% to 50% of their tensile strength, composites can maintain 70% to 80% of their strength in fatigue loading. For instance, unidirectional carbon/epoxy composites have their fatigue strength up to almost 90% of their static strength.

- **Design flexibility**: Composites offer a great amount of design flexibility. Different composite structures can be designed by employing different fibers with various properties and using different matrix systems. For instance, a composite material having a zero coefficient of thermal expansion can be fabricated by selecting suitable materials and the correct lay-up sequence.

- **Impact Resistance and Anti-vibration**: Composites offer good impact properties. Glass and Kevlar composite fibers provide higher impact strength than steel and aluminum. In general, long continuous fibers provide three to four times improved impact properties than short fiber composites. In addition, vibration and noise characteristics for composites are better than metals. Composites dampen vibrations an order of magnitude better than metals as used in a variety of applications such as airplane structures and golf clubs.

3.2 Composite Constituents and Materials Selection

General properties for two different types of composite materials are provided in Table 10. There are four steps involved in determining an appropriate material combination. The first step is to understand and define the requirements. Based upon the requirements, possible materials systems and manufacturing processes that meet the minimum or maximum requirements should be determined. The next step is to determine the candidate materials for the application. More than one material system and manufacturing method can be chosen to provide a wide choice of creative and innovative designs. Lastly, composite parts must be prototyped and tested to validate the design.

Table 10. General properties of thermoset and thermoplastic composites [13].

Property	Thermoset Composites	Thermoplastic Composites
Fiber volume	Medium to high	Low to medium
Fiber length	Continuous and discontinuous	Continuous and discontinuous
Molding time	Slow: 0.5 to 4 hours	Fast: less than 5 min
Molding pressure	Low: 1 to 7 bars	High: greater than 14 bars
Material cost	Low to high	Low to medium
Safety / handling	Good	Excellent
Solvent resistance	High	Low
Heat resistance	Low to high	Low to medium
Storage life	Good (6 to 24 months with refrigeration)	Indefinite

The composite materials are made up of at least two constituents. The structural constituent, usually the fiber reinforcement, provides the internal structure of the composite. The body constituent,

i.e. matrix, is used to enclose the structural constituent and provide its bulk form. The following sections describe different types of structural and body constituents [11, 16,17].

3.2.1 Structural Constituents (Fibers) and Their Cost Per Pound

Fibers consist of thousands of individual filaments, where each filament has a diameter of 5 µm to 15 µm. One exception is thick boron fibers, which may have diameters on the order of 100 µm. The most widely used fiber materials are E-glass, S-Glass, carbon/graphite, boron, and aramid/Kevlar. Properties are shown in Table 11. Note that the price per pound or area differs for different types, properties, and manufacturing companies.

3.2.1.1 *Glass Fibers*

Due to their low (E-glass) to moderate (S-glass) costs with high mechanical properties, glass fibers are used extensively in composite applications, accounting for more than 70% of the structural constituents for thermosetting resins. E-glass was first developed for production of continuous fibers and has become the most common glass fiber produced today. S-glass is a high-tensile strength glass with a tensile strength that is 33% greater than E-glass. The modulus of elasticity of S-Glass is about 20% greater than that of E-glass. S-glass is generally used for aerospace applications due to its higher strength-to-weight ratio and fatigue limit; however, it costs much more than E-glass. In general, the cost of E-glass is around $0.75 to $1.25 per pound (J. Gibson, Composites One, private communication, Jan. 12, 2016) while S-glass is around $5.00 to $7.00 per pound [13].

3.2.1.2 *Carbon Fibers*

Carbon or graphite fibers are the ideal structural constituent for lightweight, high-strength, and high-stiffness structures. Carbon fibers are relatively expensive compared to other fibers. Continuous tows contain several hundred to thousand filaments per strand and generally fall into either high modulus (intermediate-strength) or high strength (intermediate-modulus) category. The high modulus fibers are more expensive than the high strength fibers. The cost of carbon fiber varies from $8.00 to $40.00 per pound [13].

3.2.1.3 *Kevlar (Aramid) Fibers*

Among all the fiber types, Kevlar has the highest tensile strength-to-weight ratio. Kevlar is commonly used when the objective is to produce tough, impact-resistant structures. The fibers were originally developed to replace steel in tires, but they have found more use in impact-resistant products. Kevlar 29 is a low density, high strength fiber used for ballistic protection, whereas Kevlar 49, with a higher modulus, is more commonly used as a reinforcement for plastic composites in aerospace, marine, and sports equipment. One disadvantage of Kevlar is its difficulty to cut or machine. Kevlar fibers cost approximately $15.00 to $20.00 per pound [13].

Table 11. Properties of individual fibers and conventional bulk materials[13].

Material	Diameter (mil)	Unit weight (lbf/ft^3)	Tensile Modulus (Msi)	Tensile Strength (ksi)	Melting Point (°F)	% Elongation at Break	Relative Cost
Fibers							
E-glass	0.28	158	10	500	2800+	4.8	Low
S-Glass	0.60	156	12.5	653	2800+	5.7	Moderate
Carbon, high modulus	0.30	118	58	261	>6300	1.5	High
Carbon, high strength	0.30	106	35	378	>6300	0.8	High
Boron	5.1	162	58	507	4200	-	High
Kevlar 29	0.47	90	11.6	406	930	3.5	Moderate
Kevlar 49	0.47	90	19	551	930	2.5	Moderate
Bulk materials							
Steel		490	29	0.34-2.1	2700	5-25	<Low
Aluminum alloys		168	10	0.14-0.62	1100	8-16	Low

3.2.2 Fiber Styles

The body constituents in composite materials can have either a non-specific fiber arrangement, such as chopped fibers (nonwoven), or long fibers grouped together, called tows or yarns. Tows and yarns may then be assembled into fabrics using either weaving or braiding methods. Different forms of fiber reinforcements are summarized in Table 12.

3.2.2.1 *Chopped Fibers*

Chopped fibers are made by cutting continuous fibers during the fabrication processes. Continuous fibers are chopped by a machine into small pieces in length ranging from 0.125 in to 3 in and blended with various resin systems before their applications [12,28]. While the shorter chopped fibers are best suited for blending with thermoplastic resin systems for injection molding, longer chopped fibers are mixed with thermoset resin systems for compression and transfer molding processes. Note that the mechanical properties of the formed product are much lower than continuous fiber composites due to the presence of randomly oriented chopped fibers. One product example is the chopped strand mats, which are made by depositing chopped fibers and resins on a conveyer belt. These mats are typically used in non-structural composite parts with limited load carrying capability.

3.2.2.2 *Unidirectional Fibers*

There may be an application that 80% of structural loads occurs in one direction. In this case, orienting 80% of structural fibers in the same direction can be efficient. Because of producing fabrics with 80% of their fibers in one direction would not be stable for practical applications, the fibers are coated together with resin systems in a sheet form. These materials are called pre-pregs (short for pre-impregnated with the matrix resin). Pre-pregs with all fibers are oriented in the same direction are called unidirectional pre-pregs or tapes. As the resin is already embedded in the fibers, and no additional agents are needed, pre-pregs must be kept refrigerated to prevent them curing prematurely.

Dry unidirectional fabrics are also available, but they will always require at least a small amount of material running perpendicular to the primary fiber direction to maintain stability in the fabric.

Compared to a yarn with twisted continuous fibers (filaments), a tow is an untwisted bundle of filaments that generally contains hundreds to tens of thousands of filaments [18]. Tow size is usually expressed in terms of a "k" value where a 30k tow contains 30,000 filaments.

3.2.2.3 *Multi-axial Fibers*

Woven fabrics consist of at least two threads which are interlaced. Long tows are aligned parallel in the warp direction while a second tow is passed back and forth in the weft direction. The amount of fiber in different directions is controlled by the weave pattern. The weave style can be varied according to crimp and drapability (ability to conform tool surface during preforming or lay-up stage). In general, low crimp fabrics provide better mechanical performance because straighter fibers can carry large loads. Drapable fabrics are designed to be easier to lay up over complex forms. Common weave styles are illustrated in Figure 3.

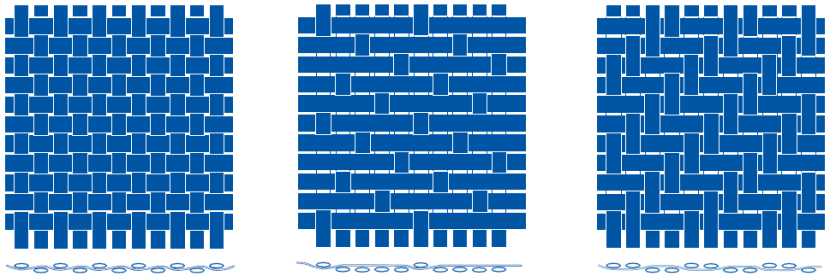

Figure 3. Fabric weave styles: (A) plain weave, (B) satin weave, and (C) twill weave. [19].

Stitched fabrics provide a mechanical connection between the fibers allowing the completed preform to be handled without shifting. Stitching has been implemented for more than two decades to provide many additional benefits, such as through-the-thickness reinforcement and improving damage tolerance [11]. Non-crimp fabrics (NCF) are manufactured by stitching unidirectional yarns in a base layer to additional layers of unidirectional yarns laid down at an angle to the primary direction. This process allows for better handle-ability and enhances the out-of-plane properties of the composite. With the advancement of composite fabrication methods, this non-crimp stitched fabric has been widely adopted in the aerospace industry [20]. Different fiber materials can be used in NCFs including carbon, glass, and aramid fibers. One challenge, however, relates to the potential for fabric damage during the stitching process. As the needle passes from one side of the stack to other, yarns and fibers are easily damaged. As a result, the density of the stitched portion should be low enough to limit damage but high enough to achieve the desired properties of the composite [21]. The non-crimp stitched fabric manufacturing process is illustrated in Figure 4.

Table 12. Various forms of fiber reinforcements [12,19]

Reinforcement		Advantages	Applications
Chopped Fibers		• High strength in compression and injection molded parts	Injection molding
Unidirectional	UD Prepreg	• High strength and stiffness in one direction • Low fiber weights; approx. 100 g/m^2 • High fiber weights; approx. 3000 g/m^2 for glass fiber and 800 g/m^2 for carbon fiber	Sports goods Aircraft Primary structures Wind energy Load carrying structures
	Single Tow	• Suitable for filament winding • Very narrow width for accurate fiber placement (1 mm)	Pressure vessels Drive shafts Tubes
	Slit Tape	• High strength and stiffness in one direction • Low fiber weights; approx. 134 g/m^2 • Ideally suited for high deposition of complex parts	Aerospace primary structures
	Fabrics (> 80 % warp)	• For components requiring predominant strength and stiffness in one direction • Good handling characteristics • Weights from 160 to 1000 g/m^2	Aerospace Industrial Sport and leisure
Multi-axials	Woven Fabrics	• Strength and stiffness in two directions • Very good handling characteristics • Good drape • Choice of weave styles • Possible to mix fibers • Weights from 20 to 1000 g/m^2	Aerospace Industrial Sport and leisure Wind Energy
	Non-Crimp (stitched) Fabrics	• Time-saving, cost-effective technology • Strength and stiffness in multiple directions • Unlimited ply orientation • Ability to optimize weight distribution within a fabric • No crimp • Less waste for complex lay-ups (cross plies) • Reduced processing cost • Heavy weights achievable	Aerospace Automobile Wind energy (blades)

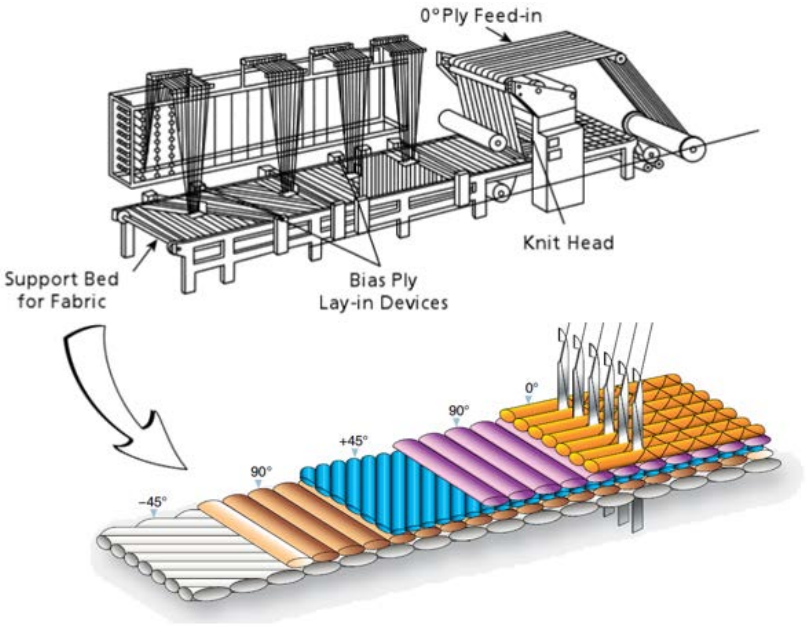

Figure 4. Non-crimp stitched fabric (NCF) manufacturing process [22]

3.2.3 Body Constituents (Matrices) and Their Cost per Pound

The matrix, usually a resin, accounts for 30 to 40 percent of a composite by volume. The matrix properties influence the transverse mechanical properties, inter-laminar shear characteristics, and operational temperature of the composite. The matrix serves two important functions: (1) by surrounding the fibers, it holds the fibers in place and (2) under applied forces, it deforms and distributes the internal stresses to the higher modulus structural constituent. Both of these factors influence the materials selection, fabrication methods, and tool design. The matrix can be categorized as either thermoset or thermoplastic based upon its polymer chain structures. The formation of crosslinks for each matrix type are shown before and after processing in Figure 5.

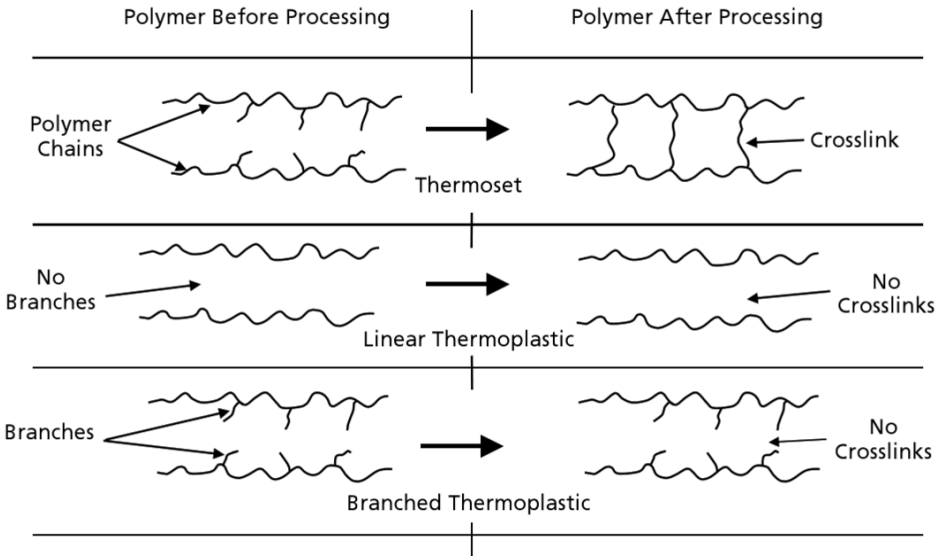

Figure 5. Comparison of thermoset and thermoplastic polymer structures.

During the curing process, thermosets are converted into three dimensional cross-linked structures that are infusible and insoluble. As curing progresses, by either exothermic heat or externally supplied heat, the chemical reactions accelerate resulting in less mobility of molecules and increased viscosity. After the resin is cured, i.e. forms a rubbery solid, it cannot be re-melted. In contrast, thermoplastics are not chemically cross-linked with heat and therefore do not require a long cure time. Unlike the thermosets, they can be re-melted and then cooled to form a different shape. A major obstacle of thermoplastics is that they are highly viscous and are difficult to combine with continuous fibers in a viable production process [12,23]. The total market share for thermosets is about 60%-65% and the market share for thermoplastics is about 35%-40%. For thermosets, unsaturated polyester is estimated at about 85%, epoxy about 10%, and the remaining 5% for all the others. In thermoplastics, poly-propylene is generally used with Nylon 6,6 and PEEK[23].

The following sections describe different types of thermoset and thermoplastic matrices with estimated cost for each resin system. The current resin costs were were obtained from the on-line publication *Plastic News* [24].

3.2.3.1 *Thermosets*

Polyester (unsaturated)

Unsaturated thermoset polyesters, or simply polyesters hereafter, are the most commonly used thermoset resin type for composites. *Unsaturation* is a term applied to organic molecules that contain the carbon-carbon double bond. They are extensively used in commercial applications, such as boats, corrugated sheets, and golf carts due to their mechanical and electric properties and resistance to chemical attack. Their cost is also relatively low. Polyesters are priced about 30% - 50% less than epoxy and 25% less than vinyl esters [28]. They are generally not recommended for use with carbon or Kevlar fibers. This is due primarily to the relatively low mechanical properties of polyester resin as compared to the relatively higher mechanical properties for carbon and Kevlar fibers. Also, the sizing agents that are applied to carbon fibers to promote bond between the matrix and the fibers are typically formulated to react with epoxies and vinyl ester resins. Polyester resin costs about $1.74 - $1.94 per pound with very large volume[24] but generally costs around $2.50 per pound [25].

Vinyl ester

Vinyl esters are a combination of polyester and epoxy resins that are primarily used with glass fibers. Vinyl esters are commonly used in pultrusion, filament winding, compression molding, and resin transfer molding manufacturing processes. Vinyl esters have similar mechanical properties to polyesters but are tougher and have better moisture and chemical resistance. The resin costs around $4.50 per pound [25].

Epoxy

Epoxy resin is almost exclusively used in high performance composite products. It is almost three times stronger than the next strongest resin type and adheres very well to most composite fibers. Although depending upon hardeners and curing processes, epoxies generally have very good mechanical properties, good electrical and chemical resistance. They have better temperature performance than polyesters and vinyl esters and can be used at temperatures up to 275 °F. Epoxies are relatively expensive and cost around $7.50 per pound [25].

Phenolic

Phenolic resins are used in public transport vehicles, oil rigs, and buildings because of their good heat resistance. The resins are also extensively used for aircraft interiors. Similar to other thermoset resins, phenolic resins have good mechanical properties, electrical, and chemical resistances. Phenolic resins have limited flexibility though and can be difficult to process. Phenolic resins are generally less expensive than polyesters.

Bismaleimide and polyimide

These resin types are used for high temperature composite applications. The glass transition temperature of these resins are above 550 °F, which is considerably higher than aforementioned resins. Polyimides are exclusively used in high performance composites, especially in the form of pre-pregs. The lack of use of these resins is attributed to their processing difficulty. Bismaleimide resin starts at $50.00 per pound [26].

Table 13. Typical room temperature properties of thermoset polymers [13,27,28]

Material	Unit weight (lbf/ft^3)	Tensile Modulus (ksi)	Tensile Strength (ksi)	Compressive Strength (ksi)	Elongation (%)	Glass Transition Temperature (°F)	Coefficient of Thermal Expansion (10^{-6}/°F)
Polyester	68-94	174-275	5.8-13	13-36	2-5	122-212	33-110
Vinyl ester	72	435-580	9.5-13	18.5	1-5	212-302	28-31
Epoxy	67-87	290-870	5-19	14.5-29	1-8.5	122-482	25-61
Phenolic	75-87	390-595	5-8.7	-	2-3	-	5.6
Bismaleimide	82	520-595	7-11.3	29	1-6.6	482-572	28-44
Polyimide	89-118	450-710	10-17.4	-	1.5-3	536-608	50

3.2.3.2 *Thermoplastics*

Thermoplastic resins are generally ductile and tougher than thermoset resins. They are resistant to damage from low velocity impact and are widely used with and without reinforcements. They can be melted by heating and solidified by cooling to allow for repeated reforming. As shown in Figure 5, thermoplastic resins are not cross-linked and their strength as well as stiffness are based upon the monomer properties and the degree of entanglement of the polymer chain. This is the reason why thermoplastics show lower creep resistance than thermosets. Some typical materials properties of selected thermoplastic resins are shown in Table 14.

Table 14. Typical unfilled thermoplastic resin properties

Material	Unit weight (lbf/ft^3)	Tensile Modulus (ksi)	Tensile Strength (ksi)	Compressive Strength (ksi)	Elongation (%)	Glass Transition Temperature (°C)	Coefficient of Thermal Expansion (10^{-6}/°C)
PP: Polypropylene	56	145-232	25-41	-	100-600	-4-23	81-100
PEEK: Polyether ether ketone	83	464-580	92-100	-	50-150	289	26
PPS: Polyphenylene sulfide	81-87	479-493	70-80	110	3	410	28-55.5
Nylon 6	69-75	232-551	95	34	40-80	134	80.6
PS: Polysulfone	77	363	70-75	-	50-100	374	31-55.5

Polypropylene (PP)

Polypropylene, the lightest thermoplastic resin, is one of the most widely used engineering matrix materials. Polypropylene is often combined with fiber materials to obtain FRP composites[27,29]. PP resins possess good mechanical properties at ambient temperature and have a high cost to performance index. Although PP shows good electrical insulating properties, even in a wet environment, it is sensitive to ultraviolet light and has poor creep behavior. PP resin generally costs around $1 per pound [24].

Polyether ether ketone (PEEK)

PEEK resins are also one of the most widely used high-performance thermoplastics systems. Due to their excellent mechanical, chemical, and electrical properties as well as good creep resistance and fatigue behavior, PEEK resins have been well-suited for exterior applications in aerospace applications. PEEK resins absorb water 10 times less than epoxy. One drawback is its cost; around $50.00 per pound [13,24].

Polyphenylene sulfide (PPS)

PPS resins have very good resistance to heat and do not dissolve in any solvent under 392°F. The resin also provides resistance to acids, alkalis, bleaches, and abrasions. PPS resin generally costs around $5 per pound [24].

Nylon (polyamides)

Nylon is the brand name of an aliphatic polyamide plastic produced by DuPont. Nylon resins are generally used for various pultruded and injection molding processes and provide a good surface appearance once cured. Different types of Nylon include Nylon 6 and 6,6. Nylon 6,6 absorbs less moisture and has a melting point around 500°F. Both cost around $1.60 per pound[24].

Polysulfone (PS)

Similar to PPS, PS resins have high toughness and stability under high temperature. They are frequently used in warm water pumps and are insensitive to microwave radiation enabling its wide application in the electronics industry. PS resin generally costs around $5.5 per pound[24].

3.2.4 Material Selection Summary

The critical factors to be considered during the material selection phase include[23]:

- Anticipated service-life
- Temperature (both average and extremes)
- Environment (outdoor exposure, light, moisture, radiation, etc.)
- Physical properties (transparency, gas permeability, tribological properties etc.)
- Mechanical properties (cyclic stresses, impact etc.)
- Chemical exposure (risks of corrosion, environmental pollution, pollution etc.)
- Electrical properties (influence of moisture, temperature and aging)
- Dimensional tolerance
- Weight
- Lifecycle costs including the expenses of fabrication, assembly, and maintenance

Price per pound for the aforementioned composite fibers and matrix materials are listed in Table 15. Note that all material costs depend upon quantity purchased and current market prices. For composite bridge girder fabrication, multi-axial E-glass NCF fibers and vinylester resin are recommended due to their high strength and stiffness, easier resin flow, good chemical resistance, and relatively inexpensive material costs.

Table 15. Price per Pound for Matrix and Fiber Materials [13,24]

Matrices					
Thermosets					
	Polyester	Vinylester	Epoxy	Phenolic	Bismaleimide
$/lb.	1.8-3.5	4.0-5.0	7.5-10.0	1.0-1.5	~ 50.0
Thermoplastics					
	Polypropylene	PEEK	PPS:	Nylon 6	PS:
$/lb.	0.8-1.2	~ 50.0	4.5-5.5	1.2-2.0	5.0-6.0
Fibers					
Type	E-glass*	S-glass	Carbon	Kevlar	
$/lb.	0.8-2.0	5.0-7.0	8.0-40.0	15.0-20.0	

*(Vaar, J., Vectorply, private communication, Apr. 11, 2016)

3.3 Composite Manufacturing Processes

Most composite manufacturing processes can be described as liquid molding. This process involves impregnating the matrix (resin) into a fiber network bed to saturate all the empty spaces between the fibers with resin [30]. The resin from a reservoir is transferred into the mold under positive pressure or drawn by subjecting the mold to a vacuum. Thermoplastic resins are not typically used due to their high

viscosity, which requires very high injection pressure. Thermoset resins are preferred in the liquid molding process due to their low viscosity. There are various liquid molding composite fabrication methods, and selection of a method depends on materials, part design, application, cost, and the available facilities. Some common methods are resin transfer molding (RTM), vacuum infusion process (VIP) or vacuum assisted resin transfer molding (VARTM), Seemann's composite resin infusion molding process (SCRIMP), and autoclave manufacturing methods.

3.3.1 Resin Transfer Molding (RTM)

Resin transfer molding (RTM) is one of the most developed and widely used composite molding process [11]. The basic RTM process (Figure 6) consists of the following steps: a dry composite preform is first placed a rigid die mold and the mold is closed. Next, a low viscosity thermoset resin is injected to the mold under pressure and the part in the closed mold is cured at elevated temperature. Finally, the cured part is removed and cleaned up. Although RTM is an excellent process for fabricating large parts with complex geometries, it has a several drawbacks. One major disadvantage is the cost of tooling. A well-designed tool is a pre-requisite for fabricating a fine composite part. The other is related to fiber content. If a high volume of continuous fibers are present in the dry preform, smooth resin flow is hindered. This will prevent rapid manufacturing. The compression RTM, shown in Figure 6, was developed as the result to fill the need enabling short mold filling times [18].

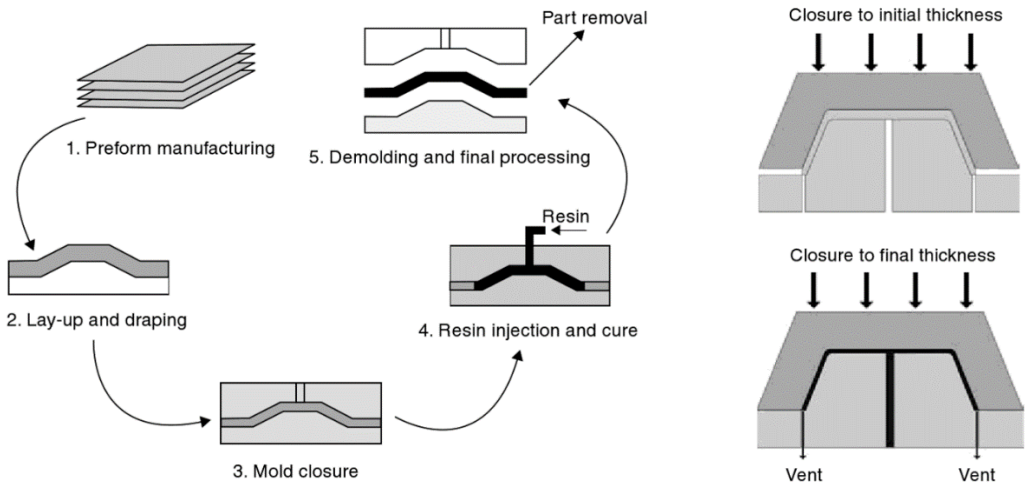

Figure 6. Schematics of (left) typical RTM and (right) Compression RTM (CRTM) processes [18].

There have been several variations developed from RTM to fabricate near net molded composite parts at a lower cost. Well-known methods include vacuum infusion or vacuum assisted resin transfer molding (VIP/VARTM) and SCRIMP.

3.3.1.1 *Vacuum-Assisted Resin Transfer Molding (VARTM)*

VARTM, as also known as VIP (vacuum infusion process), offers numerous advantages over traditional RTM in terms of tooling costs, room temperature processing, and scalability for large structures [31]. VARTM uses a vacuum to draw the resin through the dry preform instead of injecting positive pressure into the mold. Because only a single-sided mold is used along with a vacuum bag, the tooling costs are reduced. The process also enables the fabrication of large parts because they can be cured at room temperature, eliminating the requirement of autoclave curing. Although the autoclave is not required, ovens or integrally heated tools are normally used with lightweight tools since the

pressure applied is limited to one atmosphere. The resins used for VARTM processing should have even a lower viscosity than those used for traditional RTM. Resin viscosities less than 100 centipoise are desirable to give the flow needed to impregnate the preform at vacuum pressure [11]. Figure 7 provides a schematic of the VARTM process. A single-sided rigid mold is used and the mold is sealed with a flexible bag by drawing a vacuum to remove the air from the mold and compacting the preform placed on the tool surface. The resin is drawn into the mold from a reservoir at atmospheric pressure. The VARTM process results in very low void content and excellent mechanical properties due to the relatively high glass content. The ultimate fiber content is determined by fiber architecture and pressure [32].

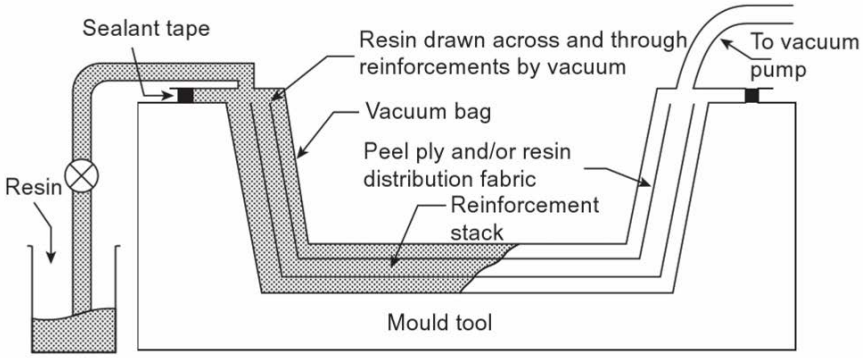

Figure 7. Typical vacuum-assisted resin transfer molding process [33]

3.3.2 Seemann Composite Resin Infusion Molding Process (SCRIMP) and Controlled Atmospheric Pressure Resin Infusion (CAPRI)

One major drawback of VARTM is its slow resin filling due to the low pressure differential between the inlet and the exit. Bill Seemann invented SCRIMP™ (Seemann Composite Resin Infusion Molding Process) technology in 1990 to overcome the slow filling by adding a resin distribution medium (a series of flow channels) between the fiber preform and the vacuum bag. This distribution medium of high porosity allows the resin to easily flow in the in-plane direction due to the high permeability of the materials used [18]. Figure 8 (top) shows a typical SCRIMP™ schematic. Note that the resin flow medium is placed underneath the vacuum bag, which enables faster feeding of resin through the fibers and saturating the part faster than VARTM. This rapid resin filling is possible because it only needs to penetrate across the thickness direction as compared to the in-plane directions that are generally required for RTM process. The design of the distribution medium must ensure complete mold filling as the resin could reach the vent before completely saturating the dry preform.

Another vacuum infusion process similar to VARTM is Boeing's proprietary CAPRI (Controlled Atmospheric Pressure Resin Infusion) process invented in 1999 [20]. The main feature of this process is that the resin is infused into the preform at less than one atmospheric pressure (~7 psi) to maintain a pressure differential between the outer and the inner sides of the mold. This not only promotes resin flow but also creates a pressure differential normal to the vacuum bag surface. This outside normal pressure compacts the preform and enables laminate fiber volumes of nearly 60% [34], which is a higher fiber volume fraction than normal VARTM processes. This results in better mechanical properties that could rival those of the state-of-the-art pre-pregs cured in autoclave environments. Figure 6 (bottom)

shows that resin is fed through the dry preform by a vacuum-induced pressure differential as well as distribution media.

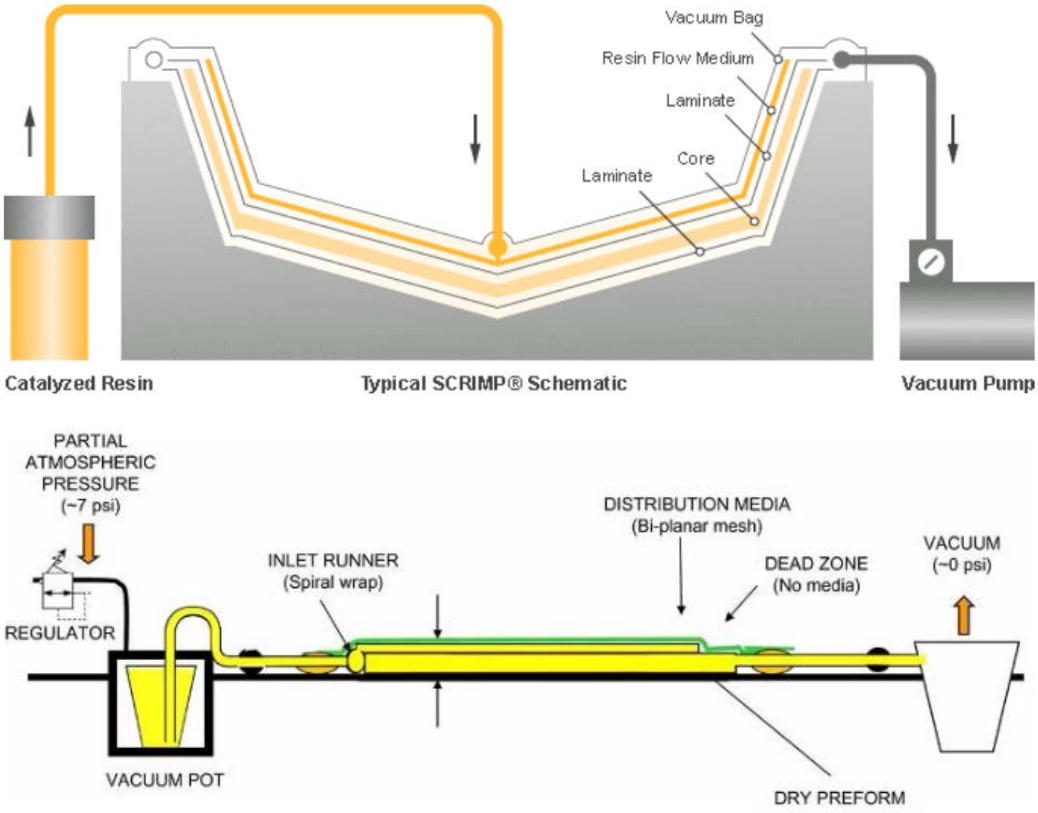

Figure 8. Schematics of (top) SCRIMP Process [31] and (bottom) CAPRI Process [22].

3.3.3 Autoclave Curing

Autoclave curing process has been the method of choice to fabricate continuous fiber reinforced thermoset composite components for high-performance applications, such as primary aircraft composite structures [18]. Fibers are pre-impregnated with resin (prepreg) then cut and stacked to form desired composite components or shapes, which also can be combined with other materials, such as honeycomb core, pre-cured composite stiffeners, and structural adhesives to promote bond. The structural part is then covered with various cloth layers and sealed inside a vacuum bag (Figure 9). The part is cured with vacuum under high pressure and temperature in a predetermined cure cycle. These external sources enable high fiber volume fraction and remove any voids that may develop during the resin cure [11]. Note that the vacuum bagging pressure should be less than the autoclave pressure to ensure compaction of the cured components. Although the autoclave process produces higher strength composite components with fewer trapped voids, there are disadvantages including the high cost associated with initial investment and the part size limitation due to the size of the autoclave.

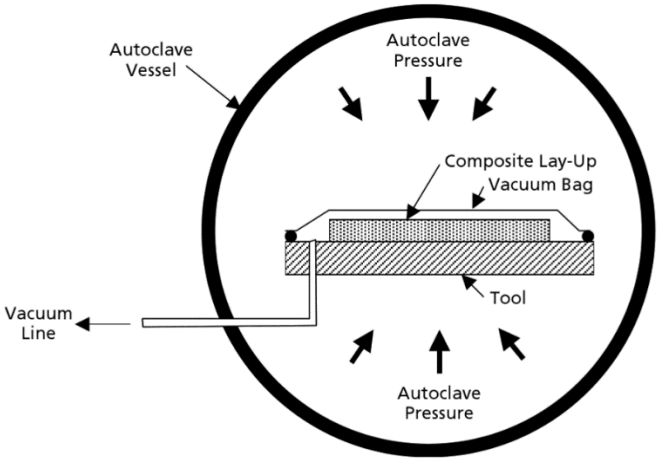

Figure 9. Schematic of Autoclave Curing Principle [11]

3.3.4 Pultrusion

In the pultrusion process, continuous yarns and tapes are saturated with resin and pulled through a die that forms the desired shape. Pultruded shapes can range from simple round bars to complex I-beams or other hollow-core structures. Additional discussion on the use of pultruded FRP sections for bridge girder applications is provided in Section 4.2 and Chapter 11. The overall complexity of the pultrusion process is illustrated in Figure 10. Glass FRP reinforcing bars and carbon FRP prestressing cables are fabricated using the pultrusion process.

Figure 10. Pultrusion machine at Strongwell Corp.[35]

4. Current Applications of FRP Bridge Girders

The use of FRP composite materials in highway bridges has a long history dating back to the early 1990's. A 2013 FHWA project report on composite bridge decks [36] indicates that more than 100 FRP bridge deck/structures projects had been implemented in the U.S. at the time of the report. A comprehensive review of all FRP bridge deck projects is beyond the scope of the current study, but there have been notable examples of FRP composite bridge girders and FRP flat slab bridges that serve as valuable baseline data for the present work. This section provides examples of different FRP bridge girder systems that have been implemented around the U.S. and in Europe. Each sub-section addresses a different FRP technology. The following framework was used to organize each sub-section:

1. General Description of the Technology
    a. Materials and manufacturing methods
    b. Research and development effort
2. Example Bridges
    a. Date of construction
    b. Basic bridge geometry
    c. Monitoring and evaluation
    d. Current status

4.1 Flat-Slab FRP Composite Panel Bridges

4.1.1 General Description

The earliest examples of FRP composite bridges discovered in the literature were flat-slab FRP composite panels. The motivation for developing this technology was a perceived market for the rapid replacement of short-span bridges (< 30 ft) on existing piers. The overall concept was developed by Kansas Structural Composites, Inc. (KSCI) with the support of an FHWA IDEA grant [37]. The concept involved developing an inventory of standard-sized FRP panels that could be deployed anywhere within a 500 mile radius in less than 24 hours. The desired on-site installation time was 4 to 8 hours [38].

Each FRP panel consists of two face laminates (one for the top and one for the bottom), a honeycomb core, and two edge frames that allow for adjacent panels on the bridge to be joined together in the field. All of the components were constructed using a wet lay-up method. The honeycomb core consists of corrugated panels that are bonded to flat sheets and stacked on edge until the required width of each panel is obtained (Figure 11). The honeycomb core is then bonded to the bottom face laminate by setting the core in place before the resin on the bottom face laminate has cured.

After the individual panels have cured and are delivered to the site, the desired bridge width is obtained by joining panels together using a tongue and groove system. An adhesive bonding agent is used to secure the panels together and a cast-in-place polymer concrete wearing surface is installed in the field to increase friction on the driving surface (Figure 12).

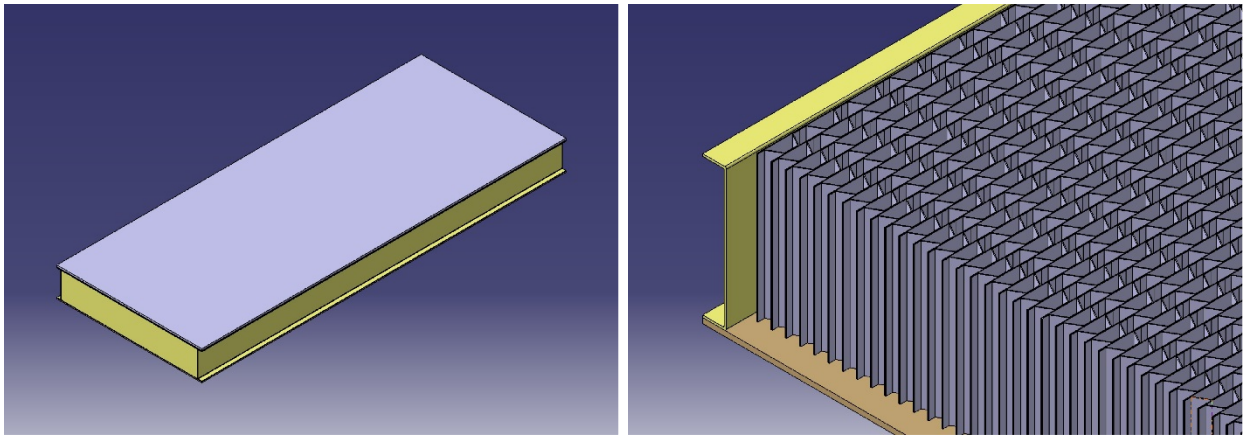

(A) (B)

Figure 11. Flat-slab FRP composite bridge panel: (A) Completed panel and (B) Detail of honeycomb core (model based on verbal description provided in [38]).

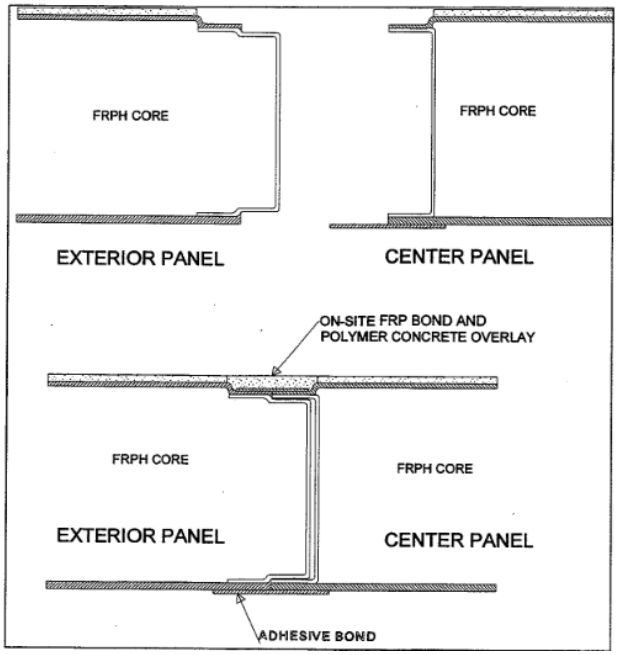

Figure 12. Schematic for joining panels in the field [38]

Preliminary testing of this design concept included tensile testing of samples representing the face laminates as well as flexural testing of a small-scale beam. Details of the small-scale beam were not provided, so interpreting results is difficult. The exact laminate architecture was also difficult to characterize from the data provided in the final report, but the laminates were constructed using a combination of 0/90 woven glass fabric and chopped strand mat with Owens-Corning 7RCP polyester resin (no additional data was provided for the matrix material). Laminate tensile testing results are provided in Table 16.

Table 16. Laminate tensile properties for FRP Honeycomb flat-slab bridge.

Sample ID	Tensile strength (ksi)	Thickness (in)	Yield stress (1% offset) (ksi)	Young's modulus (psi)
Face 1 – Long.	33.9	0.493	17.5	2.19×10^6
Face 1 – Perp.	10.9	0.518	8.9	1.04×10^6
Face 2 – Long.	31.2	0.941	17.8	1.80×10^6
Face 2 – Perp.	6.7	0.813	Not Reported	0.49×10^6

There were several key innovations supported by the IDEA grant:

1. Manufacturing methods for the relatively large honeycomb structure
2. FRP railing system to prevent lateral egress
3. Connection geometry between adjacent panels to ensure load distribution (Figure 12)
4. Anchorage system to connect the panels to the substructure
5. Lifting system for moving panels from the transport vehicle to the substructure
6. Simplified design methods for FRP Honeycomb structures

4.1.2 Example Bridges

Name	Location	Construction date	Span (ft)	Width (ft)	Lanes	Still in service?
No-Name Creek Bridge	Russell, KS	November 1996	21.25	27	2	Yes
St. Francis St. Bridge	St. James, MO	November 2000	26.25	27.33	2	Yes
FA-114-01.64	Huron County, OH	August 2008	16.75	25.75	2	Yes

4.1.2.1 *No-Name Creek Bridge, Russell, Kansas*

The first documented example of a Flat Slab FRP composite panel bridge is the No-Name Creek Bridge outside of Russel, Kansas. The bridge consisted of three FRP honeycomb panels that were 23.25 ft long in the span direction and 9.25 ft wide. The bottom laminate thickness was 0.75 in, the top laminate thickness was 0.5 in, and the depth of the honeycomb core was 20.5 in. A 0.75-in polymer concrete wearing surface was applied to each panel in the factory. Once on-site, the bridge panels were laid across the span and additional composite material was placed in the lap joint region between the panels. The remaining void was filled with additional polymer concrete overlay material to create a smooth roadway surface.

Figure 13. Load testing of No-Name Creek bridge after installation in November 1996.

Monitoring and evaluation of the No-Name Creek Bridge has continued over the years. Immediately after installation, several load tests were performed to validate the bridge's performance and measure deflections (Figure 13). The rear tandem-axles of two trucks were positioned at midspan (one in each lane) for a total load on the bridge of 84.5 kips with a resulting deflection of 0.181 in ($\Delta/L = 1410$). Additional load testing was completed in February and March of 1997, but no significant differences in deflection were reported.

Subsequent static and dynamic load testing was conducted by researchers from Kansas State University in 2004 [39]. No significant differences in bridge stiffness were reported after eight years of service. Results from a subsequent FHWA sponsored research project [40] were published in 2012 that describe a long-term monitoring program for the No-Name Creek Bridge. The emphasis of this study was on temperature-induced deformations that result from diurnal heating of the roadway surface. During the initial load testing of the structure in 1996, it was observed that deformations resulting from temperature effects were on the same order of magnitude as the deformations obtained from the truck loading. The 2012 study reported a displacement range of 0.365 in due to diurnal temperature effects over a 1-year period (max minus min) while the displacements measured during the 2004 study due to truck loading were on the order of 0.157 in. One additional point to note about this particular bridge is that though the performance has generally been good over the years and the bridge is still in service, the average daily traffic (ADT) is very low (10 vehicles per day) [41].

Current Status: The Embry-Riddle Aeronautical University (ERAU) research team contacted the Kansas DOT. Responses to question about the current status of the No-Name Creek Bridge are provided below:

Is the bridge still in service?

Yes it is still in service.

Have there been any maintenance concerns over the years?

Only one that I am aware of, rail damage due to vehicle contact.

Are there any plans to replace the bridge in the near future?

Not aware of any, however you would have to contact Russell County as they are the owners.

Have any other bridges been built utilizing composite materials after this bridge?

Three other structures have been constructed in Kansas, all are still in service but two will be replaced soon. These structures all had the same issues, the top structural surface would debond from the core and required repair of the surface.

Are there any plans to use composite materials like this in any future bridge projects?

Not at this time. Cost preventative.

4.1.2.2 *St. Francis Street Bridge, St. James, Missouri*

In the late 1990's and early 2000's, the Missouri DOT investigated several different FRP technologies for short-span bridges. The study was comprised of both experimental work and four demonstration bridges. The FRP technologies deployed in the demonstration bridges included:

- St. Francis Street Bridge: flat-slab FRP honeycomb bridge (similar to the No Name Creek bridge in Kansas)
- St. Johns Street and Jay Street Bridges: traditional steel stringers/girders with FRP honeycomb deck panels
- Walters Street Bridge: simply-supported precast concrete panels reinforced with FRP bars

A 2002 report [42] documents the construction of each bridge and several laboratory experiments. The experimental work investigated the basic FRP material properties as well as the overall behavior of small-scale beam/panel specimens. Load testing was performed for the FRP-reinforced concrete panels and the flat-slab FRP honeycomb panels. Note that the laminate tensile properties (Table 17) exceed the minimum requirements from the FDOT structures guidelines for tensile strength (30 ksi) but do not meet the criteria for Young's Modulus (3×10^6 psi). A detailed description of the laminate architecture was not provided in the report. A weight fraction of 40% fiber was obtained and an isophthalic polyester resin was used. All of the components were constructed using a hand lay-up method. Coupon samples were also exposed to different environmental regimes (freeze-thaw, moisture, and saline solution), but negligible deterioration was reported.

Table 17. Laminate tensile properties for FRP panels used in St. Francis St. bridge.

Sample ID	Tensile strength (ksi)	Young's modulus (psi)
C2	40.8	2.07×10^6
C3	40.2	2.57×10^6
C5	44.2	2.16×10^6
C6	46.8	2.23×10^6
Average	43.0	2.27×10^6

Experimental results for the small-scale FRP honeycomb samples warrant some discussion. Two beams were loaded to failure in four-point bending. The total span length was 13 ft (3-ft spacing between load points at midspan) and the total depth of the panels was approximately 23.25 in. Complete panel dimensions are provided in Figure 14. The equivalent web thickness of the honeycomb was 1.9 in.

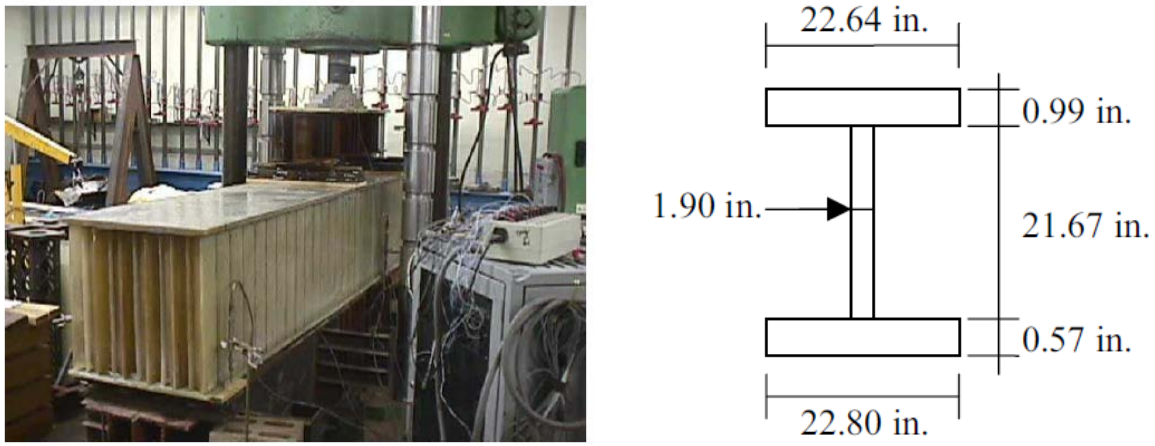

(A) (B)

Figure 14. Small-scale FRP honeycomb flat-slab bridge sample. Testing completed at the University of Missouri – Rolla. [42]

The observed failure mode for both specimens was shear debonding at the honeycomb core/FRP panel interface (Figure 15). These failures occurred when the tensile stress in the FRP panels was on the order of 12.5 ksi for Beam 1 (roughly 30% of the ultimate tensile strength, which was 43 ksi) and 19.1 ksi for Beam 2 (44% of the ultimate tensile strength). The manufacturer, KSCI, had specified an equivalent tensile strength at failure of 9.8 ksi based on their previous experience with this type of honeycomb panel.

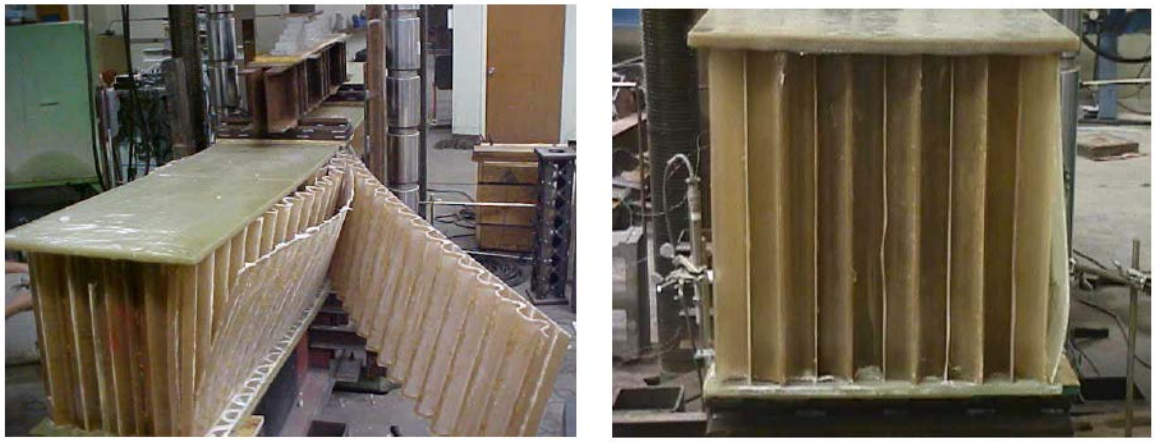

(A) (B)

Figure 15. Failure modes for FRP honeycomb beam samples. Delamination of the (A) top plate for Beam 2 and the (B) bottom plate for Beam 1.

Load vs. displacement data are provided in Figure 16. The ultimate failure load for Beams 1 and 2 were dramatically different with Beam 1 failing at 194 kips and Beam 2 failing at 288 kips. This was in spite of a slightly thicker top plate on Beam 1. These results suggest that predicting the conditions which result in shear failure between the honeycomb core and the FRP panels would be difficult. An important qualification, however, is that the deformation experienced by the beam would ultimately control the design. If L/1000 is used as the serviceability criteria for this structural element, the capacity

of the section would be reached at a displacement of 0.156 in and a load of approximately 25 kips (based on the slope of the load vs. displacement plot). This load would result in an equivalent normal stress in the FRP panels of 1.6 ksi (3.7% of the ultimate tensile strength) at the service limit state.

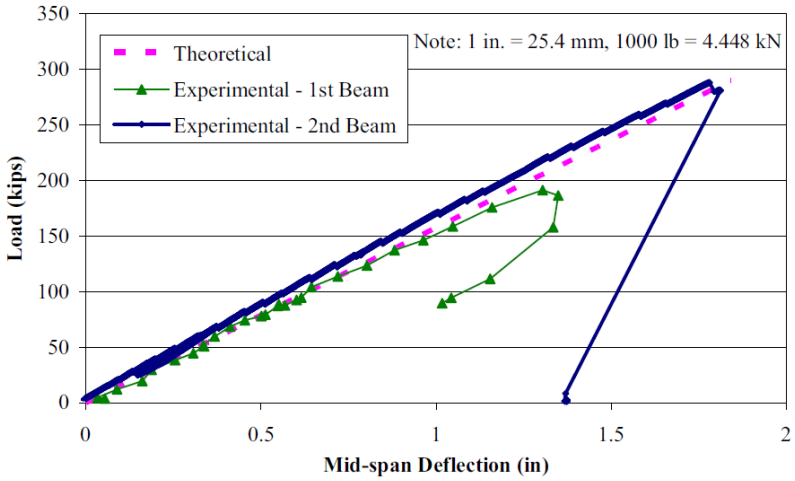

Figure 16. Load vs. displacement data for FRP honeycomb beam tests completed at University of Missouri – Rolla [42].

The St. Francis Street bridge was constructed in November 2000. The bridge consisted of four FRP honeycomb panels (6.83 ft wide x 26.25 ft long). Baseline load-testing data was collected using the 47.88 kip truck shown in Figure 17(B). Holdener and Myers (2007) [43] published a follow-up study that included in-situ load testing after six years of service. Load test results from 2000 and 2007 are compared in Figure 18. The researchers noted some apparent softening of the structure and estimated that the equivalent modulus of elasticity had decreased by 18%. The information provided in the paper was difficult to reconcile with previous information about the FRP panels provided in the original 2002 study [42]. The computed value for Modulus of Elasticity based on 2001 data averaged 7.47X106 psi while the Modulus of Elasticity based on 2007 data averaged only 6.154×10^6 psi (an 18% decrease), but the measured modulus of elasticity from the 2002 report averaged 2.27×10^6 psi based on the coupon testing. In any case, Holdener and Myers expressed concern over the apparent softening of the structure after six-years of service.

Current Status: The ERAU research team contacted the city engineer for St. James, MO. This communication confirmed that the St. Francis Street Bridge is still in service and is maintained by the city. The bridge was performing well and there have not been any maintenance concerns. It was also reported that one of the other bridges that relied on the FRP panel deck with steel stringers had experienced problems with the polymer concrete overlay and that several FRP deck panels had separated over time and needed to be re-glued.

(A) (B)

Figure 17. St. Francis Street bridge, St. James, MO, November 2000 [42]. (A) Installation and (B) load testing.

Figure 18. Comparison of load-test results (midspan deflection) for St. Francis Street bridge after six years of service [43].

4.1.2.3 *FA-114-01.64, Huron County, Ohio*

A third flat-slab FRP honeycomb bridge with significant documentation was identified in Huron County, Ohio. A 2013 report by the University of Toledo documents laboratory testing of a small-scale sample, bridge installation, and subsequent field monitoring [44]. The field monitoring component included load testing immediately after the bridge was commissioned in 2008 and after the bridge had been in-service for a two year period. The report also includes observations from bridge inspections completed in 2011 (almost three years after the bridge was constructed).

The report documents one improvement to the fabrication process for the FRP honeycomb panels. In an effort to improve the bond between the honeycomb core and the FRP face laminates, the construction process was modified so the core was “pressed” into the face laminate before the matrix had cured. Recall that the failure mode for the University of Missouri – Rolla study was debonding between the core and the face laminates at significantly different load levels. A similar failure mode was

encountered during the laboratory testing of the small-scale sample (Figure 19(A)). The specimen failed at a total load of 270 kip, but the service limit of L/1000 was reached at a total load of only 30 kip.

The load testing that occurred after two-years of service did not reveal any significant loss of stiffness of the overall bridge. Two concerns were noted during the bridge inspection that occurred after three years of service. First, water was observed to be dripping from one of the panels. Second, the polymer concrete wearing surface was showing signs of distress (Figure 19(B)).

(A) (B)

Figure 19. Flat-slab FRP honeycomb bridge for Huron County, Ohio [44]. (A) Failure mode of sample from laboratory experiment and (B) polymer concrete wearing surface showing degradation after ~3 years of service.

Current Status: The ERAU research team contacted the county engineer for Huron County, Ohio, and obtained the following responses to questions about the bridge:

Is the bridge still in service?

Bridge is still in service. 2015 BR 86 Rating of 9A (FRP Innovative Bridge) In service since 7/1/2008.

Have there been any maintenance concerns over the years?

No major maintenance work as of this date, Epoxy surface is showing some signs of wear… FRP Slabs still great shape…Future deck maintenance, not sure if epoxy or asphalt ???

Are there any plans to replace the bridge in the near future?

No plans to replace… Still looks good, GR anchors still functioning as designed….Bridge Railing have NOT been hit , repairs could be expensive, because of attachment to deck slabs..

Have any other bridges been built utilizing composite materials after this bridge?

No, because of cost, still more cost effective to use Concrete boxes or poured beams on short spans…(ex. Clear Span 15’-5”)

Are there any plans to use composite materials like this in any future bridge projects?

Not currently…. Waiting on ODOT to approve and standardize plans and specification… Need cost effective suppliers…

4.1.3 Summary of Flat-Slab FRP Honeycomb Bridge Panels

The flat-slab FRP honeycomb bridge panels described in this section represent an important benchmark when considering the use of FRP composites in bridge girder applications. When assessing the FRP honeycomb panels, it is important to first acknowledge the overall objective driving the development of the technology in the first place: rapid deployment and replacement of short-span superstructures on existing substructures. It is also important to note that a short-span bridge represents a unique case where flat-slab reinforced concrete construction and beam-slabs with steel stringers are in constant competition from an efficiency standpoint (at least in areas outside of the Southeast where pre-cast concrete is not as competitive). Both of these bridge types, however, are susceptible to corrosion from the use of de-icing salts in the winter. The fact that this market niche was identified for superstructure replacement on existing piers also suggests that the source of the corrosion damage is coming from the top of the bridge and not the bottom (as we expect for bridge girders in extremely aggressive environments).

Composite materials offer significant advantages for this specific application due to their high strength to weight ratios and corrosion resistance. The typical weight per unit area of an FRP honeycomb panel that is capable of spanning 23 ft is around 28.4 lbf/ft^2 (37.7 lbf/ft^2 including the polymer concrete wearing surface). The total weight of a 30-ft-wide bridge would be on the order of 26 kips. A similar flat-slab reinforced concrete bridge would be on the order of 12-in thick and have a weight per unit area on the order of 150 lbf/ft^2. The same 30-ft-wide bridge would have a total weight of 103.5 kips. The FRP honeycomb option could presumably reduce transportation costs by a factor of 4. The size of the equipment and associated costs required to place the panels once on-site could also be reduced considerably.

Regarding material costs, none of the reports discovered on the FRP honeycomb panels provide any details. Using the raw material costs described in Section 3, it is possible to estimate the cost of the raw materials in the FRP honeycomb panels. Assuming a fiber weight fraction of 40%, E-glass fibers at $1.50 per pound, and vinylester resin at $4.50 per pound, the material costs for the FRP honeycomb panels can be estimated at $94 per square foot (not including the polymer concrete overlay). A 2003 paper [45] in the Journal of Management in Engineering compared the life cycle costs of short-span FRP bridges and traditional materials. The authors used the St. Francis Street Bridge in a case study and reported material costs for the bridge at only $45 per square foot. This can be compared to a material cost of about $20 per square foot for a traditional steel-reinforced flat-slab bridge (assumed 23-ft span, 30-ft width, 20-in depth).

If other life-cycle costs, such as manufacturing, construction, maintenance, and disposal are considered, the long-term economic advantages of FRP honeycomb panels for short-span bridges are not obvious. The study by Nystrom et al. essentially concluded that FRP materials would never become cost-competitive over traditional flat-slab reinforced concrete construction for short span bridges:

> *The original research question was: ‘‘Are the advanced composite materials capable of supporting industrial production of short-span bridges that are cost competitive with traditional RC bridges?’’ The answer is: ‘‘Probably not.”*

Table 4. Life-Cycle Costs

Description	RC bridges	Future bridge	FRP premium
Construction costs	$430/m^2	$740/m^2	$310/m^2
Impact of disposal	$45/m^2	$9/m^2	($36/m^2)
Total cost including disposal	$475/m^2	$749/m^2	$274/m^2
Impact of replacements	$119/m^2	$67/m^2	($52/m^2)
Total cost including disposal and longer life	$594/m^2	$816/m^2	$222/m^2

(A)

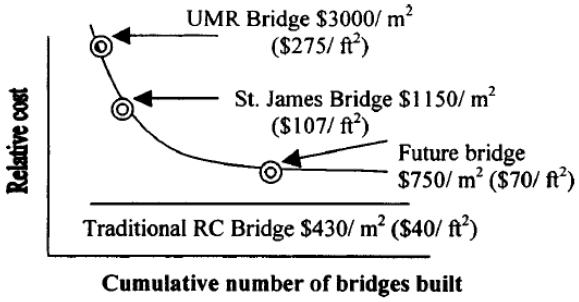

(B)

Figure 20. Comparison of lifecycle costs for FRP and RC short-span superstructures [45]. The "Future Bridge" is an attempt to characterize future economies of scale and efficiency improvements that were envisioned in 2003.

There are several other factors worth considering about the nature of the FRP honeycomb panels described in this section. Most importantly, the design of these bridges is governed entirely by deflection control. An FHWA report from 2011 [46] addresses serviceability limits and the economics of steel girder bridges. The following quote is noteworthy:

> *For lower strength steel, the deflection limits have not encroached on bridge economics. With the introduction of high performance steel (HPS) in bridge design, the deflection limit has become more critical in design. HPS designs require less steel that result in larger deflections and, thus deflection limits can impact the economy of a bridge.*

This concern appears to be magnified considerably for the case of glass FRP materials. The ultimate tensile strength of glass FRP materials that would be considered suitable for bridge applications, 30 ksi (Table 8), is at least comparable to the yield strength of A36 steel (36 ksi). At first glance, the strength to weight ratio of the FRP would appear to provide a significant advantage. If you compare the modulus of elasticity between the FRP and steel, however, some major challenges emerge. The modulus of elasticity for the FRP honeycomb bridge panels was on the order of 2.0×10^6 to 2.3×10^6 psi. The minimum allowable modulus of elasticity for FRP materials in current standards is 3.0×10^6 psi (Table 8), which is less than

the modulus of elasticity for steel by nearly a factor of 10. The end result is an FRP cross-section that is highly overdesigned from a strength perspective to meet the required deflection criteria.

4.2 Pultruded FRP Bridge Girders

Around the same time that KSCI was developing the flat-slab FRP honeycomb panels for short-span bridges, researchers from Virginia Tech were in collaboration with Strongwell, Inc., a Virginia-based FRP pultrusion manufacturer, to develop a pultruded FRP bridge girder. Two unique cross-sections were developed and deployed in superstructure replacement projects during the Summer of 1997 and in October 2001. Two Virginia Transportation Research Council reports [47,48] were identified that document laboratory testing, bridge construction, in-situ load testing and subsequent field monitoring. Detailed design guidelines that include section and material properties are also provided by Strongwell [49].

The pultrusion process employed by Strongwell for these beams involves unidirectional carbon-fiber tows in the flange area and four different E-glass reinforcements in the flanges and webs. Including the carbon-fiber tows enhances the apparent modulus of elasticity of the beams significantly. For example, an all-glass version of the 8x6 EXTREN DWB has an equivalent modulus of elasticity (measured through flexural testing) of $4x10^6$ psi while the hybrid glass-carbon version of the same section has an equivalent modulus of $5.66x10^6$ psi (a 42% increase). Another reason for the increased modulus of elasticity is the higher fiber volume fraction that can be achieved with the pultrusion process. The EXTREN DWB structural shapes achieve fiber volume fractions on the order of 55%, while the hand lay-up methods are limited to ~40%.

The enhanced modulus of elasticity does increase the cost. The all-glass versions of the 8x6 and 36x18 EXTREN DWBs currently sell for approximately $80 and $300 per linear foot, respectively. Including the unidirectional carbon-fiber tows increase the price to $140 for the 8x6 and $600 for the 36x18 (Browing, S. Strongwell Corp., private communication, August 2, 2015, and April 15, 2016).

The carbon-fiber tows also have implications for the behavior of the beams at their ultimate capacity. Figure 22 illustrates an observed delamination that occurred in the compression flange during a flexural test of a 36x18 EXTREN DWB section. The flexural capacity of the section was reached when buckling occurred in the compression flange at midspan directly underneath load application point. It isn't clear if the buckling occurred before or after the delamination.

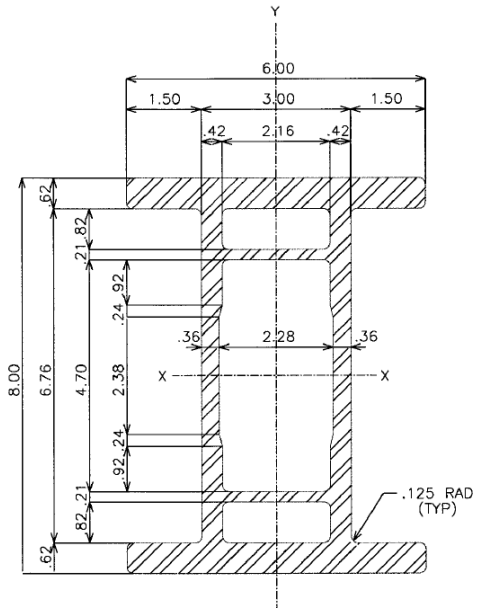

NOMINAL SECTION PROPERTIES

I_{xx}	=	129 in^4
S_{xx}	=	32.2 in^3
r_{xx}	=	3.07 in
A	=	13.7 in^2
$A_{2\ webs}$	=	5.36 in^2
$A_{2\ flanges}$	=	7.44 in^2
I_{yy}	=	31.8 in^4
S_{yy}	=	10.6 in^3
r_{yy}	=	1.52 in
Weight	=	11.2 lbs/lf

(A)

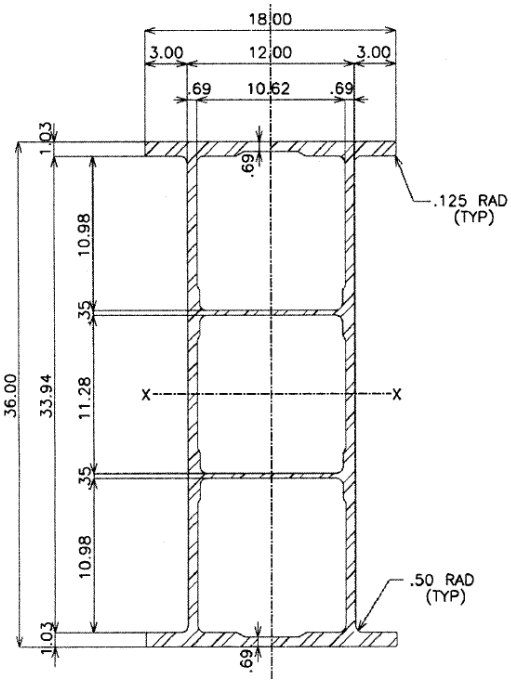

NOMINAL SECTION PROPERTIES

I_{xx}	=	15291 in^4
S_{xx}	=	849 in^3
r_{xx}	=	12.9 in
A	=	91.2 in^2
$A_{2\ webs}$	=	50.1 in^2
$A_{2\ flanges}$	=	34.0 in^2
I_{yy}	=	2626 in^4
S_{yy}	=	292 in^3
r_{yy}	=	5.37 in
Weight	=	70 lbs/lf

(B)

Figure 21. Pultruded FRP bridge girders by Strongwell, Inc. [49] (A) 8”x6” EXTREN DWB and (B) 36”x18”EXTREN DWB.

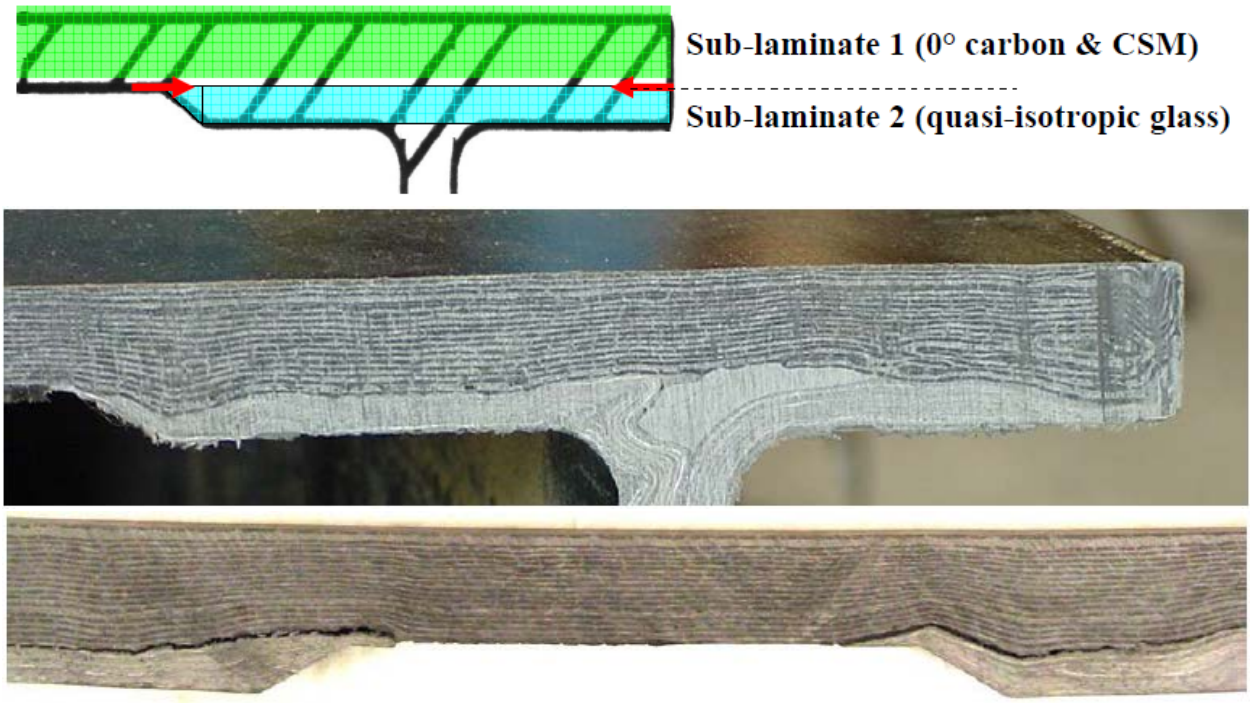

Figure 22. Delamination between quasi-isotropic glass and carbon/CSM laminates during laboratory beam test of 36x18 EXTREN DWB. Section was taken away from rupture zone at midspan [48].

(A) (B)

Figure 23. Four-point bending test of 36x18 EXTREN DWB (Note 48, pg. 27). (A) Laboratory setup and (B) failure in compression flange at loading point.

The EXTREN DWB design manual provides moment capacities for each cross-section along with an equivalent modulus of elasticity measured through flexure. The ultimate tensile strength of the pultruded material is not discussed, but it is possible to estimate the equivalent normal bending stresses at rupture using the relationship between normal stress and internal bending moment. The results, summarized in Table 18, once again highlight the challenges associated with the anisotropic nature of composite materials. The ultimate tensile stress for a uni-directional carbon FRP laminate should be on the order of 120 ksi [50]. This value cannot be realized in a flexural element due to the pultrusion's limited ability to transfer shear stress throughout the depth of the cross-section. This problem is amplified as the span length increases. The shear capacity of the 36x18 section was shown to decrease from 157 kips at a span of 15 ft to 67.4 kips at a span of 60 ft.

It is important to note, however, that from a bridge design perspective, the deflection criteria are going to control the design. Nonetheless, these properties of pultruded sections highlight the difficulties that one would face in attempting to evaluate strength limit state criteria. These characteristics also suggest that service limit states for fatigue and rupture would also require special attention and that the tensile stress limits imposed by AASHTO for concrete-filled tubes may not transfer directly to sections that fail in shear.

Table 18. Equivalent normal stress at failure for glass-carbon hybrid EXTREN DWB sections.

Section	Ult. moment (k-ft)	E (psi)	I (in^4)	Normal stress at failure (ksi)
8x6 EXTREN DB	36.1	$5.66x10^6$	129	26.9
36x18 EXTREN DB – 30-ftspan	964	$5.76x10^6$	1529	13.6
36x18 EXTREN DB – 40-60-ft span	635	$5.76x10^6$	1529	9.0

4.2.1 Example Bridges

Name	Location	Construction date	Span (ft)	Width (ft)	Lanes	Still in service?
Tom's Creek Bridge	Blacksburg, VA	Summer 1997	18	24	2	Yes
Rt. 601 Bridge over Dickey Creek	Sugar Grove, VA	October 2001	39	30	2	Yes

4.2.1.1 *Tom's Creek Bridge, Blacksburg, Virginia*

The first bridge utilizing pultruded FRP bridge girders was identified as the Tom's Creek bridge in Blacksburg, VA. A 2003 report (Note 47) documents the bridge's installation, laboratory load testing, in-situ load testing, and field monitoring. The 18 ft simple span bridge utilized a laminated lumber deck supported by 24-8"x6" EXTREN DWB hybrid carbon-glass pultruded beams (Figure 24). The laminated lumber deck was attached to the composites girders using through bolts at over 300 locations across the bridge. A total of 6 inches of asphalt was applied on top of the laminated lumber to serve as a wearing surface.

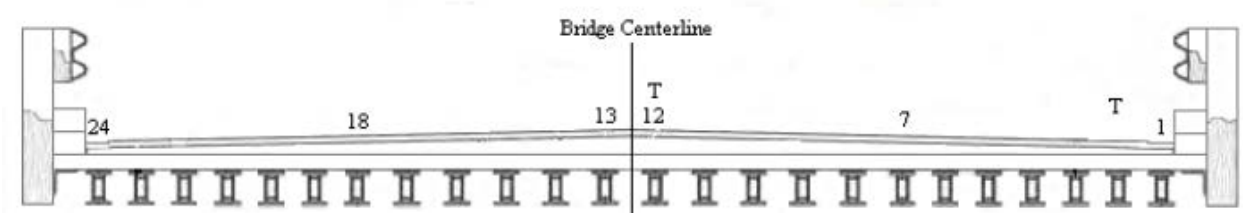

Figure 24. Cross-section of Tom's Creek bridge in Blacksburg, VA. [47]

The bridge was designed to meet a deflection criteria of L/425, but actual service live-load deflections were closer to L/800. The researchers attributed this increased performance on the composite action that developed between the timber deck and the composite girders. Two of the

bridge girders were removed and replaced after 15 months of service and laboratory fatigue testing was conducted. No significant degradation in stiffness or strength was observed.

Using cost data provided by Strongwell, the total cost of the pultruded girders can be estimated as $140 per square foot (20 ft x 24 beams x 140$/ft x (1/480ft^2)).

Current Status: The ERAU research team contacted the city engineer for the Town of Blacksburg, VA, who provided the following responses to questions about the bridge:

Is the bridge still in service?

Yes

Have there been any maintenance concerns over the years?

No, Virginia Tech students performed additional research on the bridge after installation and did not find any issues and the Town has not observed any maintenance issues with the bridge.

Are there any plans to replace the bridge in the near future?

No

Have any other bridges been built utilizing composite materials after this bridge?

Not in the Town of Blacksburg. The Town's street and transportation network has not required the construction of any additional bridges.

Are there any plans to use composite materials like this in any future bridge projects?

As stated above, new transportation system construction in the Town does not typically require the construction of a bridge. If the need for bridge construction would arise, the Town would review the construction options and choose the best option for the conditions. If the use of composite materials was a viable option, the Town would review its use along with any other options.

4.2.1.2 *Dickey Creek Bridge, Rt. 601, Sugar Grove, Virginia*

A second bridge using the 36x18 EXTREN DWB was built in October 2001. The associated research, once again, involved describing the bridge's installation, laboratory load testing, in-situ load testing, and field monitoring. The bridge included eight pultruded beams spaced at 36 in on center and spanning 39 ft. A laminated timber deck was used with an asphalt wearing surface. The report stated that the bridge was designed assuming no composite action between the deck and the girders, but steel double-angles were used to connect the deck to the webs of the EXTREN DWBs. The bridge was designed to meet a deflection criteria of L/800.

Using cost data provided by Strongwell, the total cost of the pultruded girders can be estimated as $170 per square foot (39 ft x 8 beams x 600$/ft x 1/1092ft^2).

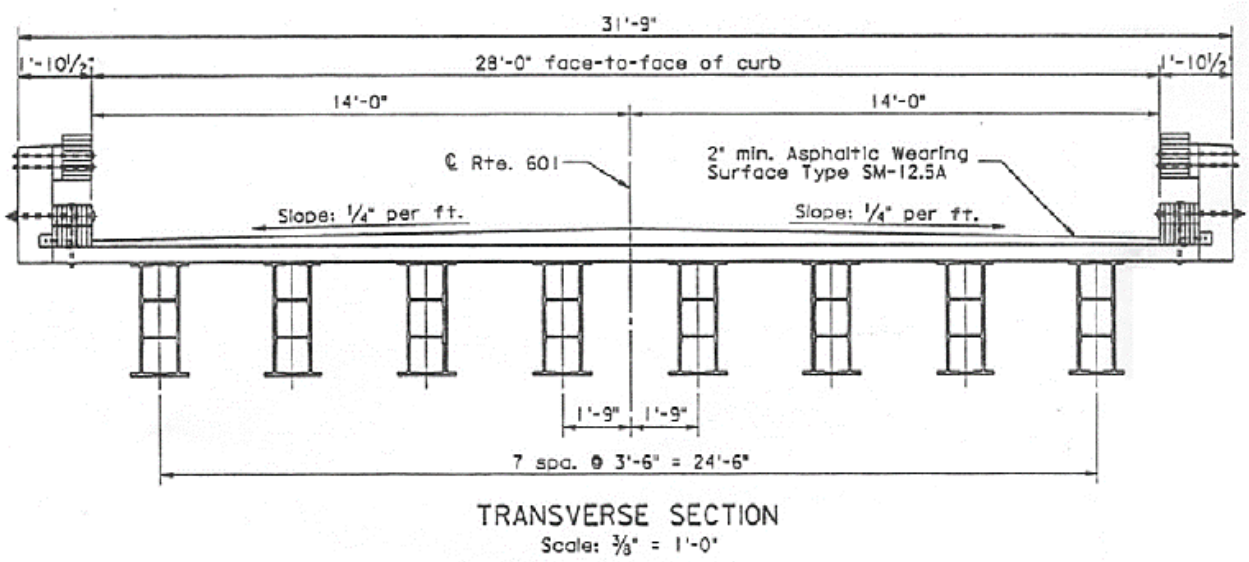

Figure 25. Cross-section of Dickey Creek bridge, Rt. 601, Sugar Grove, VA [48].

Subsequent monitoring over the first two years of service did not reveal any damage or deterioration in the pultruded bridge girders. Inspections in the Fall of 2003 and Summer of 2004 did reveal some splintering, blistering, and cracking of the girders. The researchers concluded that this damage most likely occurred during construction. The location of the damage ruled out possible debris strikes during flooding. And because the splintering did not occur near the midspan of the girders, the researchers also ruled out damage due to overloading. Live load testing was completed after the damage was discovered and there were no discernable effects caused by the damage. The researchers ultimately concluded that the damage needed to be monitored for future growth.

Current Status: The ERAU research team contacted the Virginia DOT and received the following responses to questions about the bridge:

Is the bridge still in service?

Yes

Have there been any maintenance concerns over the years?

All interior beams on bottom of bottom flange have longitudinal cracking, (Can feel with fingernail) full width x full length. Exterior beam (Beam #1) has this same cracking for a length of 8' at Abutment A. Note: Manufacture calls these cracks "crazes". Beam #5: Bottom flange at mid-span has small splinters on bottom upstream corner in a 5" long area and 1/16" deep. Beam #6: Bottom flange on bottom downstream corner, 4'-5" from Abutment B end of beam, has small splinters in a 2 1/2" long area and 1/32" deep, (No significant change since last inspection). Diaphragms at mid-span have chalking.

Are there any plans to replace the bridge in the near future?

No

Have any other bridges been built utilizing composite materials after this bridge?

No, but a similar bridge exists in Blacksburg [Tom's Creek, described above].

Are there any plans to use composite materials like this in any future bridge projects?

Not at this time

4.3 FRP U-Girders

Research conducted at the University of Texas at Austin in the early 2000s investigated numerous FRP bridge girder options for short-span bridges [51]. In the mid 2000s, two FRP bridges were constructed using FRP composite U-Girders. The general fabrication process using the hand lay-up method is outlined in Figure 26. A major divergence from the previously described FRP systems is the effort to develop composite action with the cast-in-place concrete deck. Steel pipes (1.5 in diameter @ 16" on center) were passed through the webs near the top of the section and a polystyrene foam was used to prevent concrete from completely filling the inside of the girder.

Figure 26. FRP U-Girders for FM 3284 bridge in San Patricio County, TX [52].

4.3.1 Example Bridges

Name	Location	Construction date	Span (ft)	Width (ft)	Lanes	Still in service?
FM 3284	San Patricio County, TX	2005	30 x 2	32	2	Yes
FM 1684	Refugio County, TX	Fall 2007	50	32	2	Yes

4.3.1.1 *FM 3284, San Patricio County, Texas*

Details for the first FRP U-girder bridge were obtained from an internal Texas DOT presentation [52]. The bridge was fabricated using the hand lay-up method (Figure 26). A detailed study by Ramirez et al. [53] describes an acoustic emissions testing program that was developed to certify the girders after fabrication. The San Patricio Bridge consisted of two 30-foot simple spans (total length = 60 ft) and had a width of 32 ft. A total of 12 girders spaced at 2'8" on center were used for each span.

The most detailed description of the specimens was located in a paper by Chen et al.[54] The lay-up was described as 37 layers of 0/90 E-glass fibers and a vinylester resin. The total weight of FRP in a single span (12 girders) was reported as 21.8 kips. Assuming a 50% fiber weight fraction and the middle range values for E-glass ($1.50/lbf) and vinylester resin ($4.50/lbf) reported in Section 3, the approximate girder cost per square foot of bridge is $68. Chen did report that a material cost savings of up to 58% might be obtained if the depth of the section was increased from 22.25 to 27.25 in.

4.3.1.2 *FM 1684, Refugio County, Texas*

A second FRP U-girder bridge was built in Texas in 2007. This bridge spans 50 ft and is 32-feet wide. Eight girders were spaced at 4 ft center-to-center, and the total weight of each beam was approximately 5,000 lbf [55]. These beams were constructed using a VARTM method, and a report by the manufacturer indicates that 3,300 lbf of E-glass fiber and 1,700 lbf of vinylester resin were used for each beam [56]. This results in a relatively high fiber weight fraction of 66%. Using the material prices described in Section 3, the cost per square foot of these FRP girders is approximately $63.

Current Status: Both the San Patricio and Refugio bridges are still in service. The Texas DOT Bridge Division provided the NBI rating sheets for both bridges and the superstructures received a rating of 8 (VERY GOOD CONDITION – No problems noted).

4.4 Concrete-Filled FRP Tubes (CFFTs)

The AASHTO LRFD Guide Specifications for Concrete Filled FRP Tubes (CFFT) was described in Section 2.1.2. The Concrete Arch Bridge System (CABS, formerly known as Bridge-in-a-Backpack) is the most widely used version of the CFFT concept. A detailed review of the literature surrounding the development of the CABS is beyond the scope of the current report, but there is a wealth of published data from research sponsored by the Maine DOT [57]. The following section highlights some of the main design features of CABS and includes a table of typical CABS bridges for reference. Section 4.4.2 highlights the King's Stormwater Channel bridge that utilized CFFTs in pure flexure.

4.4.1 Concrete Arch Bridge System (CABS)

The basic geometry of a CABS bridge is illustrated in Figure 27. The first step in the construction process involves excavation and casting the reinforced concrete bottom footings. Next, pre-cured FRP arch tubes (without concrete) are secured to the footings and corrugated decking is attached perpendicular to the tubes (Figure 28). The decking serves two primary functions: (1) to stabilize the tubes, and (2) provide transverse load transfer from the compacted backfill and roadway to the tubes. Once the tubes are in position, concrete is poured into each tube from a hole drilled in the center. This results in the primary load-bearing arch. After the concrete cures, compacted soil is used to backfill the bridge to the desired depth. This is followed by placing the roadway subbase and the final roadway surface (Figure 29).

The FRP tubes used in CABS bridges constructed between 2008 and 2012 were fabricated using carbon fiber. Later bridges have typically been constructed with GFRP tubes. Tube diameters range between 12 in and 15 in. One major advantage associated with the FRP tubes is that they are light enough to be picked up and moved by several construction workers. A crane is required to place the tubes across the river/stream, but the required crane capacity is minimized. Completed span lengths to date range between 24 ft and 56 ft (Table 19). The estimated total cost per square foot of bridge deck is currently $100 to $120, which is within the range of reinforced concrete flat-slab bridges in Florida ($115 to $160 per square foot according to 2018 FDOT Structures Guidelines, Section 9.2.3).

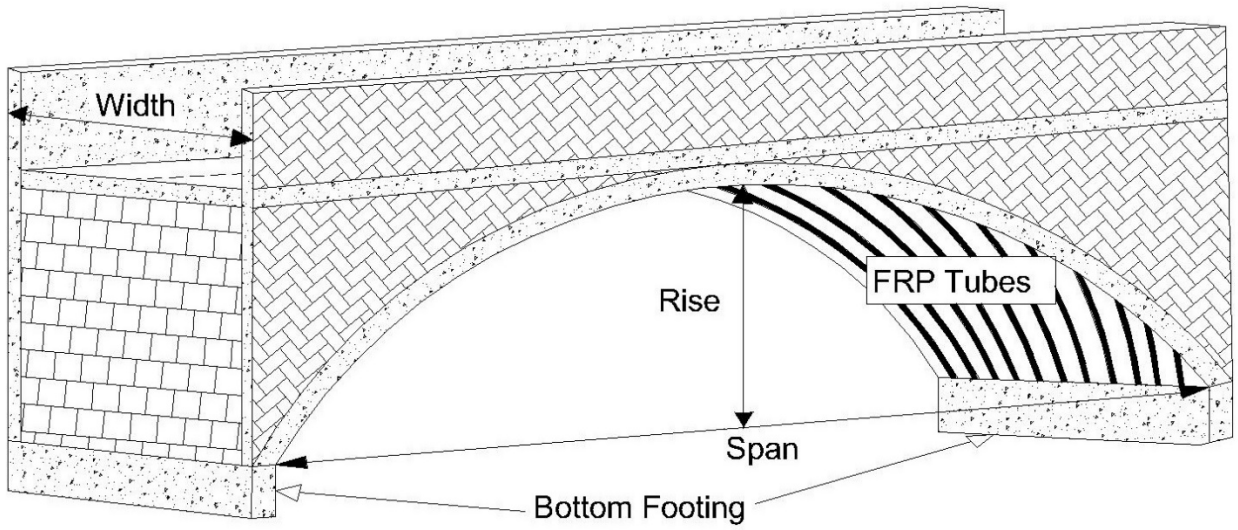

Figure 27. Concrete-filled FRP tube arch bridge.

Figure 28. CABS construction and finished bridge.

Table 19. Summary of existing CABS bridges

Name	Location	Date	Span (ft)	Width (ft)	Rise (ft)	Lanes	# of Tubes	Dia. (in)	Mat.
Neal Bridge	Pittsfield, ME	2008	28.8	45	7.5	2	23	12	CFRP
McGee Bridge	Anson, ME	2009	27.6	25	4.4	2	9	12	CFRP
Perkins Bridge	Belfast, ME	2010	47.6	45	11	2	16	15	CFRP
Royal River bridge	Auburn, ME	2010	38	38	9.5	2	13	12	CFRP
Jerkins Bridge	Bradley, ME	2010	28.5	34	6	2	12	12	CFRP
Tom Frost bridge	Hermon, ME	2010	44.5	12	6.8	Ped.	3	12	CFRP
Scott Reservoir Outlet	Fitchburg, MA	2011	37.6	36	5.8	2	15	12	CFRP
NHDOT Maintenance	Lot Pinkham's Grant, NH	2011	23.8	26	6	2	6	12	CFRP
Farm Access Underpass	Caribou, Maine	2011	54.2	55	12	2	22	15	CFRP
C19 of 32092	Harbor Beach, MI	2012	37.6	52	7.1	2	16	12	CFRP
B & A Overhead Bridge	Lagrange, ME	2012 /13	36.1	58	12	2	13	12	GFRP
Greys Brook	Ellsworth, ME	2012 /13	34.3	50	14	2	11	12	GFRP
B04 of 23052	Sunfield, MI	2013	37.7	48.4	8.7	2	24	12	GFRP
Wanzer Brook	Fairfield, VT	2013 /14	35	38	7	2	9	12	GFRP
Route 53 & Route 57	Weston, CT	2015	40.3	40	6	2	10	15	GFRP
Tide Mill 2	Edmunds, ME	2015	56	46	11	2	13	15	CFRP
M-100 over Thornapple Drain	Eaton County, MI	2015	32	47.7	11	2	12	15	GFRP
JV 135-SR 1001 Section 004 Over Spruce Run	Union County, PA	2016	43	30	6.5	2	10	15	GFRP
JV 136- 36 1001 Section 019 Over Spruce Run	Union County, PA	2016	38	30	5.7	2	10	15	GFRP

4.4.2 King's Stormwater Channel Bridge

An earlier research/bridge construction project completed in 2001 by researchers at UC-San Diego provides an interesting example of a CFFT bridge [58] where the girders are subjected to bending and shear with no axial load. The King's Stormwater Channel bridge consisted of two 30-foot spans (continuous over the center support) and was 42.5-ft wide. A total of six filament wound CFFTs with a diameter of 14.25 in and a wall thickness of 0.394 in. The CFFTs were filled with lightweight concrete. Additional discussion of the laminate architecture for these girders is provided in Section 8.1.5.3. The bridge deck included open-cell FRP panels with a polymer concrete wearing surface.

The King's Stormwater Channel (KSC) bridge was originally constructed as a demonstration project for a much larger undertaking known as the I-5/Gillman Advanced Technology Bridge project. The I-5/Gillman bridge was planned to be a 450-ft long cable-stayed bridge that incorporated CFFT main girders (Figure 30). The site of the KSC bridge was chosen as a rural location near the Salton Sea on California SR 86 with a low ADT. Shortly after the bridge was constructed, the highway saw an uptick in heavy truck traffic from Mexico. This ultimately led to problems with the polymer concrete wearing surface. In 2013, the bridge was replaced due to maintenance concerns with the FRP deck. During a phone conversation the California DOT, it was reported that the CFFT girders performed well during the 12 years they were in service and did not pose any maintenance concerns.

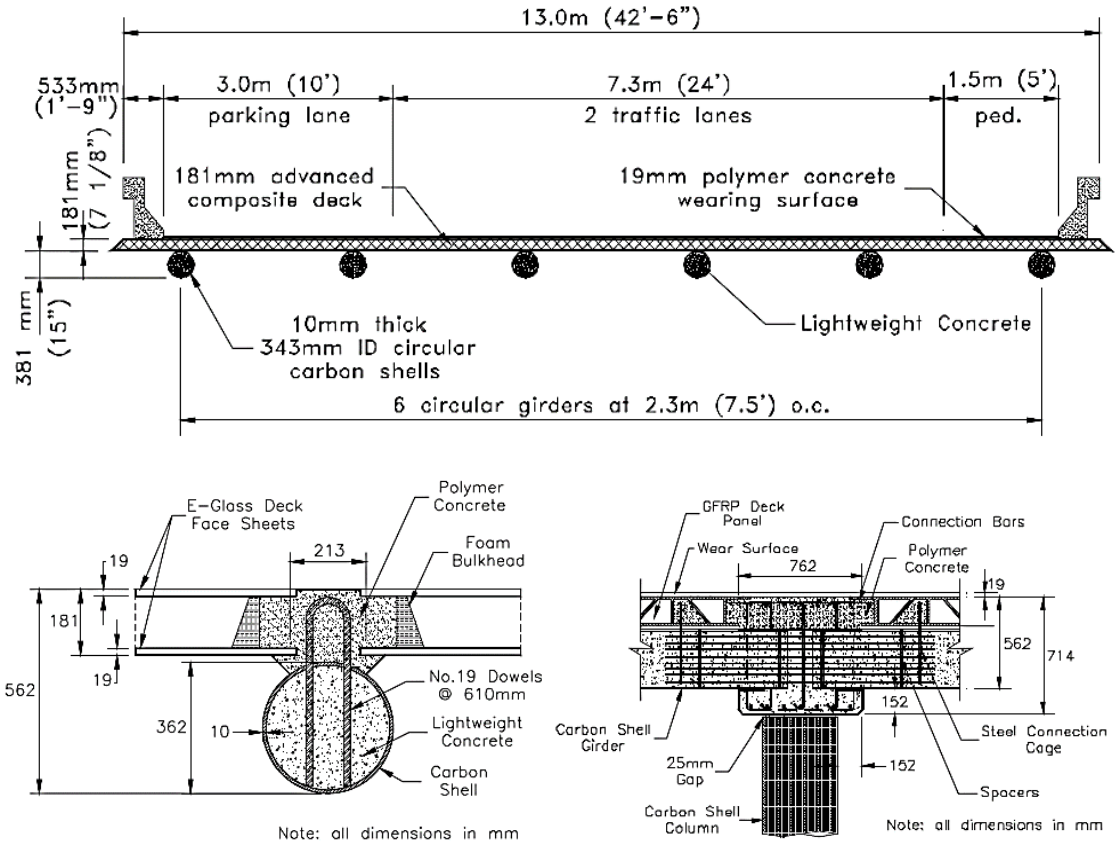

Figure 29. Kings Stormwater Channel bridge near the Salton Sea on California S.R. 86 [58].

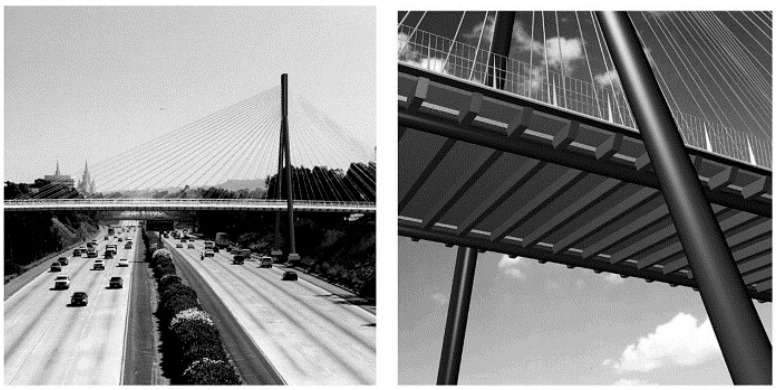

Figure 30. Rendering of I-5/Gillman Advanced Technology Bridge Project. [59]

Figure 31. King's Stormwater Channel bridge. California State Highway 86 near the Salton Sea.

4.5 Hillman Composite Beams

The Hillman Composite Beam is a patented [60], hybrid composite beam (HCB) system. Research has been published on the performance of this system based on installed bridges in the State of Missouri [61]. The company's website provides nine case studies for highway bridges, two railway bridges, one military bridge, and one pier. The novelty of this hybrid system is that each bridge girder contains a tied arch. A foam material is used to form the arch within the FRP composite shell, and steel tendons tie the arch ends together. These tendons are bonded directly to the FRP composite, which provides environmental protection for the entire system (Figure 33). A list of completed HCB bridges is provided in Table 20. Span lengths for traditional girder bridges range from 32 ft to 70 ft. Two bridges with span lengths of 106 ft were also constructed, but these were larger box-girder cross-sections.

Since the current study began in June 2015, construction has begun on the Halls River bridge project in FDOT District 7 just outside of Homasassa Springs. The HCBs used in this project span approximately 37 ft and are spaced at approximately 7 ft, center to center. The estimated cost of the HCBs was $444 per foot. In addition to incorporating HCBs as the primary flexural members, the concrete deck, cast-in-place barriers, and pile bents are reinforced entirely with GFRP bars. Both the rectangular piles and pre-cast concrete sheet piles for the project are prestressed with CFRP.

Table 20. Summary of existing HCB bridges

Name	Location	Date	Total length (ft)	Width (ft)	Lanes	# of girders	Span length (ft)
High Road Bridge	Lockport Township, IL	September 2008	58	42	2	6	58
NJ Rt. 23 over Peckman's Brook	Cedar Grove, NJ	November 2009	32	66	4	5	32
Rt. 76 (B0439) over Beaver Creek	Douglas County, MO	November 2010	178	26	2	5	60
Knickerbocker Bridge	Boothbay Harbor, Maine	June 2011	540	32	2	8	70
Rt. 49 (B0478) over Ottery Creek	Reynolds County, Missouri	August 2012	101	26	2	6	50.5
Rt. 97 (B0410) over Sons Creek	Dade County, Missouri	September 2012	106	30	2	3	106
Rt. 205 over Tide Mill Stream	Colonial Beach, Virginia	March 2013	48	32	2	8	48
Dry Branch Bridge	Charleston, West Virginia	September 2013	106	24	2	3	106
Potomac Hollow Rd. Bridge	Barton, Maryland	September 2014	30	25	2	6	30
Halls River Bridge	FDOT Dist. 7	Est. 2018	186	58	2	9	37

Figure 32. Missouri DOT Bridge B0439, Douglas County, MO. Images obtained from HCB website [62]

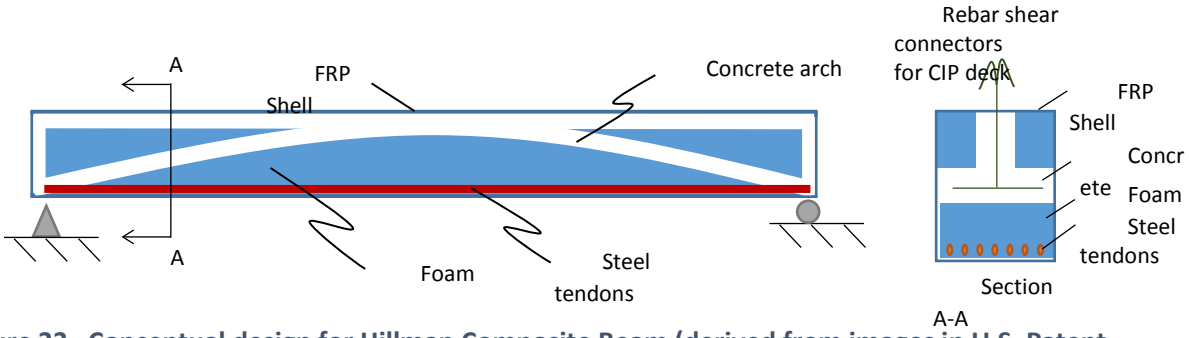

Figure 33. Conceptual design for Hillman Composite Beam (derived from images in U.S. Patent #7562499 B2)

4.6 European FRP Bridge Girder Demonstration Projects

A 2008 paper in the ASCE Journal of Bridge Engineering [63] describes experimental testing for a full-scale carbon FRP bridge girder. A demonstration project (the Pumacon Bridge) using the same configuration had been completed in Spain in 2004. A large foam core was wrapped with pre-impregnated carbon fiber fabrics, which was then subjected to vacuum assisted low-temperature curing cycle at 80 °C. Pultruded GFRP shapes were bonded to the top of the girder to serve as shear connectors between the girder and the slab.

Figure 34. Full scale carbon FRP bridge girder test (European demonstration project). Photo from *ASCE Journal of Bridge Engineering* paper by Gutierrez et al. [25].

A 2012 conference paper by Carlo Paulotto et al. [64] describes the evolution of full-scale FRP bridge girder demonstration projects across Europe. In addition to the Pumacon bridge that was completed in 2004, Paulotto discusses two identical FRP girder bridges that were erected in 2007 in Madrid, Spain. These bridges each consisted of 3 simple spans (33 ft, 46 ft, and 33 ft). The girders were fabricated using both carbon and glass pre-impregnated fabrics that were placed in an open, reusable, steel mold (no foam core was utilized). The total weight of the 46-ft girder was ~4.7 kips. As an interesting point of reference, a 46 ft long Florida I-beam that is 36 in deep (FIB 36) is estimated to weigh over 38 kips [65].

Figure 35. Carbon/glass FRP bridge girder erected in 2007 in Madrid, Spain. Photos from 2012 CICE conference paper by Paulotto et al. [64].

A third project discussed by Paulotto was a 78-ft simple span pedestrian bridge girder that was constructed from glass FRP using a vacuum infusion process (VIP)—also commonly referred to as vacuum assisted resin transfer molding (VARTM). In this method, dry glass fabric is placed in an open steel mold to achieve the desired thickness and a vacuum bagging material is used to seal off the surface. Once sealed, a vacuum is pulled between the bag and the mold and resin is allowed to infuse the part. This process eliminates the need for large volumes of pre-impregnated fabrics and allows the entire part to be saturated simultaneously.

Figure 36. Glass FRP pedestrian bridge girder manufactured in 2010 using the VIP/VARTM method. Photos from 2012 CICE conference paper by Paulotto et al. [26].

Current Status: The ERAU research team contacted the researchers who published the work in 2012 regarding the current status of FRP composite bridge girders in Europe. The group confirmed that the bridges are all still in-service and have not had any major maintenance concerns. They did state, however, that they are not aware of any on-going efforts to build any new vehicular bridges using FRP composites.

More recent research that included the fabrication, full-scale load testing, and installation of an FRP U-girder vehicle bridge in Poland was recently discovered [132]. A detailed description of this work and how it was used to validate finite element models in the current study is provided in Section 9.2.1.1.

5. Advances in Composites in the Aerospace Industry

To gain a competitive advantage in the marketplace, next-generation transport aircraft typically aim to achieve a 20% higher operating efficiency than existing designs. New airframe architectures that include lightweight composite materials are a significant factor in the overall efficiencies of these new designs. FRP composites have also gained popularity due to the growing demand for reduced energy consumption in the aviation/aerospace industry.

The advanced strength of composites is a result of the fiber reinforcement's microstructure and texture. A fiber may be described as a particle with a length-to-diameter ratio of greater than ten to one [10]. A small fiber diameter compared to its length results in fewer flaws and voids. This leads to the "size effect" where the strength of fibers is closer to the theoretical value compared to the bulk material [66]. Moreover, if the fibers are made of graphite, carbon layers tend to lay up perpendicular to the fiber axis hence the modulus of elasticity is higher at the longitudinal direction; however, special care should be taken to establish an optimal bond between the fibers and the matrix since interlaminar shear strength and bonding is one of the major issues for the integrity of the structure. Paradoxically, matrix/fiber bond that is too strong can degrade the properties of some types of composites just as a weak bond degrades the properties of others [7,67,68].

Interestingly, the high tensile modulus of composites does not show an accompanying increased compression strength since the compressive failure mechanism is totally different from that of tension. The compression strength of the composites is usually 50-60% lower than their tensile strength. Fibers of low modulus tend to buckle and form kink bands normal to the longitudinal axis while fibers with high modulus undergo shear deformation and form kink bands at an angle of 45^{o} to the fiber axis [69]. Therefore, reinforcements of high tensile modulus have decreased compression strength, shear modulus and flexural strength. Other parameters that can negatively affect the structural behavior of a laminate are impact damage, misalignment of fibers during manufacturing, the presence of fully damaged fibers or fibers with flaws and microcracks during production, weak matrix/fiber interface, and poor elastic properties of the matrix that cannot adequately support the reinforcement and suppress fiber microbuckling [70]. An ongoing issue for engineers is the lack of a commonly accepted method for testing and validating the strength of composites in compression [71].

A typical composite system demonstrates low strain to failure and shear strains resulting from compression, tension or combined loading. In contrast to metals or cases that metallic matrices are applied, the composite systems show elastic deformation up to fracture with minimum plastic deformation [66]. In every case, special care should be exercised for the interlaminar stresses that can lead to delamination and matrix cracking as well as those stresses present at the free edge surfaces[66]. Delamination is one of the most common failure mechanisms in composites. Recent manufacturing problems in the new 787 Dreamliner, which consists of 50% carbon fiber materials by weight, led to delamination issues that were traced to the assembly of the aft fuselage section [72]. This phenomenon can affect the stacking sequence of the final laminate.

Proper sequencing leads to compressive interlaminar stresses at the free edges, which are less likely to cause delamination [73,74]. The optimum design of a laminate can also simplify the analysis of their complex behavior. It can solve structural issues that arise due to the coupling phenomena by implementing symmetrical stacking sequences and balanced arrangements, thus eliminating shear, bending-torsion and stretching-bending coupling between different layers [66]. An alternative approach

to improve the delamination resistance of a laminate is offered by stitching technology. Through-the-thickness stitching with liquid-crystal fibers has been shown to suppress damage growth, eliminate the use of bolts and fasteners and enable for cost-effective, fast and straightforward production [34,75,76]. The crack-stopping process offers superior strength and performance since stitched panels can operate well in the post-damage regime [20].

The tailoring of composite properties depending on the unique requirements of each application is considered as one of the most important advantages of these systems over the use of conventional materials. This can be accomplished by selecting the appropriate matrix/reinforcement material and type, applying more fibers in the direction of the maximum anticipated loads, using variable angle fibers or by just altering the stacking sequence. The final properties found in a variety of modern applications would not be possible to achieve with the use of conventional materials. The advanced tailoring characteristic of composites is widely studied in the aerospace sector. Aeroelasticians gain great benefits by tailoring laminates to increase divergence and flutter speed, increase crashworthiness and payload of aircrafts, minimize the drag and reduce the gust loads [77,78,79,80,81]. Although these studies seem to be very promising and can lead to potentially efficient and superior airframes, they are still not fully-exploited by the aerospace industry due to fabrication and cost-related issues.

Another property that plays an important role during the service life of any structure is resistance to static loading (creep) and cyclic loading (fatigue). Fatigue causes extensive damage throughout the specimen volume, leading to failure from general degradation of the material instead of a predominant single crack. A predominant single crack is the most common failure mechanism in static loading of isotropic, brittle materials such as metals. There are four basic failure mechanisms in composite materials as a result of fatigue: matrix cracking, delamination, fiber breakage and interfacial debonding. The different failure modes, combined with the inherent anisotropies, complex stress fields, and overall non-linear behavior of composites, severely limits our ability to understand the true nature of fatigue. Moreover, fatigue resistance can be degraded by environmental factors like absorption of moisture, corrosion, high temperature, impact damage, imperfect fiber alignment, and the presence of bolts and rivets [82,83,84,85].

Detection of damage and defects in composites caused by fatigue stress or applied loads outside the design level is not an easy task due to their complex structure and high anisotropy. Non-visible damage is currently one of the main performance issues in composite structures. In 2014, “hairline cracks” on the wings were reported during the manufacturing procedure of 40 Dreamliners raising new questions about the repair cost and time of aircrafts that consist of composites [86]. Radiographic and microwave methods, infrared thermography, acoustic emission methods and ultrasonic techniques are some of the available inspection solutions depending on the current composite structure and needs [87,88,89]. Lately, optical fiber sensors have gained popularity among the available non-destructive testing methods and in-service health monitoring of composites since temperature, pressure, strain, and chemical characteristics values can be reliably measured [90,91].

The non-homogeneous nature and anisotropic mechanical properties of composites raise major issues in the ongoing effort to fully exploit the advantages that these advanced materials are capable of providing. Micromechanical and macromechanical analyses can be applied to predict the strength and stiffness of the composite, but a number of assumptions are inevitably considered. The fibers are assumed to be homogeneous, linearly elastic, isotropic, regularly spaced, perfectly aligned, and of

uniform length, the matrix is assumed to be homogeneous, linearly elastic, and isotropic and the fiber/matrix interface is assumed to be perfect, with no voids or disbands [10]. Idealization of the structure is also considered to some degree in the Classical Plate Theory (CPT), First and Second order Shear Deformation Theory (FSDT, SSDT) when they are implemented during the structural analysis to determine the relationship between stresses/loads and strains/deformations or the vibrational behavior of these systems [92,93]. Moreover, the prediction of failure in composites is still an open issue for the engineers since the current methods seem to produce more reliable results for the fibers tension failure than matrix failure and the delamination growth [10]. Except from the extended use of finite element softwares, current trends with promising results and good correlation with experimental tests include the utilization of probabilistic methods and computational analyses that takes into account inherent voids and flaws [94,95,96].

Since their first implementation in high-performance applications in early 1960's, the composites market has been constantly expanding; however, their growth was not as high as it was initially anticipated, especially in the aerospace sector, due to their elevated cost as well as design, maintenance, repair and inspection requirements [10]. The superiority of composites over metallic materials created visions of 50% weight savings for airframe structures, but today this is true only for limited aircraft components [82]. In a recent aircraft crash during landing (Asiana Flight 214), the investigation revealed that the 777's tail, which is made of composites, broke off whereas the aluminum alloy fuselage stayed intact resulting in saved lives [97]. This example suggests that more studies on the crashworthiness of composite structures are required before aircraft designers are able to implement composite materials efficiently.

In summary, although composites are lighter, the economic utility of composite primary structures is often diluted by their higher fabrication costs due to (1) required large autoclaves (2) out-time limitations for Pre-pregs, and (3) higher number of required fasteners and detail parts. Additionally, there are several performance issues with the composite structures such as (1) poor damage tolerance, (2) catastrophic failure due to damage, (3) non-visible damage, (4) weak out-of-plane bonds properties, and (5) separation between skin and flanges with small out-of-plane deformations, which all lead to heavier designs that can obtain certification and desired safety. To address the composite fabrication and performance challenges, researchers at NASA's Advanced Composite Technology Wing Program started researching the feasibility of unitized stitched-composite concepts for use in aircraft airframe applications [98].

Conventional manufacturing is achieved through the assembly of numerous small parts. Although fabrication of each part is simple, the assembly process requires significant touch labor and tooling as well as extensive use of fasteners that ultimately leads to structural discontinuities, corrosion and fatigue. Stitching manufacturing techniques allow for structural unitization to be achieved, which results in a reduction of parts in critical areas. This reduces the potential for corrosion around fasteners and reduces overall fastener maintenance. Unitized structures enable an integral one-piece panel construction that is capable of enhancing out-of-plane loads and local stress concentrations inherent in built-up panel assemblies. Additionally, the z-direction reinforcement improves the damage tolerant properties of composite structures, by which it would meet the conventional crack-growth and damage-arrest methodologies [99]. This method forms the basis for the stitched approach; it uses through-thickness stitching to increase the out-of-plane tension strength of the layered composite material system which enables higher levels of structural integration.

The fundamental premise of improving structural performance is to create a unitized composite structure using stitching that has an equivalent level-of-safety and crashworthiness to that of proven state-of-the-art aluminum structures. The overall goal is to achieve structures that are multi-load path, redundant, damage tolerant, and capable of redistributing internal loads to the undamaged regions of a damaged panel assembly while simultaneously reducing fabrication costs. Pursuing these objectives resulted in a new concept for manufacturing unitized airframe structures: the Pultruded Rod Stitched Efficient Unitized Structure (PRSEUS) system.

5.1 PRSEUS Structural Concept

5.1.1.1 *Basic Design*

The highly integrated PRSEUS structural concept is based on stitched-composite technologies, which were first introduced 20 years ago, and uses dry warp-knit fabric materials to create a preform of the full structural unitized panel that is fabricated outside the autoclave. Consequently, the damage-arrest characteristics of stitched structures can be fully exploited, as well as the unique processing advantages inherent in dry carbon fabrics. An illustration of the PRSEUS arrangement is shown in Figure 37.

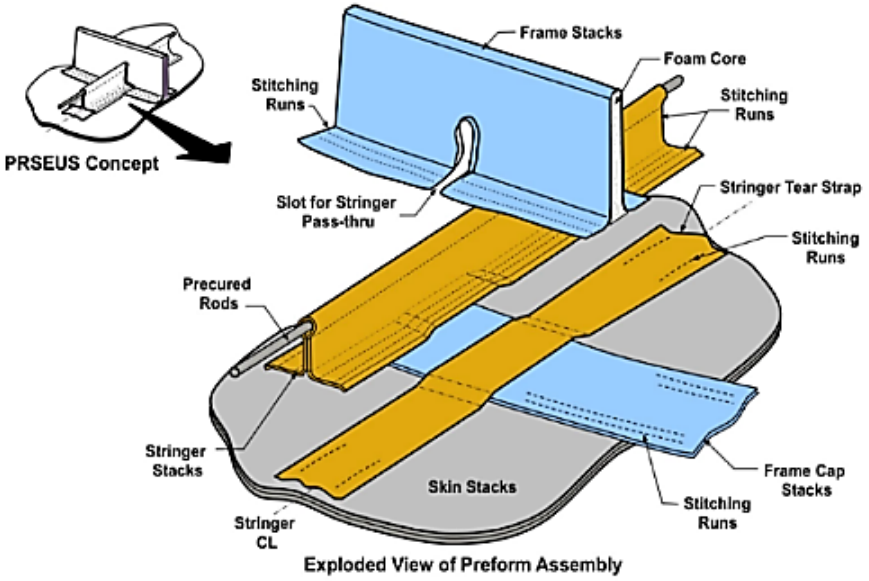

Figure 37. PRSEUS components and assembly [100]

The basic building blocks of the PRSEUS concept consists of five main components:

1. The stacks of the outer skin
2. Stringer support layers and stack material
3. A pultruded carbon fiber rod
4. Frame cap support stacks and layers wrapped over Rohacell foam
5. The frame cap

Each stack has a nine-layer core (±45°/0°/0°/90°/0°/0°/±45°) of Hercules, Inc. AS4 carbon fiber, stitched together with Vectran liquid-crystal fibers. The stringer stacks (yellow color) are positioned perpendicular to the frame stacks (blue color) to achieve high stiffness in both directions and provide

continuous load paths. A small opening in the frame web ensures load path continuity at the stringer-frame intersection. The stringers consist of a 0-degree carbon-fiber dominated pultruded rod and a carbon-epoxy overwrap. The rod offers two main advantages; it increases panel stiffness along the longitudinal direction and improves panel's bending capability because it is placed higher than the skin. The frame elements feature a lightweight foam core and are stitched directly on the inner moldline (IML) skin surface without metallic fasteners or bolts. The total weight of the structure is considerably reduced. They also feature carbon-epoxy overwraps that increase the stiffness of the panel in the spanwise direction.

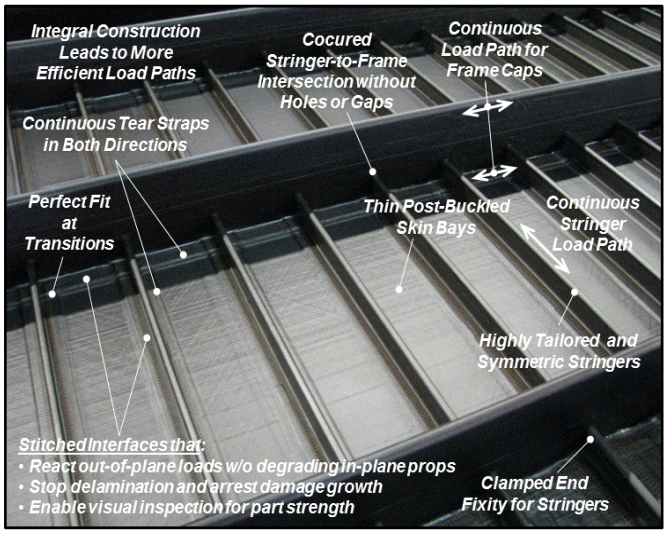

Figure 38. Structural advantages of PRSEUS panel construction [100].

5.1.2 PRSEUS Manufacturing

Preform assembly begins with the warp-knit fabric on a cutting table. This fabric is cut into small pieces, which are intertwined with rods and foam-core details. These pieces are then positioned and stitched in place. The stringer stacks are positioned perpendicular to the frame stacks and no mechanical fasteners are needed in any step of the manufacturing process. Upon completion of the preform net-molding, the preform is placed in a vacuum bag and sealed against the cure tool. At this point, the Boeing-patented CAPRI out-of-autoclave process is used to infuse the preform with HEXFLOW VRM34, a two-component epoxy resin. The resin is infused into the preform rapidly at 140˚, and cured at 200˚. Once cured, the temperature is raised to 350˚, and post-cured. After successful curing, the final shaping takes place.

Figure 39. Robot arm performing through-the-thickness stitching [100].

Using the PRSEUS concept, structural continuity is maintained by eliminating mechanical attachments, gaps, and mouse holes to provide uninterrupted load paths between the skin, stringer, and frame elements (Figure 37). Load paths at the stringer-to-frame intersection are maintained in both directions by passing the rod-stiffened stringer through a small keyhole in the frame web while keeping both frame caps continuous. The high-modulus rod embedded in the stringer cap increases the local strength and stability of the stringer section while simultaneously shifting the neutral axis away from the concentrated material near the skin. Frame members are stitched directly onto the skin to eliminate shear tie details and are designed to take advantage of carbon fiber tailoring by placing bending and shear-conducive layups where they are the most effective. Since all of the interfaces are stitched together to provide through-thickness strength, a higher degree of fiber tailoring is possible even with composite material systems which are known to be brittle, layered, and prone to delamination.

The highly integrated nature of the structure is attributed to the use of stitching technology which enables this unique manufacturing process with dry material forms, self-supporting preform design, and no out-time or autoclave limitations. Through-the-thickness stitching allows for easy handling of the dry materials as well as cost-effective, fast, and straightforward production. Stitching is performed by a six-axis robot arm (Figure 39) that features a fast one-sided sewing process. The net-molded preform is self-supporting and ready for resin infusion with minimal labor. Experience gained during the last 10 years of PRSEUS manufacturing procedures has demonstrated that it is feasible to easily construct highly integrated, larger, and more complex panel geometries [100].

5.1.3 Advantages of PRSEUS

The use of fail-safe design methods enabled by the stitched-composite technology of PRSEUS makes its weight competitive. Most importantly, these methods offer enhanced load-carrying capacity after damage, up to a specified level, while still maintaining safety of flight. The ability of stitched composites to contain damage growth within the stringer and frame elements is considered to be one of the major advantages of PRSEUS concept. The whole crack-stopping process offers superior strength and performance to PRSEUS panels since they can operate well in the post-damage regime. This phenomenon has been demonstrated in many experiments regarding flat and curved PRSEUS panels under tensile or combined loading [101,102,103]. In a damaged stiffened panel under tension, experimental results showed that stress intensity is reduced in the vicinity of the crack tip, and if load

levels exceed an upper limit, the damage is propagated until a stitching interface is reached. The propagation of damage will then follow the stitching path until it reaches the frame-stringer intersection (Figure 40). Similar studies on 3-stringer stiffened panels demonstrated the damage-arresting capabilities of the PRSEUS structural concept, and it was shown that failure occurred at a level 32% higher than the design load limit [100]. Under combined tension and internal pressure loading on a 7-stringer 5-frame PRSEUS panel, the failure occurred at 85% higher than the design load limit. The enhanced capacity was attributed to the stitching configuration [101,102]. Stitching arrested damage to permit 3 times higher than initiation loading, and during pressure testing, flat PRSEUS panels achieved 3P loading (27.6 psi) without pressure loss after failure. Therefore, high levels of residual panel strength can be achieved since PRSEUS panels are capable of withstanding additional loads after the initiation and propagation of damage, and the remaining undamaged structure is able to operate at its full design capability.

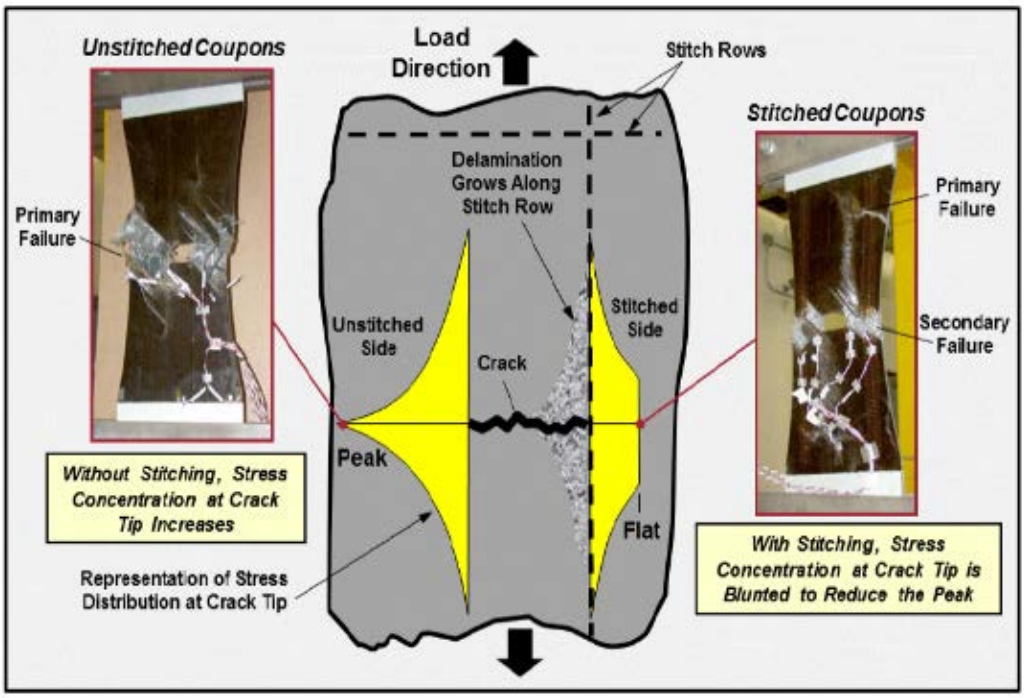

Figure 40. Stitching blunts stress concentration at crack tip [39]

The damage-tolerant design and fail-safe approach applied to stitched composites is radically different from the conventional laminate design which results in oversized and heavier structures. Common composite design practice is to achieve Design Ultimate Loading (DUL) in the Barely-Visible Impact Damage (BVID) condition without detrimental damage growth by employing a conservative no-growth design criteria. On the other hand, designers are able to fully exploit the advanced property of stitching technology like crack arrestment and turning capabilities by making highly-integrated, lighter and stronger structures. The relationship between damage size and residual panel strength is shown in Figure 41. The fail-safe panel design enables for 50% or more than the damage initiation load compared to the ultimate design load used for conventional composites.

- PRSEUS's unique design offers weight savings compared to the other common panel concepts like a blade-stiffened panel or an I-stiffener. A comparison between the bending and axial stiffness (EI and EA respectively) of the normalized section of these arrangements are shown in Figure 42. A blade-stiffened panel needs approximately 2.5 times more material to match PRSEUS's bending capabilities while the I-stiffener is comparable to a PRSEUS panel due to the presence of flange material far from the neutral axis; however, I-stiffener and blade-stiffened panels should be 20% heavier to match the axial stiffness of the PRSEUS panel due to the presence of the unidirectional carbon-fiber rod.

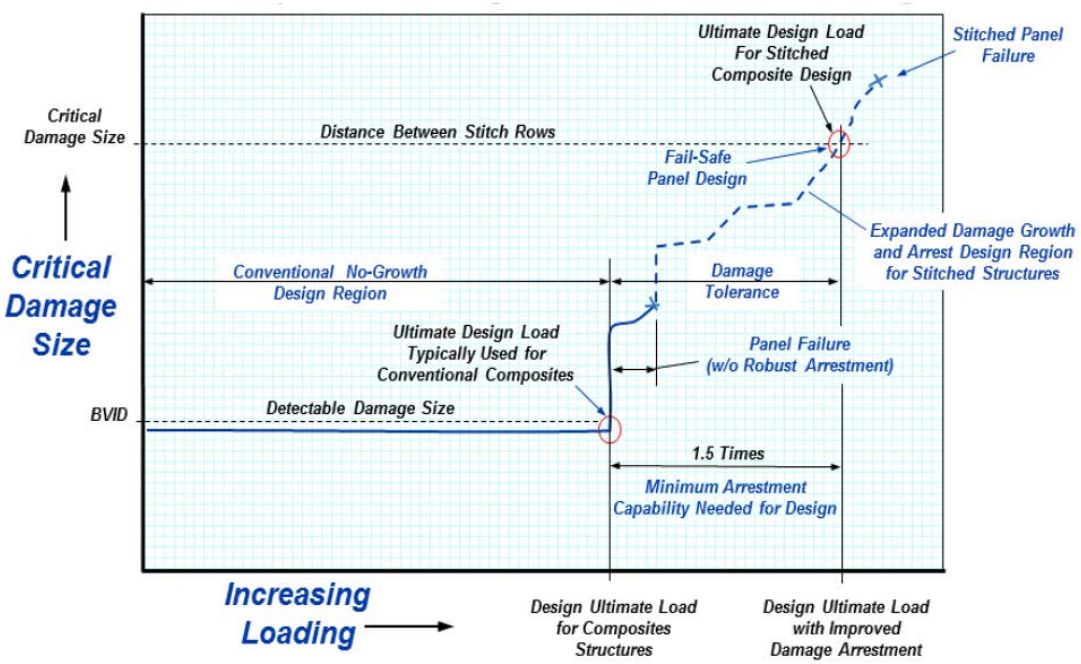

Figure 41. Relationship between damage size and residual panel strength [100]

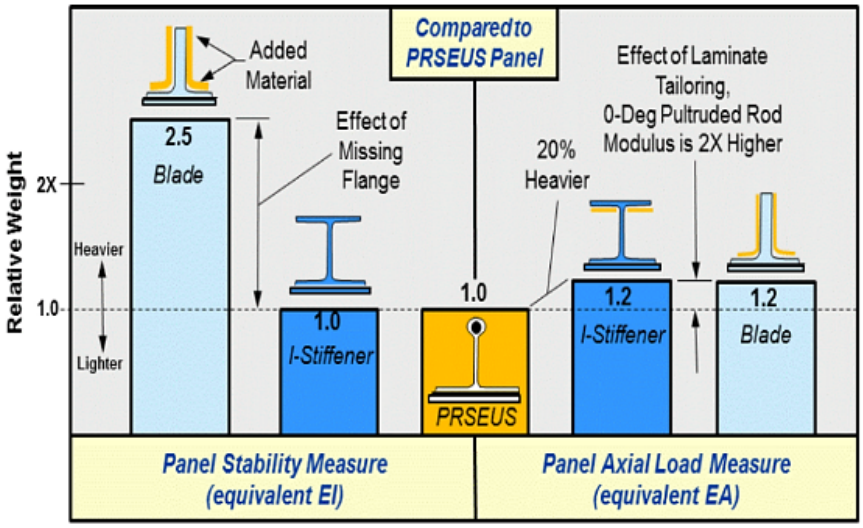

Figure 42. Normalized comparison of panel section properties [39].

5.1.4 Previous Experimental Work (By Others)

Bergan *et al*. studied the improved damage-containment capabilities of the PRSEUS concept for a curved fuselage panel [101]. The panel was subjected to axial tension, internal pressure, and combined axial tension and internal pressure load conditions up to fracture and inspections were performed in the vicinity of the notch tips where damage progression occurred. Critical strain values are also calculated through simulations and experiment. The advantages of stitching technology are demonstrated and a failure analysis is described.

In large scale experiments, Yovanof *et al*.[104] designed, tested and analyzed the structural behavior of a PRSEUS pressure cube test article to assess three-dimensional effects. The pressure cubes achieved 2P (18.4 psi) loading without pressure loss or visible damage. Velicki tested three large pressure subcomponent specimens to observe the structural responses for axial and pressure-type loadings. Through experimental and computational methods, they were able to demonstrate that these specimens exceeded preliminary load capacity limits. Jegley [105] showed that there is no evidence fatigue cycling had any effect on the failure loads of single-rod-stiffened frame specimens and that the fatigued and unfatigued specimens fail in the same manner.

The goal for improved buckling stability was also achieved since stringer and frame elements failed at 75% higher loads than strength design allowable. Yovanof and Jegley [106] reported computational and experimental results for a two frame panel under compression and demonstrated the benefit of hybrid wing body configuration gains using a PRSEUS integral frame and stringer arrangement. A damaged three-frame-panel, modeled by applying a central crack, sustained loading due to the stitching arrangement of the frames and stringer's web. A critical strain value in the vicinity of the notch tip was determined.

A number of other important studies concerning the design and utilization of nondestructive testing for PRSEUS configurations have been completed. Johnston [107] utilized ultrasonic methods to demonstrate the damage-arrest properties of the stitching technology in PRSEUS. Johnson also reported some of the technical difficulties that these methods face. Full ultrasonic inspection of some critical areas, like the highly-stressed inner fillet of the integral caps, was not possible due to the geometry of these arrangements. In another study, Bergan *et al*. [101] examined the damage propagation of a curved PRSEUS panel utilizing nondestructive and destructive techniques such as visual inspection, ultrasound, flash thermography, X-radiographic computed tomography, ply-by-ply teardown and fractography. The analyses of the failed specimen revealed delamination in the skin region between the notch tips and adjacent stringers, widespread stitch failures, skin/stiffener disbanding, extensive matrix cracking along the surface-ply-fiber-direction and misaligned fiber distribution due to the warp-knitting.

Due to the unique arrangement of PRSEUS, a critical issue arises regarding the testing of various structural features. Boeing, proposed a rod push-out test-method and conducted preliminary tests to assess the strength of the rod-wrap bondline [108]. The analysis of this computational and experimental study evaluates the resistance of rod-wrap during a push-out test by modeling the interface as a cohesive zone. There is agreement between numerical predictions and the average test failure of four specimens, within 5%. The average maximum push-out force during the brittle fracture is considered about 2,800 lbs. Jegley showed also that the panel's failure load can be increased if additional local

reinforcement, made by the same stack material of the PRSEUS design, is applied to the frame/stringer intersection [109].

5.2 PRSEUS Concept in Commercial Aircrafts

Applications of composites in commercial aircrafts and space shuttles are present since 1972 under the NASA Aircraft Energy Efficiency Program and the NASA Advanced Composites Program [110]. However, conventional laminate composite technology seems unable to meet modern eco-friendly requirements for even lower airframe weights, reduced manufacturing costs and decreased acoustic emissions. NASA and The Boeing Company are working together to design, manufacture, and test aircraft configurations that will incorporate all of the advanced properties of PRSEUS to meet future air transportation needs under the Environmentally Responsible Aviation (ERA) Project. Toward this direction, a novel airframe design was developed that features a non-circular pressure cabin, large unitized wing/fuselage components and higher lift-to-drag ratios. The design is called a Hybrid Wing Body (HWB) vehicle [106,104] (Figure 43).

Figure 43. Experimental HWB aircraft (NASA Dryden Flight Center Photo Collection) [10].

The HWB structural analysis reveals a radically different load case than that encountered by the conventional tube-and-wing fuselage systems. The present aircraft arrangements face much higher streamwise (N_x) than spanwise load magnitudes (N_y) while the HWB structure is more susceptible to equal loads in each direction due to the high-aspect-ratio wing-body configuration and flat geometry [104]. In addition, the near-flat panel geometry must also transmit internal pressure loads (N_z) and withstand secondary bending forces. Additional bending moment is also induced by flexure of the wings during maneuvers (Figure 44). Conventional aerostructure technology is unable to meet these requirements since these structures mainly consist of stringers along the primary longitudinal direction. Shear clips are used to attach these members to the frame, creating at the same time numerous discontinuities and stress concentration areas along spanwise direction. This ultimately makes the structure inefficient and incompatible with the loads experienced by HWB vehicles. Implementing conventional composite systems, like traditional layered materials, would result in high weight penalties because such systems are unable to suppress delamination and join adjacent structural elements without utilizing a large number of fasteners. Moreover, the high manufacturing and repair cost of a conventional composite structure makes it a non-viable option for HWB aircrafts [104].

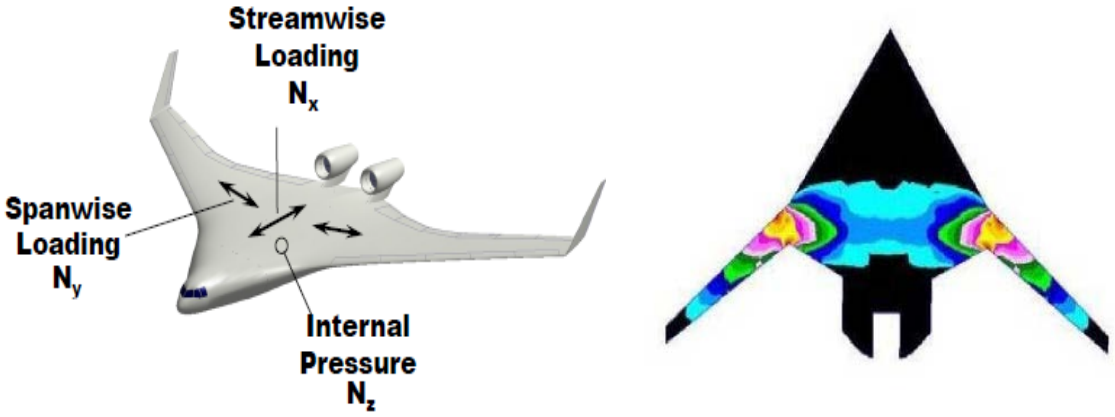

Figure 44. Applied loads in a HWB aircraft are almost equal in two directions (Nx = Ny). Stress concentration areas in the outer shell are located between inner and outer wings section [111].

Although PRSEUS was primarily optimized for the HWB design space, the PRSEUS concept is a unique configuration which offers numerous advantages and can be also utilized in other applications in the future. A large number of tests have already been conducted, both experimental and computational, to verify theoretical structural advantages and weight-saving assumptions of the PRSEUS concept. One of the first critical steps towards the design of PRSEUS configurations for aircrafts was the utilization of optimization methods. Design, analysis, and sizing methods for PRSEUS configurations have been developed and incorporated into the HyperSizer Structural Sizing Software; a computer aided engineering (CAE) software used for stress analysis and sizing optimization of metallic and composite structures. In the case of the HWB aircraft, the load criteria was based on the FAR-25 (Federal Aviation Regulations Part 25 - Airworthiness Standards: Transport Category Aircraft) standards resulting in thirteen critical cases that were applied in the optimization process [111].

5.3 PRSEUS in Civil Infrastructure?

Direct applications of the current PRSEUS concept to civil infrastructure may be cost prohibitive at the present time. Nonetheless, many of the issues that concern bridge owners regarding the use of composite materials (e.g. unpredictable delaminations and rapid loss of section capacity) are being actively addressed with this technology. Incorporating 3-D stitching in critical areas may provide opportunities for visible damage to manifest on the surface of the composite while still retaining an adequate reserve capacity. Integrating pultruded carbon FRP rods may also provide much needed improvements in girder stiffness. Again, incorporating 3-D stitching into this process will be critical to ensure that the strength of these rods can be better-realized as opposed to simply debonding from the surface once the shear capacity of the laminate has been exceeded.

6. Alternatives for Further Development

After reviewing the relevant literature and investigating the performance of existing FRP bridge girder systems in Task 1, three alternative FRP girder geometries were identified for additional analysis and evaluation. Task 2 focused on developing an overall design framework for FRP composite bridge girders and the comparison/evaluation of the three alternatives. Specific variables that were investigated include:

- Girder geometry
  - U-shape FRP girder
  - Round concrete-filled FRP tube (CFFT)
  - Strongwell DWB-36
- Span length (30 ft, 40 ft, 50 ft, 60 ft, and 75 ft)
- Number of girders/girder spacing
- Laminate architecture and material properties

The following elements related to structural analysis and design methodology were also investigated:

- Applicable limit states from LRFD-7 and LRFD-FRP (applies to all alternatives)
- Optimization for least weight using FEA, quadratic programming and genetic algorithms
  - U-shape FRP girder
- AASHTO distribution factor method for single-girder design
  - U-shaped FRP girder
  - CFFT
- Comparison of distribution factor results for moment from AASHTO Table 4.6.2.2.2b-1, Type “e”, with FEA results for optimized U-shaped girder cross-section (50-ft span only).
- Composite vs. non-composite action with cast-in-place deck
  - CFFT
- Influence of barriers on deflection calculations
  - U-shaped FRP girder (all span lengths)
    - Effect on FEA optimization results
    - Effect on deflection calculations per AASHTO LRFD-7 Section 2.5.2.6.2 and FDOT SDG Section 2.8.2
  - Strongwell DWB 36 (30 ft span only)
- Shear strength provisions
  - U-shaped FRP girder
    - Effect on FEA optimization results
    - Influence of concrete and FRP strength on single girder design using AASHTO distribution factors
  - CFFT
    - Evaluation of LRFD-FRP provisions for shear strength
    - Influence of concrete and FRP strength on single girder design using AASHTO distribution factors

The following elements were considered in the evaluation phase of the study:

- Estimated manufacturing costs
- Construction
    - Establishing shear connection between FRP girder and concrete deck
    - Cast-in-place deck – formwork and casting sequence
- Maintenance
- Expected service life

Significant technological advancements have occurred in FRP composites manufacturing and design since several FRP composite girder bridges were constructed in the late 1990s to mid 2000s:

- **Material Properties** – Glass fabrics used in the first generation of FRP bridge girders were either multidirectional fiberglass matt or traditional woven fabrics. The use of stitched, non-crimp fabrics has increased considerably in recent years. Composite laminates made using non-crimp fabrics have considerably higher material strength properties than standard woven fabrics.
- **Manufacturing Methods** – Vacuum-assisted Resin Transfer Molding (VARTM) technology has also advanced in the past decade. The hand-lay-up methods used in the first of two Texas FRP U-girder Bridges failed to meet certain acceptance criteria based on acoustic-emissions testing [55]. Parts manufactured using VARTM methods are generally considered to be of much higher quality and achieve higher material strength properties. The infusion processes used to create the FRP shell in the Hillman Composite Beam is another example of the versatility the VARTM method affords.
- **Design Methodology** – A new AASHTO design standard related to the use of FRP materials in vehicle bridges has been adopted since the Texas bridges were constructed [112]. Allowable stress limits for different environmental exposure conditions (e.g. normal and aggressive) and different loading conditions (e.g. strength and creep rupture) can now be used to evaluate proposed cross-section dimensions. These allowable stress limits serve as the basis for a two-pronged approach to design in the current study: (1) design based on AASHTO distribution factors used to determine the demand imposed on a single bridge girder, and (2) design based on finite element analysis and advanced structural optimization techniques that are currently used in the design of aerospace structures.

The current study optimized the generic cross-section properties for FRP U-girders and concrete-filled FRP tubes. An existing pultruded FRP bridge girder (Strongwell DWB36) was also investigated to determine the number of girders for span lengths ranging from 30 ft to 75 ft.

6.1 U-Shaped FRP Girder

The U-shaped FRP girder is derived from the generic GFRP cross-section used in bridges in Refugio County and San Patricio County, Texas. The overall conceptual design for an FRP U-girder bridge is provided in Figure 45.

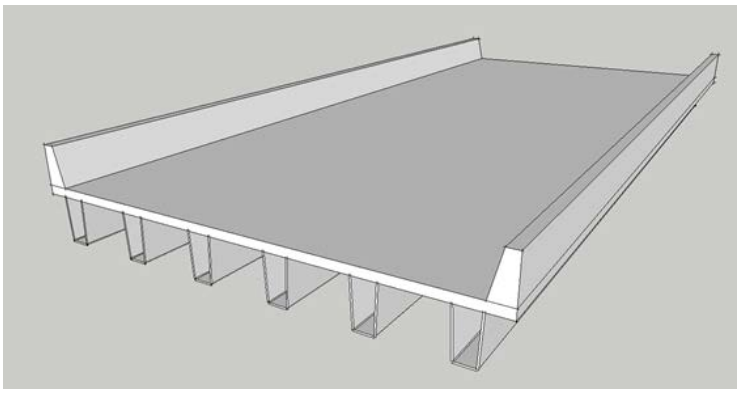

Figure 45. Conceptual design for U-shaped composite girder bridge.

6.2 Concrete Filled FRP Tube (CFFT)

The Concrete Filled FRP Tube (CFFT) alternative was previously used in the King's Stormwater Channel bridge. While this bridge was ultimately removed from service due to maintenance and durability concerns related to the FRP bridge deck, the CFFT girder elements were reported to have performed well over their 13-year service life. CFFTs have also been used extensively in multiple Concrete Arch Bridge System (CABS) bridges (formerly "Bridge-in-a-Backpack") around the world. The current AASHTO LRFD Design Specifications for CFFTs in pure flexure provides a closed form solution for evaluating the moment capacity and shear capacity of the CFFT at the strength limit state. In the current study, the CFFT will develop composite action with a standard 8" thick reinforced concrete deck. The general concept is highlighted in Figure 46.

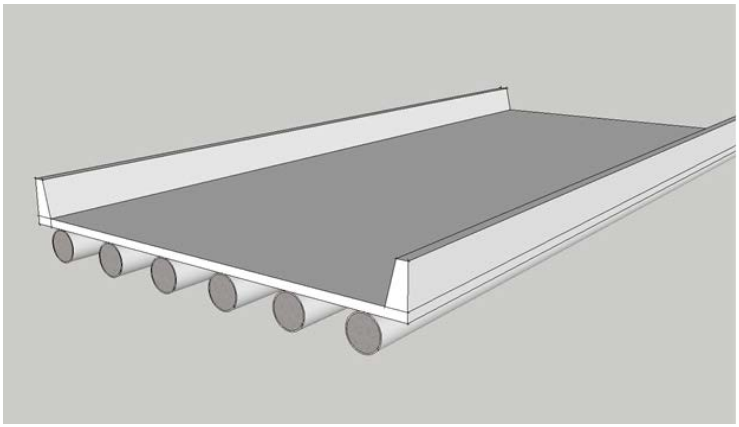

Figure 46. Conceptual design for concrete-filled FRP tube (CFFT) girder bridge.

6.3 DWB36

The Strongwell DWB is a pultruded glass-carbon hybrid FRP bridge girder. Two bridges have been constructed in Virginia utilizing this girder following extensive research and development at Virginia Tech in the late 1990's and early 2000's. The two pilot bridges utilized a laminated timber deck and very little composite action between the girders and the deck was considered in the original design. The current study investigates the use of the Strongwell DWB36 in conjunction with a cast-in-place reinforced concrete deck in an effort to increase the overall stiffness of the bridge.

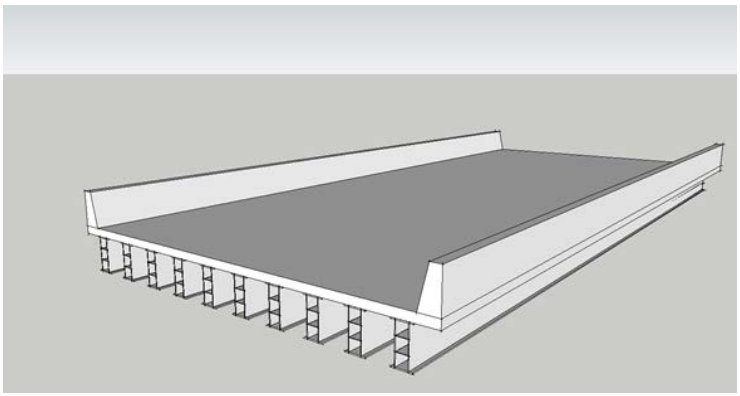

Figure 47. Conceptual design for Strongwell DWB36 pultruded girder bridge.

7. Design Space Variables

The working design space for the current study includes the following general parameters:

- Roadway/Geometry Cross-Section (fixed for current study)
- Span length (variable)
- Number of girders present in the superstructure (variable)
- Girder geometry (variable)
- FRP material properties (variable)

7.1 Roadway Geometry/Cross-Section

The roadway geometry and cross-section (Figure 48) was derived from the Florida Slab Beam (FSB) Superstructure Package for a 32-ft clear roadway width (D30032). An 8-in-thick reinforced concrete slab was used for all span length/number of girder combinations. The FDOT Structures Design Guidelines (FDOT-SDG) requires a slab thickness of at least 8 inches for bridges less than 100 feet in length. The slab was assumed to act as part of the composite section for both the U-Shaped FRP Girders and the Strongwell DWB36 pultruded girders. For the CFFT option, separate analyses were performed to investigate the impact of composite vs. non-composite action with the bridge deck.

A 36-in Single-Slope Barrier (D427) was assumed to act along the edge of the slab on both sides. The dead load of the barrier was always accounted for, but the structural contribution of the barrier was treated as a design variable. A simplified barrier geometry was adopted for finite element modelling purposes. The dimensions of the simplified barrier were selected such that the area and moment of inertia were similar to the standard detail.

There is significant disagreement between AASHTO LRFD-7 and the FDOT Structures Design Guidelines regarding the treatment of barriers for meeting deflection criteria. LRFD-7 provides the following guidance for situations where the bridge owner chooses to impose deformation criteria:

> **LRFD-7 (2.5.2.6.2):** *For composite design, the stiffness of the design cross-section used for the determination of deflection should include the entire width of the roadway and the structurally continuous portions of the railings, sidewalks, and median barriers.*
>
> **LRFD-7 (2.5.2.6.2):** *When investigating the maximum absolute deflection for straight girder systems, all design lanes should be loaded, and all supporting components should be assumed to deflect equally.*
>
> **LRFD-7 (4.6.3.1):** *[For refined methods of analysis,] a structurally continuous railing, barrier, or median, acting compositely with the supporting components, may be considered to be structurally active at service and fatigue limit states.*

The relevant text from the FDOT Structures Design Guides reads as follows:

> **FDOT SDG (2.8.2):** *Traffic and pedestrian railings and raised sidewalks are not to be used for the determination of deflections or for service or fatigue limit state checks.*

Additional discussion regarding the influence of barriers on both the finite element analysis results and the AASHTO distribution factor results are discussed in Section 9.1.

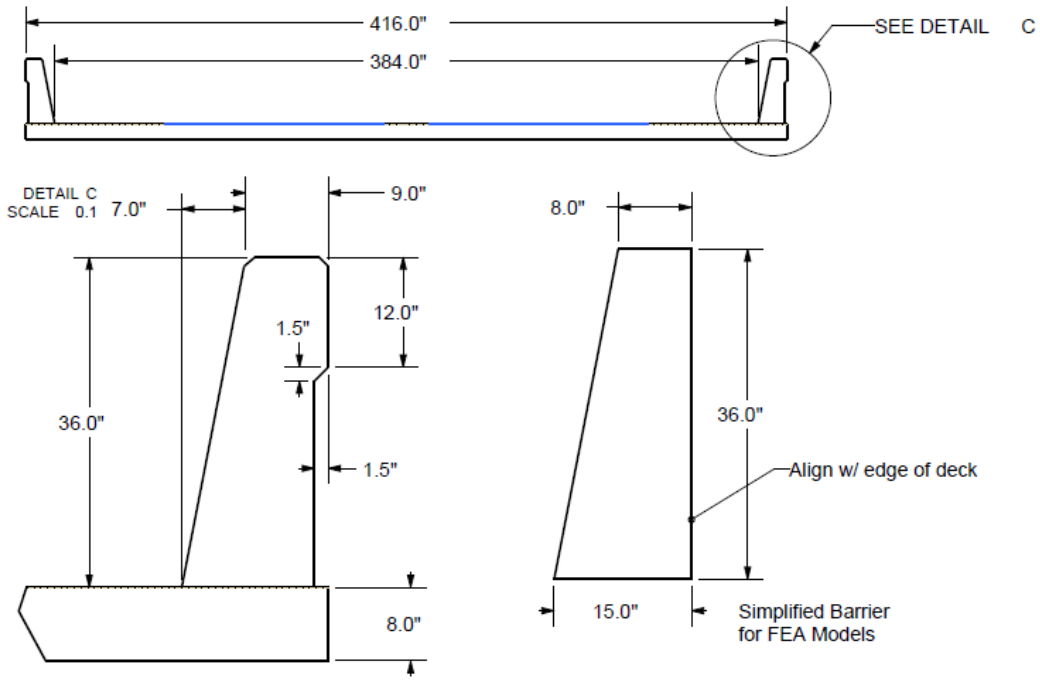

Figure 48. Roadway geometry/cross-section used throughout current study.

7.2 Span Length

Span lengths of 30 ft, 40 ft, 50 ft, 60 ft, and 75 ft were evaluated for each of the three girder alternatives. These span lengths have been identified as part of an effective "span range gap" [113]. Traditional prestressed Florida I-Beams are capable of achieving span lengths greater than 200 ft, but span lengths less than 80 ft are generally considered inefficient for the FIB-36". The prestressed Florida Slab Beam (FSB) is a viable alternative for span lengths up to 65 ft [114], but the long-term performance (i.e. 75 year design life) of this system in an "extremely aggressive" coastal environment has not been demonstrated. A typical application for the proposed FRP bridge girder alternative would be short-span relief bridges in coastal areas where the freeboard to saltwater bodies is on the order of several feet.

7.3 Number of Girders

The number of girders utilized in previous/existing FRP girder bridges varies significantly. The King's Stormwater Channel bridge in California used a total of six CFFTs for a two-span continuous bridge (30-ft spans) with a clear roadway width of 39 ft (girder spacing = 7.5 ft). The first FRP U-girder bridge constructed in Texas (San Patricio County), used 12 girders for a 30-ft, two-span simply-supported bridge. The roadway width was 32 ft and the corresponding girder spacing was 32 in. Finally, the second FRP U-girder bridge built in Texas (Refugio County) used eight girders (4 ft spacing c/c) for a 32-ft roadway width spanning 50 ft.

For the majority of analysis cases in the current study, the outermost edge of each girder is always positioned to align with the inside face of the 36-in traffic barrier. Any deviations from this practice will be noted. The resulting center-to-center spacing varied slightly depending on the width of the girder. Resulting girder spacing ranges for a 12-in girder width are summarized in Table 21.

Table 21. Center-to-center beam spacing for different girder numbers in bridge cross-section (for 12-in-deep girder base)

	Number of Girders, N_b								
	4	5	6	7	8	9	10	11	12
Spacing, S (ft)	10.33	7.75	6.2	5.17	4.43	3.89	3.44	3.1	2.82

7.4 Girder Geometry

Girder geometry parameters varied for each girder option. The U-shaped FRP girder option involved two separate investigations with slightly different girder geometry parameters. Parameters used in the FEA optimization study are shown in Figure 49a. The range of values investigated in the FEA optimization study are provided in Table 22. Parameters used in the AASHTO distribution factor/stress-strain compatibility method are shown in Figure 49b.

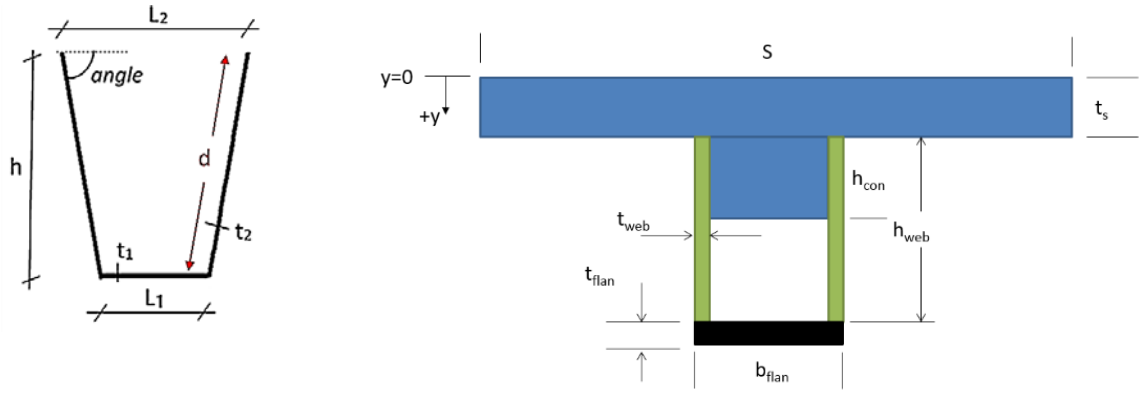

(a) (b)

Figure 49. U-Shaped FRP Girder cross-section geometry variables. Parameters considered for (A) FEA optimization (slab not shown) and (B) AASHTO distribution factor/stress-strain compatibility method.

Table 22. Design variable ranges for U-shaped FRP girder structural optimization

Variables	Range
# girders	4 -12
Height, *h*	(0.04 – 0.07) x Span length
L_2, in.	≥ 10
t_1 (base thick.), in.	0.50 – 2.00
t_2 (sides thick.), in.	0.50 – 2.00

The geometry of the CFFT is defined by each girder's diameter and FRP tube thickness (Figure 50a). A cast-in-place shear key is also provided to develop a shear connection with the cast-in-place concrete slab. The DWB36 had fixed dimensions based on the manufacturer's specifications (Figure 50b).

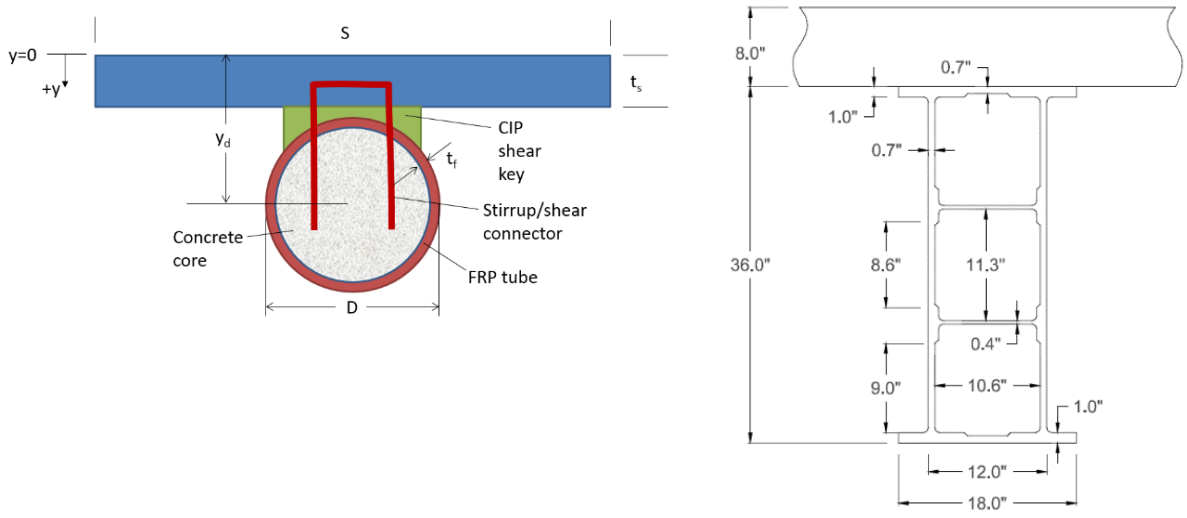

(A) (B)

Figure 50. Design parameters for (A) concrete-filled FRP tube and (B) overall dimensions for Strongwell DWB36.

7.5 FRP Material Properties

A primary advantage of FRP composites is that the direction of the fiber reinforcements can be tailored to match the structural demands imposed by a given set of loading conditions. The basic building block for FRP composites laminates is a single ply (lamina) of unidirectional fibers and matrix. These lamina are then stacked at specified orientation angles to obtain a laminate. The material properties of the fibers, matrix, and the relative proportion of each material (i.e., the fiber volume fraction) affects the overall behavior of a given lamina. Micro-mechanics models can be used to predict lamina stiffness and strength properties, but that level of detail is beyond the scope of the present study. It is important, however, to have a clear understanding of the orthotropic nature of a given lamina and how these lamina properties will interact to determine the overall strength and stiffness of a specified laminate.

Typical single-ply lamina properties are provided in Table 23 (stiffness properties) and Table 24 (strength properties). The manufacturing method (pre-preg, VIP, or filament winding) and resulting fiber volume fraction, υ_f, have a significant influence on the resulting lamina properties. The tables also highlight the highly orthotropic nature of single-ply lamina. The 1 subscript refers to the primary fiber direction (strong axis) while the 2 subscript refers to the transverse direction (weak axis). For carbon fiber lamina, the modulus of elasticity in the primary fiber direction, E_1, is roughly 13 times greater than the modulus of elasticity in the transverse direction, E_2. This is caused by the relatively high tensile modules of the carbon fibers. The ratio of E_1 to E_2 for glass fiber lamina is closer to 3. For the strength properties provided in Table 24, the + and – superscripts refer to tension and compression, respectively. The S_{12} value provided in Table 24 refers to the ultimate in-plane shear strength of the single-ply lamina. The axis directions for the single-ply lamina coordinate system, as well as the strength parameters in shear and tension, are illustrated in Figure 51. These single-ply strength and stiffness properties ultimately combine to form the strength and stiffness properties of an FRP laminate.

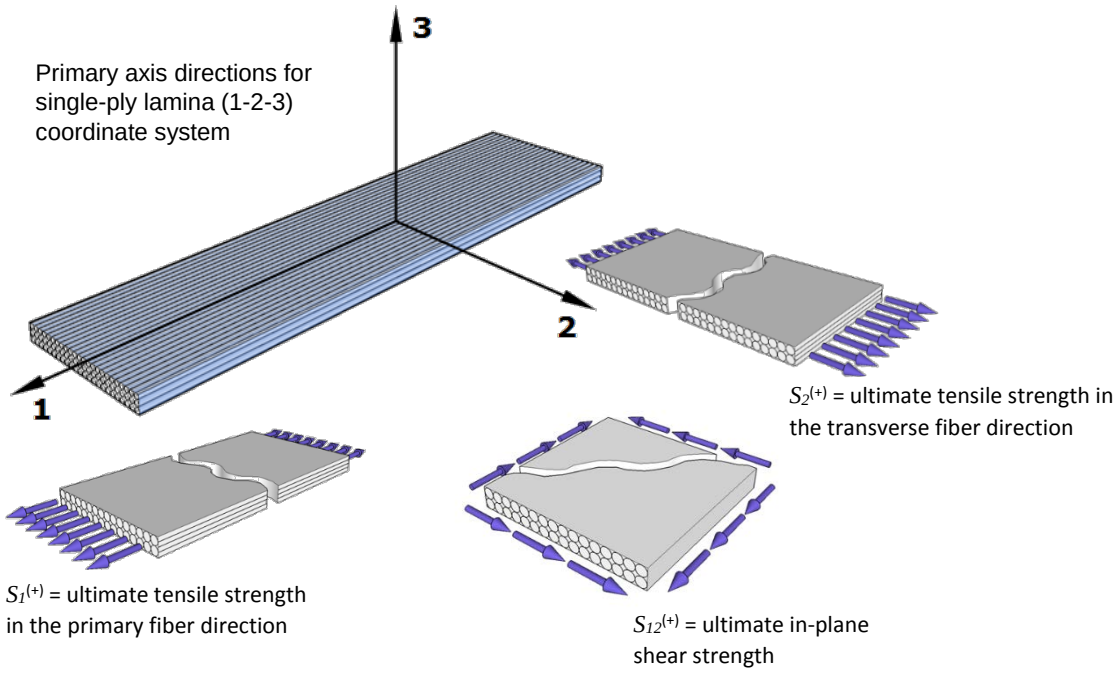

Figure 51. Single-ply lamina coordinate system.

Table 23. Typical single-ply lamina properties (stiffness parameters)

Material	E_1 (ksi)	E_2 (ksi)	G_{12} (ksi)	ν_{12}	υ_f
Carbon-fiber					
AS3501 [115] (ep)	20,000	1,500	1,000	.3	.65
"Typical" [116] (ep)	23,100	1,580	930	.38	.63
Filament wound [117] (ep)	17,500	1,000	700	.3	--
Fyfe Tyfo SCH-41 [50] (ep)	13,900	--	--	--	--
Glass-fiber					
E-glass/vinylester [115]	3,540	1,000	420	.32	.30
"Typical" [116] (ep)	5,660	1,450	600	.25	.46
Vectorply E-T 2200 (vinyl.) [118]	5,694	2,080	657	.25	.52
Fyfe Tyfo SEH-51A [119]	3,790	--	--	--	--

Single-ply laminae are used exclusively in pre-preg composite systems. Because the uni-directional fibers are pre-impregnated with an activated matrix (a resin where the chemical hardener has already been added), pre-preg materials must be stored at freezing temperatures to inhibit curing. Once they are removed from the freezer, each product has a defined "out-life", or time, that the single-ply materials can be cut and placed in a mold to achieve the desired stacking sequence and laminate thickness. Once in the mold, a vacuum bag used to ensure that the stacked lamina make solid contact during the curing process. The composite must then be subjected to an elevated temperature schedule to fully cure the matrix material.

Table 24. Typical single-ply lamina properties (strength parameters)

Material	$S_1^{(+)}$ (ksi)	$S_1^{(-)}$ (ksi)	$S_2^{(+)}$ (ksi)	$S_2^{(-)}$ (ksi)	S_{12} (ksi)
Carbon-fiber					
AS3501 [115] (ep*)	210	170	7	36	9
"Typical" [116] (ep)	250	198	6.1	33.4	13.8
Fyfe Tyfo SCH-41 (ep)	143	50	--	--	--
Glass-fiber					
E-glass/vinylester [115]	85	116	6.2	27.1	9.3
"Typical" [116] (ep)	160	87	5.2	20	11.3
Vectorply E-T 2200 (vinyl) [120]	106	106	16.0	16.0	9.9
Fyfe Tyfo SEH-51A** [119] (ep)	83.4	--	3.75	--	--

*ep = epoxy, vinyl = vinylester

** The Tyfo SEH-51A fabric does contain a small amount of woven transverse reinforcement

For larger structures, such as boat hulls, utility scale wind turbine blades, or FRP bridge girders, obtaining the desired thickness using single-ply lamina would be extremely labor intensive. Typical single-ply lamina thicknesses for pre-preg composite systems are on the order of 0.008 inches. Achieving the required elevated temperature schedule to cure these large parts also requires very large ovens or autoclaves. The solution is to place un-impregnated (i.e. dry) fabrics into a mold and saturate the fibers with resin using a wet lay-up or vacuum assisted resin infusion process. The fabrics themselves consist of well-defined yarns that are either woven or stitched together. The weaving/ stitching simply ensures that the fibers remain dimensionally stable during cutting and placement in the mold.

There are three fundamental categories of fiber reinforcement fabrics:

- Multi-directional strand mat
- Woven fabrics
- Non-crimp fabrics (NCF)

Multi-directional strand mat consists of either chopped fibers or continuous strand fibers that are oriented randomly and held together with a binding agent. These fabrics can be on the order of 0.04 to 0.06 in thick and are typically used for non-structural applications that require significant bulk. Multi-directional chopped fiber composites can also be created using continuous strand roving that is fed through a chopper gun, impregnated with resin and then sprayed on the surface of a mold. This method has been used in a bridge repair application on the University Boulevard bridge in Jacksonville, Florida.

Woven fabrics (illustrated in Figure 52A) are commonly used in structural applications. There are numerous weave patterns available that provide different levels of conformity to mold surfaces. All woven fabrics include a series of parallel yarns that run in the warp direction and an additional set of parallel yarns that run perpendicular in the weft direction. The weft yarns are woven from side to side as the warp yarns are lifted and dropped to obtain the desired pattern. While weaving does achieve the desired goal of maintaining dimensional stability for the fibers, one downside is that the crimping/ bending that occurs in each yarn will reduce the overall strength of the resulting laminate.

Non-crimp fabrics attempt the provide the same dimensional stability and formability of woven fabrics but also retain as much of the strength properties as possible in relation to uni-directional single-ply lamina. This is achieved by keeping the warp and weft yarns straight and introducing a multiaxial stitching fiber that serves to hold the two layers together (Figure 53). Strength properties are not as high the laminates constructed by stacking single-ply lamina, but they are much improved over woven fabrics.

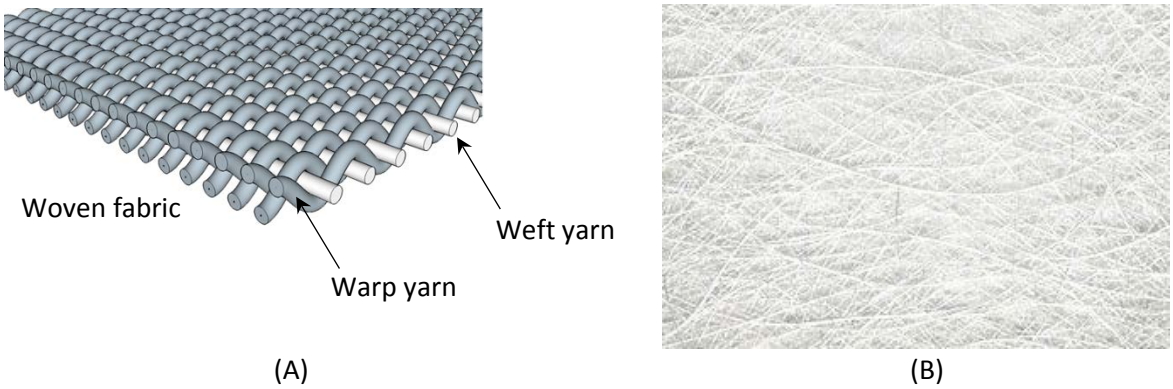

Figure 52. Fiber reinforcement fabrics. (A) Woven and (B) continuous strand mat [121].

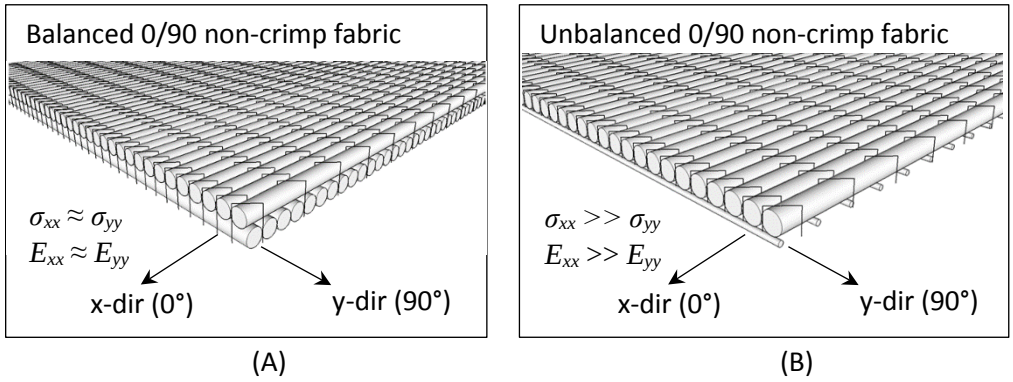

Figure 53. Non-crimp stitched fabrics. (A) Balanced strength and stiffness properties in the 0/90 directions and (B) Unbalanced strength and stiffness properties with greater strength/stiffness in the x-direction.

Material properties that were obtained from manufacturer's data sheets are summarized in Table 25. Obtaining strength data for different reinforcement fabric types was extremely difficult. Only one supplier that we identified, Vectorply, published typical composite strength data for their fabrics. The σ_{xx} values and σ_{yy} values refer to the laminate strength properties in the warp and weft directions, respectively. The in-plane shear strength of the laminate is given as τ_{xy}. Modulus of elasticity, E_{xx} and E_{yy}, values are also provided. Hexcel does provide fabric strength data (measured in lbf/in) for their woven reinforcements, but they do not provide anything similar for their non-crimp stitched fabrics. Fabric strength is obtained by performing a tension test on the dry, un-impregnated fabric. The values for σ_{xx} and σ_{yy} for the Hexforce fabric were obtained by dividing the fabric strength by the nominal fabric thickness. Even though a direct comparison between laminate strength and fabric strength cannot be made, there does appear to be a significant strength difference between Hexcel's 0/90 woven fabric

(HexForce 1597) and the 0/90 non-crimp fabric (E-LT-4400 from Vectorply—see Figure 53A). Both of these alternatives are "balanced" with an equal proportion of the fibers running in the 0° and 90° directions. Keeping the warp (0°) and weft (90°) yarns straight appears to double the tensile strength of the laminate.

Another interesting comparison can be made between the E-LT-4400 laminate and the E-LT-5500 laminate. Both consist of NCF, but the E-LT-5500 has a much larger percentage of fibers running in the 0° direction (50.97 oz/yd^2) versus the 90° direction (3.36 oz/yd^2) while the E-LT-4400 is essentially balanced (21.76 oz/ yd^2 in the 0° direction and 21.99 oz/yd^2 in the 90° direction). The resulting strength increase in the 0° direction is significant (120.4 ksi vs. 73.8 ksi). There is not, however, a corresponding strength gain for shear.

Table 25. FRP composite material properties

Fabric Type	Manufact.	ID	σ_{xx} (ksi)	σ_{yy} (ksi)	τ_{xy} (ksi)	E_{xx} (Msi)	E_{yy} (Msi)	Thickn./ layer (in.)
NCF 0/90 RI	VectorPly	E-LT-4400	73.8	74.2	13.1	3.9	3.92	0.044
NCF $0^+/90^-$ RI	VectorPly	E-LT-5500	120.4	46.6	13.1	6.57	2.44	0.054
NCF Carbon 0 RI	VectorPly	C-L 1800	198.7	4.2	7.9	16.56	1.43	0.024
Woven 0/90*	Hexcel	HexForce 1597	34.4	37.0	--	--	--	0.0378
Filament wound	WacoBoom	n/a	52.0	50.0	11.3	3.9	3.1	n/a
Pultruded carbon/ glass hybrid	Strongwell	n/a				5.76	1.69	n/a

*Strength values refer to the fabric breaking strength and do not include the contribution of the resin.
Note: RI = Resin Infused

Fiber orientation angle also requires consideration. The material properties described in Table 25 are based on a 0° orientation angle that aligns with the warp direction of the fabric. In the current study, this is assumed to be in same direction as the primary axis of the bridge girder. The relatively low shear strength for the balanced 0/90 laminates can be enhanced considerably by rotating the fibers 45 degrees—essentially creating a +/- 45 laminate. Consider the material properties for the E-LT-4400 provided in Table 26. A rotation angle of 45 degrees results in an ultimate shear strength of 26.9 ksi (more than double the shear strength of the 0/90 laminate). The downside, however, is a 47 % decrease in elastic modulus and a 73.5% decrease in tensile strength in the longitudinal direction. These properties are illustrated in Figure 54.

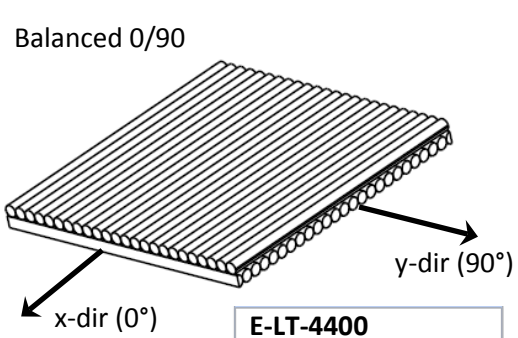

E-LT-4400	
Rotation angle = 0°	
σ_{xx}(ksi)	73.8
σ_{yy}(ksi)	74.2
τ_{xy}(ksi)	13.1
E_{xx}(Msi)	3.9
E_{yy}(Msi)	3.92

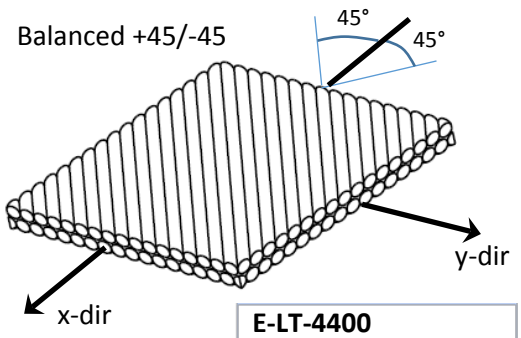

E-LT-4400	
Rotation angle = 45°	
σ_{xx}(ksi)	19.4
σ_{yy}(ksi)	19.4
τ_{xy}(ksi)	26.9
E_{xx}(Msi)	2.04
E_{yy}(Msi)	2.04

Figure 54. Comparison of non-crimp fabric laminate properties (0/90 vs. +/- 45).

For the E-LT-5500 laminate, the issue is complicated even further due to the unbalanced laminate strength properties. The maximum shear stress capacity is achieved at a fiber orientation angle of 135 degrees, which corresponds to aligning the principal tensile stresses in the primary fiber direction. Once again, the corresponding decrease in elastic modulus (70%) and tensile strength (82.8%) in the longitudinal direction is significant.

To avoid creating more variables than might reasonably be managed in the current study, a decision was made to investigate different laminate architectures in a global sense and rely solely on the material properties specified in the x-y direction with x corresponding to the longitudinal axis of the bridge girder. This is conservative in the sense that structural analysis results are typically generated in the primary axis directions and the σ_{xx}, τ_{xy}, and E_{xx} properties will control for the relevant limit states. A more detailed analysis that might consider failure criteria for an optimized laminate architecture is beyond the scope of the current work.

Table 26. Laminate strength properties as a function of rotation angle [118]

Laminate Type	Rotation (°)	σ_{xx} (ksi)	σ_{yy} (ksi)	τ_{xy} (ksi)	E_{xx} (Msi)	E_{yy} (Msi)
NCF 0/90 RI (E-LT-4400)	0	73.1	74.3	13.1	3.87	3.94
	15	78.2	79.3	15.2	3.16	3.20
	30	33.4	22.1	26.4	2.31	2.32
	45	19.4	19.4	26.9	2.04	2.04
	60	16.4	21.8	26.4	2.32	2.31
	75	79.3	78.2	12.9	3.20	3.16
	90	74.3	73.1	13.1	3.94	3.88
NCF $0^{+}/90^{-}$ RI (E-LT-5500)	0	120.0	46.7	13.1	6.57	2.44
	15	130.1	51.7	14.5	4.44	2.23
	30	26.4	19.2	27.2	2.60	2.00
	45	20.7	20.6	23.6	1.98	1.98
	60	19.1	26.1	22.7	1.95	2.60
	75	51.7	130.1	14.4	2.23	4.44
	90	46.7	120.0	13.1	2.44	6.57
	105	51.7	130.1	14.5	2.23	4.44
	120	19.2	26.4	23.1	1.95	2.60
	135	20.6	20.7	39.0	1.98	1.98
	150	26.1	19.1	31.0	2.60	1.95
	165	130.1	51.7	14.4	4.44	2.23
	180	120.0	46.7	13.1	6.57	2.44

8. Limit States and General Analysis Framework

Three limit states were considered in the current study:

- LS-1: Concrete compressive stress (LRFD-FRP S2.9.8)
- LS-2: Displacements (LRFD-7 S2.5.2.6.2)
- LS-3: Fatigue and creep rupture (LRFD-FRP S2.7.2)
- LS-4: Strength limit for flexure (LS-4a) and shear (LS-4b) (LRFD-FRP S2.7.3)

8.1 Limit State Criteria

8.1.1 LS-1 Concrete Compressive Stress

The initial reference for this limit state comes from LRFD-FRP Section 2.9.8. This section states that the concrete compressive stresses in FRP tubes subjected to pure flexure shall be limited to 0.45 f'_c under Service I loading conditions. The commentary cites concerns about excessive creep deformations over time if the concrete compressive stresses are too high. LRFD-7 also addresses concrete stresses under service loads in Section 5.5.2 but refers specifically to Section 5.9.4. Table 5.9.4.2.2.1-1 provides a compressive stress limit of 0.45 f'_c for non-segmentally constructed bridges after all prestress losses. It is unclear whether the requirement in LRFD-7 is limited to prestressed concrete or if the requirement in LRFD-FRP Section 2.9.8 also applies to concrete in compression that is outside of a concrete-filled tube.

8.1.2 LS-2: Deflection Control

A deflection criteria of L/1000 was used to evaluate all FRP girder options in the current study. This corresponds to the most conservative deflection criteria in LRFD-7 Section 2.5.2.6.2 for bridges that include both pedestrian and vehicular loads. Previous research/experience with composite materials in bridge applications suggests that excessive deflections is often a controlling limit state. This phenomenon is attributed to the relatively low modulus of elasticity of composites (see Table 25) compared to steel. In some cases, depending on the specific fiber orientation and weave style of the composite, the modulus of elasticity of steel may be on the order of 10 times greater than GFRP. In general, the modulus of elasticity of balanced 0/90 non-crimp fabric (NCF) laminates is roughly equivalent to normal strength concrete (~4.3E3 ksi).

The low modulus of elasticity has significant implications if a non-load-bearing foam or other fill material is placed inside the FRP girder. The GFRP U-girder bridge in San Patricio County, Texas, used polystyrene foam in the bottom 2/3 ~ 3/4 of the girder. Even though composite action was achieved with the cast-in-place concrete deck using stainless steel tubes, the very low-modulus GFRP (E_x = 2.12 E3 ksi) was still required to provide a large portion of the overall bridge stiffness. This could explain the high weight of FRP required for each 30-ft span of the San Patricio bridge (~21,800 pounds for 12 girders at a cost of $320 per foot using current estimates).

Filling the girders with concrete would increase the overall stiffness of the bridge and require less FRP to achieve the specified deflection criteria. The trade-off, however, is increased dead load that will impact the creep and fatigue rupture limit state. Another important consideration is the effect of concrete cracking on the moment of inertia of a concrete-filled FRP U-girder. LRFD-7 allows the gross moment of inertia of concrete cross-sections to be used for deflection calculations for plain and prestressed reinforced concrete (LRFD-7: S5.7.3.6.2). This assumes a much higher stiffness contribution by the reinforcing steel, which is not accounted for in the gross moment of inertia of the cross-section.

If the overall stiffness (EI) of a girder is reduced due to concrete cracking in the tension zone, this effect will be offset by the fact that the modulus of elasticity of reinforcing steel is ~ 8 times larger than the modulus of elasticity of concrete. Furthermore, the cracked moment of inertia only applies to a limited region of the beam where the moment exceeds the cracking moment. Depending on the actual distribution of flexural cracks, cracked concrete in the tension zone still contributes to the overall stiffness of the girder. Using the gross (non-transformed) moment of inertia for the uncracked section is considered an acceptable compromise for steel-reinforced sections.

LRFD-7 provides guidance on computing an "effective" moment of inertia that can be applied over the entire length of a cracked concrete girder:

$$I_e = \left(\frac{M_{cr}}{M_a}\right)^3 \cdot I_g + \left[1 - \left(\frac{M_{cr}}{M_a}\right)^3\right] \cdot I_{cr} \leq I_g \quad \text{Eq. 8-1}$$

where

I_e = effective moment of inertia
M_{cr} = cracking moment
M_a = maximum moment at stage for which I is being computed
I_g = gross moment of inertia
I_{cr} = moment of inertia of the cracked section, transformed to concrete

In the current study, a decision was made to use the gross moment of inertia, I_g, for the cross-section with the FRP transformed to concrete. An additional design variable was added to include the effect of concrete depth in the FRP U-girder. Deflection calculations were performed for concrete depths within the FRP U-girder equal to 0%, 50%, and 100% of the overall U-girder depth.

Another important issue that was investigated regarding deflections is the influence of cast-in-place reinforced concrete barriers. Six design scenarios were investigated for the FRP U-girders to determine the impact of different assumptions about gross vs. cracked moment of inertia and the presence/absence of cast-in-place barriers (Table 27). The most conservative case, LS-2a, assumes no concrete is present in the FRP U-girder and the barriers are not included. The least conservative case, LS-2f, assumes the entire FRP U-girder is filled with concrete and the traffic barriers are also present. The section on the AASHTO Distribution Factor Method for FRP U-girders addresses all six of these scenarios. The section on FEA optimization for FRP U-Girders only considers LS-2a and LS-2d. Only LS-2c was investigated for the CFFT option.

Table 27. Design scenarios for displacement criteria (FRP U-girders).

Design Scenarios for LS-2	Barriers	Concrete Depth in girder
LS-2a	None	0%
LS-2b	None	50%
LS-2c	None	100%
LS-2d	Present	0%
LS-2e	Present	50%
LS-2f	Present	100%

8.1.3 LS-3: Fatigue and Creep Rupture

Criteria for LS-3 were derived from LRFD-FRP Section 2.7.2. To prevent failure due to long-term creep rupture and fatigue loading, the maximum longitudinal stress that develops in the FRP material should be limited to the following:

- For carbon-based FRP: 0.55 f_{ful}
- For glass-based FRP: 0.20 f_{ful}
- For aramid-based FRP: 0.30 f_{ful}

where f_{ful} is the design tensile strength of the FRP laminate in the longitudinal direction including an appropriate reduction factor. The design tensile strength is obtained by multiplying the manufacturer's specified tensile strength by an environmental reduction factor, C_E (Table 28). The AASHTO specifications for concrete filled FRP tubes (LRFD-FRP) provide lower C_E values for GFRP than the values prescribed by the AASHTO specification for GFRP reinforcement (LRFD-GFRP Reinforcement). The GFRP reinforcement specification makes a distinction between concrete that is exposed to earth and weather vs. concrete that is not exposed to earth and weather (as opposed to "normal environment" vs "aggressive environment" in LRFD-FRP). The C_E value for concrete that is exposed to earth and weather is 0.7 (vs. 0.5 for GFRP in an extremely aggressive environment). The reduced C_E values for GFRP girders is likely due to the fact that the exterior surface is fully exposed to the environment while GFRP reinforcing bars are afforded some protection by the surrounding concrete. It should also be noted that the C_E values for GFRP reinforcing bars provided in the LRFD-GFRP Reinforcement specification are identical to the values established in ACI 440.01R15.

Table 28. Environmental reduction factors, C_E, from LRFD-FRP S2.6.1.2

	C_E	
Fiber Type	**Normal environment**	**Aggressive environment**
Glass	0.65	0.50
Carbon	0.85	0.85
Aramid	0.75	0.70

Table 29. Environmental reduction factors, C_E, from LRFD-GFRP Reinforcement S2.6.1.2

	C_E	
Fiber Type	Concrete not exposed to earth and weather	Concrete exposed to earth and weather
Glass	0.8	0.7

The loading for this limit state is described in LRFD-FRP as all permanent loads (i.e. dead loads) with a load factor of 1.0 along with the fatigue truck described in LRFD-7 S3.6.1.4 with a load factor of 0.75 applied to the fatigue vehicle (including impact). LRFD-7 S3.6.1.4 includes the provision that the rear axle spacing for the design vehicle shall be fixed at 30 ft.

For glass-based FRP, these requirements effectively limit the maximum tensile stress in the FRP due to dead loads and a fatigue vehicle in each lane to 10% of the manufacturer's specified tensile strength. For the case of concrete structures that are reinforced with GFRP bars, ACI 440.01R15 limits the sustained tensile loading to 14% of the manufacturer's specified tensile strength. This limit is achieved

through an environmental reduction factor of 0.7 for GFRP bars in concrete exposed to earth and weather and a creep/fatigue-rupture factor of 0.2.

8.1.4 LS 4a: Strength – Flexure

The strength limit state in flexure is based on provisions provided in LRFD-FRP S2.7.3. These provisions are intended for CFFT elements, but the general concepts should translate to both the U-girder and DWB-36 alternatives. The basic design equation used to evaluate LS 4(a) is:

$$M_u \leq \Phi \cdot M_n \quad \text{Eq. 8-2}$$

where

M_u = factored moment demand
M_n = nominal resistance
Φ = resistance factor

The factored moment demand, M_u, is obtained directly from Section 3 of AASHTO LRFD (Strength I Load Combination). Discussion on lateral and transverse vehicle location to maximize the effects due to live load are provided for each girder alternative in their respective sections.

The nominal resistance, M_n, is based on one of two possible failure modes in flexure: (1) concrete crushing or (2) the maximum tensile stress in FRP exceeding the allowable limit (i.e. the manufacturer's specified tensile strength multiplied by the environmental reduction factor, C_E, from Table 28). Specific details regarding the methods used to determine the flexural capacity of each girder type are provided in their respective sections.

The resistance factor, Φ, is based on the anticipated failure mode of the section in flexure. The balanced reinforcement ratio, ρ_b, is defined as the reinforcement ratio corresponding to simultaneous concrete crushing and FRP tensile rupture. It is important to note that the FRP tensile rupture strength is based on the reduced value for tensile strength after the environmental factor, C_E, is applied to the manufacturer's specified tensile strength. For the case of CFFTs that do not achieve composite action with the RC deck, the balanced reinforcement ratio is significantly less than what would be required to achieve a balanced failure in an FRP U-girder that does rely on composite action. The amount of concrete that must be crushed in the non-composite CFFT is limited to the area of concrete above the neutral axis of the tube. Furthermore, as the number of girders decreases and the effective flange width of the RC deck increases, the amount of FRP reinforcement required to achieve a balanced failure mode in the FRP U-girder will also increase.

LRFD-FRP provides detailed guidance for computing the balanced reinforcement ratio for non-composite action CFFTs in Section 2.7.3.2. This methodology is of limited use in the current study. In an effort to keep the preliminary designs conservative, it was assumed that the amount of GFRP provided will be less than what is required to ensure concrete crushing. Unless otherwise noted, a resistance factor of 0.55 was used for LS-4(a) throughout the entire design study.

8.1.5 LS-4b: Shear

The general design equation used to evaluate LS-4(b) from LRFD-FRP is:

$V_u \leq \Phi \cdot V_n$ Eq. 8-3

$V_n = V_c + V_{frp}$ Eq. 8-4

where

V_u = factored shear demand
V_n = nominal resistance
V_c = shear resistance provided by concrete
V_{frp} = shear resistance provided by FRP
Φ = resistance factor (0.75 for shear per LRFD-FRP S2.7.3.2)

Considerable research has been conducted on the shear behavior of CFFT structural elements over the years, but there is a relative dearth of information on the shear behavior of FRP U-girders. The literature review completed for the current study did not reveal a direct approach to evaluating the nominal shear resistance provided by an FRP U-girder. Before proceeding with a proposed methodology, the following sections briefly summarize how other projects involving FRP bridge girders have addressed shear capacity and how various design guidelines determine the shear capacity for CFFTs.

8.1.5.1 *Texas U-Girders*

The final design for the FRP U-girder bridge constructed in San Patricio County is summarized by Ziehl et al. (2009) [122]. The specified material strength and stiffness requirements for this project were extremely conservative to allow for hand lay-up fabrication of the girders. The modulus of elasticity, E, for the FRP was only 2,120 ksi (one of the non-crimp fabrics we are evaluating in the current study has a longitudinal modulus of 5,670 ksi), which resulted in a deflection controlled design. The design methodology relied on a stress ratio criteria, and the large cross-sections that were required to meet the deflection limits (L/800) resulted in a stress-ratio (allowable/developed) greater than 6. It is unclear if this refers to stresses that developed under service loads or factored loads. This result does explain, however, why there was so little emphasis given to stress calculations in the design process.

The FRP U-girder optimization study completed by Chen and Zeihl [54] did not consider the overall shear strength of the section near the supports as a design variable. Oddly enough, the full-scale FRP U-girder that was load-tested to failure as part of that study actually failed in shear near the base of girder at the support. This girder did not contain concrete in the bottom 2/3rd of the cross-section. They were only able to complete the test and verify the flexural capacity of the girder by reinforcing the end-zone with wood blocks to establish support for the cast-in-place concrete portion of the girder. In the subsequent optimization study, they only considered the bearing stress of the shear connectors at the FRP/steel-tube interface, but the FRP wall thickness required to establish the shear connection never controlled the design. The researchers concluded that by filling the end region of the girder with concrete they could avoid the premature shear failure that was observed during the flexural test.

8.1.5.2 *Hillman Composite Beams*

The design manual for the Hybrid-Composite Beam (HCB) [123] provides some discussion on shear strength for HCBs but does not explicitly address designing a section for internal shear near the support or evaluating the shear capacity of a proposed HCB configuration. The document points to three primary mechanisms for shear transfer:

- The internal concrete arch directs shear forces into the support as a concrete compression force.
- The quad-weave fabrics in the HCP shell provide high shear capacity by virtue of the +/- 45 degree fiber orientation of select FRP layers.
- A thin concrete web (~3 in wide) connects the concrete deck to the arch. This web provides shear force transfer from the deck to the arch.

An earlier NCHRP IDEA Program report on HCBs [124] provides additional insight into determining HCB shear strength. The principle relies on first determining the net internal shear force, V_{net}, after the vertical component of the compression-arch force is subtracted from the total internal shear demand (Figure 55).

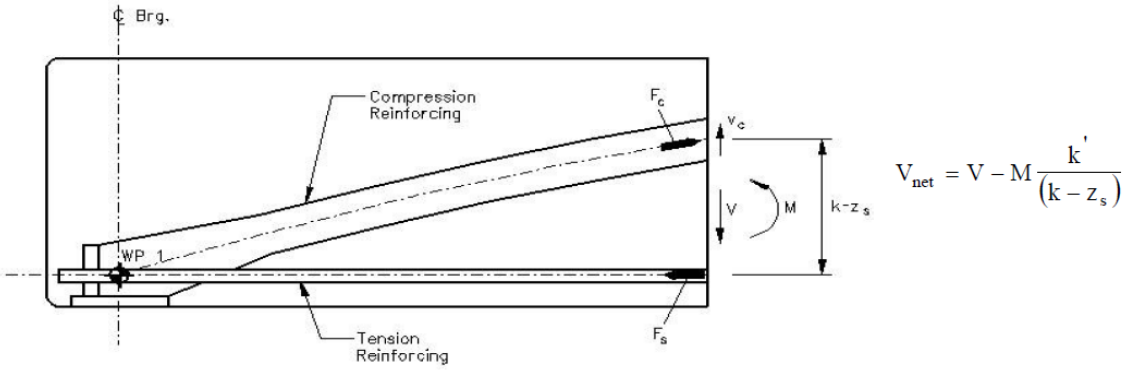

Figure 55. Schematic illustrating net shear force calculations in HCBs (from Hillman (2003)[124])

Once V_{net} is determined, the resulting shear stress that develops in the FRP webs can be determined. Hillman proposes the following relationship for determining the shear stress in the FRP webs:

$$\tau_{web} = \frac{V_{net}}{2 \cdot h \cdot t_w} \quad \text{Eq. 8-5}$$

where

τ_{web} = shear stress that develops in the FRP web
V_{net} = portion of internal shear force not resisted compression arch
h = height of FRP web
t_w = thickness of FRP web

Once the shear stress in the FRP web has been determined, the resulting value can be compared to an allowable shear stress value. In the report cited [124], a shear strength of 15 ksi (obtained through experimentation of the quad-weave fabric) is used along with a strength reduction factor of 0.5 to

obtain an allowable shear stress of 7.5 ksi. This translates into a factor of safety of 2 against the service load demand.

The methodology described by Hillman does not translate directly to the FRP U-girder. There is no compression arch to redirect the internal shear to the support through compression. Furthermore, the treatment of the shear strength contribution of the FRP webs (something that needs to be established for the current study) is potentially problematic for two reasons. First, the shear stress distribution in the webs is non-uniform. For a rectangular cross-section subjected to transverse shear, the maximum shear stress occurs at the neutral axis and is 1.5 times greater than the average shear stress. Second, the strength reduction factor of 0.5 is consistent with what LRFD-FRP applies to the manufacturer's specified tensile strength of GFRP in an extremely aggressive environment. But this reduced FRP tensile strength is used to verify that the section provides adequate capacity at the strength limit state—not the Service I limit state. There is also an additional strength reduction factor of 0.75 that should be applied to the section's nominal strength.

8.1.5.3 *CFFT Research by Burgueno*

Dissertation research completed by Rigoberto Burgueno at the University of California-San Diego in the late 90's provides the most comprehensive treatment of concrete-filled FRP tubes for bridge girder applications. This work served as the basis for the King's Stormwater Channel bridge described in Section 4.4. Burgueno relies on a model previously developed by Priestley et al. [125] to determine the shear strength contribution from the FRP tube:

$$V_{frp} = \sum_{i=1}^{N_{layers}} \frac{\pi}{2} \cdot D_o \cdot t_i \cdot \Phi \cdot \left(\frac{1}{2} \cdot f_{(\theta+\alpha_i)_{comp}} + \frac{1}{2} \cdot f_{(\theta+\alpha_i)_{tens}} \right) \cdot cot(\theta) \quad \text{Eq. 8-6}$$

where

V_{frp} = Shear resistance provided by frp (kip)
D_o = Outer tube diameter (in)
t_i = FRP layer thickness (in)
Φ = Material strength reduction factor (use C_e)
f = Lamina strength at specified angle (tension or compression)
α_i = Lamina winding angle
θ = Angle of shear crack (assumed to be 45 deg.)

The off-axis lamina strength, *f*, can be determined for each ply angle using the following relationship that is based on the Tsai-Hill failure criteria [115]:

$$f_{\theta+\alpha_i} = \left(\frac{1}{\frac{\cos(\beta)^4}{S_L^2} + \left(\frac{1}{S_{LT}^2} - \frac{1}{S_L^2}\right) \cdot \sin(\beta)^2 \cdot \cos(\beta)^2 + \frac{\sin(\beta)^4}{S_T^2}} \right)^{\frac{1}{2}} \quad \text{Eq. 8-7}$$

where

f = lamina strength at specified angle
β = $\theta + \alpha_i$
α_i = lamina winding angle
θ = angle of shear crack (assumed to be 45 deg.)
S_L = lamina strength in the primary fiber direction
S_T = lamina strength perpendicular to the primary fiber direction
S_{LT} = lamina shear strength

Specific values for S_L and S_T will depend on whether the lamina experiences tension or compression. $S_L^{(+)}$ and $S_T^{(+)}$ are used for tension while $S_L^{(-)}$ and $S_T^{(-)}$ are used for compression. There is some degree of uncertainty surrounding the notation that Burgueno used in the original presentation of the formula:

$$V_j = \sum_{i=1}^{n} \frac{\pi}{2} D t_i \phi \left[\frac{1}{2} f_{\theta+\alpha_i^-} + \frac{1}{2} f_{\theta+\alpha_i^+} \right] \cot\theta$$

The -/+ superscripts (attached to the $\theta+\alpha_i$ subscripts) typically refer to the compressive and tensile strength of the lamina, respectively.

Subsequent work completed by Burgueno and Bhide [117] resulted in a sophisticated model for predicting the shear strains that develop in CFFTs due to transverse loading. The model accounts for the state of stress in concrete and FRP due to combined axial load, bending, and shear. The model also considers concrete cracking and adjusts the amount of shear transferred via concrete based on concrete crack width and maximum aggregate size. Experimental results from Burgueno's dissertation work were used to validate the model, and there was generally good agreement between the analytical and experimental results. Unfortunately, the model could not be validated at the ultimate strength in shear because the experiments were designed to investigate the flexural capacity of the CFFTs. Nonetheless, there are several results from this work worth highlighting that are relevant to the current study.

First, going back to the original dissertation, Burgueno reports shear strain data from two unfilled FRP tubes loaded in 4-point bending. Shear strains were measured at the neutral axis of the cross-section corresponding to the location of the maximum shear stress (Figure 57). The maximum shear stress at the neutral axis of a thin tube can be determined with the following:

$$\tau_{max} = \frac{2 \cdot V}{A} \quad \text{Eq. 8-8}$$

where

V = internal shear force
A = total area of thin tube

The slope of the line, *m*, in Figure 57(B) can be used to determine the equivalent shear modulus, G_{LT}, for the FRP tube laminate (note: The L subscript indicates the longitudinal direction the T subscript indicates the transverse or hoop direction). The estimated shear modulus based on these experimental data is approximately 1000 ksi. The estimated shear modulus using classical laminate theory was 1100 ksi for Design Lay-up 1 and 1000 for Design Lay-up 2. These results simply indicate that the strain measurements recorded during the load test of the unfilled FRP tubes are in general agreement with the relationships developed for maximum shear stress from classical mechanics and the equivalent laminate behavior as predicted by classical laminate theory.

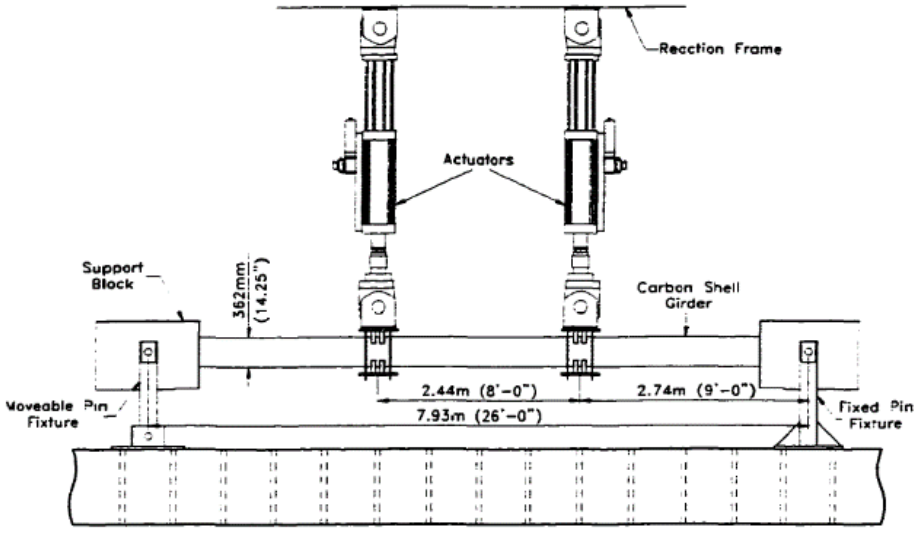

Figure 56. Experimental setup for CFFT flexural testing [116].

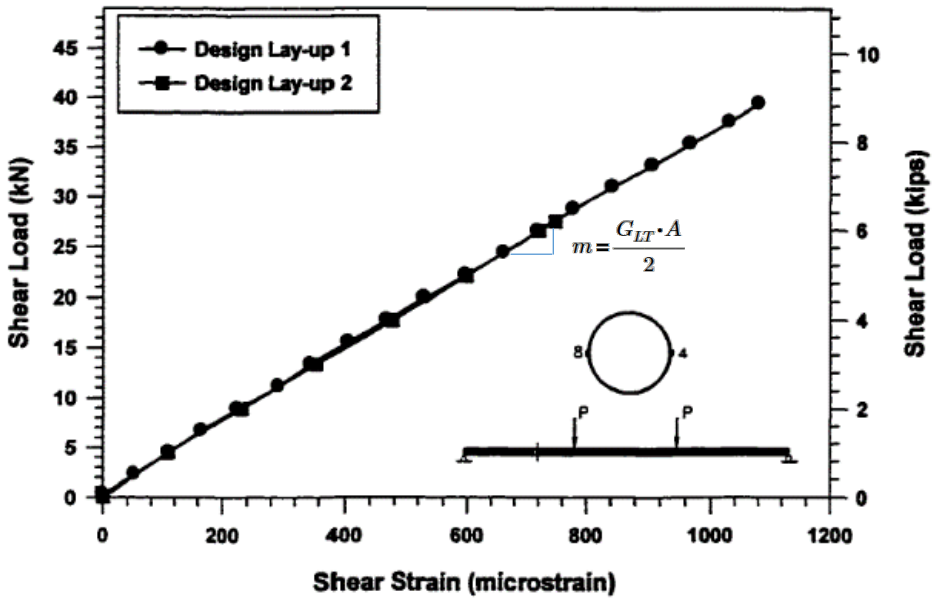

Figure 57. CFFT shear strain data for unfilled tube [117].

For FRP tubes filled with concrete, the shear strain distribution over the depth of the section becomes quite complex (Figure 58B). The analytical model developed by Burgueno is reasonably close to the experimental data, but the important question that these results fail to answer is this: at what value of internal shear force, V, will the FRP tube laminate fail in shear? The CFFT beam utilizing Design Lay-up 1 failed in flexure at an ultimate shear load, P, of 56.3 kips. Experimental shear strain data and corresponding analytical model output are only provided up to this ultimate value.

The shear strain profile (Figure 58B) data indicates that the location of the maximum shear stress for a concrete-filled FRP tube varies as the internal shear force increases. Figure 58C provides a plot of maximum shear stress (derived from the model output for shear strain presented in Figure 58B) vs. internal shear force. In an effort to estimate what level of internal shear force would result in a shear-stress failure of the FRP tube laminate, a 2nd-order polynomial curve-fit was applied to analytical model output using Matlab's curve-fit tool. The estimated maximum shear strength, based on classical laminate theory, for the FRP laminate used in Design Lay-up 1 is 14.6 ksi. This corresponds to an internal shear force of 128 kips.

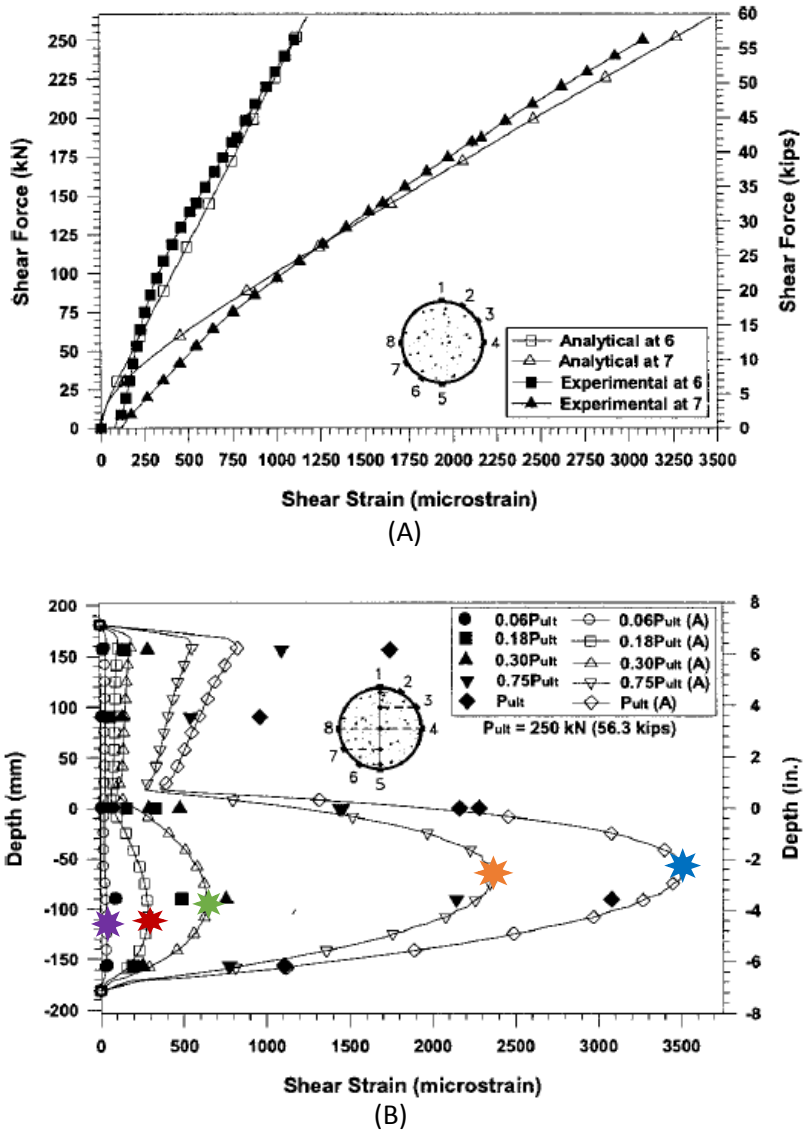

Figure 58. CFFT shear results for concrete-filled tube (Design lay-up 1). (A) Shear force vs. shear strain at mid-height and (B) Shear strain profile at select load intervals.

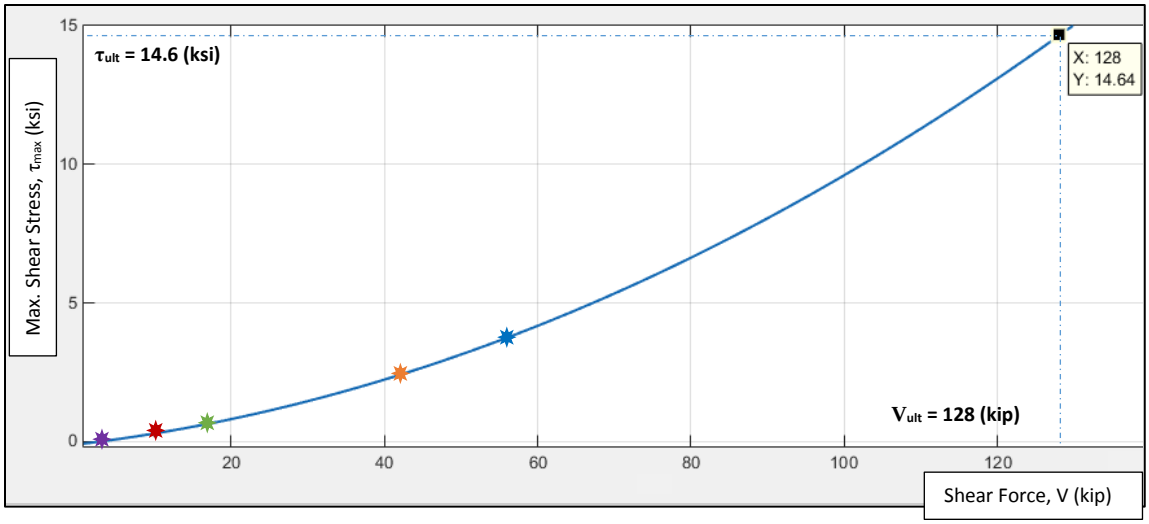

Figure 59. Maximum shear stress vs. shear force for Design lay-up 1

The extrapolated results from Burgueno's analytical model should not be taken as conclusive. Nonetheless, the ultimate shear force value of 128 kips provides a useful benchmark for comparing the estimated shear capacity of CFFT cross-sections using the different models available in the literature.

8.1.5.4 *CFFT research by Ahmad, Zhu, Mirmiran, and Fam*

A slightly modified equation for predicting the shear strength contribution of an FRP tube is proposed by Ahmad et al. [126]:

$$V_{frp} = \sum_{i=1}^{N_{layers}} \frac{\pi}{2} \cdot D_o \cdot t_i \cdot f_{(\theta+\alpha_i)_{tens}} \quad \text{Eq. 8-9}$$

where

V_{frp} = shear resistance provided by frp (kip)
D_o = outer tube diameter (in)
t_i = FRP layer thickness (in)
f = lamina tensile strength at specified angle
α_i = lamina winding angle
θ = angle of shear crack (assumed to be 45 deg.)

Again, there is uncertainty regarding the subscripts attached to the lamina ply strength at the specified angle. The relationship seems to prefer ply angles that are perpendicular to the assumed crack angle of 45 degrees. For example, if a ply is oriented at +45 degrees (parallel to the crack), the specified angle for *f* would be 90 degrees. This would correspond to the tensile strength of the ply perpendicular to the primary fiber direction. If a ply is oriented at -45 degrees (perpendicular to the crack), the specified angle for *f* would be 0 degrees. This would correspond to the tensile strength in the primary fiber direction. The ± symbol in the equation doesn't appear to serve any purpose.

8.1.5.5 *Shear Capacity of CFFTs using Chinese Technical Code for Infrastructure Application of FRP Composites*

A 2011 paper by Yu and Teng [127] describes how the *Chinese Technical Code for Infrastructure Application of FRP Composites* treats the shear strength contribution of an FRP tube as follows:

$$V_{frp} = \sum_{i=1}^{N_{layers}} \frac{\pi}{2} \cdot t_i \cdot E_i \cdot \varepsilon_{fa} \cdot \frac{(D_o + D_i)}{2} \cdot (sin(\alpha_i) + cos(\alpha_i)) \cdot sin(\alpha_i) \quad \text{Eq. 8-10}$$

where

t_i = FRP ply thickness
E_i = modulus of elasticity in primary fiber direction
ε_{fa} = design ultimate tensile strain (set to .004 per ACI 440)
D_o = FRP tube outer diameter
D_i = FRP tube inner diameter
α_i = FRP winding angle for ith layer

This equation is similar in form to those utilized by Burgueno and Ahmad. The design tensile strain in each lamina is set to 0.004 and then multiplied by the modulus of elasticity in the primary fiber direction, E_i, to obtain a design tensile strength. The ply orientation angle is accounted for by the sin/cos terms involving the winding angle. Finally, $(D_o+D_i)/2$ is simply the average tube diameter.

8.1.5.6 *Shear Capacity of CFFTs using AASHTO-LRFD*

AASHTO-LRFD Section 2.12.2 provides specific guidance on computing the shear capacity of CFFT beams. The shear strength contribution provided by the concrete, V_c, is given as:

$$V_c = 0.158 \cdot \sqrt{f'_c} \cdot A_c \quad \text{Eq. 8-11}$$

where

V_c = shear resistance provided by concrete (kip)
f'_c = concrete compressive strength (ksi)
A_c = effective concrete area (in^2)

The effective concrete area is the area of the compression zone in the cracked section under the axial load and bending moment at the section under consideration. The code permits calculating A_c for a cracked section with no axial load using a neutral axis depth of 0.3 D_o, where D_o is the outer diameter of the FRP tube.

This methodology for determining the shear strength provided by the concrete, V_c, is equivalent to the methodology described in ACI 440.1R, *Guide for the Design and Construction of Structural Concrete Reinforced with FRP Bars*. For a traditional steel-reinforced concrete section, the basic concrete contribution to shear strength from ACI 318 is as follows (note that f'_c is specified in ksi):

$$V_c = 0.063 \cdot \sqrt{f'_c} \cdot b_w \cdot d \quad \text{Eq. 8-12}$$

where

V_c = whear resistance provided by concrete (kip)
b_w = width of the concrete web (in)
d = depth to the main longitudinal reinforcing steel (in)

ACI 440.1R modifies this equation for a rectangular cross-section to account for the fact that the modulus of elasticity of an FRP bar is less than the modulus of elasticity of a traditional steel bar. This results in a reduced compression zone depth for an equivalent area of FRP reinforcement. When shear cracks develop in the concrete, the opportunity for continued shear transfer throughout the tension zone of the section due to aggregate interlock is limited. Furthermore, the FRP bars are assumed to provide less shear transfer via doweling action than steel bars. The ACI 440.1R version accounts for these differences by limiting the depth of the section to the depth of compression zone in a cracked concrete section, kd. The associated multiplier, 0.063, is also increased by a factor of 2.5. With f'_c specified in ksi units, the ACI 440.1R version of the shear equation is as follows:

$$V_c = 0.158 \cdot \sqrt{f'_c} \cdot b_w \cdot (kd) \quad \text{Eq. 8-13}$$

where

kd = depth of the compression zone in a cracked concrete section

The strength contribution of the FRP is given as:

$$V_{frp} = 2 \cdot t \cdot d_v \cdot f_{fe} \quad \text{Eq. 8-14}$$

where

t = FRP tube thickness (in)
d_v = Effective depth of FRP tube, taken as 80% of tube outer dia. (in)
f_{fe} = tensile hoop stress in the tube laminate (ksi)

$$f_{fe} \leq 0.004 \cdot E_{fh}$$

where E_{fh} is the modulus of elasticity in the hoop direction (ksi)

The tensile hoop strain limit of 0.004 is intended to capture the combined effects of hoop strain due to confinement pressure generated by any axial force as well as strain from the shear force component carried by the FRP. If no axial force is present in the CFFT, the entire strain (0.004) can be allocated to shear resistance.

8.1.5.7 *Proposed FRP Shear Strength Model*

With the exception of the simple model proposed by Hillman, none of the aforementioned models that predict the FRP contribution to ultimate shear capacity incorporates the actual shear strength of

the FRP laminate. Preliminary calculations using the AASHTO model resulted in ultimate shear capacities that might not be obtainable due to shear strength limitations. A simple model based on mechanics of materials principles is proposed in an effort to address these potential shortcomings.

The shear strength contribution of concrete is taken as described in ACI 440.1R-15 for FRP U-girders and as described in AASHTO LRFD-FRP for circular cross-sections. The shear strength provided by the FRP is derived from basic mechanics of materials principles and is limited by the shear strength of the FRP. For FRP U-girders, the strength of FRP is given as:

$$V_{frp} = \frac{\tau_{max} \cdot A_{webs}}{1.5} \quad \text{Eq. 8-14}$$

where

τ_{max} = design strength of FRP in shear ($\tau_{max} = \tau_{ult} \cdot C_e$)
τ_{ult} = shear strength of FRP reported by manufacturer
C_e = environmental reduction factor
A_{webs} = Area of FRP webs

For CFFTs, the strength of FRP is given as:

$$V_{frp} = \frac{\tau_{max} \cdot A}{2} \quad \text{Eq. 8-15}$$

where

A = total area of FRP tube

8.1.5.8 *Comparison of Shear Strength Models for CFFTs*

Four different models for evaluating the shear strength of a CFFT were identified in the literature:

- Burgueno's model (based on Priestley et al. (1996) [125]) – M1
- Ahmad et al. (modification of Priestley's model) – M2
- Chinese Technical Code for Infrastructure Application of FRP Composites – M3
- AASHTO LRFD-FRP – M4

A new, simpler model (M5) was also proposed to in an effort to overcome some of the perceived shortcomings in the models listed. The goal of this section is to compare the shear strength results provided by each model for a series of laminate architectures that might be encountered in FRP bridge girder applications. The discussion will be limited to CFFTs, but these results could also be extended to FRP U-girders by modifying the equations. Specifically, the $\pi/2$ term for circular cross-sections should be replaced by 2 for rectangular U-girders.

The first step in evaluating these models was to establish a basic set of unidirectional lamina properties for glass and carbon FRP (Table 30). The stiffness properties for the GFRP are rough averages of the values provided in Table 23. The stiffness properties for the CFRP were taken directly from

Burgueno [117] to validate the classical laminate theory calculator that was developed for the current study (Burgueno also provides equivalent stiffness properties for the laminate architecture used in the King's Stormwater Channel bridge). Strength properties for both the GFRP and CFRP are also rough averages of the values listed in Table 23.

Table 30. Unidirectional lamina properties for shear capacity evaluation

Properties	Glass FRP	Carbon FRP
E_1 (Msi)	5.5	17.5
E_2 (Msi)	1.5	1
G_{12} (Msi)	0.5	0.7
ν_{12}	.25	0.3
$S_1^{(+)}$ (ksi)	120	200
$S_1^{(-)}$ (ksi)	80	180
$S_2^{(+)}$ (ksi)	5	6
$S_2^{(-)}$ (ksi)	20	20
S_{12} (ksi)	10	11

Six different laminate architectures, shown in Table 31, were investigated. Laminate architecture 1 (LA-1) consisted of a unidirectional laminate with all fibers assumed to the be running on the longitudinal direction of the CFFT girder. LA-2 assumes that all fibers are running in the transverse or hoop direction. LA-3 is a 0/90° laminate while LA-4 contains plies oriented at ±45°. LA-5 is the laminate architecture used in the King's Stormwater Channel Bridge, and LA-6 is identical to the laminate architecture of Tube Type IV reported by Ahmad et al.[126]. LA-1 through LA-4 have 18 layers of uniform ply thickness equal to 0.02 in and an inner tube diameter of 13.5 in. The ply thicknesses and inner tube diameters for LA-5 and LA-6 were obtained from their respective sources.

Table 31. Laminate architectures and FRP tube properties for shear capacity evaluation

Lay-up ID	Stacking Sequence	Ply thickness (in)	Laminate thickness (in)	FRP tube D_i (in)
LA-1	$[0_{18}]$	0.02	0.36	13.5
LA-2	$[90_{18}]$	0.02	0.36	13.5
LA-3	$[(0/90)_9]$	0.02	0.36	13.5
LA-4	$[\pm 45_9]$	0.02	0.36	13.5
LA-5*	$[90_2/\pm 10_2/90_2/\pm 10_2/90_2/\pm 10/90_2/\pm 10/90_3]$	90° = 0.01 10° = 0.02	0.35	13.5
LA-6**	$[-88/3/-88_2/3_2/-88/3_2/-88/3_2/-88]$	-88° = 0.022 3° = 0.017	0.25	12.0

Note*: Laminate architecture used for King's Stormwater Channel Bridge
Note**: Laminate architecture for Tube S-9 in Ahmad et al.

After establishing the single lamina properties and laminate architectures, the equivalent laminate properties were determined for each laminate in the longitudinal and transverse (hoop) directions (Table 32). Each of the five FRP shear strength models rely on different lamina/laminate properties. The model used by Burgueno (M1) depends on the average of the tensile and compressive strength of each individual ply with respect to an assumed crack angle of 45 degrees. The model used by Ahmad (M2) relies only on the tensile strength of each individual ply (also measured with respect to a 45 degree

crack angle). The Chinese Technical Code (M3) depends only on the lamina modulus of elasticity in the primary fiber direction and the winding angle. All of these values can be obtained from Table 30 and Table 31. The values provided in Table 32 are needed for the AASHTO LRFD-FRP model (M4) and the proposed model (M5) based on laminate shear strength. The AASHTO LRFD model requires the modulus of elasticity of the laminate in the hoop direction while the proposed model requires the ultimate laminate shear strength, S_{LT}.

One important note about Table 32 relates to LA-4 (±45°). By orienting the fibers at ±45°, the shear strength of the laminate is expected to increase because the primary fiber directions are aligned with the principle stresses if the laminate is loaded in pure shear. For the GFRP version of LA-4, the corresponding increase in shear strength from the 0/90 degree fiber orientations is 39% (10 ksi to 13.9 ksi). For the CFRP version, the increase in shear strength is more dramatic (597%, or from 11 ksi to 76.7 ksi). This difference is caused by the relatively high ratio of E_1/E_2 for the CFRP (17.5 for CFRP vs. 3.67 for GFRP). As this ratio increases, a higher percentage of the total load is resisted by the fibers aligned with the principal stresses. First-ply failure occurs for both laminates when the transverse tensile strength, $S_2^{(+)}$, is exceeded for the -45° plies (assuming the shear stress is positive). The value of $S_2^{(+)}$ is only 5 ksi and 6 ksi for the GFRP and CFRP, respectively, but the higher stiffness ratio for the CFRP ensures that more of the principle stresses in tension are carried by the +45° plies.

Table 32. Equivalent laminate properties in longitudinal (L) and hoop (T) direction

Property	LA-1 (0°)	LA-2 (90°)	LA-3 (0/90)	LA-4 (±45°)	LA-5	LA-6
Glass FRP						
E_L (Msi)	5.5	1.5	3.52	1.6	4.07	3.38
E_T (Msi)	1.5	5.5	3.52	1.6	2.75	3.60
G_{LT} (Msi)	.5	.5	.5	1.6	.587	.503
$S_L^{(+)}$ (ksi)	120	5	62.5	20	82.5	59.67
$S_T^{(+)}$ (ksi)	5	120	62.5	20	9.5	65.56
S_{LT} (ksi)	10	10	10	13.9	11.75	10.03
Carbon FRP						
E_L (Msi)	17.5	1	9.3	2.44	11.7	8.61
E_T (Msi)	1	17.5	9.3	2.44	6.22	9.58
G_{LT} (Msi)	.7	.7	.7	4.5	1.0	.705
$S_L^{(+)}$ (ksi)	200	6	103	22	135.8	98.2
$S_T^{(+)}$ (ksi)	6	200	103	22	38.6	108.2
S_{LT} (ksi)	11	11	11	76.7	15.8	11.04

The final FRP shear strength contribution values are summarized in Table 33. The first point to make relates to the shear strength predicted for LA-1 through LA-3 for M1, M2, and M5 (all strength-based models). The values between the models differ (M1 = 107.9 kips, M2 = 71.9 kips, and M5 = 78.4 kips), but the values do not change as long as the fibers are oriented along the 0° or 90° direction. M3 and M4 (based on the modulus of elasticity at a specified strain of .004) produce very different results for LA-1 through LA-3. According to M3, fibers oriented in the 0° direction will offer no resistance to shear while a maximum value is obtained when all of the fibers are aligned in the hoop direction (LA-2). For LA-3, the shear resistance provided by the FRP is 50% of the value obtained for LA-2. A similar trend is

observed for the AASHTO LRFD-FRP model (M4) with a maximum shear resistance predicted for LA-2 (90°).

Model predictions for LA-4 (±45°) also require some discussion. For the GFRP, the two strength models that rely entirely on lamina tensile/compressive strength properties, M1 and M2, generate extremely high shear resistance values (M1 = 452.4 kips and M2 = 502.6 kips). The value for M5 is a more reasonable 108.9 kips. M1, M2, and M3 all predict very high values of shear resistance for the ±45° CFRP laminate. Models M3 and M4 both generate shear resistance values for the ±45° laminate that are less than the values predicted for the 90° laminate.

Key findings:

- Models M3 and M4 are somewhat erratic with regards to shear strength as a function of fiber orientation angle. Furthermore, it isn't clear if or how the environmental strength reduction factor, C_E, should be incorporated into this model.
- Models M1 and M2 generate extremely high values for GRFP laminates oriented at ±45°.
- Model M5, which is based on the ultimate shear strength of the FRP laminate, predicts reasonable shear resistance values for GFRP laminates across all of the fiber orientation angles investigated.

Table 33. Shear strength contribution of FRP Tube

Laminate Architecture	M1 Burgueno	M2 Ahmad	M3 Chinese Code	M4 LRFD-FRP	M5 Proposed
Glass FRP					
LA-1 (0°)	107.9	71.9	0	49.1	78.4
LA-2 (90°)	107.9	71.9	172.4	180.2	78.4
LA-3 (0/90°)	107.9	71.9	86.2	115.3	78.4
LA-4 (±45°)	452.4	502.6	86.2	52.4	108.9
LA-5	108.8	73.8	56.1	87.5	89.5
LA-6	66.0	43.8	56.6	72.3	48.4
Carbon FRP					
LA-1 (0°)	119.9	84.7	0	32.8	86.2
LA-2 (90°)	119.9	84.7	548.6	573.4	86.2
LA-3 (0/90°)	119.9	84.7	274.3	304.7	86.2
LA-4 (±45°)	816.2	828.2	274.3	79.9	601.1
LA-5	120.8	86.7	178.5	197.8	120.3
LA-6	73.3	51.6	180.2	192.4	53.3

The current recommendation is to rely on M5 to determine the shear strength contribution of GFRP laminates with any fiber orientation angle and CFRP laminates with fibers oriented in the 0/90 direction. Additional research is needed for ± 45° CFRP laminates to determine if the high shear resistance values predicted by this model can actually be realized.

In summary, the shear strength contribution provided by FRP for U-girders is given in Equation 8-14 and the shear strength provided by FRP for CFFTs is given in Equation 8-15. The ultimate shear strength

for the FRP material, τ_{ult}, can either be the shear strength of the FRP laminate as reported by the system manufacturer or the equivalent laminate shear strength, S_{LT}, as determined by classical laminate theory. Additional research may be necessary to investigate how different failure criteria might influence S_{LT}.

8.2 Loading

8.2.1 Dead Load (DL)

Material self-weight is summarized in Table 34. The unit weight for concrete was taken as 150 pcf (assuming a normal-weight, FDOT Class IV concrete for extremely aggressive environments with f'_c = 5.5 ksi). Unit weight for the GFRP was obtained from the Vectorply data sheets for the specified laminates.

Table 34. Self-weight for structural elements

Element	Material	Unit weight (pcf)	Weight/area (lbf/in^2)	Weight/length (lbf/ft)
Cast-in-place deck (8")	Concrete	150	100	n/a
36" single-slope barrier	Concrete	150	324 (16" strip)	432
Future wearing surface[1]	--	n/a	15	n/a
Girder (U-Shape/CFFT)	GFRP	118	n/a	varies
Pultruded DWB36	G/CFRP	105	n/a	70

Note 1: A 15 lbf/in^2 future wearing surface is provided in accordance with the FDOT Structural Design Guidelines (Section 2.2(A)).

8.2.2 HL-93 Live Load (LL)

Standard HL-93 live loading was used throughout the current study. General properties are summarized in Table 35. For the finite element modeling, the truck was positioned in the longitudinal direction based on the results from a shear and moment envelope study conducted for a simply-supported beam. Tire patch surface areas of 10 in x 20 in were assumed, and single factored wheel loads were applied to these areas as a uniform pressure. Lane loading was applied as a uniform pressure (unfactored magnitude = .064 ksf) over a 10-ft-wide strip acting in the center of each lane.

Initial evaluation efforts using refined analysis (FEA) and optimization methods did not consider the lateral positioning of vehicles and lane loads as a design variable. For the preliminary investigations, lane loads and vehicles were located on the bridge according to the layout provided in Figure 60. For limit states related to maximum shear, some effort was made to position the vehicles such that the shear force developed near the support by aligning a line of the wheel loads along the centerline of a girder. Subsequent analyses revealed that lateral positioning of vehicles and lane live loading does have a significant influence on the maximum live load effects. After the initial analysis results were used to identify the most efficient macro-level laminate architectures, additional design studies were completed to investigate the influence of lateral vehicle positioning. These results were also compared to AASHTO distribution factors.

Table 35. Summary of HL-93 live load

Load type	Axle 1 (kip)	Axle 2 (kip)	Axle 3 (kip)	Axle 1/2 spacing (ft)	Axle 2/3 spacing (ft)[1]	Lane load (kip/ft)
Truck	8	32	32	14	14	--
Tandem	25	25	--	4	--	--
Lane	--	--	--	--	--	0.64

Note 1: 14 ft rear axle spacing controls for all limit states except fatigue/creep rupture. AASHTO LRFD-FRP calls for 30-ft rear axle spacing when evaluating fatigue/creep rupture.

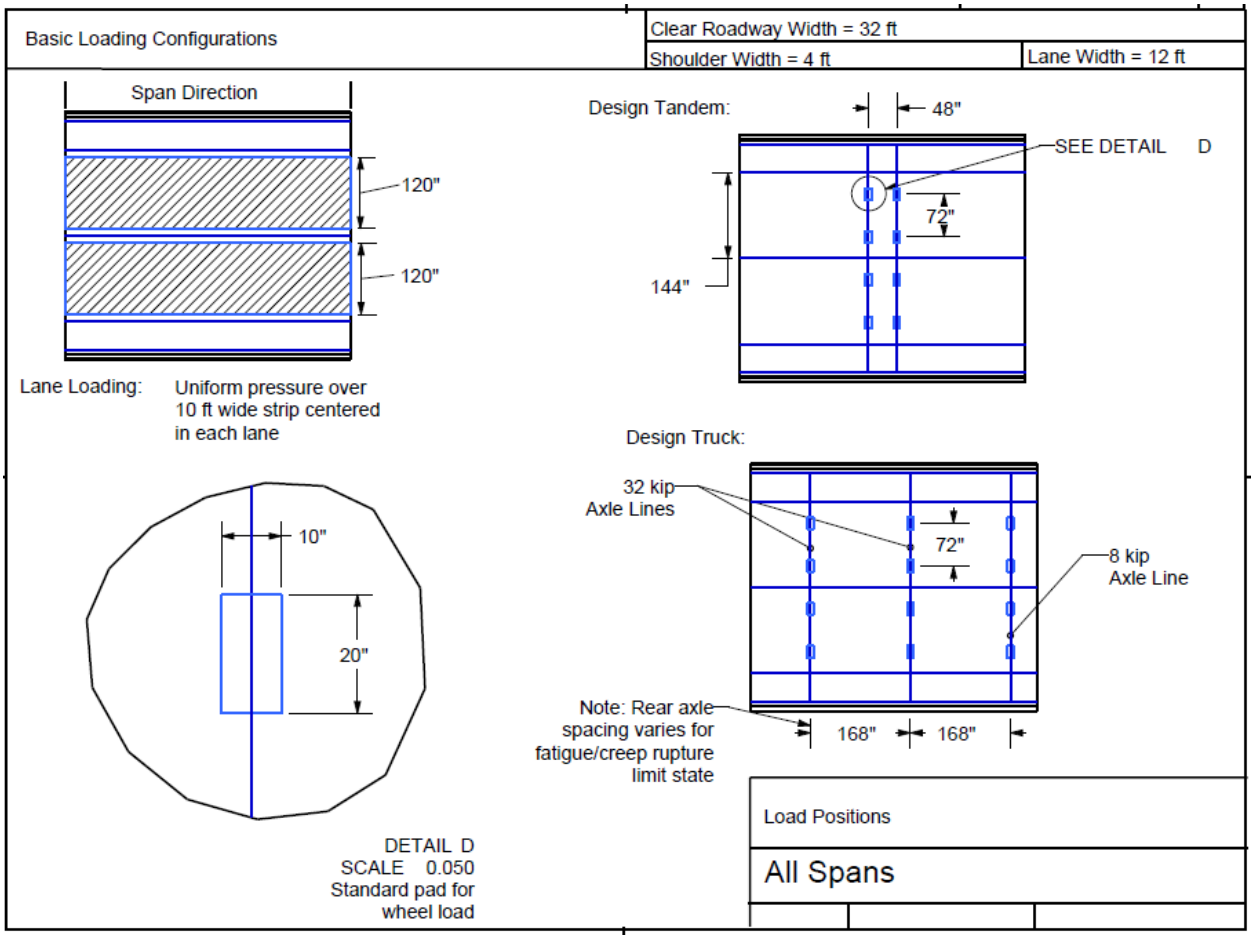

Figure 60. Basic geometry for transverse positioning of vehicle loads. Vehicle position in the longitudinal direction varies by span length and limit state.

8.3 Load Combinations

The load combinations and their respective load factors are summarized in Table 36. Limit States 1, 2, and 4 were derived from AASHTO LRFD-7 while Limit State 3 is based on a provision in AASHTO LRFD-FRP. An impact factor (IM) of 1.33 was applied to all vehicle live loads (impact was not applied to live lane loading).

Table 36. Load combination factors

Limit State	Impact	LL – Tr/Tan	LL – Lane	DL	DL-FWS
LS-1: Concrete comp. stress	1.33	1	1	1	1
LS-2: Displacements	1.33	1	0	0	0
LS-3: Fatigue and creep rupt.	1.33	.75	0	1	1
LS-4: Strength	1.33	1.75	1.75	1.25	1.5

9. U-Shaped FRP Girders

Two unique analysis and design approaches were investigated for the FRP U-girder alternative:

- Single girder design using the AASHTO distribution factor method
- Comprehensive structural optimization using FEA, quadratic programming and genetic algorithms

After completing an initial round of structural optimization using FEA, it was determined that lateral positioning of the design vehicles has a significant influence on the required girder geometry. Furthermore, there is little established history of using AASHTO distribution factors for designing FRP bridge girders. Distribution factors for the San Patricio FRP U-girder bridge were obtained using a spring model and compared to values obtained for timber beams supporting a reinforced concrete deck[122]. Research studies [128,129] for both of the pultruded FRP girder bridges built outside of Blacksburg, Virginia, included live load testing aimed at determining distribution factors, but neither effort treated span length as a variable. In the present study, AASHTO distribution factors that were obtained using cross-section "e" from LRFD-7 are compared with results from a finite element model for a 50-ft span length. These results are presented in Section 9.3.

9.1 AASHTO Distribution Factor Method

This section describes a methodology based on the AASHTO distribution factor method that will lead to acceptable FRP U-girder designs for the limit states discussed in Section 8.1. After describing the general analysis framework, structural analysis, and U-girder design/optimization process, this methodology is used to estimate the materials and manufacturing costs associated with short-span FRP U-girder bridges ranging from 30 ft to 75 ft.

9.1.1 General framework for analysis and design

The AASHTO distribution factor method is an approximate method for determining the demand experienced by an individual structural element due to live load. The critical values that are required for any girder design operation are the factored shear demand, V_u, and the factored moment demand, M_u. Once the structural demands are determined for each limit state, a proposed cross-section configuration can be evaluated to determine if the section's strength is sufficient. The design challenge presented by FRP U-girders is that the cross-section dimensions are initially unknown and the material strength properties can vary depending on the laminate architecture. A major goal of this design study is to establish basic size parameters for FRP U-girders as a function of span length and the number of girders present for a given bridge geometry.

The overall analysis and design framework is illustrated in Figure 61. To determine the FRP U-girder size requirements for a specific span length, the overall bridge geometry and loading parameters must be specified. A graphical user interface was developed in Matlab to facilitate data exchange with a larger piece of software that was developed to automate the analysis and design process. The required inputs for bridge geometry and loading parameters are presented in the GUI format in Figure 62. The exposure condition variable is used to determine the appropriate environmental knock-down factor, C_E, that is applied to the FRP material strength.

Required material properties and girder size parameters are highlighted in Figure 63. Girder height below the slab, h_{web}, and the thickness of the FRP U-girder, t_{flan}, were the two main cross-section design

variables investigated in the current study. The amount of concrete placed inside the U-girder, h_{con}, was also investigated to determine its influence on a girder's ability to meet the specified deflection criteria. The total flange width, b_{flan}, can be changed by adjusting the overall depth to width ratio. The web thickness can also be defined separately by specifying the desired flange to web thickness ratio. For the current study, the overall depth to width ratio was held constant at 1.5 and the flange to web thickness ratio was held constant at 1.0. The material properties shown in Figure 63 are based on the E-LT 4400 (0/90) non-crimp fabric from Vectorply described in Table 25. There is still some uncertainty regarding the ultimate shear strength of this specific resin-infused laminate, but the value of 10 ksi is conservative relative to the value provided by the manufacturer (13.1 ksi). These material properties were held constant in the current study. The FEA optimization method described in Section 9.2 does treat the FRP material properties, overall girder width to depth ratio and flange to web thickness ratio as design variables.

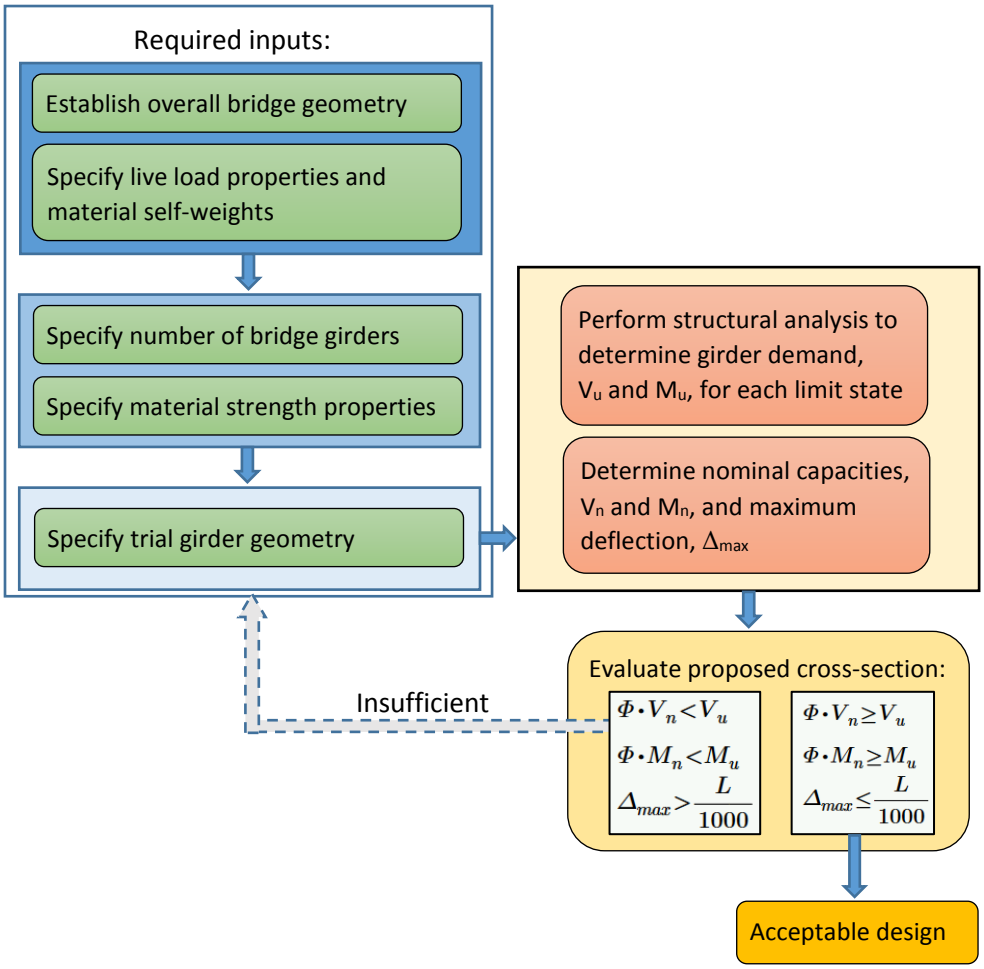

Figure 61. General analysis and design framework for the AASHTO distribution factor method

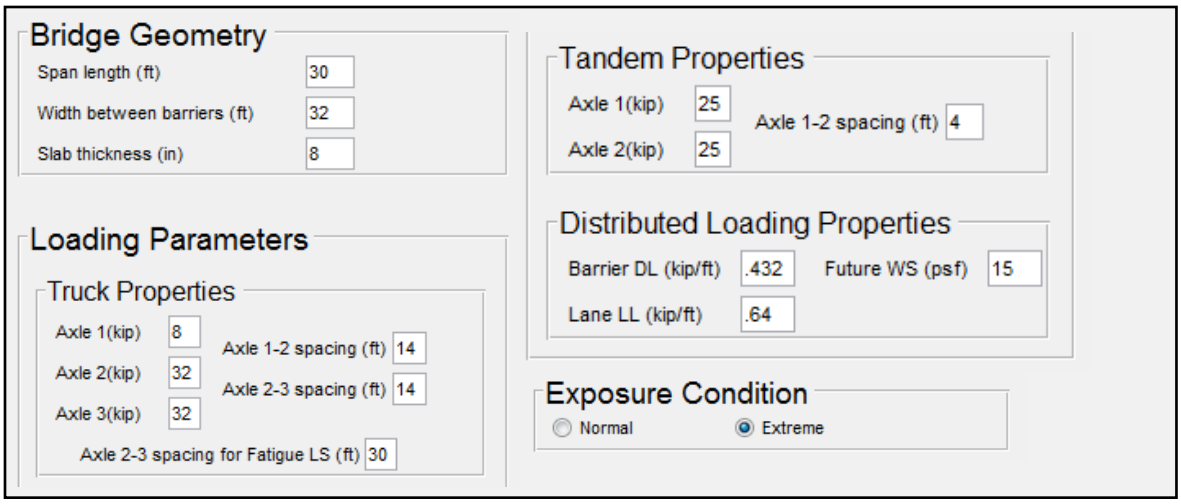

Figure 62. Required inputs for bridge geometry and loading parameters

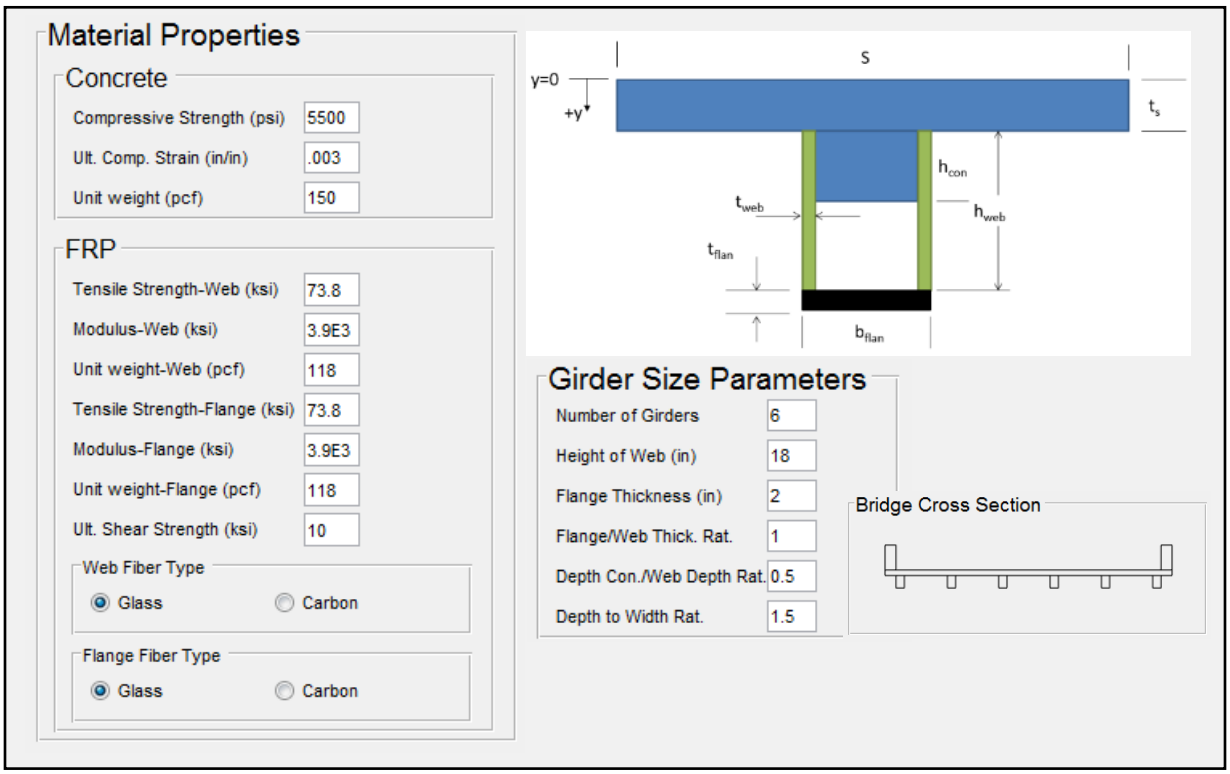

Figure 63. Required inputs for material properties and girder size parameters.

9.1.2 Structural analysis

The primary advantage of the AASHTO distribution factor method is that the structural analysis is simplified to a one-dimensional simply-supported beam model. Live load analysis was completed assuming one vehicle (truck or tandem) occupied a single lane and an unfactored uniform distributed lane loading (0.64 kip/ft) was applied along the entire length of a simply supported beam. The resulting shear and moment envelopes were then treated with the appropriate load factors for each limit state.

Next, an AASHTO distribution factor was applied to the shear and moment envelopes to determine the effect of the live load acting on a single girder.

Dead load analysis was completed on a per-girder basis with uniform distributed loads for the slab, traffic barriers, self-weight of the concrete below the slab (in the FRP girder), and self-weight of the FRP composite. The self-weight of the barriers was distributed uniformly amongst all of the girders present. The weight of the slab attributed to each girder was modified depending on the number of girders present and the width of the girder flange. The self-weight of the FRP and the self-weight of any concrete placed inside the U-girder was also variable depending on the cross-section under consideration.

The AASHTO distribution factor for moment was computed for a given bridge/girder geometry using Table 4.6.2.2.2.b-1 in LRFD-7. Assuming that each of the FRP U-girders is filled with concrete, the bridge cross-section geometry matches Section Type e in Table 4.6.2.2.2.1-1. The corresponding equation for computing the distribution factor for moment for an interior girder is:

$$DF_{2LL\_m} = 0.075 + \left(\frac{S}{9.5}\right)^{0.6} \cdot \left(\frac{S}{L}\right)^{0.2} \cdot \left(\frac{K_g}{12 \cdot L \cdot t_s^{\,3}}\right)^{.1} \quad \text{Eq. 9-1}$$

$$DF_{1LL\_m} = 0.06 + \left(\frac{S}{14}\right)^{0.4} \cdot \left(\frac{S}{L}\right)^{0.3} \cdot \left(\frac{K_g}{L \cdot t_s^{\,3}}\right)^{.1} \quad \text{Eq. 9-2}$$

where

DF_{2LL_m} = moment distribution factor for two lanes loaded
DF_{1LL_m} = moment distribution factor for one lane loaded
S = girder spacing (ft)
L = span length (ft)
t_s = slab thickness (in)

$$K_g = n \cdot \left(I_{girder} + A \cdot e_g^{\,2}\right)$$

$$n = \frac{E_{girder}}{E_{slab}}$$

I_{girder} = moment of inertia of girder beneath the slab (in^4)
A = area of girder below the slab (in^2)
e_g = distance from centroid of slab to centroid of girder (in)

This relationship is only applicable for K_g values ranging from 10,000 in^4 to 7,000,000 in^4. The value for K_g is highly dependent on the amount of concrete that is present in the FRP U-girder. For the girder section dimensions illustrated in Figure 12 (assuming only 50% of the web is filled with concrete and ignoring the contribution of the FRP) K_g was computed as 8,532 in^4. If the entire web is filled with concrete, K_g increases to 42,336 in^4. For the half-filled girder, if the effects of the FRP webs and flange were considered, the actual value should be somewhere in between. What is important to note, however, is that an increasing K_g value leads to a larger distribution factor (i.e., more conservative). To stay within the range of applicability for K_g and use a relatively conservative estimate at this point in the study, a decision was made to compute K_g for each cross-section assuming that the girder was completely filled with concrete. There are several unresolved issues related to computing deflections that may provide some clarification on which way to proceed, but, for the current study, the K_g values used to determine distribution factors for shear and moment are conservative.

The distribution factor for shear was computed in accordance with Table 4.6.2.2.3a-1:

$$DF_{2LL\_s} = 0.2 + \frac{S}{12} - \left(\frac{S}{30}\right)^2 \quad \text{Eq. 9-3}$$

$$DF_{1LL\_s} = 0.36 + \frac{S}{25} \quad \text{Eq. 9-4}$$

where

DF_{2LL_s} = shear distribution factor for two lanes loaded
DF_{1LL_s} = shear distribution factor for one lane loaded

Distribution factor and single-girder factored demand results for the bridge/girder geometry shown in Figure 62 and Figure 63 are provided in Figure 64. Only the factored moment values, M_u, are relevant for Limit States 1 through 3. For Limit State 4, the tandem loading controls for the flexural design (M_u = 7,753 kip-in) while the truck loading controls for the shear design (V_u = 109.3 kips). For the current study, the critical section for shear was taken to be the face of the support. This is a conservative assumption based on the remaining uncertainties surrounding the actual shear capacity of FRP U-girders. Additional discussion and validation of the live load distribution factors computed using Table 4.6.2.2.2.b-1 in LRFD-7 are provided in Section 9.3.

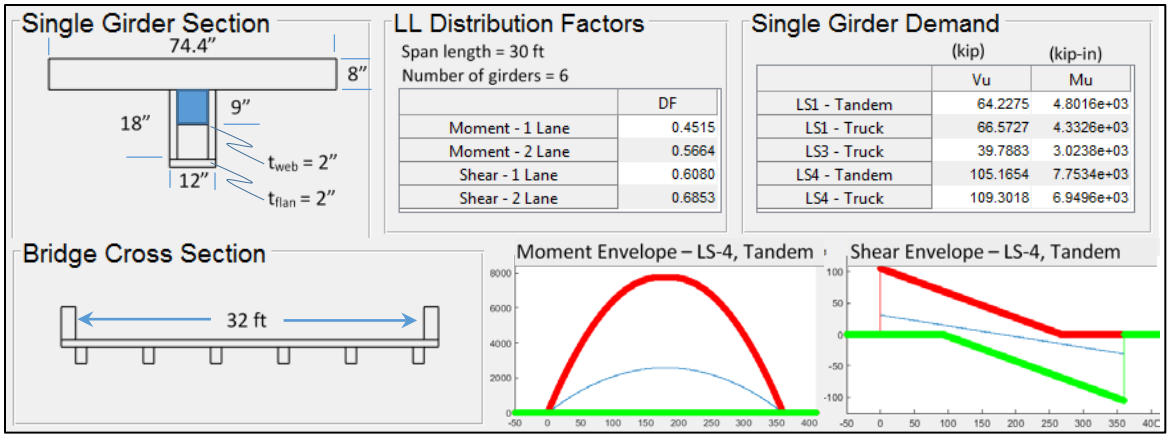

Figure 64. Factored demand results for single FRP U-girder based on AASHTO distribution factor method for live load.

9.1.3 Cross-section Capacity and Optimization

Once the structural demand for a single girder has been established using the AASHTO distribution factor method, the analysis can proceed to determining the capacity of the girder for each limit state based on the girder geometry and material properties. In this section, the general process for evaluating the capacity of a fully-specified girder will be illustrated using the parameters provided in Figure 62 and Figure 63 with one minor adjustment. For this example, the ratio of concrete depth to FRP web height in the FRP U-girder will be set to 1. The ratio of FRP flange to web thickness will also be set to 1.

First, the capacity will be evaluated for an FRP thickness value of 2 inches (assumed maximum value) followed by an analysis for an FRP thickness 0.25 inches (assumed minimum). The thickness value of 2 inches results in a cross-section that far exceeds the criteria established in limit states 1 through 4. The thickness value of 0.25 inches is insufficient to meet these criteria. Once that is established, the process for determining the minimum FRP thickness required to satisfy all five limit states for a given girder depth will be discussed. Finally, the method will be applied to a feasible range of girder depths (in this case 12 in to 36 in) and a framework for identifying the optimal girder depth and FRP thickness combination is presented. Hand calculations for a fully specified girder and bridge geometry for a 50-ft span length are provided in Appendix A.

9.1.3.1 *Capacity Analysis for Fully-Specified FRP U-Girder*

The cross-section profiles and the corresponding factored demands for the two example sections are highlighted in Figure 65. The depth of concrete below the slab is 18 in and the total girder width is 12 in for both girders. The total girder height varies based on the FRP flange thickness. The cross section for the 2-in thickness is 1.75 in deeper than the 0.25-in section, which results in a slightly larger dead load component. This is reflected in the minor increase in factored demand for each limit state for the 2-in girder. The factored demand values in Figure 65 also illustrates how increasing the depth of concrete from 50% (Figure 64) of the girder web height to 100% of the girder web height impacts the overall demand. The factored moment demand for the strength limit state (LS-4) increases by 1.6% if the girder is entirely filled. The factored shear demand at LS-4 increases by 1.3%.

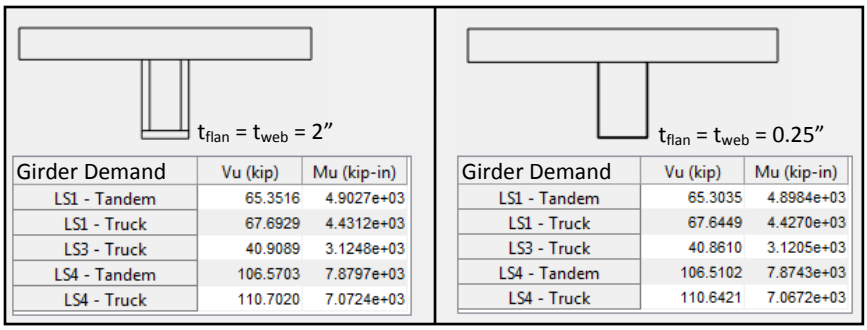

Girder Demand	Vu (kip)	Mu (kip-in)
LS1 - Tandem	65.3516	4.9027e+03
LS1 - Truck	67.6929	4.4312e+03
LS3 - Truck	40.9089	3.1248e+03
LS4 - Tandem	106.5703	7.8797e+03
LS4 - Truck	110.7020	7.0724e+03

Girder Demand	Vu (kip)	Mu (kip-in)
LS1 - Tandem	65.3035	4.8984e+03
LS1 - Truck	67.6449	4.4270e+03
LS3 - Truck	40.8610	3.1205e+03
LS4 - Tandem	106.5102	7.8743e+03
LS4 - Truck	110.6421	7.0672e+03

Figure 65. Girder profiles and factored demand used to illustrate single-girder capacity analysis.

Each limit state is controlled by specified stress criteria. For example, Limit State 1 is reached when the concrete compressive stress equals 0.45 x f'_c. Limit State 3 is reached when the maximum normal stress in the FRP equals 0.5 x 0.2 x f_{uf}. The 0.5 is the environmental reduction factor, C_E, for glass FRP in an extremely aggressive environment and the 0.2 is the creep and fatigue rupture for glass FRP specified in LRFD-FRP S2.7.2 and f_{uf} is the ultimate tensile strength reported by the manufacturer. Limit State 4 is reached when the maximum normal stress in the FRP achieves a value of C_E x f_{uf} or the ultimate compressive strain in the concrete (0.003) is reached. The corresponding internal bending moments resulting in these stress levels are then considered to be the nominal moment capacity, M_n, for that specific limit state. For Limit State 4 (ultimate strength) an additional Phi-factor of 0.55 is applied to the nominal moment capacity to obtain the factored resistance.

The nominal moment capacities for LS-1 and LS-3 can be obtained using a simple cracked/transformed section analysis. Details and discussion on this matter are provided in the hand-calculations located in the Appendix. Determining the moment capacity at the strength limit state, however, requires a more sophisticated approach because the strength limit state is defined by two different stress criteria (i.e., the maximum compressive stress in the concrete and the design tensile strength of the FRP). The controlling mechanism depends on the cross-section dimensions and the relative amount of FRP tension reinforcement provided. The so-called balanced reinforcement ratio, ρ_b, occurs when the concrete reaches its ultimate compressive strength simultaneously as the FRP reaches its design tensile strength. Section 7.2.1 in ACI 440.1 R-15 provides a detailed discussion on solution process required for the flexural capacity of a concrete section with FRP rebars. A closed-form solution is available for the case where the reinforcement ratio provided exceeds ρ_b. However, a direct application of this method to the current problem of FRP U-girders is complicated by the fact that the FRP webs contribute to the overall flexural capacity. For the FRP rebar case where the provided reinforcement ratio is less than ρ_b, there is no closed-form solution for the flexural strength of a cross-section and numerical methods (e.g. moment-curvature diagrams) must be used.

In the current study related to the AASHTO distribution factor method, moment-curvature relationships were used to determine the moment capacity of a specified cross-section for each limit state. A non-linear stress-strain relationship was used for concrete in compression until the ultimate compressive strain is achieved. A linear stress-strain relationship was used for concrete in tension up to the point where the ultimate tensile strain is exceeded. Finally, the FRP materials in the webs and flange were modeled using a linear stress vs. strain relationship. Complete details for the material stress vs. strain relationships are provided in the hand calculations located in the Appendix.

Moment-curvature (M-Φ) diagrams for the 2-in-thick and 0.25-in-thick cross-sections are provided in Figure 66. The corresponding results for section capacity are provided in Table 37. The unfactored moment capacity of the 2-in-thick cross-section is 40,953 kip-in. This value of moment results in concrete crushing. For the 0.25-in FRP thickness, the nominal capacity, M_n, is only 6,525 kip-in and occurs when the FRP in the flange reaches a maximum allowable stress of C_E x f_{uf} (36.9 ksi). After applying a strength reduction factor of 0.55 to the nominal moment capacities, factored resistances of 22,524 kip-in and 3,589 kip-in are obtained for the 2-in and 0.25-in FRP thicknesses, respectively. Comparing these resistance values to the factored demand of 7,880 kip-in indicates that the 2-in FRP thickness is overdesigned for flexure and the 0.25-in thickness is insufficient.

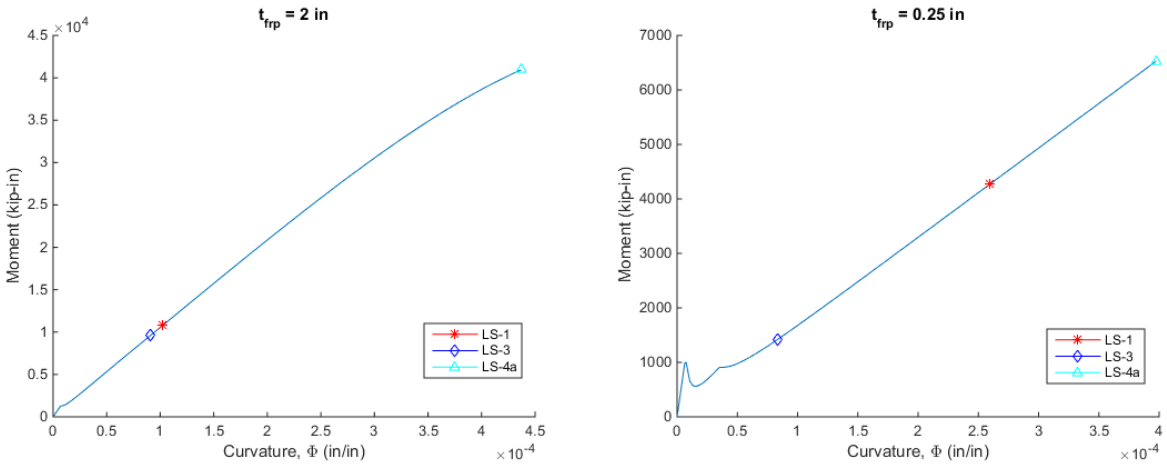

(A) (B)

Figure 66. Moment-curvature results for (A) 2-in-thick FRP cross-section and (B) 0.25-in-thick FRP cross-section.

Table 37. Capacity analysis results for 2-in and 0.25-in-thick FRP cross-sections.

	$t_{flan} = t_{web}$ = 2”	$t_{flan} = t_{web}$ = 0.25”	Factored Demand
M_n (kip-in)	40,953	6,525	--
M_n – LS-1 (kip-in)	10,796	4,273	4,902
M_n – LS-3 (kip-in)	9,578	1,428	3,125
ΦM_n – LS-4a (kip-in)	22,524	3,589	7,898
V_c (kip)	36.9	22.2	--
V_{frp} (kip)	240	30	--
ΦV_n – LS-4b (kip)	207.7	39.1	110.7
EI_{bridge} (kip-in^2)	1.078E9	0.91E9	--
Δ_{max} – LS-2 (in)	0.11	0.132	L/1000 = 0.36

A similar conclusion can be drawn for the strength limit state in shear (LS-4b). The factored shear resistances for the 2-in and 0.25-in thicknesses are 207.7 kip and 39.1 kip, respectively. The factored demand, V_u, for a single girder is 110.7 kip. One point of interest relates to the shear resistance

provided by concrete, V_c, for each section. The V_c for the 2-in thickness, 36.9 kip, is significantly larger than the V_c value obtained for the 0.25-in thickness (22.2 kip). This is somewhat counterintuitive because the total concrete area for the 0.25-in cross section (11.5 in x 26 in) is larger than the 2-in section (8 in x 26 in). The depth to the neutral axis for the 0.25-in-thick cracked section is 5.21 in while the depth to the neutral axis for the 2-in-thick FRP section is 12.47 in. This ultimately results in a larger concrete compression block for the cracked 2-in section that participates in shear resistance. Also note that the width of the concrete section used in the area calculation does not include the entire flange width of the concrete slab between girders. Only the width of the concrete in the FRP U-girder is assumed to provide any shear resistance.

For Limit State 2 (deflections), both cross-sections are able to meet the live load deflection criteria of L/1000 (0.36 in for a 30-ft span length). The total stiffness of the bridge cross-section was computed using the gross moment of inertia for the 18-in-deep FRP U-girders and the 8-in-thin concrete slab. Barriers were not included in the calculations for this section. If the U-girders are completely filled with concrete, the resulting flexural stiffness of the entire bridge (EI_{bridge}) is relatively high (1.078 x 10^9 kip-in^2 for the 2-in cross-section and 0.91E9 kip-in^2 for the 0.25-in section). The stiffness of the 2-in cross-section is slightly larger because the FRP flange extends further below the 18-in web height.

The displacement demand for a 30-ft span length was determined by developing the displacement envelope for the HL-93 truck load assuming that two lanes are loaded. The maximum deflection occurs when the two rear, 32-kip axles are centered around the bridge midspan. The truck positioning for LS-2 for the 30-ft span is provided in Figure 67. Lateral positioning of the two vehicles is irrelevant because all six girders are assumed to deflect uniformly. The live load impact factor of 1.33 was included in this analysis. The resulting displacement demand for the 30-ft span is 1.198E8 kip-in^3. The maximum deflection for the entire bridge, Δ_{max}, is then determined by dividing the displacement demand by the bridge stiffness, EI_{bridge}.

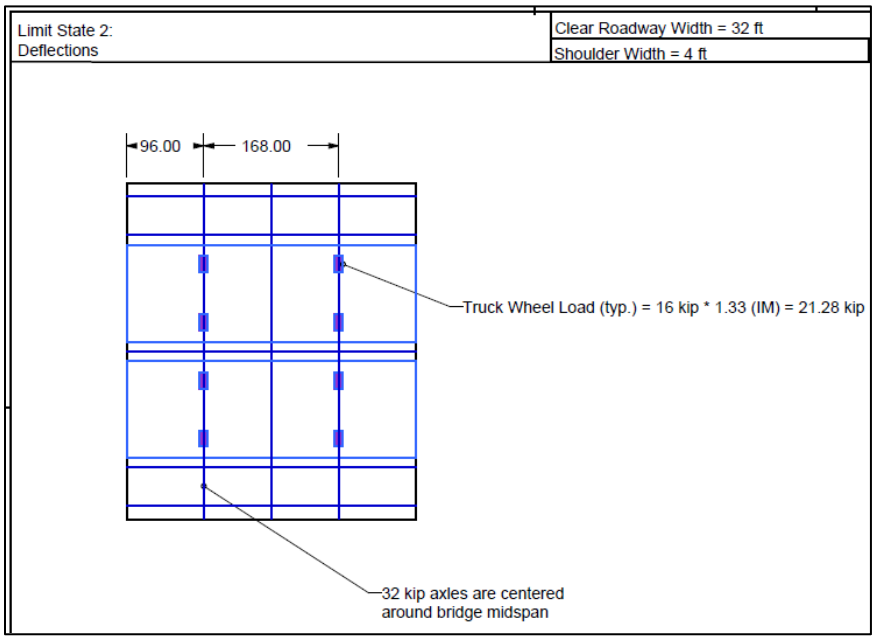

Figure 67. Vehicle positioning for LS-2 (deflections). Span length = 30 ft.

Displacement results are dramatically different if the concrete below the slab is not considered. The resulting flexural stiffness based on the gross moment of inertia for the 2-in FRP thickness is reduced to 6.275E8 kip-in^2 (a 41.8% reduction from the concrete filled section). The corresponding maximum deflection, 0.191 in, still meets the L/1000 deflection criteria. For the 0.25-in FRP thickness, the unfilled FRP U-girder bridge stiffness is reduced to 1.49E8 kip-in^2 (83.6% reduction) for a resulting deflection of 0.80 in. A complete summary of deflection calculations for LS-2 that considers all six barrier/concrete depth combinations described in Section 8.1.2 is provided in Table 38. For a 30-ft span length, the gross moment of inertia of the barriers alone is enough to satisfy the deflection criteria of L/1000. To remain consistent with the FDOT Structures Design Guidelines, cases where barriers are included in the gross moment of inertia calculations, LS-2(d,e,f), will not be addressed in the current study. If the FRP U-girders are entirely filled with concrete, LS-2a may be overly conservative. Even though the concrete is expected to crack inside the U-girder, it will still contribute to the overall stiffness of the bridge. Nonetheless, it is potentially helpful to know what the required FRP thickness would be for a completely unfilled U-girder and how other variables, such as number of girders and span length, affect this required thickness.

Table 38. Deflection calculations for LS-2 (deflections). Span length = 30 ft.

Design Scenarios for LS-2	Barriers	Concrete Depth in girder	Δ_{max} – LS-2 (in)	
			$t_{flan} = t_{web} = 2$”	$t_{flan} = t_{web} = 0.25$”
LS-2a	None	0%	0.191	0.804
LS-2b	None	50%	0.170	0.379
LS-2c	None	100%	0.111	0.132
LS-2d	Present	0%	0.049	0.071
LS-2e	Present	50%	0.046	0.058
LS-2f	Present	100%	0.037	0.040

At this point, the main conclusion that we can draw from the previous analysis of the 2-in-thick and 0.25-in-thick FRP cross-sections is that one is too heavy and the other is too light. The next section will describe the methodology used to optimize the cross section and determine the required FRP thickness needed to satisfy all of the limit states.

9.1.3.2 *Cross-section Optimization Using AASHTO Distribution Factors*

An iterative solution process based on the analysis procedure described in Section 9.1.3.1 was developed using Matlab to determine the minimum thickness of FRP required to satisfy each limit state. It was shown that for the 18-in girder depth, the required FRP thickness lies somewhere between 0.25 and 2.0 inches. Converged solution results for the 18-in girder depth example are provided in Figure 68. For this case (number of girders = 6, span length = 30 ft), the strength limit state for shear, LS-4b, would control the design with a required minimum FRP thickness of 0.946 in. If the required FRP thickness for ***any*** limit state exceeds 2 inches (the upper limit in the current study) the overall section depth must be rejected. If the required FRP thickness is less than 0.25 in (the minimum allowable value) for ***all*** of the limit states, the overall section depth would also be rejected in favor of a smaller depth with a thicker FRP flange and webs.

For the current study, the minimum FRP thickness required to satisfy all limit states will be assumed for the entire girder. Additional optimization may be possible by either tapering the FRP thickness along

the length of the girder because the section is technically over-designed for flexure at the midspan. It may also be possible to use a different laminate architecture with improved shear resistance in the high shear regions. This may be pursued in future work, but the current results are intended to provide conservative estimates of the amount of FRP required to achieve the established design criteria under the simplest possible design and manufacturing conditions.

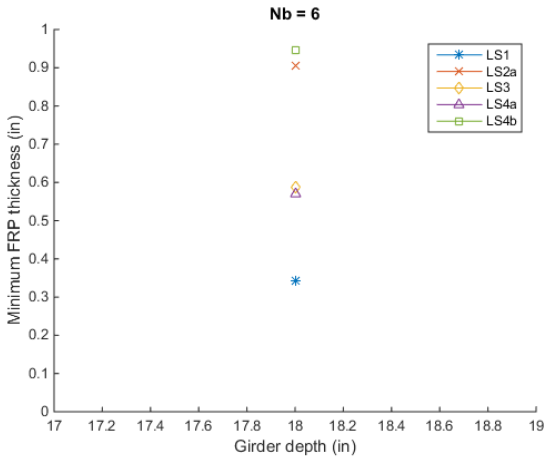

Limit state	Thickness (in)
LS-1 (concrete stress)	0.34
LS-2a (deflections)	0.91
LS-3 (fatigue/creep)	0.59
LS-4a (strength-flexure)	0.57
LS-4b (strength-shear)	0.95

Figure 68. Minimum FRP thickness for six-girder bridge (N_b = 6), girder depth = 18 in, span length = 30 ft.

After establishing the minimum FRP thickness for a specific girder depth, the process can be repeated over a range of girder depths and number of girder combinations. Results for the 30-ft span length are provided in Figure 69. The range of girders depths was established from 12 in to 36 in and results were obtained at 2-in intervals. The number of girders varied from 6 to 12 with a 2-girder interval. As the girder depth increases, the required FRP thickness decreases for all limit states. An important point to note is that as girder depth increases, the controlling limit state for FRP thickness also changes. For case of the six girder bridge (N_b=6), depths less than 16 inches would be controlled by the LS-2a limit state (deflections not accounting for concrete in the U-girder) whiles depths 18 inches or larger would be controlled by LS-4b (shear strength). Again, these calculations were completed assuming that the entire U-girder was filled with concrete. LS-2a does not account for any additional stiffness provided by the concrete beneath the slab. If the full stiffness contribution of this concrete was considered (LS-2c), the shear limit state would control for all girder depths.

Minimum FRP thickness results for all cases of LS-2 (deflections) are provided in Figure 70. Results are generated for LS-2a and LS-2b for all cases (N_b = 6, 8, 10, and 12). This indicates that when the FRP U-girder is completely empty or only half-filled with concrete, some FRP is required to meet the deflection criteria. If the entire girder is filled with concrete (LS-2c), only the six-girder bridge at a depth of 12 inches requires any FRP to meet the deflection criteria. Cases LS-2d,e,f, which all include barriers, do not appear because the stiffness of the slab, barriers, and any concrete beneath the slab provide sufficient flexural stiffness when the gross moment of inertia is considered. This will not be the case for longer span lengths.

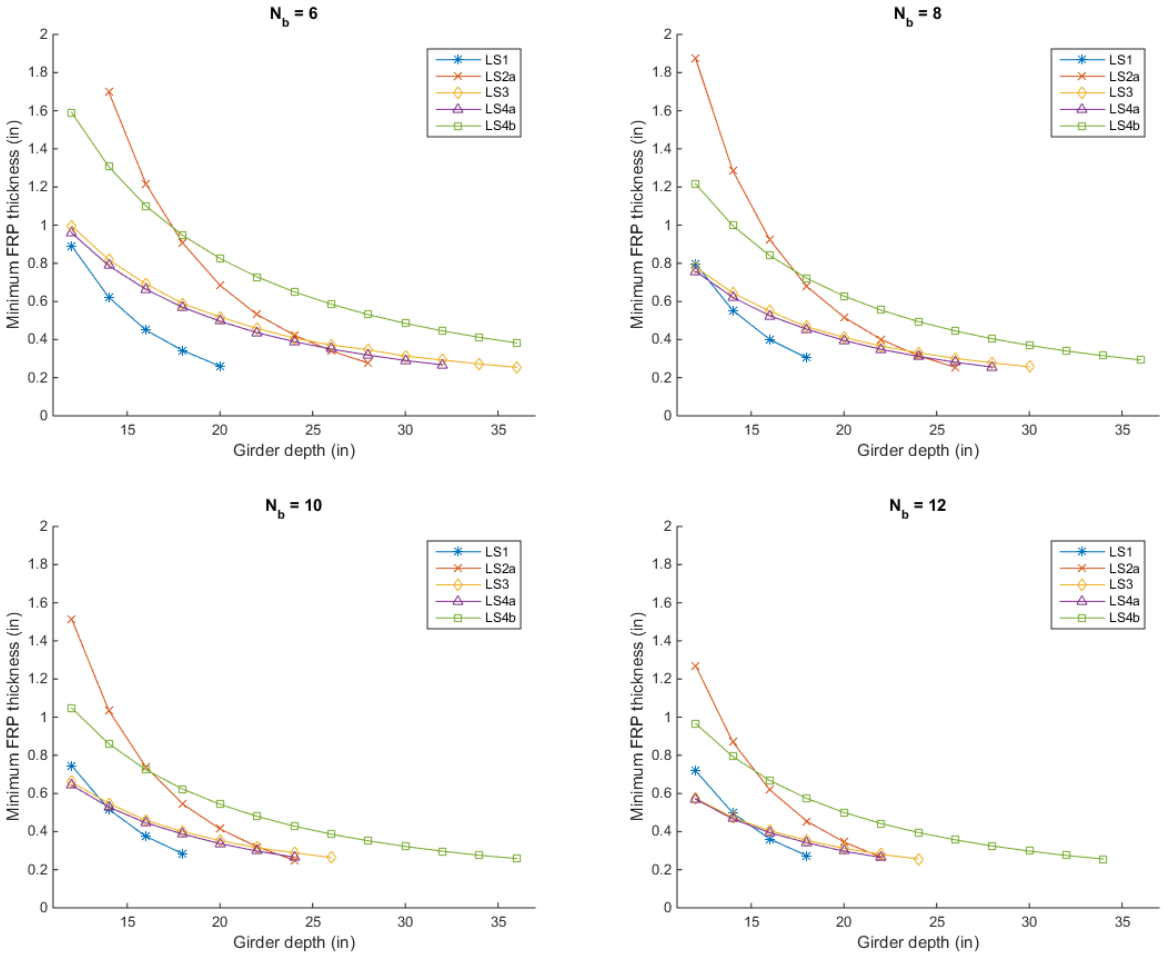

Figure 69. Minimum FRP thickness over a range of girder depths (12 in to 36 in) and number of girders (6 to 12). Span length = 30 ft.

The final step in the optimization process is to identify the girder depth/number of girders combination that results in the least cost. It is not possible to make this assessment on the weight of FRP alone. For all combinations of number of bridge girders (N_b = 6, 8, 10, and 12), the total weight of FRP simply decreases as the section depth increases (Figure 71). It is also observed that as the number of bridge girders increases, the total weight of FRP required also increases. These results were initially troubling as the change in total FRP weight for the N_b = 6 and N_b = 8 case is much smaller than the corresponding changes for the N_b = 10 and N_b = 12. For a specific girder depth, the self-weight portion of the girder is relatively constant. The only variable that changes is the tributary area for the slab. In order for an increase in the number of girders to provide any weight savings in FRP material, the corresponding distribution factor would need to decrease at a higher rate. As noted in Figure 72, the distribution factor for shear transitions from 2 lanes loaded to 1 lane loaded as the number of girders increase from 8 to 10. The corresponding drop in distribution factor is much lower between 8 and 10 than it is between 6 and 8. Therefore, even though the required FRP thickness is reduced as the number of girders increases, the fact that two more girders are required in the bridge eliminates any net advantage from the reduced shear demand.

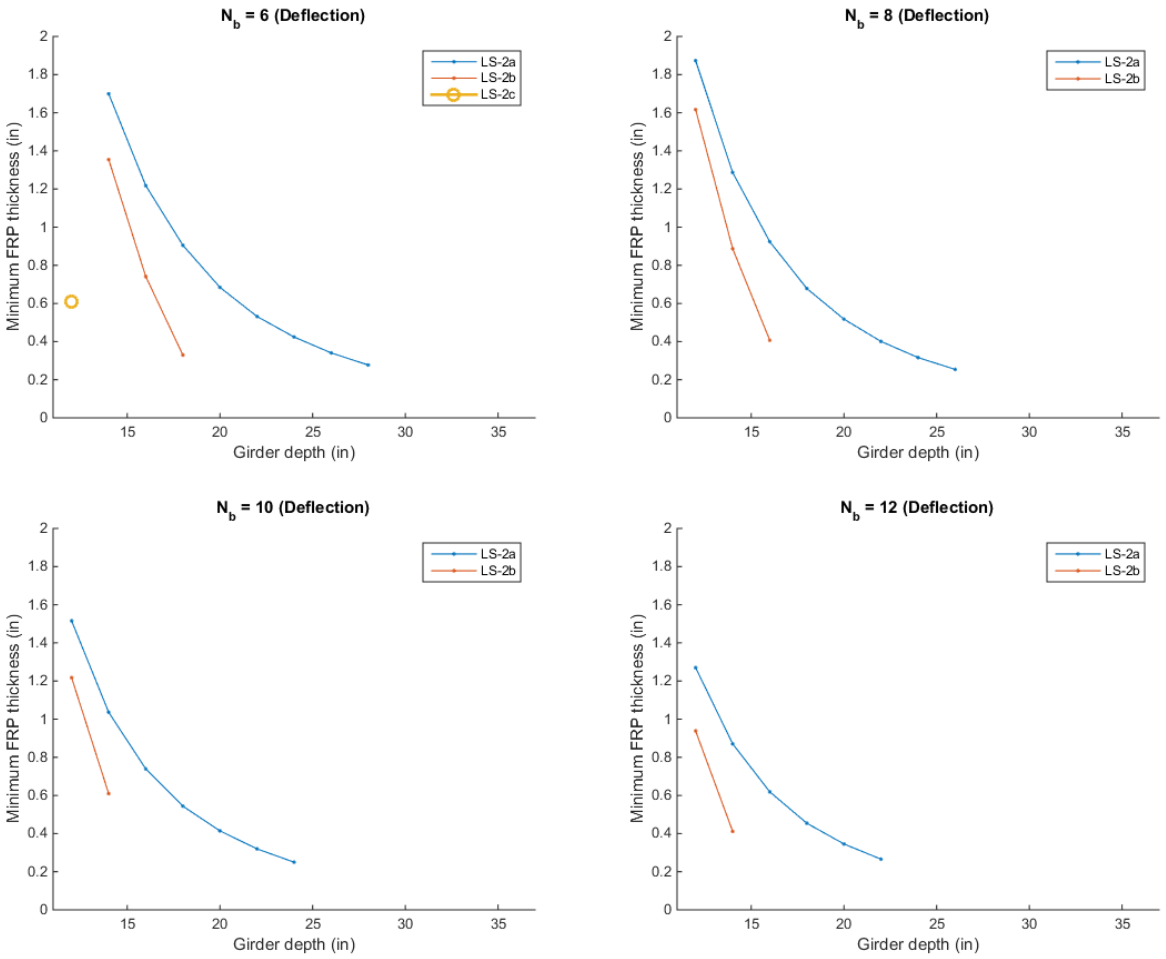

Figure 70. Minimum FRP thickness for different concrete fill depths and presence/absence of barriers (Span length = 30 ft.)

To determine the girder depth that results in the least cost, the cost of the concrete that is used to fill the FRP U-girder must also be considered. In the current study, an FRP cost of $5.25 per pound and a cast-in-place concrete cost of $0.21 per pound is assumed. After the total concrete and FRP costs are considered for all of the girders in a specific configuration (not including the concrete in the slab), a more traditional series of optimization curves is obtained (Figure 73). Unlike the curves representing total FRP weight, the total cost curves now increase as the girder depth becomes large due to the additional cost of the concrete required to fill the girders.

If the stiffness contribution of the concrete beneath the slab is included (LS-2c), the six-girder configuration with a girder depth of 14 inches results in the lowest total girder cost (Figure 73A). For LS-2a (Figure 73B), the six-girder combination with a girder depth of 18 inches results in the lowest total girder cost. The optimal depth for the 8, 10, and 12 girder combinations would be less than 12 inches, but at that point the deflection criteria for LS-2c would begin to control.

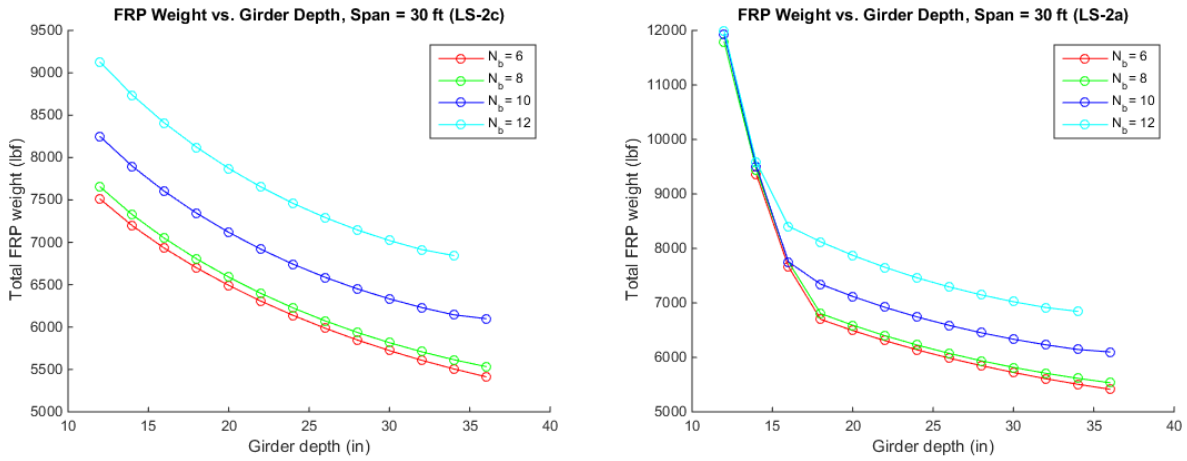

(A) (B)

Figure 71. Total FRP weight vs. girder depth for span length = 30 ft. (A) Including stiffness contribution of concrete under slab (LS-2c) and (B) excluding stiffness contribution of concrete under slab (LS-2a).

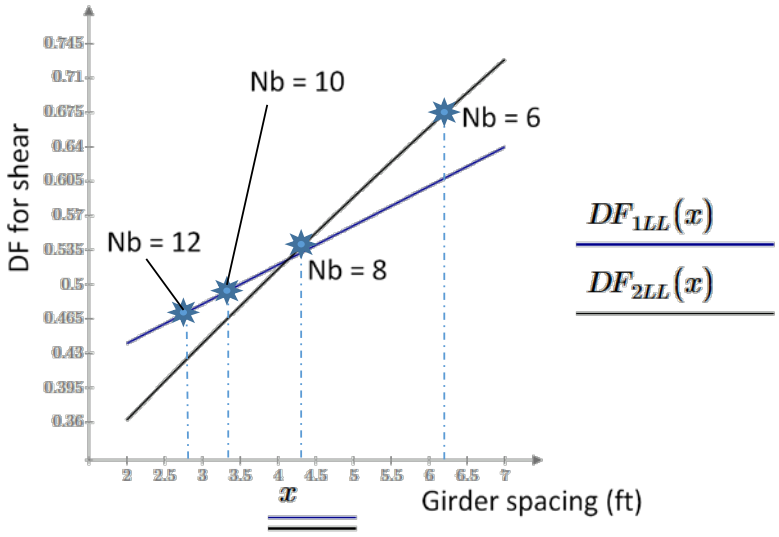

Figure 72. Distribution factor for shear as a function of girder spacing (1 and 2 lanes loaded).

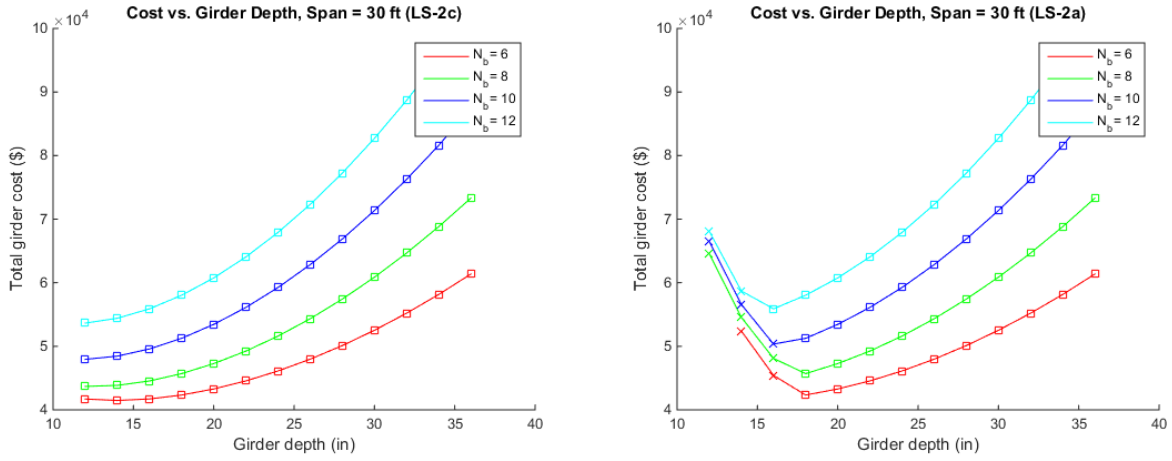

(A) (B)

Figure 73. Total girder cost vs. girder depth for span length = 30 ft. (A) Including stiffness contribution of concrete under slab (LS-2c) and (B) excluding stiffness contribution of concrete under slab (LS-2a).

9.1.3.3 *Results Summary for All Span Lengths*

The procedure described in Section 9.1.3.2 was applied to 30-ft, 40-ft, 50-ft, 60-ft, and 75-ft span lengths. The number of beams in the bridge was chosen as $N_b = 6$ and $N_b = 8$. Results are summarized in Table 39 and Table 40. The lowest total girder cost for each span length was always obtained for the six-girder bridge, but the cost per foot for each girder was lower for the eight-girder bridge. An even lower total girder cost would be obtained for a five-girder bridge configuration, but the six-girder option was considered to be more conservative as a starting point for making these initial cost estimates.

The limit state for deflections (LS-2) was evaluated using two different assumptions:

- LS-2a – 0% stiffness contribution for concrete in U-girder below slab (Table 39)
- LS-2c – 100% stiffness contribution for concrete in U-girder below slab (Table 40)

The additional stiffness resulting from the cast-in-place concrete barriers was not considered. The cost optimization curves and minimum FRP thicknesses required to meet the criteria of each limit state are provided in Appendix A. The controlling limit state varies as a function of span length and whether or not the stiffness contribution of the concrete below the slab was considered. For the 30-ft and 40-ft span lengths in the 2-a case, the interaction between LS-2a (displacements) and LS-4b (shear strength) control the optimized cross-section dimensions. For the 50-ft and 60-ft span lengths, the interaction between LS-2a and LS-3 (fatigue and creep rupture) governs. For the 75-ft span length, the limit on concrete compressive stresses (LS-1) controls the required section depth and FRP thickness.

Including the depth of concrete below the slab in the bridge stiffness calculations (LS-2c) effectively removes LS-2 from consideration. Overall, the girder depths obtained using the LS-2c assumption are less than those obtained using LS-2a. For the 30-ft and 40-ft span lengths, LS-4b (shear strength) is the controlling limit state. For the 50-ft, 60-ft, and 75-ft span lengths, the interaction between LS-1 and LS-3 determines the required girder depth and FRP thickness.

The controlling limit state results summarized in Table 39 and Table 40 provide useful guidance for future optimization studies. For example, increasing the shear strength of the FRP laminate should help to lower the cost for the 30-ft and 40-ft girders. Recall that the ultimate shear strength assumed for these results is a conservative value of 10 ksi. Increasing the shear strength to 13.1 ksi (the value provided in the manufacturer's data sheet for EL-LT 4400) results in significant cost savings for the 30-ft and 40-ft span lengths. Under the LS-2a criteria for deflections, the girder cost per foot decreases from \$235 to \$209 (12.4% decrease) if the ultimate shear strength increases from 10 ksi to 13.1ksi (31% increase). Under the LS-2c criteria for deflections, the girder cost per foot decreases from \$230 to \$181 (21% decrease). A summary of the data for 30-ft and 40-ft span lengths is provided in Table 41.

Table 39. Optimization results summary for all span lengths: LS-2a (0% concrete stiffness below slab)

Span length	Controlling limit state	h_{web} (in)	t_{frp} (in)	FRP weight (lbf)	Total girder cost (\$)	Girder cost per foot (\$)	Girder cost per SF of bridge deck (\$)
				N_b = 5			
30 ft (LS-2a)	LS-2a/4b	18	1.11	6,591	40,370	269	42
40 ft (LS-2a)	LS-2a/4b	28	0.81	9,962	73,174	365	57
				N_b = 6			
30 ft (LS-2a)	LS-2a/4b	18	0.95	6,698	42,330	235	44
40 ft (LS-2a)	LS-2a/4b	28	0.68	10,021	78,050	325	61
50 ft (LS-2a)	LS-2a/3	36	0.64	15,008	132,490	442	83
60 ft (LS-2a)	LS-2a/3	40	0.76	24,009	205,240	570	107
75 ft (LS-2a)	LS-1	42	1.16	48,066	358,490	797	150
				N_b = 8			
30 ft (LS-2a)	LS-2a/4b	18	0.72	6,804	45,700	190	48
40 ft (LS-2a)	LS-2a/4b	28	0.51	10,050	87,350	273	68
50 ft (LS-2a)	LS-2a/3	34	0.56	16,729	151,910	380	95
60 ft (LS-2a)	LS-2a/3	36	0.78	29,396	239,160	498	125
75 ft (LS-2a)	LS-1	40	1.25	65,678	471,660	786	197

Table 40. Optimization results summary for all span lengths: LS-2c (100% concrete stiffness below slab)

Span Length	Controlling limit State	h_{web} (in)	t_{frp} (in)	FRP weight (lbf)	Total girder Cost ($)	Girder cost per foot ($)	Girder cost per SF of bridge deck ($)
N_b = 5							
30 ft (LS-2c)	LS-4b	14	1.54	7,069	39,984	266	42
40 ft (LS-2c)	LS-4b	18	1.36	10,715	63,560	318	50
N_b = 6							
30 ft (LS-2c)	LS-4b	14	1.31	7,195	41,480	230	43
40 ft (LS-2c)	LS-4b	16	1.34	11,234	65,688	274	51
50 ft (LS-2c)	LS-1/3	22	1.08	15,507	99,481	332	62
60 ft (LS-2c)	LS-1/3	28	1.13	24,832	166,560	463	87
75 ft (LS-2c)	LS-1/3	38	1.28	47,923	336,760	748	140
N_b = 8							
30 ft (LS-2c)	LS-4b	12	1.22	7,325	43,690	182	46
40 ft (LS-2c)	LS-4b	16	1.02	11,447	69,751	218	54
50 ft (LS-2c)	LS-1/3	24	0.81	17,033	119,610	299	75
60 ft (LS-2c)	LS-1/3	32	0.81	27,152	208,790	435	109
75 ft (LS-2c)	LS-1/3	40	1.25	65,678	471,660	786	197

Table 41. Comparison of τ_{ult} = 10 ksi and τ_{ult} = 13.1 ksi for 30-ft and 40-ft span lengths

Span Length	Controlling limit State	h_{web} (in)	t_{frp} (in)	FRP weight (lbf)	Total girder Cost ($)	Girder cost per foot ($)	Girder cost per SF of bridge deck ($)
LS-2a (0% concrete stiffness below slab)							
30 ft (τ_{ult} = 10 ksi)	LS-2a/4b	18	0.95	6,698	42,330	235	44
30 ft (τ_{ult} = 13.1 ksi)	LS-2a/4b	20	0.68	5,383	37,,686	209	39
40 ft (τ_{ult} = 10 ksi)	LS-2a/4b	28	0.68	10,021	78,050	325	61
40 ft (τ_{ult} = 13.1 ksi)	LS-2a/3	32	0.46	7,865	75,557	314	59
LS-2c (100% concrete stiffness below slab)							
30 ft (τ_{ult} = 10 ksi)	LS-4b	14	1.31	7,195	41,480	230	43
30 ft (τ_{ult} = 13.1 ksi)	LS-4b	12	1.21	5,710	32,617	181	34
40 ft (τ_{ult} = 10 ksi)	LS-4b	16	1.34	11,234	65,688	274	51
40 ft (τ_{ult} = 13.1 ksi)	LS-1/3	16	1.10	9,218	55,506	231	43

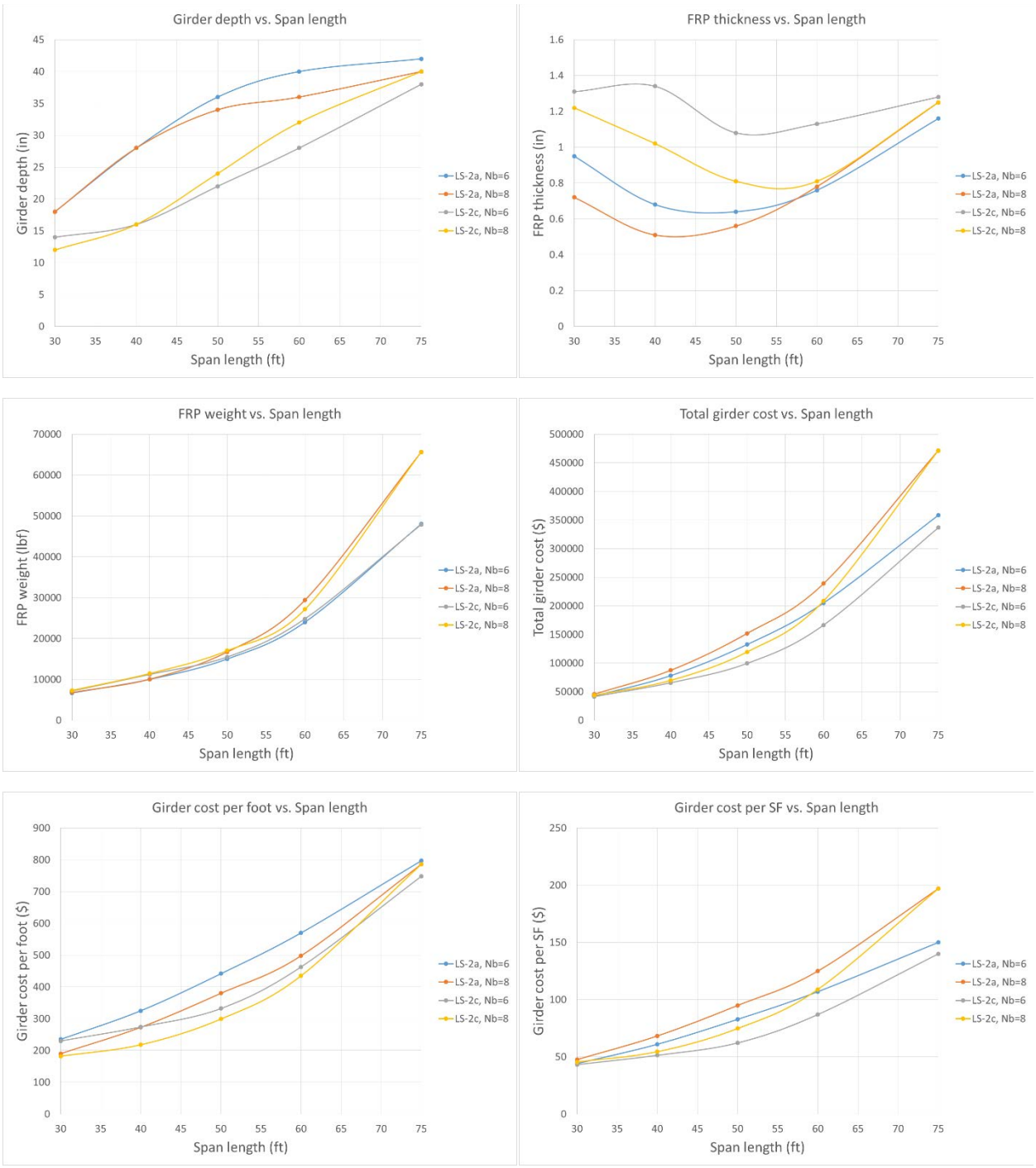

Figure 74. Results summary for all span lengths: AASHTO Distribution Factor Method

9.2 Optimization Using FEA, Quadratic Programming and Genetic Algorithms

The optimization work completed using the AASHTO distribution factor method (described in Section 9.1) involves what might be considered a "brute-force" approach. The required FRP thickness is determined for a range of span lengths, number of girders present in the bridge, and girder depths at each limit state. The results summarized in Table 39 and Table 40 required the analysis of 2970 unique bridge configuration and limit-state combinations (Span length = 30, 40, 50, 60, 75; N_b = 5, 6; h_{web} = 8, 10, 12 …72; and 9 different limit states). Not all of these combinations resulted in a viable bridge girder configuration. For example, the girder depth of 8 in has no chance of satisfying any of the limit states for a span length of 75 ft. Fortunately, the required structural analysis for each proposed configuration is relatively simple using the AASHTO distribution factor method (DFM). One area where the AASHTO DFM does become computationally intensive, however, relates to modelling the flexural behavior of each cross-section that incorporates a non-linear stress-vs. strain relationship for concrete that includes concrete cracking and the potential for different materials (FRP or concrete) to fail first depending on the cross-section geometry and material properties. Another potential downside to the AASHTO DFM is that the distribution factors themselves are generally considered to be conservative. Conservative distribution factors will translate directly into additional material costs, which might determine whether or not FRP bridge girders are a viable alternative in the first place.

An alternative analysis procedure that relies on finite element modeling of the bridge and advanced optimization techniques was also investigated in the current study. The overall analysis framework is provided in Figure 75. First, the longitudinal vehicle positioning is determined for each limit state using shear and moment envelopes for a simply supported beam. The transverse positioning was investigated using three different scenarios (described in Sections 9.2.2, 9.2.3, and 9.2.4). Once the loading conditions are established a finite element model of the bridge is developed with assumed FRP U-girder dimensions. The resulting stresses are evaluated and compared to the allowable values for each limit state. HEEDS optimization software was used to obtain the optimal shape and size of the girders. Genetic Algorithms (GA) were utilized in the first stage, and the results were refined by applying a Quadratic Programming (QP) method. The total number of iterations was approximately 300 for the first step of the optimization and approximately 100 steps were required for the final converged solution. The variables considered in the optimization process are illustrated in Figure 76.

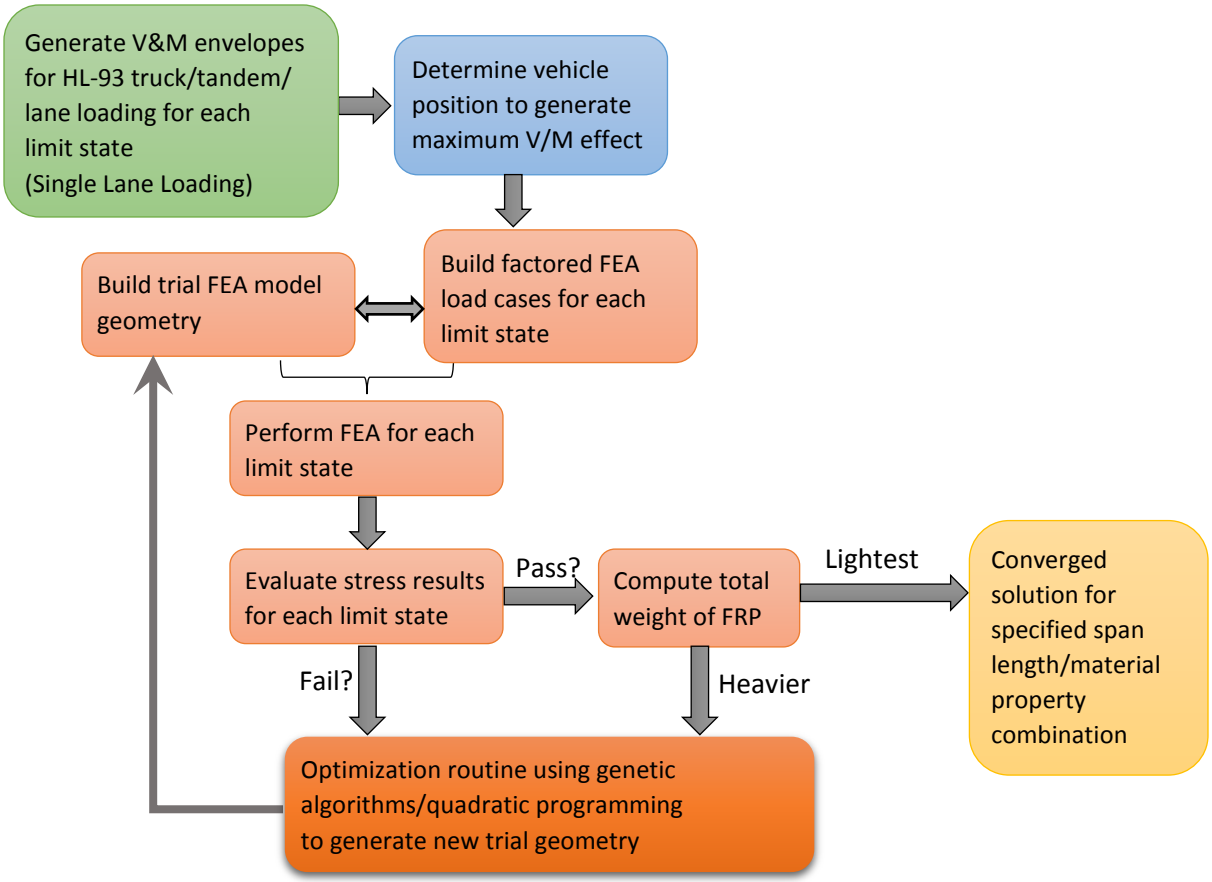

Figure 75. General framework for FEA and optimization using genetic algorithms/quadratic programming

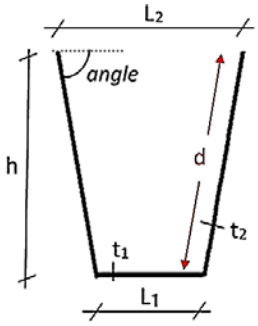

Variables	Range
# girders	4 -12
Height, *h*	(0.04 – 0.07) x Span length
L_2, in.	≥ 10
t_1 (base thick.), in.	0.50 – 2.00
t_2 (sides thick.), in.	0.50 – 2.00

Figure 76. FRP U-girder cross-section geometry variables for FEA optimization (slab not shown).

Three separate sub-studies were conducted to investigate the following general parameters:

- Laminate architecture
- Influence of cast-in-place RC barriers
- Transverse vehicle position

The following sections describe the details of each sub-study and the finite element model validation.

9.2.1 Model Validation Study

The finite element modeling procedure was verified using full-scale experimental data from the Texas U-girder study by Chen et al. [54] and full-scale experimental data from the Polish FRP bridge study by Siwowski et al.[130]

9.2.1.1 *Polish FRP Road Bridge*

A hybrid FRP/RC beam was designed, constructed and tested in Poland by the Rzeszow University of Technology [130]. The deck consists of a RC slab attached to a U-shaped composite beam. The girder was experimentally tested under static loads to evaluate its carrying capacity, and local failure was reported. Computational analysis was also performed and the results are validated by the experimental outcomes. In the current study, a FEA of the hybrid beam under static loads was carried out to validate the simulation procedure. The results are in agreement with the conclusions reported in Siwowski et al.

The girder was loaded in 4-point bending with the load case depicted in Figure 77. Concrete was placed throughout the depth of the girder at the support zone at a length equal to 1.64 ft. The girder was loaded in five stages based on the standard service load according to the Polish code for road bridges until the applied load reached the maximum capacity of the hydraulic actuators (283.26 kips). Displacement transducers and strain gauges were applied on several points of the beam specimen to measure strains and determine possible failure locations.

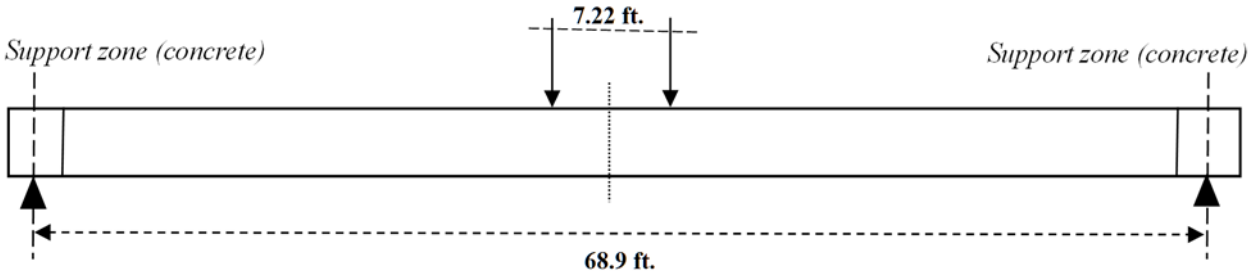

Figure 77. Load test setup for Polish FRP bridge girder [130]

The total girder length was equal to 72.18 ft. Figure 78 illustrates the cross-section of the full bridge with 4 girders and total width of 34.25 ft. Dimensions of the FRP for a single U-girder are provided in Figure 79. Glass fiber laminate is used for the top flange and a combination of glass and carbon fiber composites is applied on the base. The girder's side wall consists of a sandwich panel with a foam layer 0.59 in thick between two glass fabric laminates. Six internal diaphragms are placed along the length of the girder to increase the torsional stiffness of the structure. The concrete slab is connected to the FRP girder through galvanized steel shear connectors. A more detailed description of the girder's geometry as well as the manufacturing process can be found in Siwowski et al. (2015).

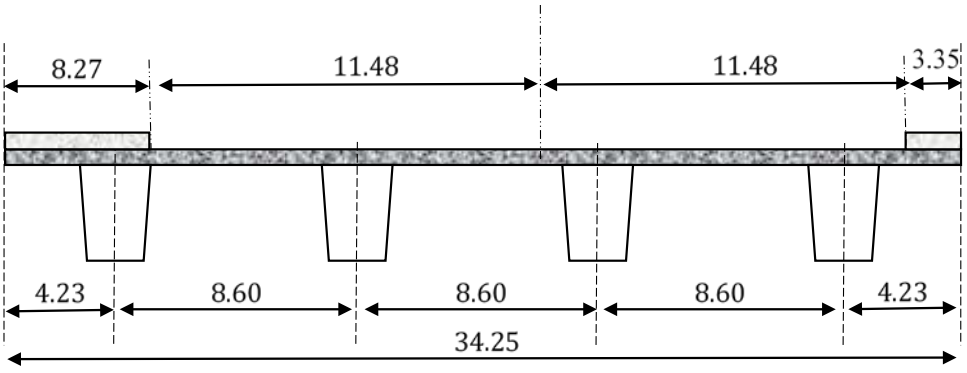

Figure 78. Cross-section of FRP U-girder bridge in Poland, dimensions in feet.

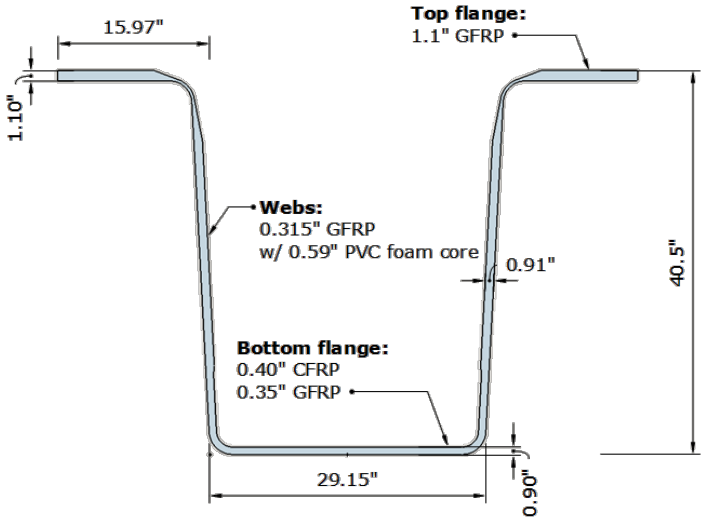

Figure 79. Single U-girder dimension for FRP girder bridge in Poland. [130]

E-glass and carbon woven fabrics were utilized during the fabrication process of the hybrid beams and vinyl ester was the matrix material. The fiber direction was different for every laminate; ±45° was utilized for the sides and a combination of 0° and ±45° was selected for the base and top flanges. Table 42 provides the material properties of the laminates that were determined through tensile testing.

Table 42. Lamina properties for Polish FRP bridge

	Fiber angle	Thickness (in)	E_x (Msi)	E_y (Msi)	v_{xy}	v_{yx}	G_{xy} (Msi)
E-Glass	± 45°	0.031	1.75	1.75	0.49	0.49	0.44
E-Glass	0°	0.031	6.11	1.58	0.29	0.075	0.39
Carbon	0°	0.024	16.8	0.83	0.41	0.021	0.48

In the current study, a FEA model was developed using the material properties and girder geometry described for the load test. A total of 11,000 4-node shell elements were implemented. The

deformation pattern of the girder at the maximum load is illustrated in Figure 80. The FEA results showed that the deflection at the top concrete surface, 40.94 in away from the centerline, was 7.72 in. This numerical result is only 4.3% higher than the experimental result (~7.32 in) (Figure 81).

The experimental testing revealed that the girder remained in the linear elastic region even after the maximum load of 283.26 kip was applied. The load vs. displacement diagram from the experiments confirms that no residual deformation was observed after the unloading of the girder. Strains were also measured at several points of the FRP/RC beam. Strain reported at 11.81 in away from the girder center on the bottom flange was 0.521% (Fig. 8). The strain calculated by the FEA of the current study is only 3.1% higher (0.531%) (Figure 82).

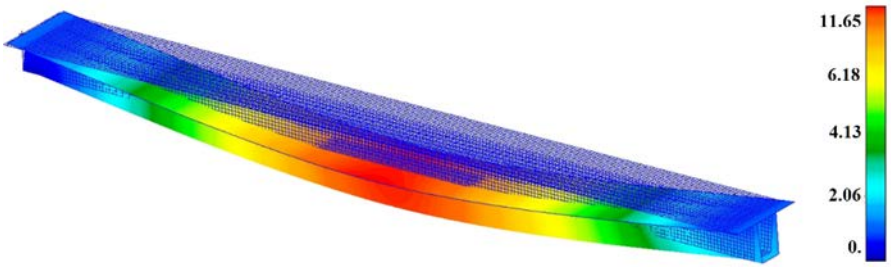

Figure 80. Displacement results for FEA of Polish FRP bridge, dimensions in inches.

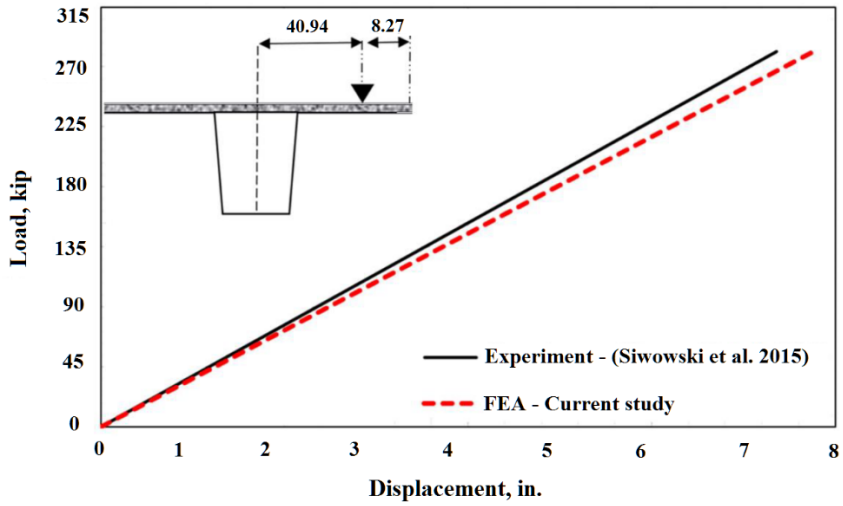

Figure 81 Comparison of experimental and FEA results (displacements) for Polish FRP bridge, dimensions in inches.

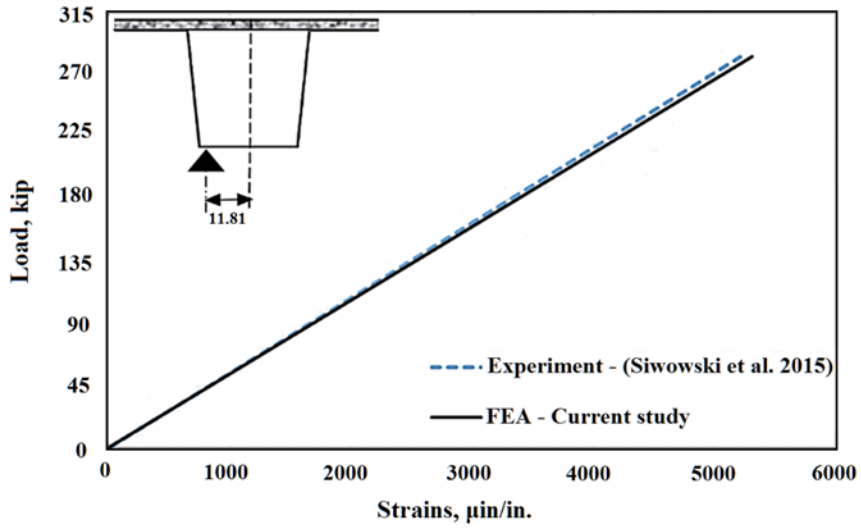

Figure 82. Comparison of experimental and FEA results (strains) for Polish FRP bridge

9.2.1.2 *Hybrid FRP/RC Bridge Superstructure System in Texas*

The bridge consists of a reinforced concrete (RC) slab and U-shaped glass-fiber reinforced (GFR) girders. Hollow tubes made of stainless steel play the role of shear connectors between the concrete and the composite beam. The FRP/RC bridge was eventually constructed in San Patricio, Texas in 2004. Experimental testing of the U-shaped FRP/RC beam is described in Chen et al. 2009 [54]. Prior to ultimate failure, the hybrid structure was able to withstand transverse loads that were 16 times higher than the design loads.

In the current study, computational results are compared with the experimental results of the FRP U-girder used in the San Patricio, Texas, bridge. The failure analysis showed that the results are in very good agreement with the experimental outcomes. A layout of the hybrid beam and the loading points are depicted in Figure 83. The experimental testing was carried out in two phases. First, only the FRP beam was subjected to static loading. Deflection, strains, and neutral axis location were determined. This experiment verified the measurements obtained by strain gages and acoustic emissions (AE) sensors. Then, reinforced concrete was added to the FRP beam to represent the actual hybrid FRP/RC beam. The system was loaded at three stages: the design load, 17.1 kips, a second load of 92.4 kips and a third one until failure (319.9 kips).

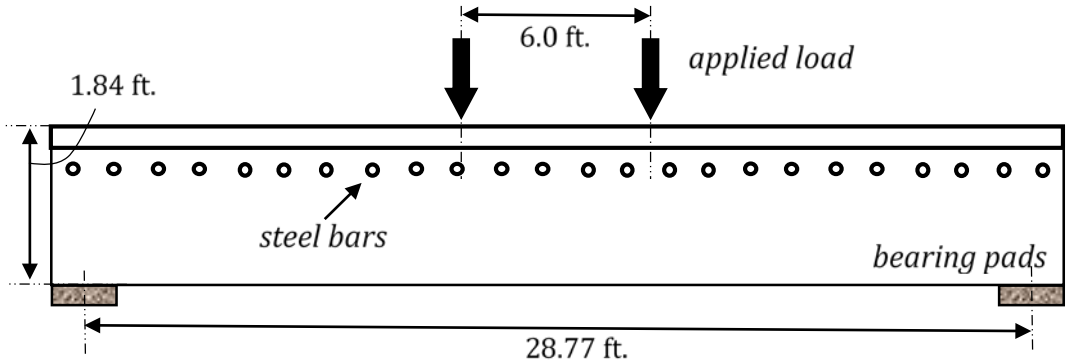

Figure 83. Load test setup for Texas FRP bridge girder

The geometry of the U-shaped girder's cross-section with and without the RC slab is presented in Figure 84. All of the reported dimensions are in inches. Equal thickness was selected for the sides and base of the hybrid girder (1.73 in) and part of the beam's interior was filled with concrete. The material properties of the E-glass laminate are provided in Table 43.

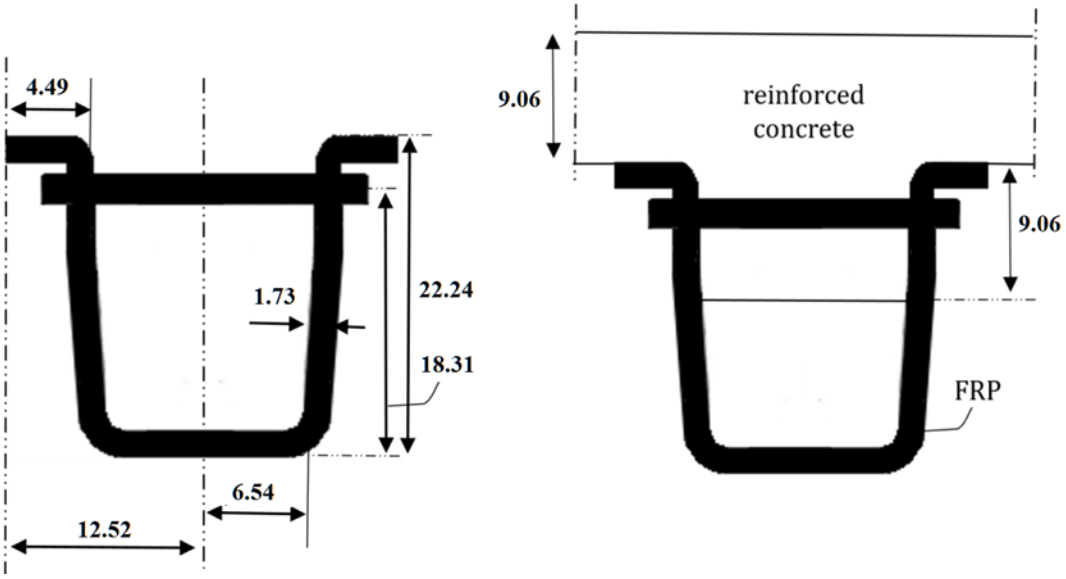

(A) (B)

Figure 84. Cross-section of Texas FRP bridge.

Table 43. Laminate properties for Texas FRP bridge

	E_x (Msi)	E_y (Msi)	G_{xy} (Msi)	$\sigma_{ult\text{-}Long.}$ (ksi)	$\sigma_{ult\text{-}Transv.}$ (MPa)
E-Glass/Vinylester	2.12	1.80	0.61	17.5	12.5

The experimental testing of the FRP/RC girder was conducted at the structural laboratory of the University of South Carolina. Load was applied with two 300 kips hydraulic actuators (total load capacity of both actuators = 600 kips). Strain gauges and linear variable resistance displacement transducers (LVR) were applied throughout the girder's surface to measure strains, deformations, and failure locations.

The first phase of the testing was performed prior to casting the RC deck to validate the quality of the girder's materials and fabrication. Acoustic emissions testing was performed during loading as part of the QA/QC process. Deflections, strain at midspan, and neutral axis (NA) location were determined. In the present study, a FE model was initially designed with 4-node shell elements for the laminate section and 1D bar elements for the hollow steel tubes (Figure 85). Static analysis was performed and the results are compared with those obtained by the first phase of the experimental testing.

Computational analysis results and those from the first phase of the experimental testing are in very good agreement.

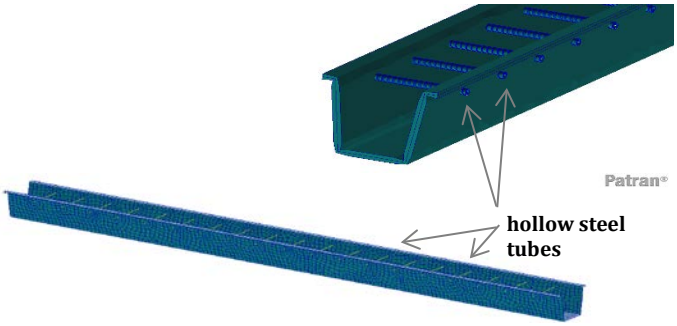

Figure 85. Finite element model of single FRP U-girder with steel

Table 44. Comparison of FEA and experimental results before concrete placement for Texas FRP U-Girder

	Chen et al. 2009 [54]	FEA	± %
Max. deflection, mm	12.0	12.2	+ 1.68
Max. Tensile Strain, μ.ε	420	402	- 4.29
Neutral axis location, mm	254	249	- 1.97

The second phase of testing was conducted to determine the load capacity of the FRP/RC structure, and at the same time to measure strains at the onset of damage. Moreover, a failure analysis would be useful to observe the damage mode and location. For the current study, a new FE Model was created to include the RC slab at the top of the girder. For this case, 3D elements were utilized for the modeling of the concrete deck, and no material was added at the interior of the beam where lightweight Styrofoam was placed prior to concrete casting (Figure 88).

The hybrid beam was loaded in a similar fashion to the first phase of the experiment. However, this time the load levels were increased in 4 stages, up to the ultimate failure of the specimen. A linear behavior was observed until the 2nd stage of the loading (99.37 kips), and no plastic deformations occurred. However, when the load reached 272.02 kips, the authors reported the following:

"*One end of the FRP specimen cracked near the web to bottom flange interface and delaminated at this level of load. It is noted that the test specimen was constructed in a similar fashion to that of the actual bridge…… The cracking was caused by the large reaction forces acting at the supports……*"

A separate finite element analysis study was completed to determine if this unexpected failure mode could be characterized. The initial computational study completed using NASTRAN indicated that a first-ply-failure occurred at a load level of 290 kips (total load) in the vicinity of the support reaction. An independent FE model was developed using ProEngineer (Figure 86). Laminate strength and stiffness properties reported by Chen et al. were used for FRP laminate in the longitudinal and transverse

directions (Table 43). The authors did not report a compressive strength for the laminate, so a value of 15 ksi was assumed for both directions.

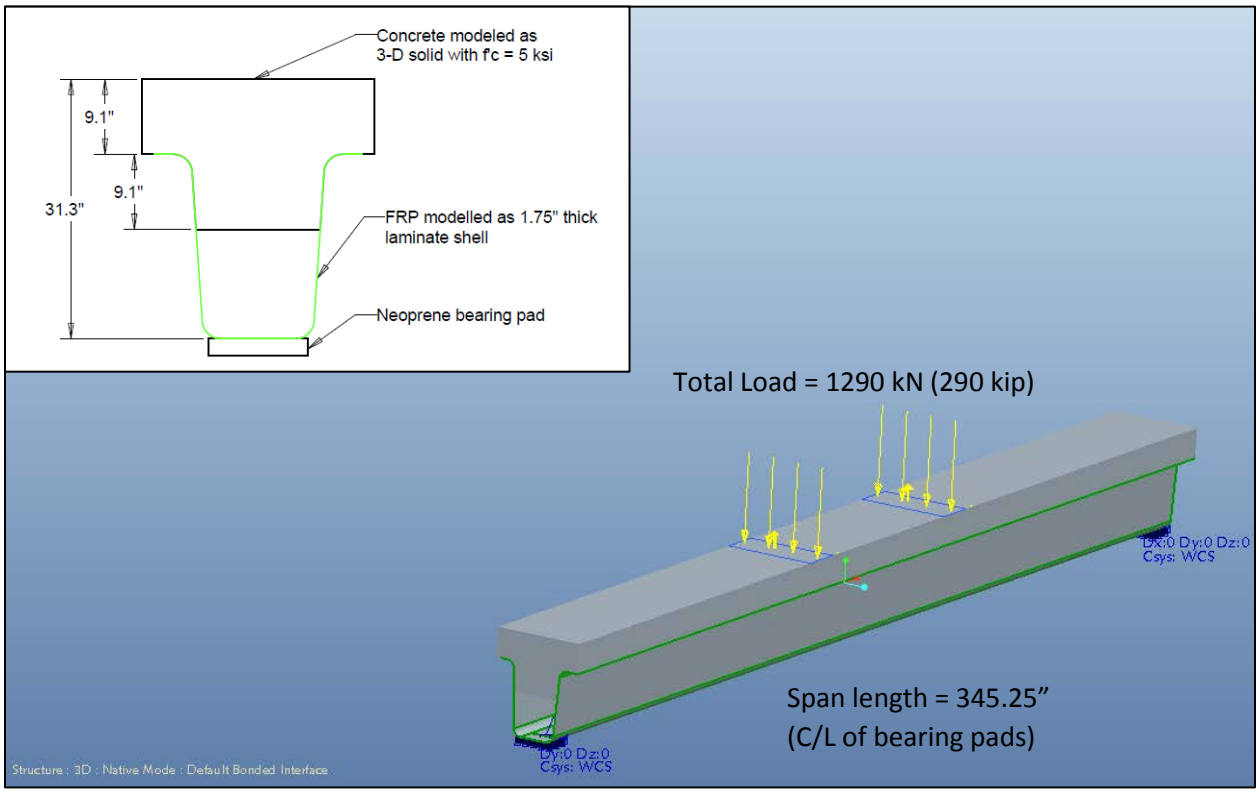

Figure 86. 3-D solid model used for failure analysis study.

The desired output for this study is the failure index. The finite element software uses classical laminate theory to determine the stresses and strains that develop in each ply of the laminate. A maximum stress criterion is then used to compute a failure index that indicates how close each ply is to failure based on the strength properties provided for the laminate. A failure index was also computed for the concrete material based on a compressive strength of 5 ksi. The failure index for concrete in tension was ignored by specifying a tensile strength nearly equal to the compressive strength. A failure index value greater than or equal to 1.0 simply indicates that the material has exceeded its specified strength.

Failure index results for the Texas U-Girder subjected to a total force of 290 kips are provided in Figure 87. The highest failure index is clearly in the vicinity of the bearing pads, which matches the observed failure from the experimental testing performed by Chen. When the failure occurs in the FRP near the support, the highest failure index related to the compressive stress in the concrete is between 0.8 and 0.85. To continue loading the beam to failure in the experimental study, wood blocking was placed between the concrete and the FRP in the U-girder at the cracked support location. Once the wood was used as supplementary support to transfer load directly from the cast-in-place RC deck to the support, the load path within the FRP was changed dramatically. The specimen ultimately held a total maximum force of 320 kips. No effort was made to capture this ultimate failure mechanism using the finite element method.

The overall load vs. deflection plot for the experimental results and the original computational model completed in NASTRAN are provided in Figure 89. The neutral axis location at the end of every load stage was also determined by the experimental data and the FEM model analysis. The results are provided in Table 45. In summary, the finite element methods used in the current study have been shown to accurately predict the behavior of full-scale FRP U-girders. The modeling techniques described for the Polish FRP U-girder and the Texas FRP U-girder were extended in the current study to include an entire FRP U-girder bridge.

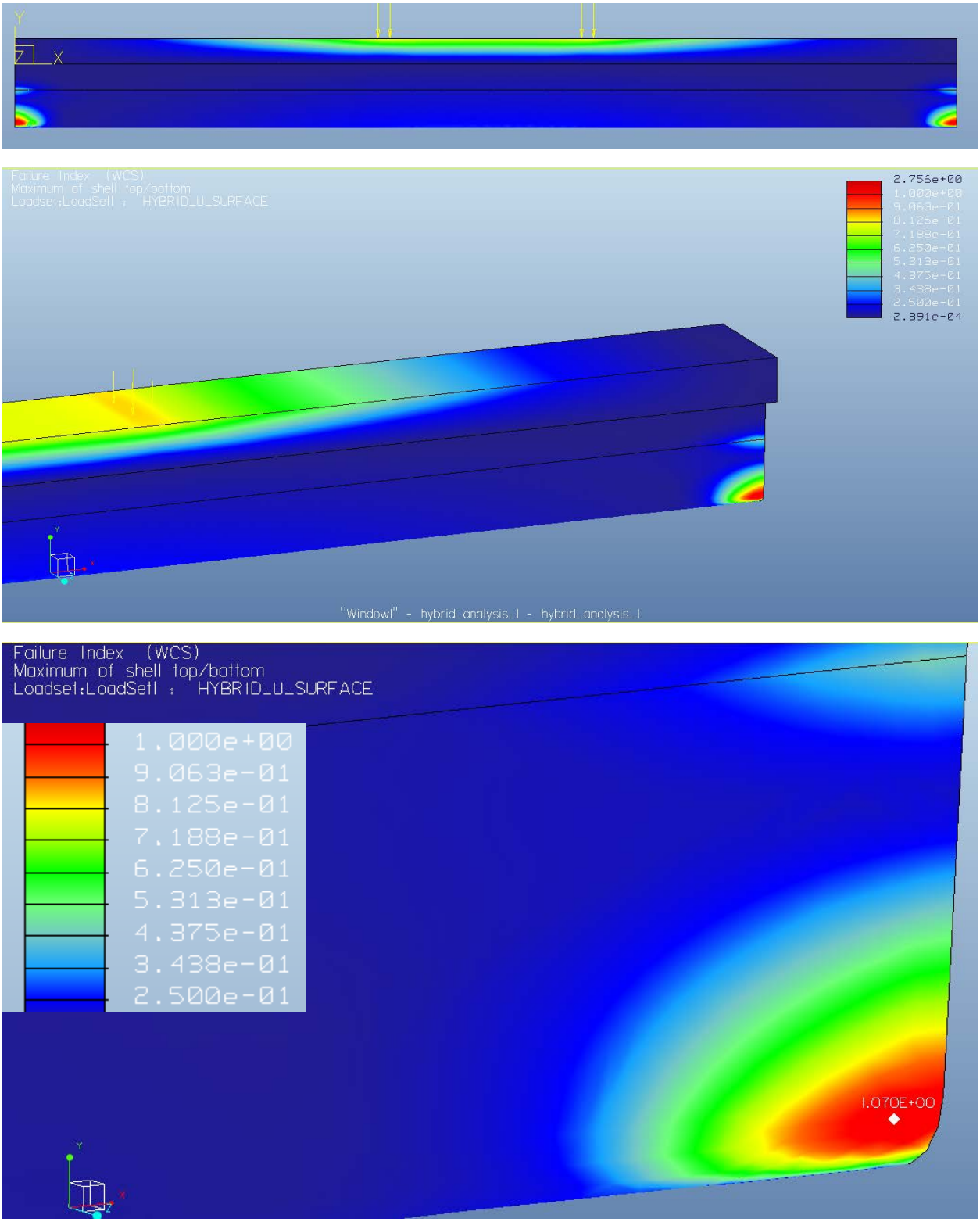

Figure 87. Failure index results for Texas U-girder.

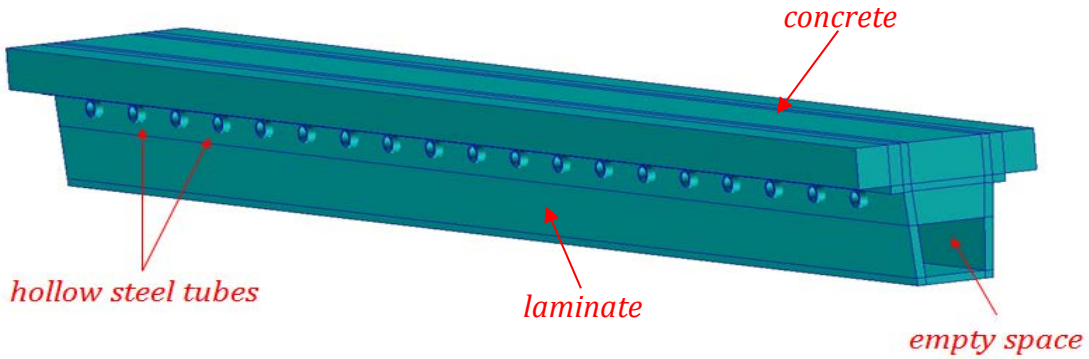

Figure 88. Finite element model of Texas FRP U-girder after concrete placement

Table 45. Comparison of FEA and experimental results: neutral axis location after concrete placement

	Chen et al. 2009 [54]	FEA	± %
Stage 1	566	573	+1.2%
Stage 2	558	568	+1.9%
Stage 3	486	499	+2.7%

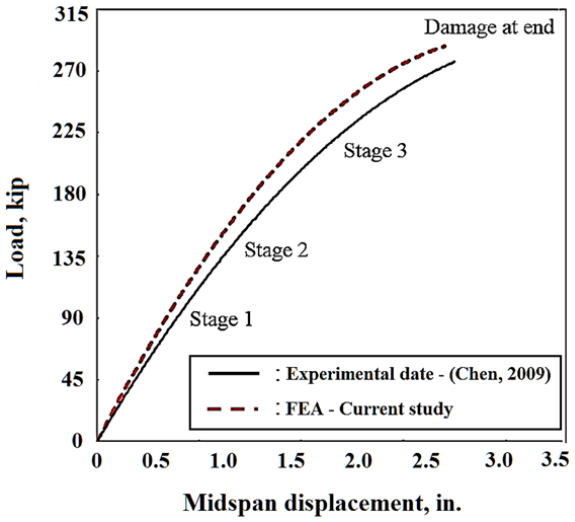

Figure 89. Load vs. midspan displacement for Texas FRP U-girder (comparison of FEA and experimental results)

9.2.2 Sub-Study 1: General Laminate Architectures

The goal of the first optimization sub-study was to investigate different laminate architectures and determine how laminate strength and stiffness properties influence the total amount of FRP required to satisfy the five limit states. A total of four different fabrics plus a filament winding option were investigated. Basic material properties for the fabrics are summarized in Table 46.

Table 46. FRP composite material properties for laminate architecture optimization study

Fabric Type	Manufact.	ID	σ_{xx} (ksi)	σ_{yy} (ksi)	τ_{xy} (ksi)	E_{xx} (Msi)	E_{yy} (Msi)	Thickn./ layer (in.)
Woven 0/90 RI	Hexcel	HexForce 1597	34.4	37.0	11.5	2.5	2.5	0.0378
NCF 0/90 RI	VectorPly	E-LT-4400	73.8	74.2	13.1	3.9	3.92	0.044
NCF $0^{+}/90^{-}$ RI	VectorPly	E-LT-5500	120.4	46.6	13.1	6.57	2.44	0.054
NCF Carbon 0 RI	VectorPly	C-L 1800	198.7	4.2	7.9	16.56	1.43	0.024
Filament wound	WacoBoom	n/a	52.0	50.0	11.3	3.9	3.1	n/a

Note: RI = Resin Infused

Six different laminate architectures were investigated:

- **LA-1**: The base material for the webs and flange is E-LT 4400 (balanced 0/90 non-crimp fabric). To provide additional stiffness for the girder, additional layers of E-LT 5500 (highly reinforced in 0-direction with a small amount of fibers placed in the 90-direction) can be added by the optimization routine in the flange area of the U-girder. The thickness of the flange and webs derived from the E-LT 4400 must be equal, but the flange thickness can be increased by the E-LT 5500 if the optimization routine determines that it will result in overall material savings.
- **LA-2**: Identical to LA-1 except that additional stiffness is achieved by adding uni-directional carbon fiber (C-L 1800) layers in the U-girder flange area. These are only added by the optimization routine if it results in a net weight savings (cost will be analyzed separately).
- **LA-3**: E-LT 4400 is used for the webs and flange. The optimizer is allowed to treat the flange thickness, t_1, as a separate variable from the web thickness, t_2.
- **LA-4**: E-LT 5500 is used for the webs and flange. The optimizer is allowed to treat the web thickness, t_1, as a separate variable from the flange thickness, t_2.
- **LA-5**: HexForce 1597 (0/90 woven fabric) is used for the webs and the flange. Flange thickness and web thickness are treated as separate variables.
- **LA-6**: Filament wound material properties were used for the webs and flange. The thickness of the webs and flange must be equal. The general idea for this laminate architecture is that a rectangular tube can be manufactured using filament winding and then cut in half (longitudinally) to obtain two girders.

9.2.2.1 *Modelling Assumptions for FEA*

The general modelling assumptions used in this optimization sub-study were intended to reflect the conditions observed by Ziehl et al. during the load testing of the U-girder bridge in San Patricio County, Texas [122]. The design scenario for the Texas FRP U-girder bridge included the following key assumptions:

- A reduced value for composite action between the FRP U-girders and the RC deck.
- Simply supported end conditions
- A lateral distribution factor of 0.73

Results from load testing, however, led to the following conclusions:

- The initial design assumptions were overly conservative
- The following changes could be made to the initial design assumptions to achieve better agreement with field testing results:
    - Assume full composite action between the deck and U-girder
    - Include the beneficial stiffening effects of concrete in the tension zone
    - Provide full rotational end-restraint
    - Use a lateral distribution factor of 0.53

These conclusions led to the following critical assumptions in the bridge finite element model used in the current optimization sub-study:

- The cast-in-place reinforced concrete barriers were present for all limit states (Note: this would not be allowed in design scenarios for FRP U-girder bridges in Florida due to limitations imposed by the FDOT Structures Guidelines. Sub-studies 2 and 3 do not include the stiffness or strength contributions of the barriers.
- Additional end-restraint was provided by supporting the bottom of the girder a distance of 12 inches from the end. This does have the net effect of reducing the overall span length by two feet.
- Full composite action was assumed between the cast-in-place RC deck and the FRP U-girders.
- No concrete was placed inside the FRP U-girder.
- Two 12-foot-wide traffic lanes were centered in the bridge. Vehicles were positioned in the center of the traffic lanes (Figure 90).

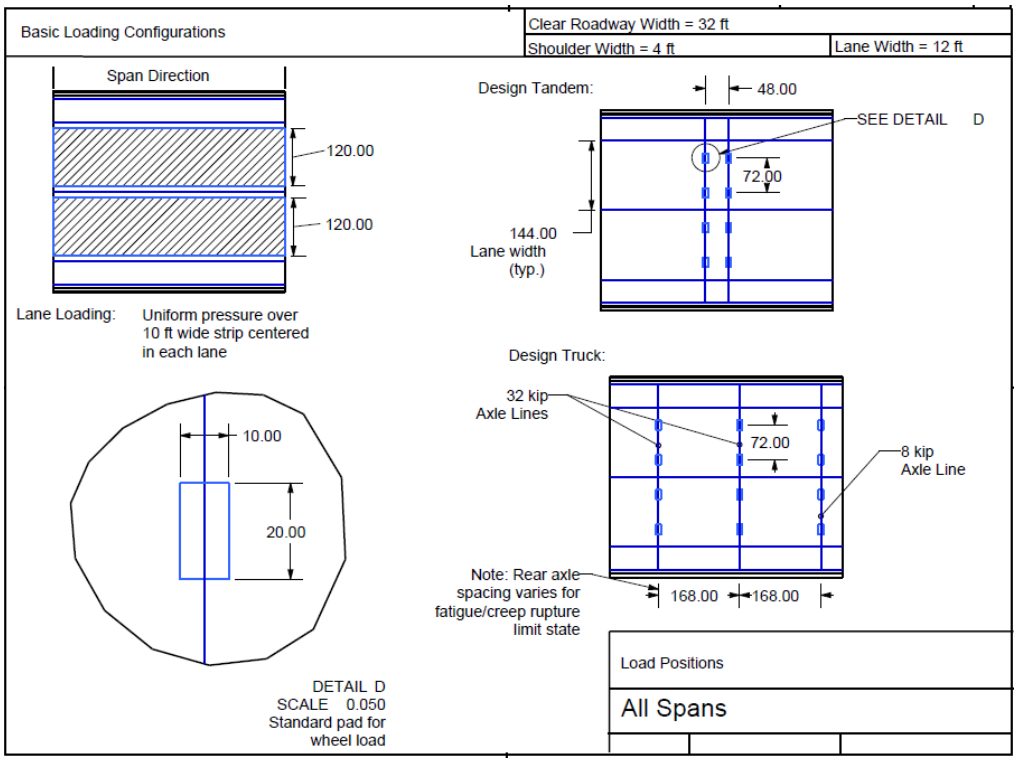

Figure 90. Basic loading configurations for Sub-Study 1 (FEA optimization)

9.2.2.2 *Optimization Results: Sub-Study 1 (Laminate Architecture)*

Results from the first FEA optimization sub-study are summarized in Table 47 through Table 56. The following critical observations were made from these results:

- The 30-ft and 40-ft span lengths are optimized with five bridge girders (Nb = 5)
- The 50-ft through 75-ft span lengths are optimized with six bridge girders (Nb = 6).
- For the 30-ft and 40-ft span lengths, the critical limit state is LS-4b (shear strength).
- For the 50-ft through 75-ft span lengths, the critical limit state is LS-2 (deflections)

Figure 91 provides a graphical summary of the FEA optimization results for Sub-Study 1. LA-2 (0/90 GFRP + unidirectional carbon) and LA-4 (0-degree GFRP with minimal reinforcement in the 90-degree direction) produce the lowest total weight of FRP required for the entire bridge. The results are generally equivalent for all of the laminate architectures when the controlling limit state is shear strength (Span length = 30 ft and 40 ft). This results from the fact that the shear strengths of the different laminate architectures are relatively similar. For longer spans, where deflections begin to control the design, laminate architectures with a higher modulus of elasticity in the longitudinal direction are preferred. LA-2 includes layers of CFRP in the U-girder flange, which increases the overall stiffness of the girder. It should be noted that the cost of CFRP is considerably higher GFRP, so direct comparison of FRP weight for LA-2 is potentially misleading with regards to overall girder cost. LA-4 also consists entirely of GFRP where a much larger percentage of the fibers are oriented in the longitudinal direction (E-LT 5500). The E_{xx} value for this material is 6.57 Msi vs. only 3.9 Msi for the balanced 0/90 NCF laminate (E-LT 4400).

Select results from the AASHTO distribution factor method (DFM) are also included in Figure 91. The plotted results were obtained for the case where the concrete stiffness beneath the slab was not included in the deflection calculations. Barriers were also excluded in this AASHTO DFM result. This is the closest match to the FE model used for the current sub-study. These AASHTO DFM results are based on five bridge girders for the 30-ft and 40-ft spans and six girders for 50-ft through 75-ft. Finally, the assumed shear strength in the AASHTO DFM case was 10 ksi while 13.1 ksi was used for the FEA optimization. This difference should be slightly offset, however, because the FEA optimization method requires that all of the shear force must be transferred through the FRP webs while the AASHTO DFM assumes that a portion of the shear force is carried by the concrete at the strength limit state.

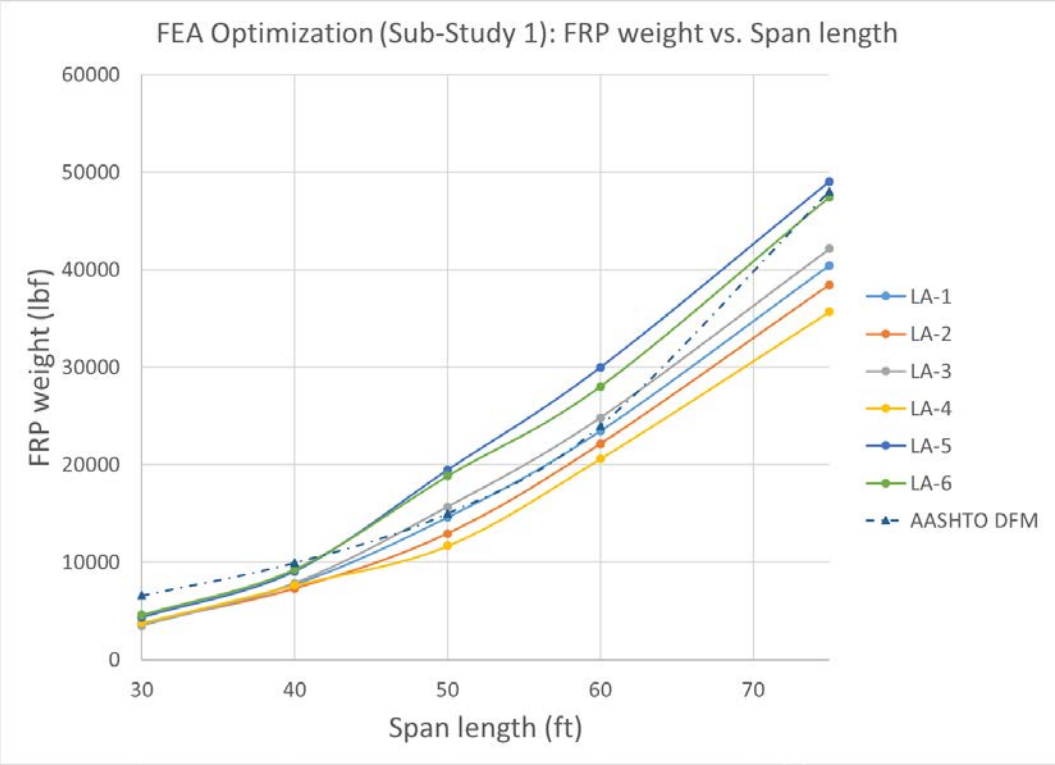

Figure 91. Sub-Study 1 FEA optimization results. Total FRP weight vs. span length.

Table 47. FEA optimization results: Sub-Study 1, Span length = 30 ft

	LA-1 NCF 0/90 +0-glass	**LA-2 NCF 0/90 +0-carbon**	**LA-3 NCF 0/90**	**LA-4 0-glass**	**LA-5 woven**	**LA-6 filament**
Total weight, lbf	3,746	3,746	3,481	3,782	4,332	4,589
Weight / girder, lbf	749	749	696	756	866	918
# girders	5	5	5	5	5	5
Height, in.	14.4	14.4	14.4	14.7	14.4	14.4
d, in.	14.44	14.44	14.44	14.74	14.44	14.44
L1, in.	9.0	9.0	9.8	9.1	9.0	8.5
L2, in.	11.0	11.0	11.8	11.2	11.0	10.5
Angle, deg.	86	86	86	86	86	86
t1 thick., base (# layers)	**0.84** (19+0)	**0.84** (19+0)	**0.53** (12)	**0.54** (10)	**0.53** (14)	**0.98**
t2 thick., sides (# layers)	**0.84** (19)	**0.84** (19)	**0.84** (19)	**0.92** (17)	**1.10** (29)	

Table 48. Critical limit state evaluation: Sub-Study 1, Span length = 30 ft

	LA-1 NCF 0/90 +0-glass	**LA-2 NCF 0/90 +0-carbon**	**LA-3 NCF 0/90**	**LA-4 0-glass**	**LA-5 woven**	**LA-6 filament**
Limit State 1 (concrete)	0.787	0.787	0.795	0.753	0.819	0.780
Limit State 2 (deflections)	0.899	0.899	0.900	0.833	0.939	0.875
Limit State 3a (fatigue – norm. stress)	0.271	0.271	0.290	0.254	0.429	0.372
Limit State 3b (fatigue - shear)	0.715	0.715	0.712	0.702	0.712	0.713
Limit State 4a (strength – norm. stress)	0.276	0.276	0.286	0.255	0.433	0.379
Limit State 4b (strength - shear)	1.000	1.000	1.000	1.000	1.000	1.000

Table 49. FEA optimization results: Sub-Study 1, Span length = 40 ft

	LA-1 NCF 0/90 +0-glass	**LA-2 NCF 0/90 +0-carbon**	**LA-3 NCF 0/90**	**LA-4 0-glass**	**LA-5 woven**	**LA-6 filament**
Total weight, lbf	7,718	7,312	7,842	7,632	9,065	9,264
Weight / girder, lbf	1,544	1,462	1,568	1,526	1,813	1,853
# girders	5	5	5	5	5	5
Height, in.	19.8	19.8	19.9	19.7	24.3	19.8
d, in.	19.85	19.85	19.95	19.75	24.36	19.85
L1, in.	9.8	9.4	9.2	9.8	16.8	10.6
L2, in.	12.6	12.2	12.0	12.5	20.2	13.4
Angle, deg.	86	86	86	86	86	86
t1 thick., base (# layers)	**1.42** (20+10)	**1.29** (20+17)	**1.58** (36)	**1.24** (23)	**0.91** (24)	**1.10**
t2 thick., sides (# layers)	**0.88** (20)	**0.88** (20)	**0.88** (20)	**0.92** (17)	**1.17** (31)	

Table 50. Critical limit state evaluation: Sub-Study 1, Span length = 40 ft

	LA-1 NCF 0/90 +0-glass	**LA-2 NCF 0/90 +0-carbon**	**LA-3 NCF 0/90**	**LA-4 0-glass**	**LA-5 woven**	**LA-6 filament**
Limit State 1 (concrete)	0.732	0.706	0.744	0.702	0.689	0.749
Limit State 2 (deflections)	0.979	0.929	0.998	0.915	0.910	0.996
Limit State 3a (fatigue – norm. stress)	0.525	0.446	0.326	0.280	0.516	0.468
Limit State 3b (fatigue - shear)	0.737	0.735	0.713	0.720	0.745	0.737
Limit State 4a (strength – norm. stress)	0.493	0.419	0.306	0.263	0.213	0.437
Limit State 4b (strength - shear)	1.000	1.000	1.000	1.000	0.998	1.000

Table 51. FEA optimization results: Sub-Study 1, Span length = 50 ft

	LA-1 NCF 0/90 +0-glass	**LA-2 NCF 0/90 +0-carbon**	**LA-3 NCF 0/90**	**LA-4 0-glass**	**LA-5 woven**	**LA-6 filament**
Total weight, lbf	14,601	12,958	15,670	11,682	19,456	18,833
Weight / girder, lbf	2,434	2,160	2,612	1,947	3,243	2,434
# girders	6	6	6	6	6	6
Height, in.	27.1	23.9	28.0	26.7	32.4	29.9
d, in.	27.17	23.96	28.07	26.77	32.48	27.17
L1, in.	9.4	9.7	9.8	11.1	10.2	9.4
L2, in.	13.2	13.0	13.7	14.8	14.7	14.0
Angle, deg.	86	86	86	86	86	86
t1 thick., base (# layers)	**1.47** (20+11)	**1.38** (20+21)	**1.72** (39)	**1.24** (23)	**1.06** (28)	**1.13**
t2 thick., sides (# layers)	**0.88** (20)	**0.88** (20)	**0.88** (20)	**0.92** (17)	**1.10** (29)	

Table 52. Critical limit state evaluation: Sub-Study 1, Span length = 50 ft

	LA-1 NCF 0/90 +0-glass	**LA-2 NCF 0/90 +0-carbon**	**LA-3 NCF 0/90**	**LA-4 0-glass**	**LA-5 woven**	**LA-6 filament**
Limit State 1 (concrete)	0.694	0.701	0.722	0.625	0.693	0.732
Limit State 2 (deflections)	1.000	1.000	1.000	1.000	1.000	0.999
Limit State 3a (fatigue – norm. stress)	0.606	0.494	0.354	0.318	0.632	0.542
Limit State 3b (fatigue - shear)	0.802	0.817	0.728	0.844	0.793	0.873
Limit State 4a (strength – norm. stress)	0.523	0.422	0.310	0.281	0.552	0.480
Limit State 4b (strength - shear)	0.910	0.917	0.998	0.771	0.949	0.964

Table 53. FEA optimization results: Sub-Study 1, Span length = 60 ft

	LA-1 NCF 0/90 +0-glass	**LA-2 NCF 0/90 +0-carbon**	**LA-3 NCF 0/90**	**LA-4 0-glass**	**LA-5 woven**	**LA-6 filament**
Total weight, lbf	23,470	22,154	24,833	20,617	29,979	28,019
Weight / girder, lbf	3912	3692	4139	3436	4997	4670
# girders	6	6	6	6	6	6
Height, in.	33.6	33.4	30.6	32.0	35.8	31.5
d, in.	33.68	33.48	30.67	32.08	35.89	33.68
L1, in.	10.8	9.5	11.6	10.6	12.0	10.8
L2, in.	15.5	14.2	15.9	15.1	17.0	16.6
Angle, deg.	86	86	86	86	86	86
t1 thick., base (# layers)	**1.62** (22+12)	**1.33** (22+15)	**1.72** (39)	**1.30** (24)	**1.70** (45)	**1.24**
t2 thick., sides (# layers)	**0.97** (22)	**0.97** (22)	**1.10** (25)	**0.97** (18)	**1.17** (31)	

Table 54. Critical limit state evaluation: Sub-Study 1, Span length = 60 ft

	LA-1 NCF 0/90 +0-glass	**LA-2 NCF 0/90 +0-carbon**	**LA-3 NCF 0/90**	**LA-4 0-glass**	**LA-5 woven**	**LA-6 filament**
Limit State 1 (concrete)	0.644	0.647	0.654	0.663	0.640	0.664
Limit State 2 (deflections)	1.000	1.000	0.999	1.000	0.999	1.000
Limit State 3a (fatigue – norm. stress)	0.675	0.620	0.690	0.377	0.640	0.564
Limit State 3b (fatigue - shear)	0.935	0.943	0.863	0.941	0.720	0.821
Limit State 4a (strength – norm. stress)	0.574	0.527	0.510	0.322	0.544	0.481
Limit State 4b (strength - shear)	0.868	0.889	0.816	0.952	0.532	0.596

Table 55. FEA optimization results: Sub-Study 1, Span length = 75 ft

	LA-1 NCF 0/90 +0-glass	**LA-2 NCF 0/90 +0-carbon**	**LA-3 NCF 0/90**	**LA-4 0-glass**	**LA-5 woven**	**LA-6 filament**
Total weight, lbf	40,465	38,467	42,149	35,679	49,059	47,447
Weight / girder, lbf	6,744	6,411	7,025	5,947	8,177	7,908
# girders	6	6	6	6	6	6
Height, in.	38.9	37.6	38.5	35.0	41.1	39.7
d, in.	38.99	37.69	38.59	35.09	41.20	37.69
L1, in.	12.3	13.5	14.6	11.1	20.4	13.5
L2, in.	17.7	18.7	20.0	16.7	26.1	22.9
Angle, deg.	86	86	86	86	86	86
t1 thick., base (# layers)	**1.73** (27+10)	**1.45** (27+11)	**1.85** (42)	**1.46** (27)	**1.89** (50)	**1.30**
t2 thick., sides (# layers)	**1.19** (27)	**1.19** (27)	**1.19** (27)	**1.19** (22)	**1.21** (32)	

Table 56. Critical limit state evaluation: Sub-Study 1, Span length = 75 ft

	LA-1 NCF 0/90 +0-glass	**LA-2 NCF 0/90 +0-carbon**	**LA-3 NCF 0/90**	**LA-4 0-glass**	**LA-5 woven**	**LA-6 filament**
Limit State 1 (concrete)	0.644	0.647	0.654	0.663	0.640	0.664
Limit State 2 (deflections)	1.000	1.000	0.999	1.000	0.999	1.000
Limit State 3a (fatigue – norm. stress)	0.675	0.620	0.690	0.377	0.640	0.564
Limit State 3b (fatigue - shear)	0.935	0.943	0.863	0.941	0.720	0.821
Limit State 4a (strength – norm. stress)	0.574	0.527	0.510	0.322	0.544	0.481
Limit State 4b (strength - shear)	0.868	0.889	0.816	0.952	0.532	0.596

9.2.3 Sub-Study 2: Influence of Cast-in-Place RC Barriers and Support Conditions

Sub-Study 2 involved modifying the bridge geometry and the boundary conditions from Sub-Study 1. For Sub-Study 2, the weight of the RC barriers was included as a dead load, but the geometry of the barriers was not included in the model. The boundary conditions that were applied at the supports were also modified for Sub-Study 2. Only the extreme bottom edge of the girder was modeled as either a pin support or roller support. Recall that for Sub-Study 1, the bottom edges of each girder were supported over 12 inches in the longitudinal direction to provide additional rotational resistance. The boundary conditions for Sub-Study 2 represent a traditional pin and roller support. Only two of the six laminate architectures were retained for Sub-Study 2 (LA-1 and LA-4). Even though LA-2 produced the lowest total material weight, preliminary cost estimates suggested that incorporating the CFRP layers in the girder flange would be prohibitively expensive (see additional discussion on cost in Section 12.1).

The total FRP weight increases for all span lengths when the cast-in-place RC barriers are removed and full rotation is allowed to occur at the supports. LA-4 is able to obtain a lower total FRP weight for span lengths because the flange thickness is allowed to be less than the web thickness and the modulus of elasticity is larger in the longitudinal direction. A summary of the optimized girder cross-section properties for Sub-Study 2 are provided in Table 58 through Table 62.

Results for total FRP weight vs. span length are provided in Figure 92. The percent change in total FRP weight from Sub-Study 1 to Sub-Study 2 for each span length is provided in Table 57. It is interesting to note how the new results compare to the results obtained using the AASHTO DFM. Compared to Sub-Study 1 (SS-1), the AASHTO DFM results were conservative for the 30-ft, 40-ft, and 75-ft span lengths with regards to total FRP required. The total FRP required for the 50-ft and 60-ft span lengths was nearly identical for the AASHTO DFM and SS-1. For Sub-Study 2 (SS-2), the AASHTO DFM result for total FRP weight falls between the two results for SS-2 for the 30-ft and 75-ft span lengths but is less conservative for the 40-ft, 50-ft, and 60-ft span lengths.

AASHTO DFM results for LS-2a are less conservative (i.e. results suggest that less FRP is required) than LA-1 using SS-2 geometry and boundary conditions for all span lengths. The material properties assumed for the AASHTO DFM and the FEA optimization for LA-1 are identical for the 30-ft span length with the exception of the ultimate shear stress. A likely explanation for this result is that when deflections are computed using the AASHTO DFM, all of the bridge girders are assumed to deflect uniformly (equal distribution of the loading across all girders). The FEA optimization method uses the maximum deflection for the entire bridge, but the girders in the middle of the bridge experience a larger deflection based on the non-uniform lateral load distribution.

In an effort to further investigate the effects of non-uniform lateral load distribution, FEA optimization results for the 30-ft span length using LA-1 (Table 58) were used to develop an independent finite element model outside of the FEA optimization framework. This investigation was also intended to serve as an independent validation study for the FEA optimization results. The loading conditions for the independent FE model were identical to the loading conditions used for Limit State 2 (deflections) and the boundary conditions at the supports matched SS-2.

The deflected shape results obtained from the independent FE model are provided in Figure 93. The solid lines represent the deflected shape results when barriers were not included in the model while the dashed lines represent the deflected shape when barriers were included. Displacement profiles running

in the longitudinal direction of the bridge (in the direction of traffic flow) are provided for both the centerline of the bridge as well and the exterior girder. The maximum deflection obtained along the centerline of the bridge (no barriers) was 0.358 inches (L/1000 = 0.36 in). This result validates the FEA optimization framework because the cross-section generated in SS-2 for laminate architecture LA-1 experiences a maximum deflection of L/1000 when subjected to the loading conditions of Limit State 2 (deflections).

For both the AASHTO DFM and the FEA optimization frameworks, the interaction of the LS-2 (deflections) and LS-4b (shear strength) limit states controlled the design for the 30-ft span length. The displacement profile obtained for the exterior girder explains why the AASHTO DFM is less conservative than the FEA optimization framework. The maximum deflection for the exterior girder is only 0.24 inches, or 33% less than the central girder. As a result, all of the girders based on the FEA optimization framework would need to be larger to meet the deflection criteria. To make an identical comparison of the FEA optimization framework to the AASHTO DFM, the truck loading in the FE model would need to be changed from pressure loads acting over the specified wheel contact areas to uniformly distributed line loads acting across the entire bridge width and parallel to the truck axles.

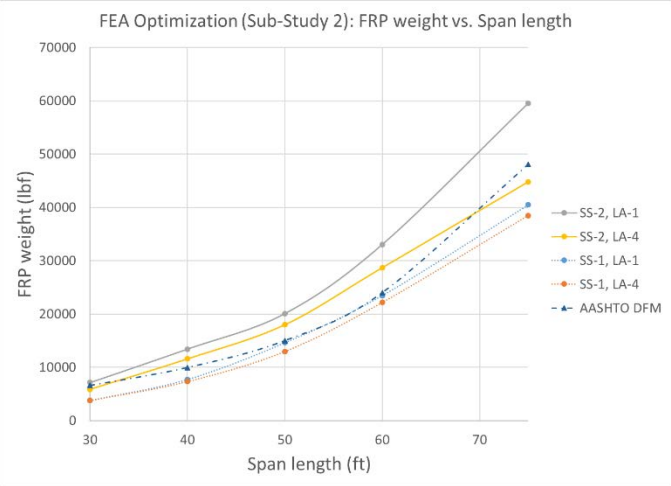

SS-2 = FEA Optimization with no barriers and simply-supported boundary conditions.

SS-1 = FEA Optimization including barriers and some rotational restraint provided at end supports.

LA-1 = 0/90 Non-crimp fabric with additional 0-degree layers in bottom flange.

LA-4 = 0-degree Non-crimp fabric. Flange and web thicknesses may be different.

AASHTO DFM = Distribution factor method result for no barriers, no stiffness contribution made by concrete in U-girder beneath the slab. 0/90 Non-crimp fabric.

Figure 92. Sub-Study 2 FEA optimization results. Total FRP weight vs. span length.

Table 57. Impact of RC barriers and support boundary conditions on total FRP weight

	% Increase in total FRP weight (Sub-Study 1 to Sub-Study -2)	
Span length (ft)	LA-1 NCF 0/90 +0-glass	LA-4 0-glass
30	47.5%	35.5%
40	42.5%	34.1%
50	27.3%	35.0%
60	29.0%	28.1%
75	32.0%	20.4%

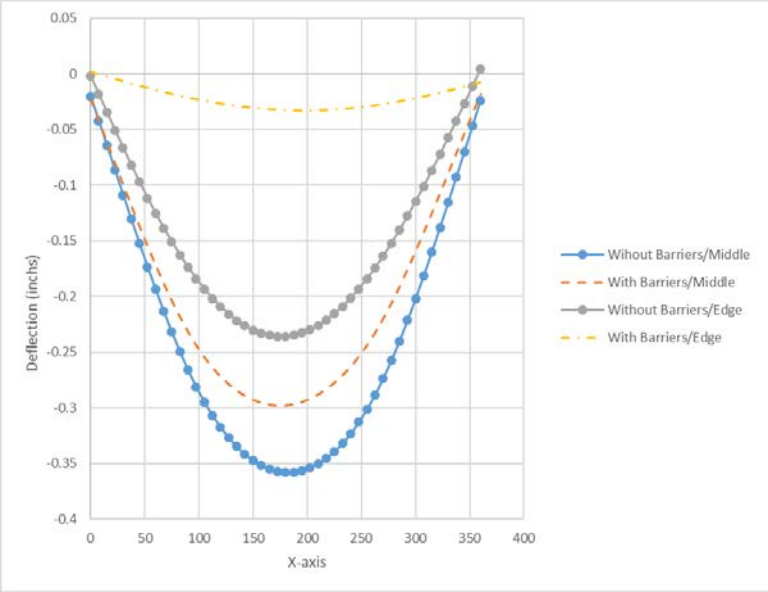

Figure 93. Deflected shape from FE model comparing deflection along bridge centerline and edge of bridge for Limit State 2 loading conditions (deflection criteria). Span length = 30 ft, cross-section/material properties for LA-1. Boundary conditions from Sub-Study 2.

Table 58. FEA optimization results: Sub-Study 2, Span length = 30 ft

	LA-1 NCF 0/90 +0-glass	**LA-4 0-glass**
Total weight, lbf	7,139	5,863
Weight / girder, lbf	1,428	1,173
# girders	5	5
Height, in.	21.5	19.4
d, in.	21.55	19.45
L1, in.	16.81	16.31
L2, in.	13.8	13.6
Angle, deg.	86	86
t1 thick., base (# layers)	**1.056** (24+0)	**0.540** (10)
t2 thick., sides(# layers)	**1.056** (24)	**1.080**(20)

Table 59. FEA optimization results: Sub-Study 2, Span length = 40 ft

	LA-1 NCF 0/90 +0-glass	**LA-4 0-glass**
Total weight, lbf	13,431	11,573
Weight / girder, lbf	2,686	2,315
# girders	5	5
Height, in.	26.4	25.2
d, in.	26.46	25.26
L1, in.	23.09	22.62
L2, in.	19.4	19.1
Angle, deg.	86	86
t1 thick., base (# layers)	**1.370** (25+5)	**0.540** (10)
t2 thick., sides(# layers)	**1.100** (25)	**1.242** (23)

Table 60. FEA optimization results: Sub-Study 2, Span length = 50 ft

	LA-1 NCF 0/90 +0-glass	**LA-4 0-glass**
Total weight, lbf	20,088	17,980
Weight / girder, lbf	3,348	2,997
# girders	6	6
Height, in.	32.9	31.5
d, in.	32.98	31.58
L1, in.	24.00	22.71
L2, in.	19.4	18.3
Angle, deg.	86	86
t1 thick., base (# layers)	**1.366** (20+9)	**0.590** (11)
t2 thick., sides(# layers)	**0.880** (20)	**1.030** (19)

Table 61. FEA optimization results: Sub-Study 2, Span length = 60 ft

	LA-1 NCF 0/90 +0-glass	**LA-4 0-glass**
Total weight, lbf	33,052	28,685
Weight / girder, lbf	5,509	4,781
# girders	6	6
Height, in.	35.9	32.9
d, in.	35.99	32.98
L1, in.	25.62	25.20
L2, in.	20.6	20.6
Angle, deg.	86	86
t1 thick., base (# layers)	**1.63** (26+9)	**1.080** (20)
t2 thick., sides(# layers)	**1.14** (26)	**1.188** (22)

Table 62. FEA optimization results: Sub-Study 2, Span length = 75 ft

	LA-1 NCF 0/90 +0-glass	**LA-4 0-glass**
Total weight, lbf	59,546	44,806
Weight / girder, lbf	9,924	7,468
# girders	6	6
Height, in.	39.2	38.7
d, in.	39.30	38.79
L1, in.	24.98	27.61
L2, in.	24.0	22.2
Angle, deg.	86	86
t1 thick., base (# layers)	**1.918** (35+7)	**1.134** (21)
t2 thick., sides(# layers)	**1.540** (35)	**1.296** (24)

9.2.4 Sub-Study 3: Lateral Truck Positioning

One final sub-study was conducted for the FEA optimization framework to investigate the influence of lateral truck positioning. The loading conditions were modified such that the 0.064 kip/sf pressure loads for each lane were placed adjacent to the centerline of the bridge. The centerline of the interior truck/tandem tire pad loads were located 24 in from the edge of centerline. This is consistent with the transverse load placement as described in LRFD-7 S3.6.1.3.1. Only one laminate architecture, LA-4, was evaluated in Sub-Study 3.

The FEA optimization framework used in Sub-Studies 1 and 2 did attempt to maximize the shear stress near the support by ensuring that at least one truck was aligned near the centerline of the girder when evaluating LS-4b. This requires special coding when the FE model is created because every time the optimization routine changes the number of beams required, the lateral position of the truck must also be adjusted. Unfortunately, this special coding was not included when the FEA optimization was completed for the final Sub-Study. The implications of this omission are highlighted in Figure 94. For the five-beam girder configuration, two wheel loads are positioned directly over the center beam. This configuration results in an increase in total FRP weight of 12.5% for the 30-ft span and 4.4% for the 40-ft span (Table 63). The impact on total FRP weight continues to decrease for the longer spans because the two adjacent wheel pads are no longer directly above a single girder and the deflection limit state (LS-2) begins to drive the design.

The modified loading conditions do push the optimization results towards a more conservative design. Furthermore, there are additional loading positions that were not investigated using the FEA optimization framework that could lead to even higher total FRP material requirements. There are, however, several issues that cast at least some doubt on using the FEA optimization framework to evaluate the effects of lateral vehicle positioning. Additional discussion on the applicability and validity of the FEA optimization framework is provided in Section 9.2.5.

Table 63. FEA optimization results: Sub-Study 3, LA-4 (0-degree) glass, all span lengths

LA-4 E-LT 5500	Span length (ft)				
	30	40	50	60	75
Total weight, lbf	6,593 (+12.5%)*	12,087 (+4.4%)	18,437 (+2.5%)	29,003 (+1.1%)	44,979 (+0.4%)
Weight / girder, lbf	1,319	2,417	3,073	4,834	8,330
# girders	5	5	6	6	6
Height, in.	19.4	25.4	31.8	32.9	38.8
d, in.	19.45	25.46	31.88	32.98	38.89
L1, in.	16.01	22.64	22.84	25.20	27.81
L2, in.	13.3	19.1	18.4	20.6	22.4
Angle, deg.	86	86	86	86	86
t1 thick., base (# layers)	0.540 (10)	0.540 (10)	0.648 (12)	1.080 (20)	1.134 (21)
t2 thick., sides(# layers)	1.242 (23)	1.296 (24)	1.030 (19)	1.134 (23)	44,979 (+0.4%)

*All % changes are relative to SS-2

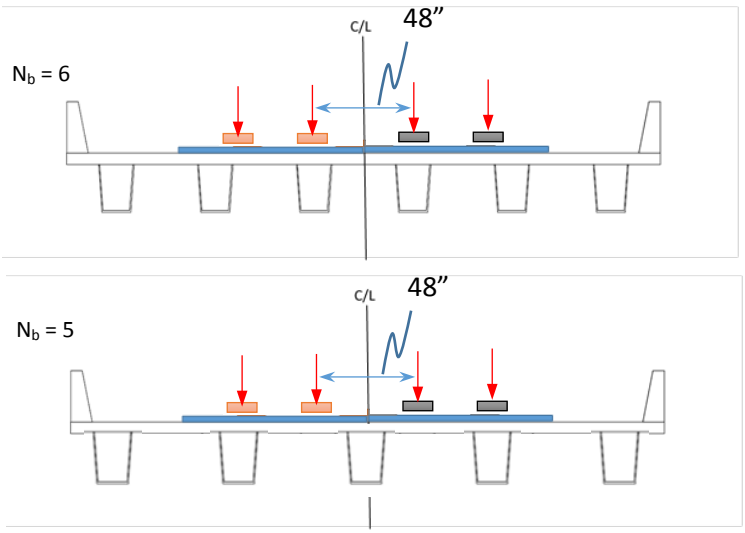

Figure 94. Revised loading conditions for Sub-Study 3 to investigate lateral positioning. Barriers shown but not included in FE model.

9.2.5 Results Summary for all Span Lengths

The FEA optimization framework described in Figure 75 was used to determine the FRP U-girder geometry configuration with the least weight of FRP material that meets all of the limit state criteria established in Section 8.1. The method was first used to evaluate six different laminate architectures over all five span lengths (30 ft, 40 ft, 50 ft, 60 ft, and 75 ft). Next, the effect of different boundary conditions and the presence/absence of barriers was investigated for the two laminate architectures that appeared most promising. To make a valid comparison with the results obtained using the AASHTO

distribution factor method (summarized in Section 9.1.3.3), overall U-girder parameters will be presented for the following cases:

- LA-1 (E-LT 4400 balanced 0/90) using boundary conditions for Sub-Study 1:
  - Barriers present
  - Additional rotational restraint provided at support boundary conditions
  - τ_{max} = 13.1 ksi
  - Number of girders = 5 for 30-ft and 40-ft span lengths. Number of girders = 6 for 50-ft, 60-ft, and 75-ft span lengths
- LA-1 using boundary conditions for Sub-Study 2:
  - Barriers not included in model geometry (barrier self-weight was included)
  - Simple pin/roller support boundary conditions
  - τ_{max} = 13.1 ksi
  - Number of girders = 5 for 30-ft and 40-ft span lengths. Number of girders = 6 for 50-ft, 60-ft, and 75-ft span lengths
- AASHTO DFM results for E-LT 4400 using deflection criteria LS-2a (0% stiffness contribution for concrete beneath slab)
  - Barriers not included in stiffness calculations
  - τ_{max} = 10 ksi
  - Number of girders = 5 for 30-ft and 40-ft span lengths. Number of girders = 6 for 50-ft, 60-ft, and 75-ft span lengths

Results for average FRP thickness, girder depth, and total weight of FRP for all span lengths are summarized in Figure 95. Two important conclusions can be made at this point. First, the required FRP thicknesses are in the realm of what would be considered technically feasible from a manufacturing standpoint using the vacuum assisted resin transfusion method (VARTM). Second, the girder depths are also consistent with traditional reinforced concrete girders for this range of span lengths. AASHTO LRFD-7 Table 2.5.6.2.3-1 provides typical section depths, including the slab, for reinforced concrete T-beams as 0.07xL and for steel I-beams as 0.04xL.

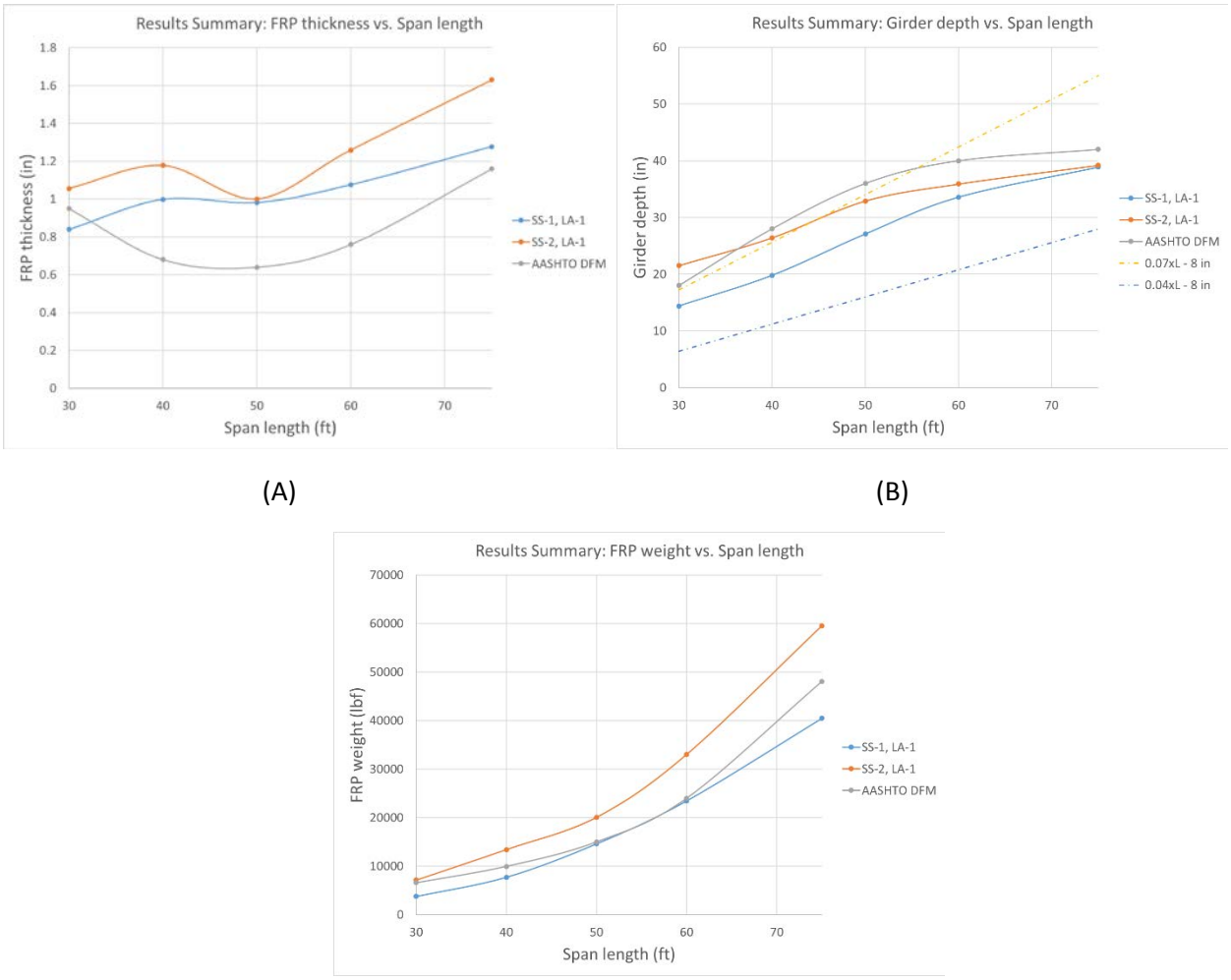

(A) (B)

(C)

Figure 95. Results summary for FEA optimization framework. (A) Average FRP thickness, (B) Girder depth below slab, and (C) Total FRP weight.

When relying on the finite element method to solve any type of modeling problem, the results are only as reliable as the assumptions made when building the model. The results from SS-1 and SS-2 for the FEA optimization framework represent relative bookends of what might be considered aggressive and conservative modeling assumptions. Arguments can certainly be made in support of each set of assumptions, and the difference in results will ultimately have a large impact on the overall cost of a specific design. When trying to assess which methodology should be used to make an overall assessment of the cost of different U-girder options, the following points need to be considered:

1. For the shear strength limit state (LS-4b), the FE model assumes a simple support along the extreme edge of each girder. The wheel pads were located a longitudinal distance of 12 in to maximize shear effects. In the actual FRP U-girder bridge, the girders would certainly be filled with concrete near the supports (and likely throughout the entire length), so the shear stresses computed by the FE model should be considered extremely conservative.

2. Incorporating the influence of the concrete into a finite element model at the strength limit state for shear is an extremely complex process that is beyond the scope of the current study. If the concrete were simply added to the linear finite element model, the shear stresses that develop in the FRP would drop significantly because the concrete would bear a majority of the load. This is not realistic, however, because once the concrete cracks, which it ultimately would under any loading conditions for a strength limit state, the FRP will assume a larger portion (still not all) of the internal shear force. In other words, including concrete in the linear FEA model will lead to the erroneous conclusion that no FRP is required. Excluding the concrete and relying entirely on the FRP for shear transfer is overly conservative and will lead to an extremely expensive FRP U-girder. This effect is magnified if the cross-section required for this unrealistic shear condition is then applied to all girders over the entire span length. In this case, relying on the AASHTO distribution factor method along with one of the models for FRP shear strength contribution described in Section 8.1.5 appears to be a more reasonable approach.
3. The FEA optimization framework is numerically intensive. If lateral vehicle positioning was incorporated into the framework as an additional design variable that needs to be established for each limit state and number of girder combinations, the process may break down and require too much time. Of course, pointing the optimization routine in the right direction from the start could reduce much of the required computational effort (the total number of girders required should probably not exceed six for the span lengths under consideration).
4. Figure 93 illustrates that using the FE method with discrete tire locations will result in non-uniform deflections with respect to lateral vehicle positioning. This contradicts a fundamental principle that is established by AASHTO for deflection criteria:
    a. “When investigating the maximum absolute deflection for straight girder systems, all design lanes should be loaded, and all supporting components should be loaded equally.”
    b. Additional commentary states “For a straight girder system bridge, this is equivalent to saying that the distribution factor for deflection is equal to the number of lanes divided by the number of beams.”
5. If a finite element model is going to be used to evaluate deflection criteria, the only way to ensure that all girders deflect equally is to apply the axle loads for each truck as uniformly distributed line loads across the entire width of the bridge parallel to the truck axles. This was not done in the current study. Furthermore, for the type of bridge systems under investigation (simply supported, short span, straight slab on beam systems), a sophisticated finite element model is not needed to evaluate deflections if the vehicle loads are distributed uniformly across the bridge.

Unfortunately, the two limit states that the FE model is the least well-suited to evaluate, LS-2 and LS-4b, end up controlling the design for the span lengths under consideration. Nonetheless, the FEA optimization framework still provides a useful validation procedure for the AASHTO distribution factor method and provides both upper and lower bounds on the amount of FRP material that is required for a range of modelling assumptions.

9.3 Distribution Factor Validation Using FEA

A final assessment was made for the FRP U-girders that involved validating the distribution factors computed according to LRFD-7 Table 4.6.2.2.2.b-1 (using section type “e” in Table 4.6.2.2.2.1-1). Section type “c”, the steel box girder, was also considered. For section type “c”, the range of applicability for girder spacing, S, and girder depth, d, fall on the extremely low end for the shorter span lengths investigated in the current study. The spacing, S, for the 5 and 6 girder bridges is 7.75 ft and 6.2 ft, respectively. The applicable range for girder type "c" is from 7 to 13 feet. For the concrete deck on multiple steel girders option, the ratio N_L/N_b must be greater than 0.5 or less than 1.5. N_L/N_b for the FRP U-girder bridges in the current study ranges from 0.2 to 0.33. To increase the overall stiffness of the bridge (and minimize deflections) it may ultimately make more sense to fill the entire FRP U-girder with concrete. Due to the relatively low "E" value for the FRP, a concrete filled U-girder would behave more like a traditional reinforced concrete T-beam.

A comprehensive evaluation of AASHTO distribution factors for all span lengths and all girder spacing combinations is beyond the scope of the current study. Nonetheless, some validation work is necessary to provide more confidence in the AASHTO DFM for FRP U-girders. The bridge configuration and cross-section geometry chosen for validation purposes was based on the results obtained for the 50-ft span length using the FEA optimization framework (SS-2).

AASHTO distribution factors were computed for interior and exterior girders using the relationships from LRFD-7 Table 4.6.2.2.2.b-1 and Table 4.6.2.2.2.d-1, respectively. No concrete was present in the U-girder under the slab. The K_g term for the unfilled U-girder was 56,890 in^4, which is within the acceptable range for interior girders assuming a type “e” cross-section in Table 4.6.2.2.2.b-1. For the exterior girders, the lever rule was used to compute the distribution factor for the one-lane-loaded (1LL) case (0.526). The AASHTO distribution factor computed for the exterior girder with two-lanes-loaded (2LL) was less than the value obtained for the interior girder, so the interior girder value was used for both cases (0.493). The distribution factor for the interior girder, 1LL, was 0.378.

AASHTO distribution factors are compared with results from FE modelling in Figure 98. The FEM results were obtained by running a series of models where the lateral position of the truck and lane loading were repositioned at 6 inch intervals from the centerline of the bridge until the lane reaches the traffic barrier Figure 96(A and B). Barriers were not included in the FE modeling and stress results that obtained for the one-lane-loaded case were multiplied by 1.2 to account for multiple presence effects. This allows for a direct comparison with the AASHTO distribution factor for one-lane-loaded, which already contains the effects of multiple presence. For each load case, the maximum stress was extracted along the extreme tension fiber of each girder. The corresponding single-girder bending moment required to generate this stress was determined using the moment of inertia and distance to the neutral axis for a single girder acting in composite action with the cast-in-place RC slab. The distribution factor was then determined for each girder by dividing this bending moment result by the maximum bending moment that would generated in a simply supported beam subjected to the uniform distributed lane loading and a single truck positioned as shown in Figure 97. For the interior girders, the value reported in the graph reflects the maximum value for all interior girders. The change in slope around X = 40 inches occurs when the interior girder that experiences the maximum bending moment changes from the girder centered at X=34.7 inches to the girder centered at X = 104.1 inches.

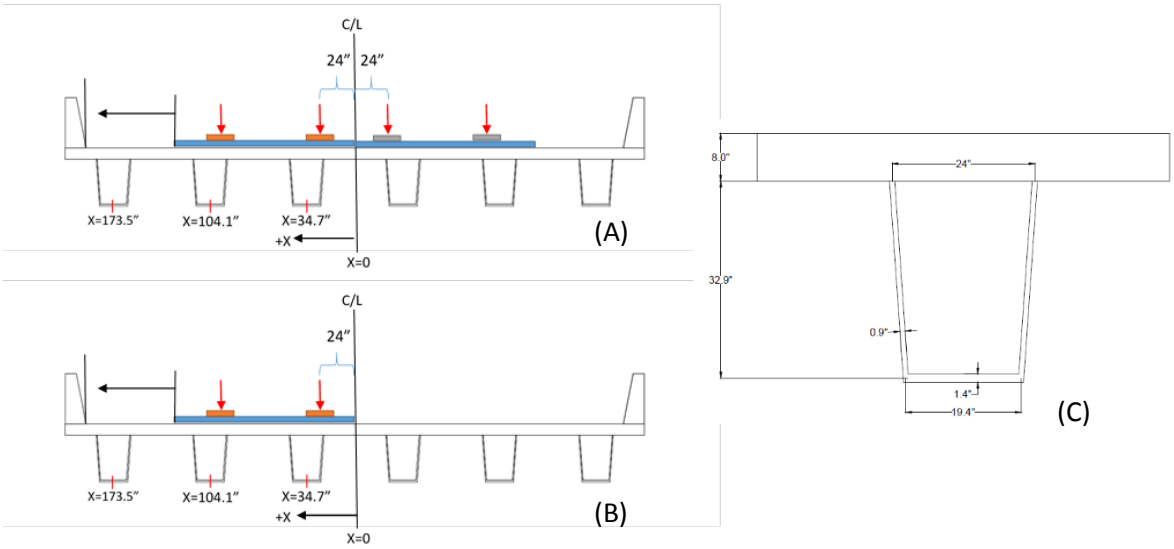

Figure 96. Lateral vehicle and lane pressure positioning for AASHTO distribution factor validation. (A) Two lanes loaded, (B) One lane loaded, and (C) Cross-section dimensions. Barriers are shown for reference only and were not considered in the FE model.

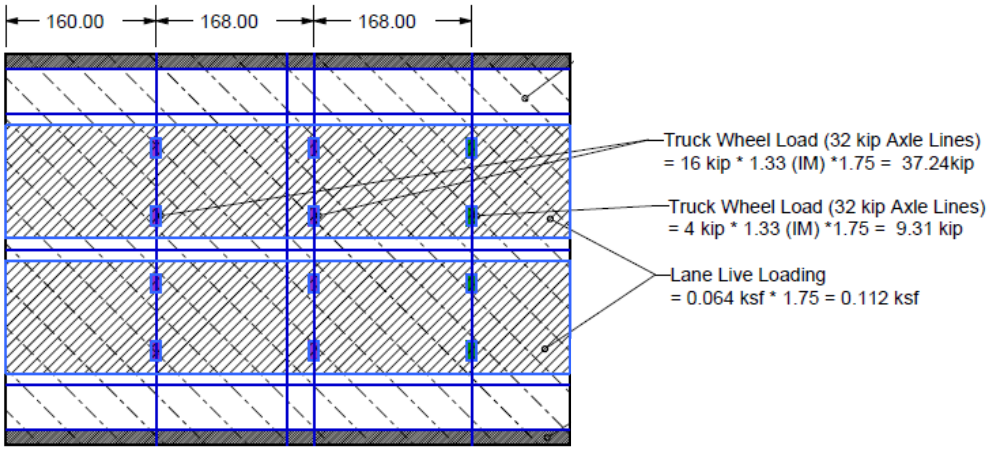

Figure 97. Longitudinal vehicle positioning for 50-ft span length, Limit State 4a (flexural strength)

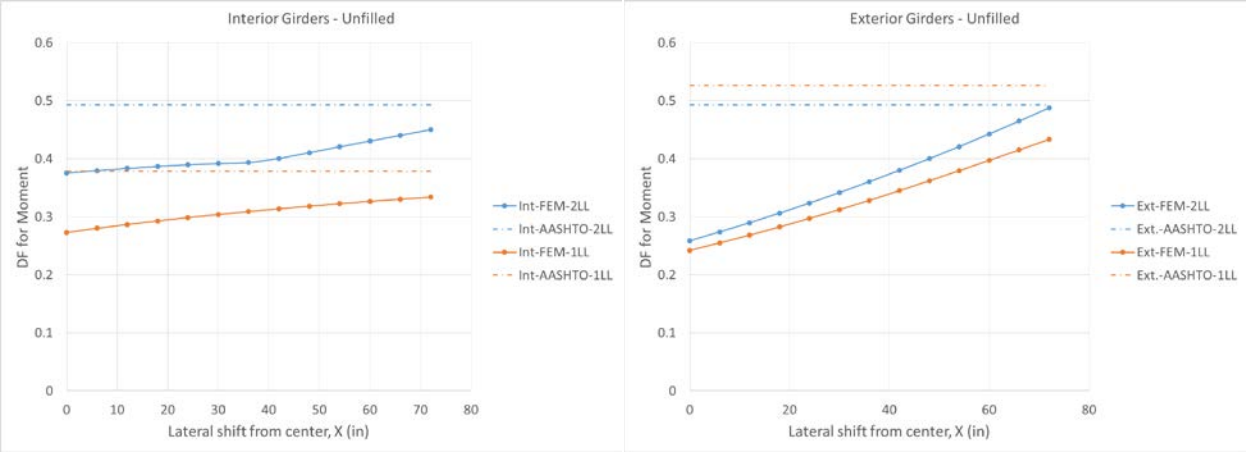

Figure 98. Distribution factor results comparing FEM to AASHTO distribution factors

Overall, the AASHTO distribution factor method generates results for the unfilled girders that are still conservative. Repeating the process for concrete-filled FRP U-girders could be done, but the behavior should be very similar to traditional reinforced concrete T-beams.

10.Concrete-Filled FRP Tubes (CFFT)

Evaluation of the CFFTs followed a procedure that was very similar to what was described for the FRP U-girders using the AASHTO distribution factor method (Section 9.1). The AASHTO LRFD-FRP document does contain provisions for evaluating the moment and shear capacity of a CFFT that assumes no composite action with any surrounding structural elements. For the case of flexure, this is likely to result in CFFT elements with very high material costs. The methodology used in the current study for evaluating the flexural capacity of CFFTs assumes composite action with the cast-in-place RC deck and follows a procedure that is similar to that used by Burgueno in the design of the King's Stormwater Channel CFFT girder bridge in California. The limit state criteria established for the FRP U-girders also applies directly to this alternative. Shear strength evaluation was performed using the proposed FRP shear strength methodology described in Section 8.1.5.7.

10.1 Cross-section Design and Optimization

The general bridge geometry and loading parameters required to begin the design and optimization process are provided in Figure 99. Girder size parameters and FRP material properties are provided in Figure 100. For the current study, the width of the cast-in-place shear key was assumed as 75% of the outer FRP tube diameter and the distance to the center of the FRP tube from the bottom of the RC slab will be taken as 1.25 times the outer FRP tube radius. The FRP material properties are the same as those used for the FRP U-girder designed using the AASHTO distribution factor method (E-LT 4400, balanced 0/90 with properties described in Table 25).

The number of CFFT girders present in the bridge for the current study was limited to N_b=6 and N_b=8. Preliminary results that included more girders (up to 12) displayed a similar trend to what was observed for the FRP U-girder option. As the number of girders increases, the overall cost of the girders also increases. N_b=6 and N_b=8 provides a reasonable girder spacing for the 32-ft-wide clear roadway width that should be accommodated with an 8 inch thick RC slab.

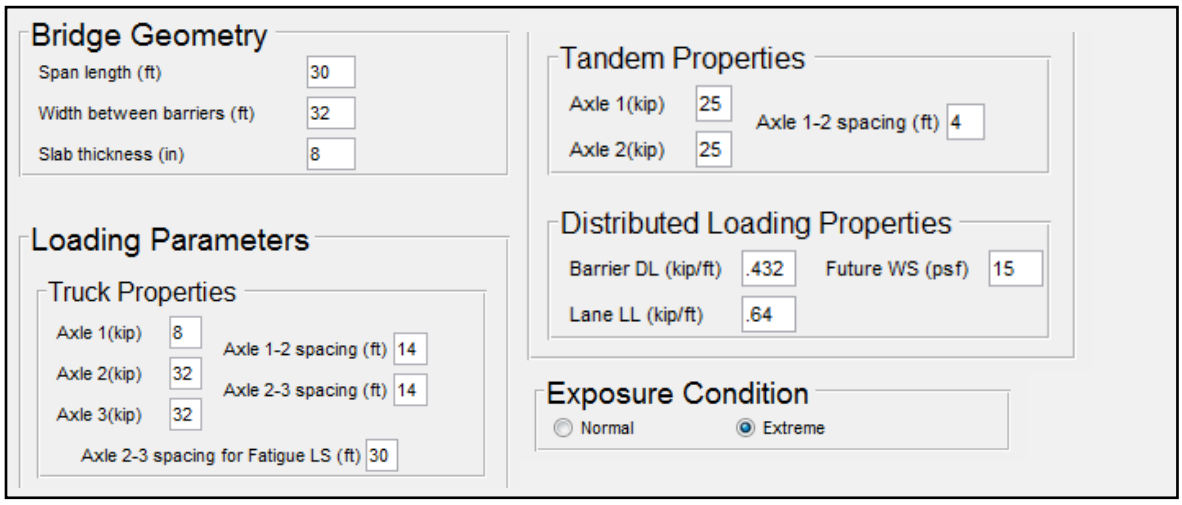

Figure 99. Required inputs for bridge geometry and loading parameters

For each span length and each specified number of girders present in the bridge cross-section, the FRP tube diameter was increased from 10 inches to 60 inches in 2 inch increments. For each tube diameter that was considered, the required FRP thickness was determined for each limit state.

Deflections were calculated assuming that all girders experience the same deflection. The concrete inside the tube was considered when determining the overall stiffness of the bridge. In the current study, the presence/absence of barriers was not considered and all deflection calculations were made assuming that the barriers did not contribute to the overall stiffness of the bridge. This scenario most closely resembles Limit State 2-c (Section 8.1.2) comparison to the FRP U-girders designed using the AASHTO distribution factor method.

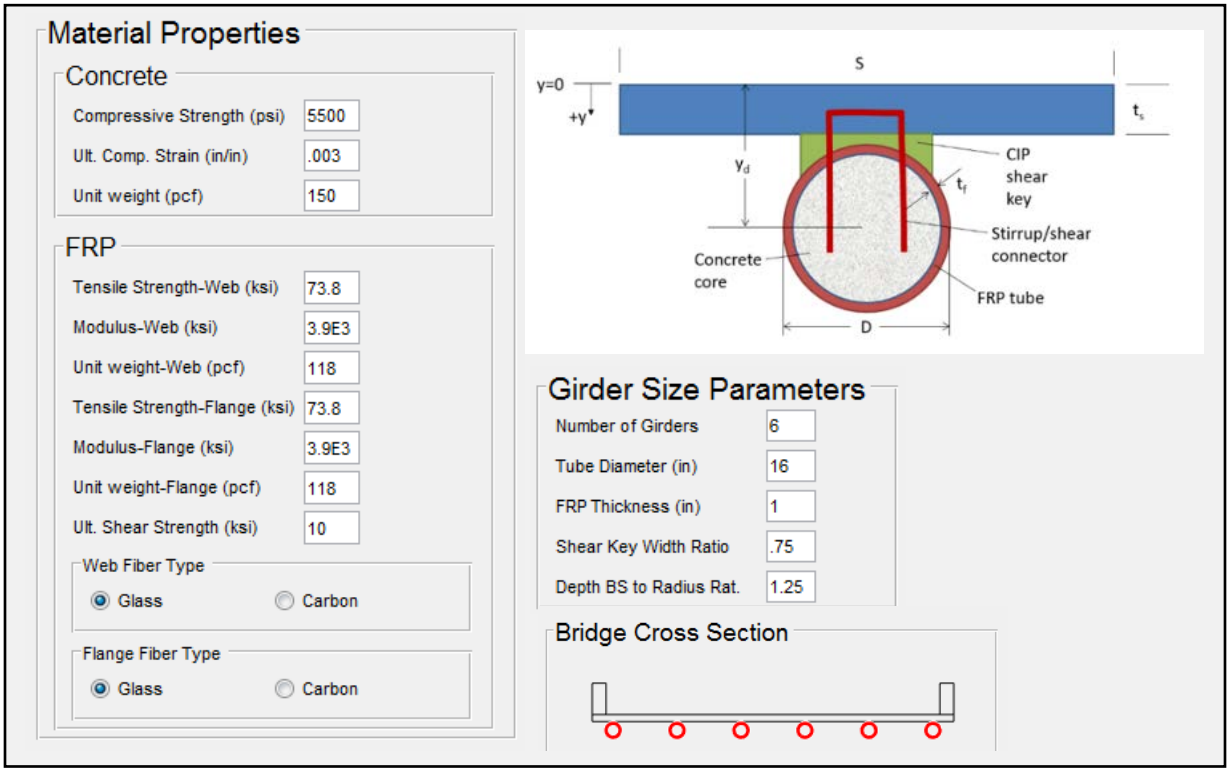

Figure 100. Required inputs for material properties and girder size parameters.

10.2 Results Summary for all Span Lengths

The required FRP thickness and total girder cost as a function of FRP tube diameter is provided for all span lengths in Appendix A. A summary of the optimal values for the N_b=6 and N_b=8 girder configurations is provided in Table 64. Quantities shown in Table 64 are presented graphically in Figure 101.

Table 64. CFFT optimization results summary for all span lengths. No barriers, stiffness of concrete inside FRP tube included in deflection criteria.

Span length	Controlling limit state	D (in)	t_{frp} (in)	FRP weight (lbf)	Total girder cost ($)	Girder cost per foot ($)	Girder cost per SF of bridge deck ($)
N_b = 6							
30 ft	LS-4b	12	1.74	8,288	45,753	254	48
40 ft	LS-1/4b	16	1.41	12,672	73,701	307	58
50 ft	LS-1/3	24	1.01	18,000	119,380	398	75
60 ft	LS-1/3	30	1.14	30,612	208,200	578	108
75 ft	LS-1/3	42	1.35	63,404	452,320	1005	188
N_b = 8							
30 ft	LS-4b	12	1.31	8,670	49,141	204	51
40 ft	LS-1/4b	18	0.91	12,780	81,494	255	64
50 ft	LS-1/3	26	0.78	20,278	147,500	369	92
60 ft	LS-1/3	32	.98	37,380	270,710	564	141
75 ft	LS-1	46	1.35	93,400	683,540	1139	285

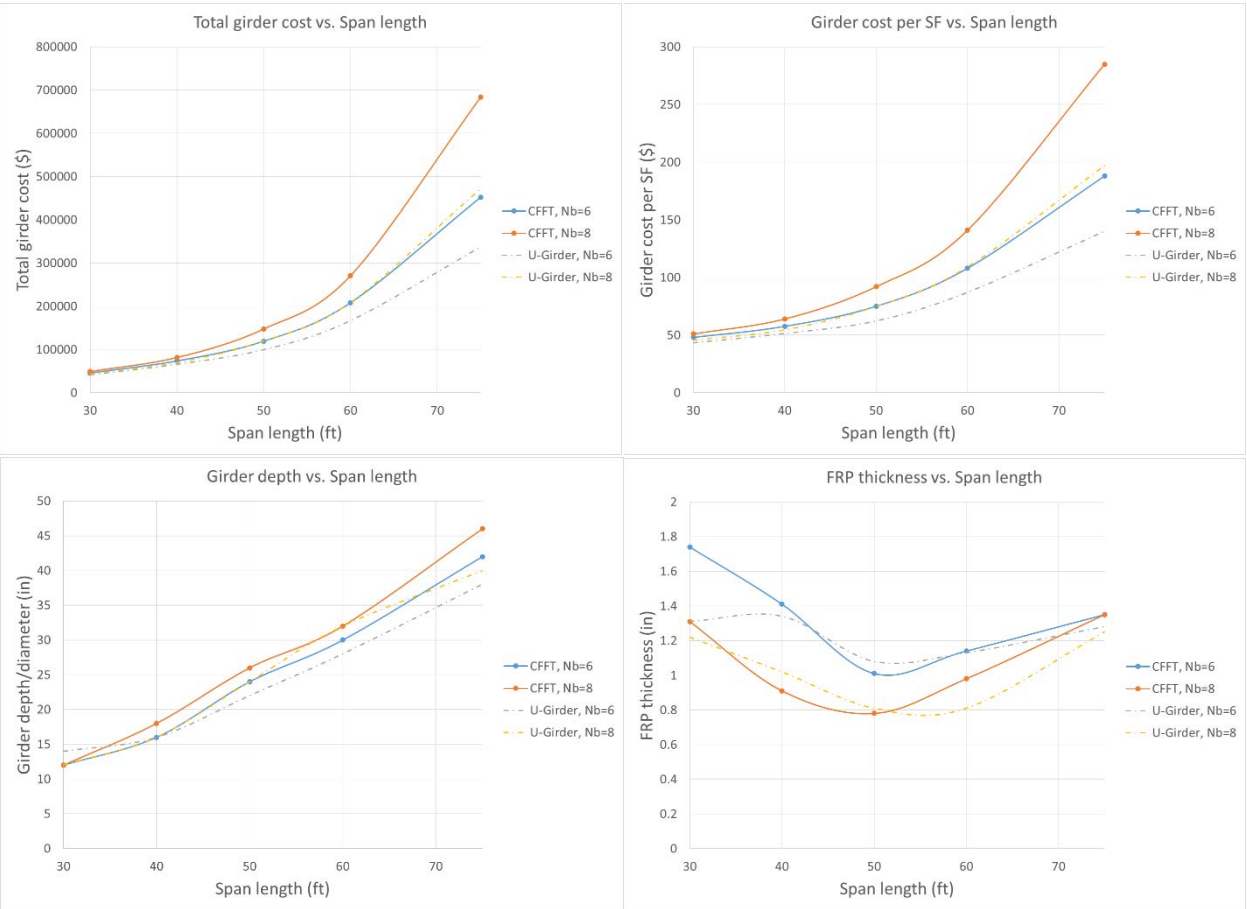

Figure 101. Optimization results for CFFT bridge girders using the AASHTO distribution factor method.

11. Strongwell DWB-36

Evaluation of the Strongwell DWB-36 was intended to serve as a representative case study for pultruded FRP bridge girders. Extensive research was completed for this alternative in the late 1990's and early 2000's at Virginia Tech. This research culminated in the installation of two Strongwell DWB bridges in Virginia. The Tom's Creek bridge used the shorter DWB-8 (8-inch depth) sections for a span length of 18 ft while the Dickey Creek bridge used the DWB-36 to span 39 ft (Figure 102). Both bridges utilized a laminated timber deck. The goal of the current evaluation is to investigate the impact of incorporating a reinforced concrete deck with full composite action. The per foot cost of these girders is relatively high compared to other FRP options (140$/ft for the DWB-8 and 600$/ft for the DWB-36). If the total number of girders for a given span length can be reduced, a significant cost savings might be achieved.

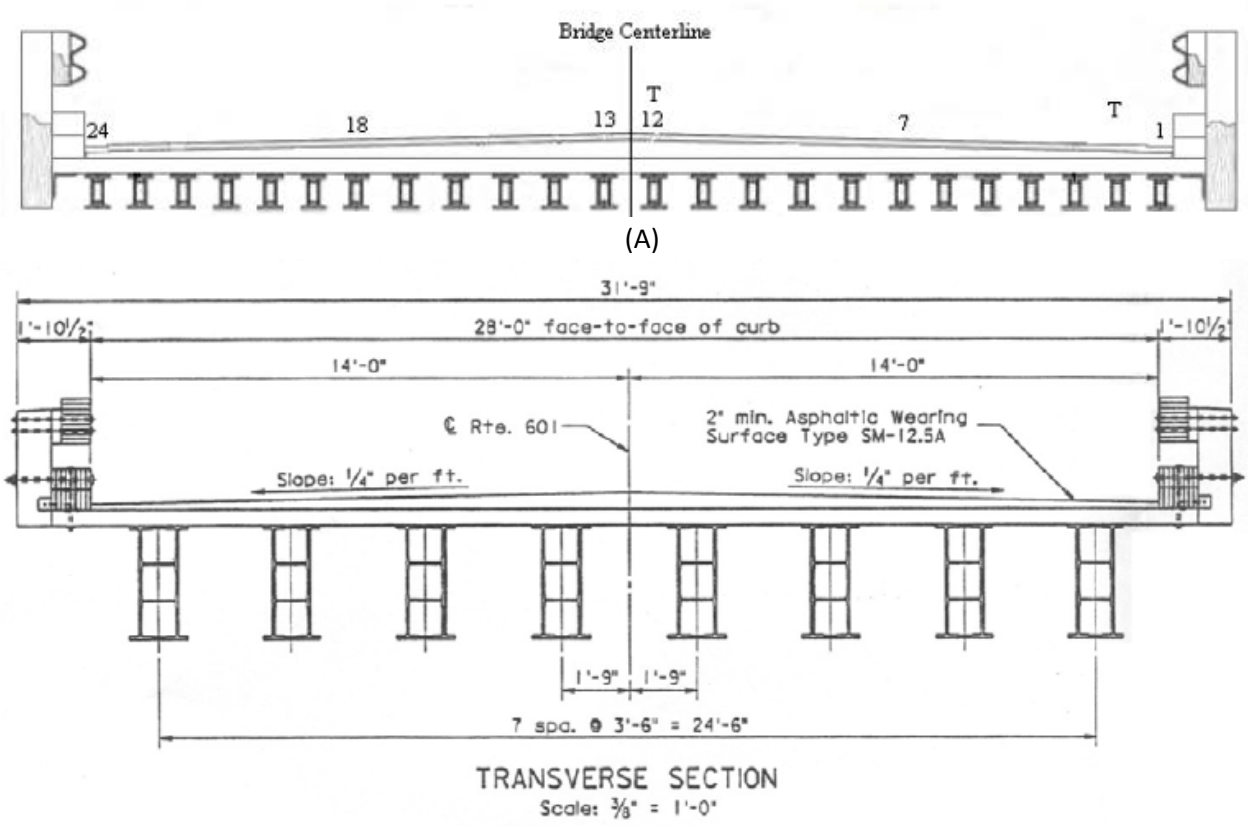

Figure 102. Previous applications of Strongwell DWB pultruded bridge girders. (A) Tom's Creek bridge and (B) Dickey Creek bridge, Rt. 601, Sugar Grove, VA.

11.1 General Analysis Framework

The strategy for evaluating this alternative focused on determining the minimum number of DWB-36 girders that are required to meet the L/1000 deflection criteria described by Limit State 2. Span lengths of 30 ft, 40 ft, 50 ft, 60 ft, and 75 ft were investigated. The finite element software ANSYS was used to model the girders and bridge deck geometry. Cast-in-place reinforced concrete barriers were included in the current study. This was intended to represent a "best-case scenario" under which the DWB-36 girders might be able to meet the deflection requirements.

If the equal deflection for all girders assumption of LRFD-7 S2.5.2.6.2 is adopted, a simple cross-section analysis of the bridge using the published values for moment-of-inertia for each girder and the geometric properties of the slab could be used to determine the number of girders required to achieve the desired global stiffness. One issue that this would not address, however, are the shear deformations that the DWB-36 girders will experience. For traditional materials, like concrete and steel, the shear modulus is typically high enough to neglect the deformations due to shear (G_{steel} = 10.9 Msi, and $G_{concrete}$ = 3.0 Msi). For FRP composites, however, the shear modulus tends to be much lower (~ 0.6 Msi). The FE model will also incorporate the torsional rigidity of each girder, which is also affected by the shear modulus. Complete orthotropic material properties for FRP used to model the DWB-36 girders are provided in Table 65. Concrete material properties for the RC deck are provided in Table 66.

A mesh convergence study was completed to ensure that enough elements were used to accurately model the behavior of the bridge. Results from the convergence study (Table 67) indicated that a maximum element size of four inches would be sufficient. The RC deck was modeled using 3-D solid brick elements and the DWB-36 bridge girders were modeled using 2-D plate elements.

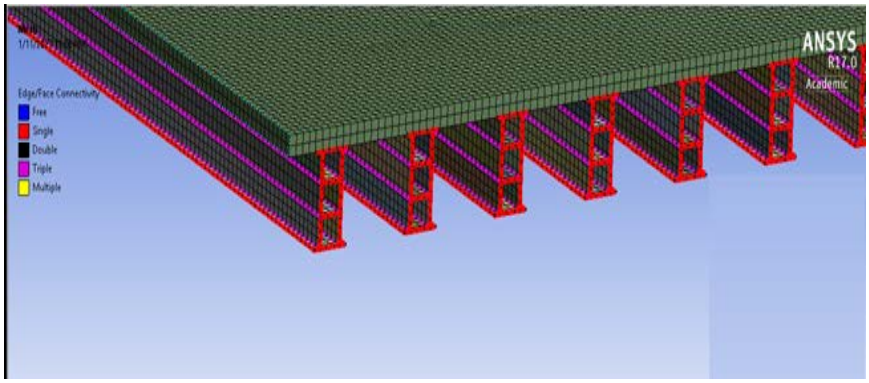

Figure 103. Finite element mesh for DWB-36 bridge girder study.

Table 65. Orthotropic Material Properties for DWB-36 bridge girders

Properties	Value	Unit
Unit weight	105	lbf/ft^3
Young's Modulus X Direction	5.76E+06	psi
Young's Modulus Y Direction	1.69E+06	psi
Young's Modulus Z Direction	1.00E+06	psi
Poisson's Ratio XY	0.3	
Poisson's Ratio YZ	0.3	
Poisson's Ratio XZ	0.3	
Shear Modulus XY	6.00E+05	psi
Shear Modulus YZ	6.00E+05	psi
Shear Modulus XZ	6.00E+05	psi

Table 66. Concrete Material Properties.

Properties	Value	Unit
Unit weight	150	lbf-ft^{-3}
Young's modulus	4.51E+06	psi
Poisson's ratio	0.3	

Table 67. Convergence study results.

Max. Element Size (in)	# of Elements	Max. Deflection (in)	Max. Compressive Stress (psi)
Default	22752	0.814	-575.3
12	22576	0.814	-585.43
10	28558	0.815	-587.93
8	37692	0.816	-586.26
6	67946	0.820	-589.06
4	155092	0.821	-589.28

11.2 Results Summary for all Span Lengths

A separate FE model was generated for each span length. The number of girders included in the model for each span length was also varied (4, 6, 8, and 10) and the maximum deflection due to the design truck (including impact) was extracted. The entire process was repeated using isotropic and orthotropic material properties for the DWB-36 girder. A typical deflected shape result for the 40-ft span length is provided in Figure 105.

Deflection results for the orthotropic material case are provided in Table 68. For the 30-ft span length, the four girder bridge results in a deflection of 0.24 in. During subsequent analysis of the FRP U-girders, it was determined that for a 30-ft span length the barriers alone are almost capable of providing enough stiffness to meet the L/1000 deflection criteria assuming that all girders deflect equally. As long as the barriers are included, it isn't surprising that four girders are sufficient for the 30-ft span length. Four girders are also sufficient for the 40-ft span length. For the 50-ft span length, the four girder option no longer satisfies the L/1000 deflection criteria. The five-girder alternative was not explicitly evaluated in the current study, but it would likely be sufficient for the 50-ft span. At 60 ft, six girders are required, and at 75 ft, a total of 9 girders are required. It is possible to use the curves provided in Figure 104 to approximate the number of girders required for any span length between 30 ft and 75 ft. To remain conservative for the current initial evaluation, the number of girders corresponding to the results highlighted in green in Table 68 were used to evaluate the remaining limit state criteria.

Table 68. Deflection results using orthotropic material properties

Material Properties	Span (ft)	Allowable L/1000 (in)	# of Girders			
			10	8	6	4
G=0.6x10^6 psi	30	0.36	0.10	0.12	0.16	0.24
E_x=5.76x10^6 psi	40	0.48	0.19	0.23	0.29	0.41
E_y=1.69x10^6 psi	50	0.6	0.33	0.39	0.48	0.65
E_z=1.00x10^6 psi	60	0.72	0.50	0.58	0.70	0.92
Poisson's Ratio=0.3	75	0.9	0.82	0.94	1.12	1.42

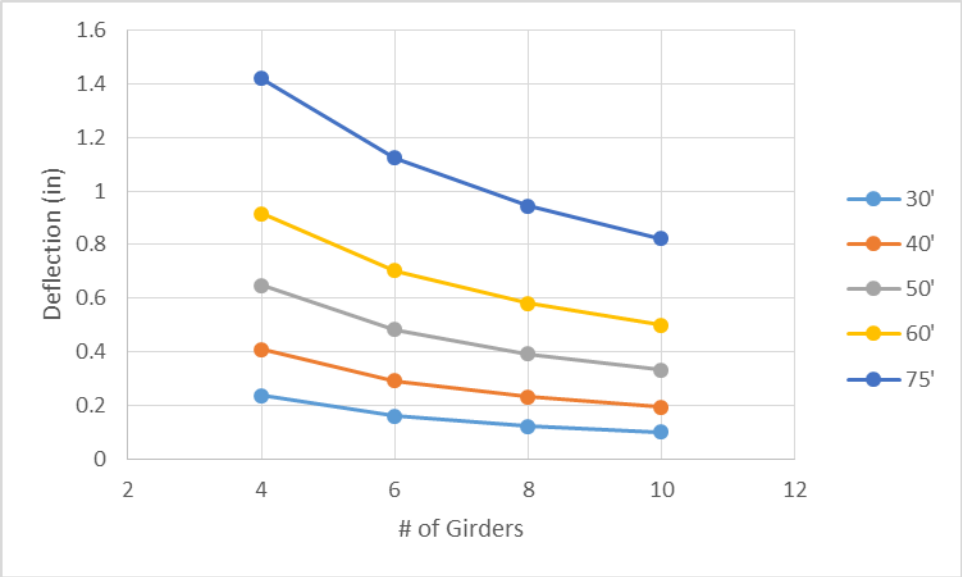

Figure 104. Maximum deflection results for orthotropic material properties.

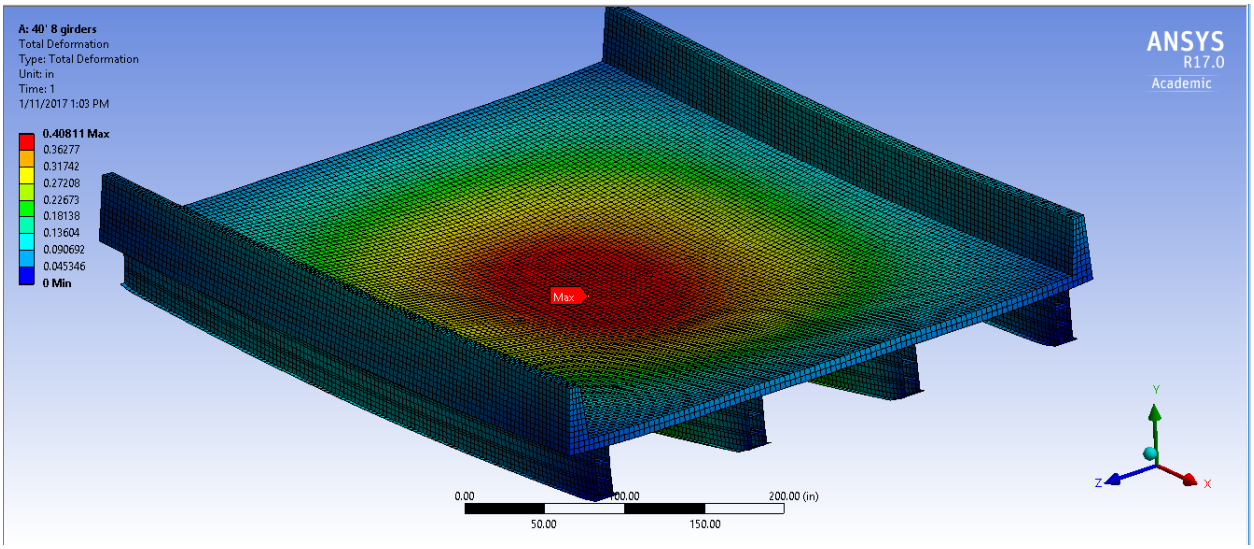

Figure 105. Deflected shape result for 40-ft span, N_b = 4, Limit State 2 (deflections).

Results using the isotropic material property assumption are provided in Table 69. It should be noted that for the isotropic material formulation, the shear modulus is determined by the specified value of modulus of elasticity, E, and Poisson's ratio. The resulting shear modulus, 2.22 Msi, is significantly larger than the typical value of 0.6 Msi for FRP composites. As expected, the resulting maximum deflections are less than the orthotropic case.

Table 69. Deflection results using isotropic material properties

Material Properties	Span (ft)	Allowable L/1000 (in)	# of Girders			
			10	8	6	4
G=2.215E+6 psi	30	0.36	0.07	0.08	0.10	0.15
E=5.76x10^6 psi	40	0.48	0.15	0.18	0.22	0.31
/	50	0.6	0.27	0.32	0.40	0.54
/	60	0.72	0.43	0.51	0.61	0.81
Poisson's Ratio=0.3	75	0.9	0.75	0.86	1.03	1.31

Once the number of girders needed to meet the deflection limit state requirements was determined for each span length, a new round of FE modeling was completed to ensure that the proposed girder configurations also satisfy the remaining limit state criteria. Barriers were not included in these models.

Critical stress results for each limit state are provided in Table 70 through Table 73. One remaining challenge is to determine an appropriate stress criteria for each limit state. The DWB-36 is a hybrid GFRP/CFRP cross-section with carbon fiber present in the flanges (and presumably experiencing the maximum tensile stress for Limit States 3 and 4a) and glass fiber present in the webs. The unidirectional tensile strength of the these pultruded CFRP tows could easily exceed 120 ksi. Even after applying the environmental reduction factor, C_E, and strength resistance factor, ϕ, the stress values obtained for LS-3 and LS-4a are still extremely conservative. The challenge, however, is determining what stress levels might be realized in the tension flange before some other failure occurs on the cross-section. Flexural testing of full-scale DWB-36 specimens revealed that the compression flange was susceptible to buckling and delamination at the CFRP and GFRP interface (Figure 106). For the current study, we are assuming that the RC deck and FRP bridge girder are perfectly bonded. This would minimize the tendency for flange buckling to occur on the actual bridge. Nonetheless, it seems unlikely that the GFRP will be capable of fully developing the CFRP tensile strength without experiencing some type of delamination failure on the cross-section (Figure 107).

At this point, the stress results obtained for the remaining limit states can be considered low enough to proceed with a preliminary cost evaluation of this alternative. But significant research would still be needed to establish the shear connection between the RC deck and the girder and then fully characterize the behavior of the composite section. It should also be noted that if composite action between the DWB-36 and the RC deck is desired, the large flange area at the top of the beam should probably be reconfigured. Additional discussion on establishing a shear connection with FRP bridge girders is provided in Section 12.2.

(A) (B)

Figure 106. Four-point bending test of DWB 36. (A) Laboratory setup and (B) failure in compression flange at loading point.

Figure 107. Delamination between quasi-isotropic glass and carbon/CSM laminates during laboratory beam test of 36x18 EXTREN DWB. Section was taken away from rupture zone at midspan.

Table 70. DBW-36 stress results for Limit State 1 (concrete compressive stress)

Span(ft)	Number of girders	Stress result (psi)	Allowable stress (psi)
30	4	-920.79	-2475
40	4	-1207.6	-2475
50	6	-1144	-2475
60	8	-1303.8	-2475
75	10	-1620.7	-2475

Table 71. DBW-36 stress results for Limit State 3 (fatigue and creep rupture)

Span(ft)	Number of girders	Stress result (psi)
30	4	2113.5
40	4	3347.5
50	6	3322.2
60	8	3484.2
75	10	4396.7

Table 72. DBW-36 stress results for Limit State 4a (flexural strength)

Span(ft)	Number of girders	Stress result (psi)
30	4	5465.8
40	4	8189.5
50	6	7910.2
60	8	8152.6
75	10	9401.9

Table 73. DBW-36 stress results for Limit State 4b (shear strength)

Span(ft)	Number of girders	Stress result (psi)
30	4	2414.4
40	4	2248.9
50	6	2042
60	8	1433.6
75	10	1900

12. Alternatives Analysis

After reviewing the literature and investigating the status of existing FRP bridges that meet the span length requirements for the current study (30 ft to 75 ft), three viable alternatives were chosen for further exploration and validation in Task 2:

- FRP U-girder
- Concrete-filled FRP tube (CFFT)
- Strongwell DWB (pultruded FRP bridge girder)

The FRP materials used to construct each girder type are similar for the different alternatives. However, each alternative represents a unique fabrication process that is subject to specific limitations. Furthermore, placing each girder at the bridge site and forming the reinforced concrete deck in such a way that composite action can be achieved also presents specific challenges. The goal of the current section is to compare the alternatives with respect to these issues as well as offer some general guidance regarding expected maintenance requirements and overall expected service life

12.1 Materials and Manufacturing Costs

12.1.1 FRP U-girder

Two FRP composite parts manufacturers with experience in VARTM/VIP parts production were consulted for the current study. Each manufacturer was provided with the cross-section dimensions and material requirements for a 30-ft and 75-ft bridge girder (details in Table 47 and Table 55). After discussing the general requirements and overall objectives of the current study, the following information was obtained:

1. Thickness requirements of 1.5 inch to 2 inch do not pose a major concern for modern vacuum infused composite parts.
2. The girder length requirements from 30 ft to 75 ft could be accommodated in the current facilities of both manufacturers.
3. Tooling costs would depend on the number of parts that would be needed from each mold. One manufacturer estimated about $100 per foot for a durable, metal tool that would support multiple bridge projects. If only five or six girders were being fabricated for a single job, the cost could be reduced considerably by using a wood mold. The specific cost of tooling was not determined.
4. Material costs (non-crimp fabric fiber and vinylester resin) were quoted between $3.00 and $3.50 per pound.
5. Labor and facilities costs were typically 50% of the total material costs.
6. The price per pound of finished FRP U-girder ranged from $5.25 to $5.75.

12.1.2 CFFT

The CFFT tubes used in the King's Stormwater Channel bridge in California were fabricated using a filament winding method. Current fabrication techniques for the Concrete Arch Bridge System (CABS, formerly known as "Bridge-in-a-Backpack") relies on vacuum infusion (Figure 108). The tube is first inflated and then placed in a frame to achieve the desired arch. Next, a vacuum is drawn around the outside of the tube and resin is infused through the fibers. Once the resin cures (less than 24 hours later), the plastic peel ply is removed and the tube is ready for placement at the bridge site.

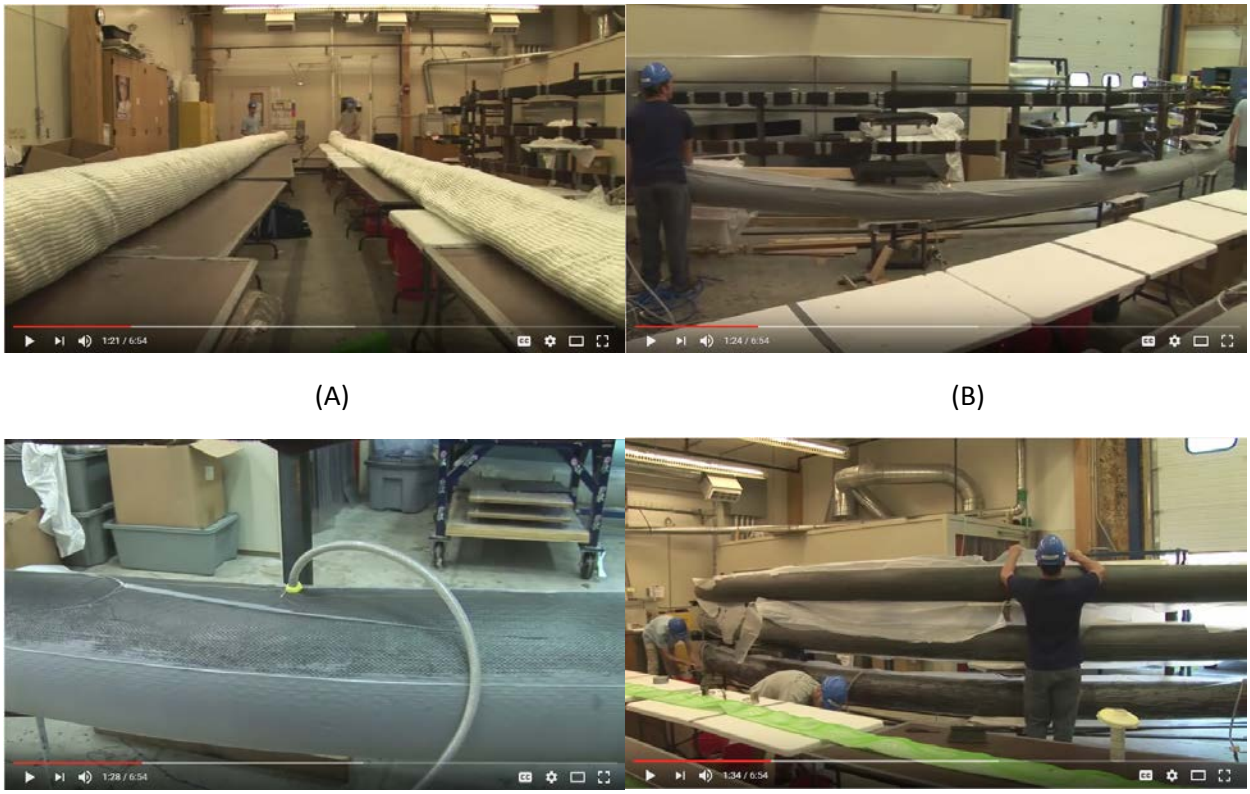

(A) (B)

(C) (D)

Figure 108. Fabrication process for CFFT using vacuum-assisted resin infusion (VIP). (A) Tube inflation, (B) Arch formation, (C) Resin infusion, and (D) Peel ply removal.

One filament winding manufacturer was contacted for a quote. This was relatively early in the process and the overall CFFT geometry had not been finalized. The following conclusions were made from the exchange:

1. Thicknesses up to two inches can be accommodated.
2. This manufacturer was currently limited to 40-ft parts, but the custom filament wound FRP piping community could likely accommodate longer parts. Additional research is needed to determine if 75 ft is a feasible length for filament wound tubes with diameters up to 48 in.
3. The quoted price was highly dependent on the desired surface finish. The advantage of FRP bridge girder components is that the surface quality can generally be very low.
4. The quoted price for a 30-ft trial girder was approximately $4.00 per pound.

The primary advantage of filament winding is to create a tubular structure that consists of continuous fibers. The most common applications of filament wound tubes are thin-walled pressure vessels and other pipes which are often subjected to internal pressure. In these cases, the principal stresses in the hoop direction dominate and the overall winding angle sequence would tend to prefer fibers in the 90-degree or hoop direction. This is not necessarily the case for CFFT bridge girders. The longitudinal normal stresses and shear stresses tend to control the design, which would favor winding

angles between 0 and 45 degrees. From a mechanical winding standpoint, these angles would seem to be more difficult to achieve.

The possibility of using non-crimp fabric sheets that are rolled around a tube or other inflatable mold and then infused with resin would likely perform better in a flexural application than a filament wound tube. The fabric could be rolled out the entire length of the girder and then rolled onto a tube. Sheets can be added until the desired thickness is obtained. The fibers in the warp direction will remain continuous and then the fibers in the hoop direction can overlap to form shear splices. The discontinuities in the hoop direction should have minimal effect on the flexural performance. Some consideration would need to be given to the shear strength of an FRP tube fabricated in this manner, but there will be greater flexibility in the overall laminate stacking sequence.

12.1.3 Pultruded FRP Girder

The Strongwell DWB36 is a proprietary design. Strongwell quoted approximately $600 per foot for the carbon fiber flange version of the DWB36. The price was reduced considerably if only GFRP was used (~$350 to $400 per foot, or between $5 and $5.75 per pound). The per pound cost of the pultruded FRP bridge girder that contains carbon in the flanges is approximately $8.57. A quote was also obtained from another FRP pultruder for smaller angle sections (3”x3”x3/8”) using a vinylester resin. The cost per pound for these shapes was $5.24.

Another important consideration regarding manufacturing for pultruded FRP composites is that the DWB-36 represents the upper limit for the overall amount of material that can be pulled through a pultrusion die and formed into a usable cross-section. The pultrusion machine used to manufacture the DWB-36 was reported to be one of the largest in the country. Development of the tooling for the pultrusion die was also supported by a federally funded project. Costs for pultrusion dies of this magnitude were reported to be close to $500,000.

12.1.4 Direct Comparison: Materials and Manufacturing Costs

There are still several unresolved issues related to structural analysis and strength assessment that may result in modified material quantities. Variables that have been investigated in the current study but still require additional research and validation include:

- Deflection calculations and the stiffness contribution of concrete in the tension zone
- Shear strength of concrete-filled FRP U-girders and CFFTs
- Appropriate values for laminate shear strength for laminates that included +/- 45-degree plies

The assumptions made surrounding these unresolved issues were generally conservative. It may also be possible to reduce the total material requirements by optimizing the girder cross-section along each girder’s length. The results obtained thus far do provide a basis for comparison and decision-making about the most appropriate alternative for future research and development.

The final cost comparison for the three alternatives is provided in Figure 109. The FRP U-girder results were obtained using the AASHTO distribution factor method assuming a 100% stiffness contribution by the concrete beneath the slab. Both the CFFT and U-girder alternatives are based on a six-girder bridge. The number of girders for the DWB-36 varies. For all span lengths, the FRP U-girder

requires the least materials cost. As the span length increases, the difference between the U-girder and the other alternatives becomes more pronounced.

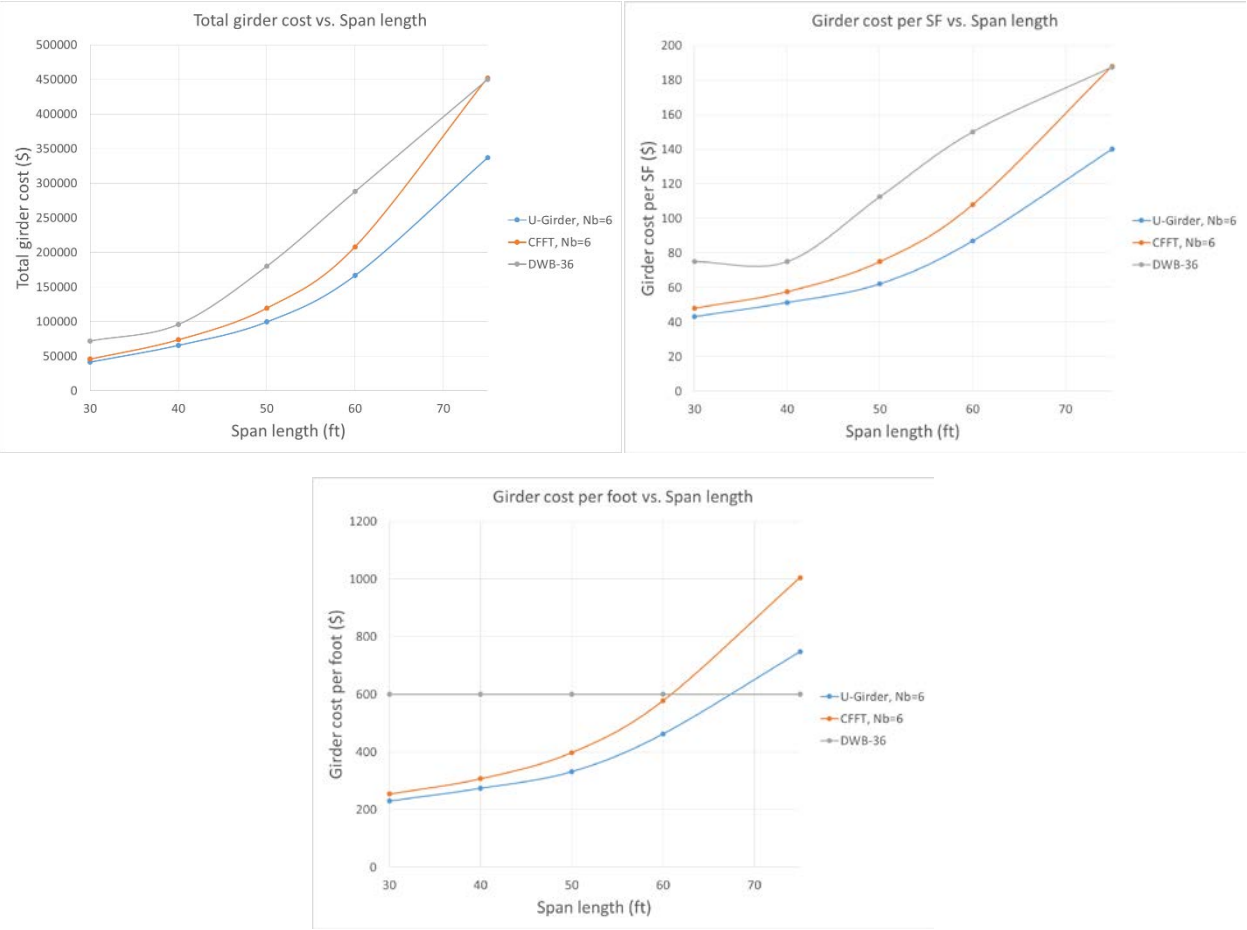

Figure 109. Final cost comparison for FRP U-girder, CFFT, and DWB-36.

12.2 Constructability

The following factors related to constructability were considered in the current study:

- Preparations for establishing shear connection
- Construction sequencing
  - Girder placement
  - Reinforcement for diaphragms and U-girders
  - Casting diaphragms and filling concrete in U-girders
  - Rebar placement for cast-in-place deck
  - Deck casting
  - Cast barriers and complete stem wall

Preparations for establishing the shear connection between the cast-in-place RC deck and FRP bridge girder refers to any work or extra consideration that must be given to the girder before it leaves the fabrication shop. This might include drilling holes or modifying the interior surface of the girder to

promote mechanical interlock between any cast-in-place concrete and the FRP. Only the most basic elements of construction sequencing are addressed in the current study.

One outstanding issue that needs to be resolved is whether or not traditional steel reinforcement will be used for the RC deck. With all of the experience that the FDOT is gaining with GFRP rebar, it might make sense to stay away from anything with the potential to corrode. Another option would be to use traditional plain reinforcing steel in the deck but also use stay-in-place formwork made of either FRP composite or galvanized metal that has been treated with a polymer coating on the soffit face (Figure 110) as described in FDOT Standard Specification 400-5.7 (2018).

If corrosion does occur in the reinforced concrete deck or the cast-in-place barriers, long-term durability of the entire bridge FRP-girder bridge could be jeopardized. In a traditional reinforced concrete structure, corrosion damage is repaired using the following general procedure:

1. The cracked and damaged concrete is removed to expose the corroded reinforcing steel. This typically requires minimal effort because the corrosion byproducts create a well-defined delaminated area that will detach easily from the structure.
2. Once the corroding bars are exposed, additional concrete must be removed from around the reinforcing bars to clean them thoroughly and to provide clearance for aggregates in the patching material. Removal of concrete around the circumference of the corroded rebar is considered critical to ensuring proper bond between the damaged bar and the repair patch concrete. This process requires jack-hammering or a high pressure water jet that may damage the surrounding structure if it is not done with care. Extra precautions would be needed if the underlying structure contained FRP composite materials, which are generally considered to be susceptible to impact damage.
3. After the bars are exposed and cleaned, formwork is attached to the structure and a patching concrete is poured to restore the original cross-section.

Figure 110. Rhino Dek stay-in-place formwork [131].

12.2.1 FRP U-Girder

12.2.1.1 *Preparations for Shear Connection*

A traditional girder to slab shear connection relies on metal studs that are either cast into a concrete structure or bolted/spot-welded onto the flanges of steel U-girders or I-beams. The FRP U-girder bridges in Texas utilized a horizontal stainless steel tube that was later surrounded by concrete when

the bridge deck was cast. One option that hasn't been thoroughly investigated involves creating a texture on the FRP surface that will enhance direct mechanical interlock between the FRP and the concrete. This concept is analogous to the rolled-on deformations in traditional reinforcing bars that enhance bond between the steel and concrete. A sample GFRP laminate was fabricated to validate the concept and the result is illustrated in Figure 111. A more aggressive textured profile was also created using leveling grout. If these deformations could be formed around the interior surface of the girder during the vacuum infusion process, the shear transfer would occur through the concrete over a large surface area along the entire length of the U-girder. Some experimental work is anticipated to validate the concept and also to determine the optimal profile of the textured surface.

In previous implementations of the FRP U-girder bridge, the top flange of the U-girder contains a 90-degree bend. In the Polish FRP bridge, holes were drilled through this top flange and metal bolts were used to establish the shear connection between the U-girder and the cast-in-place bridge deck. In the Texas bridges, the shear connection was established with stainless steel tubes. The current concept for the FRP U-girder involves projecting the U-girder approximately three inches into the cast-in-place deck and providing holes for the bottom layer of transverse deck reinforcement to pass through. These bars could either be grouted in using a supplementary adhesive or simply allowed to fill with concrete to aid in shear transfer. Additional holes will also be required on the ends of each girder to accommodate the reinforcement for the cast-in-place diaphragm at the bridge supports (Figure 112). These holes are intended to be pre-drilled as part of the fabrication process in the FRP manufacturing facility.

(A) (B)

Figure 111. Textured surface to enhance mechanical bond between FRP and concrete. (A) GFRP laminate and (B) levelling grout. AA battery included for size reference.

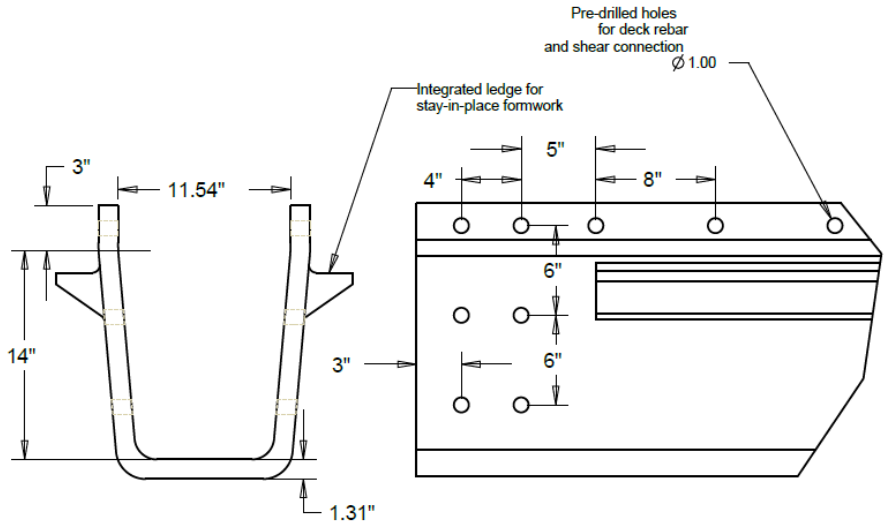

Figure 112. Pre-drilled holes for shear transfer, transverse deck reinforcement, and diaphragm reinforcement.

12.2.1.2 *Construction Sequencing*

The proposed construction sequencing for the FRP U-girders is illustrated in Figure 113 through Figure 119. These drawings assume that some type of stay-in-place formwork will be used for the cast-in-place deck. It may be desirable to include some type of integrated ledge that runs the length of the girder to support the stay-in-place forms during construction. A quote was obtained for 3”x3”x3/8” pultruded FRP angle, which could be bonded to the outside of the U-girder using a supplementary adhesive. The cost of this angle was approximately $10 per linear foot. This would add a total cost of roughly $20 per linear foot to the base cost of the girders. It may possible, however, to form this ledge using a dimensional lumber product and incorporate it into the girder during the infusion process.

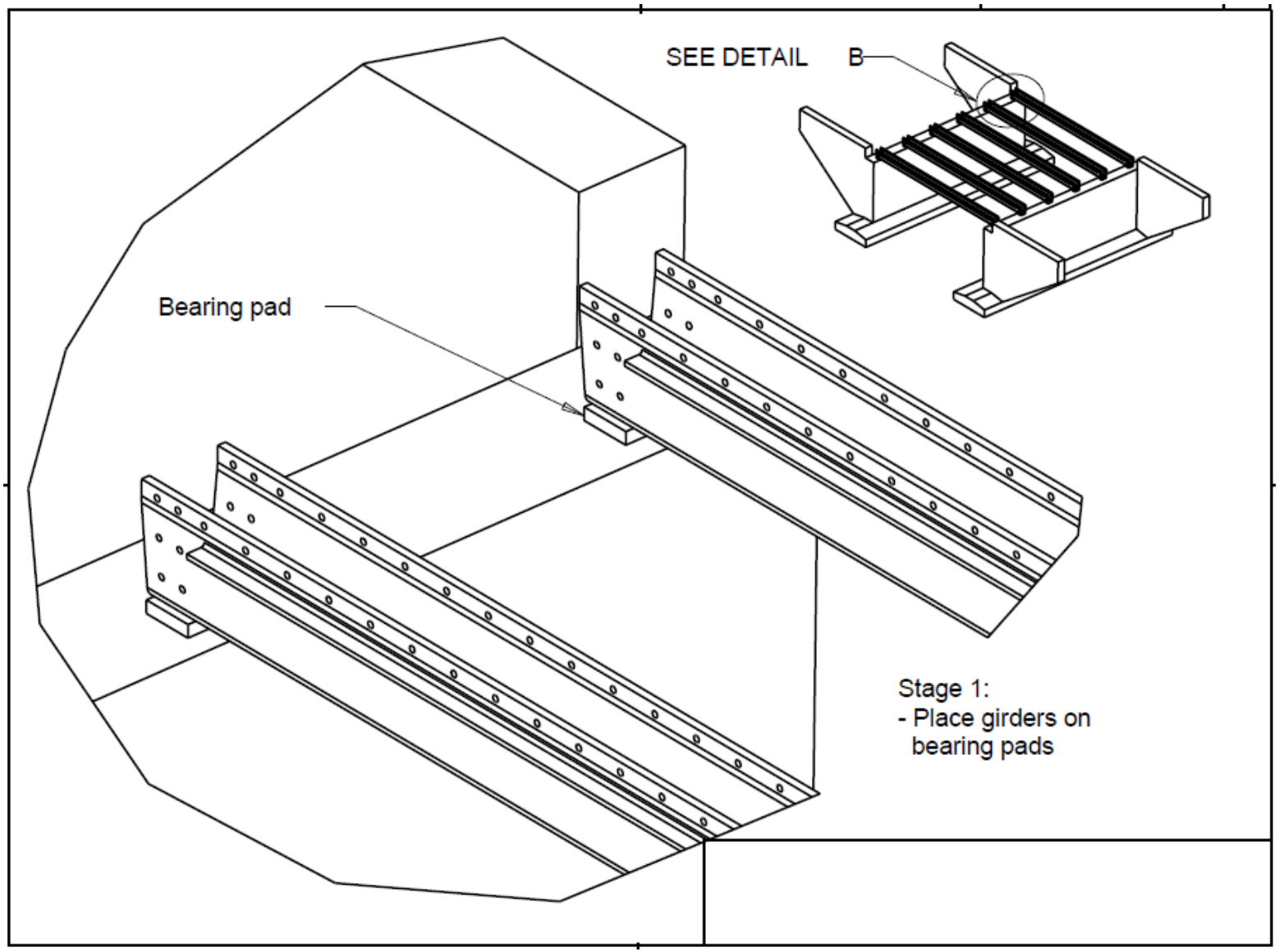

Figure 113. Girder placement

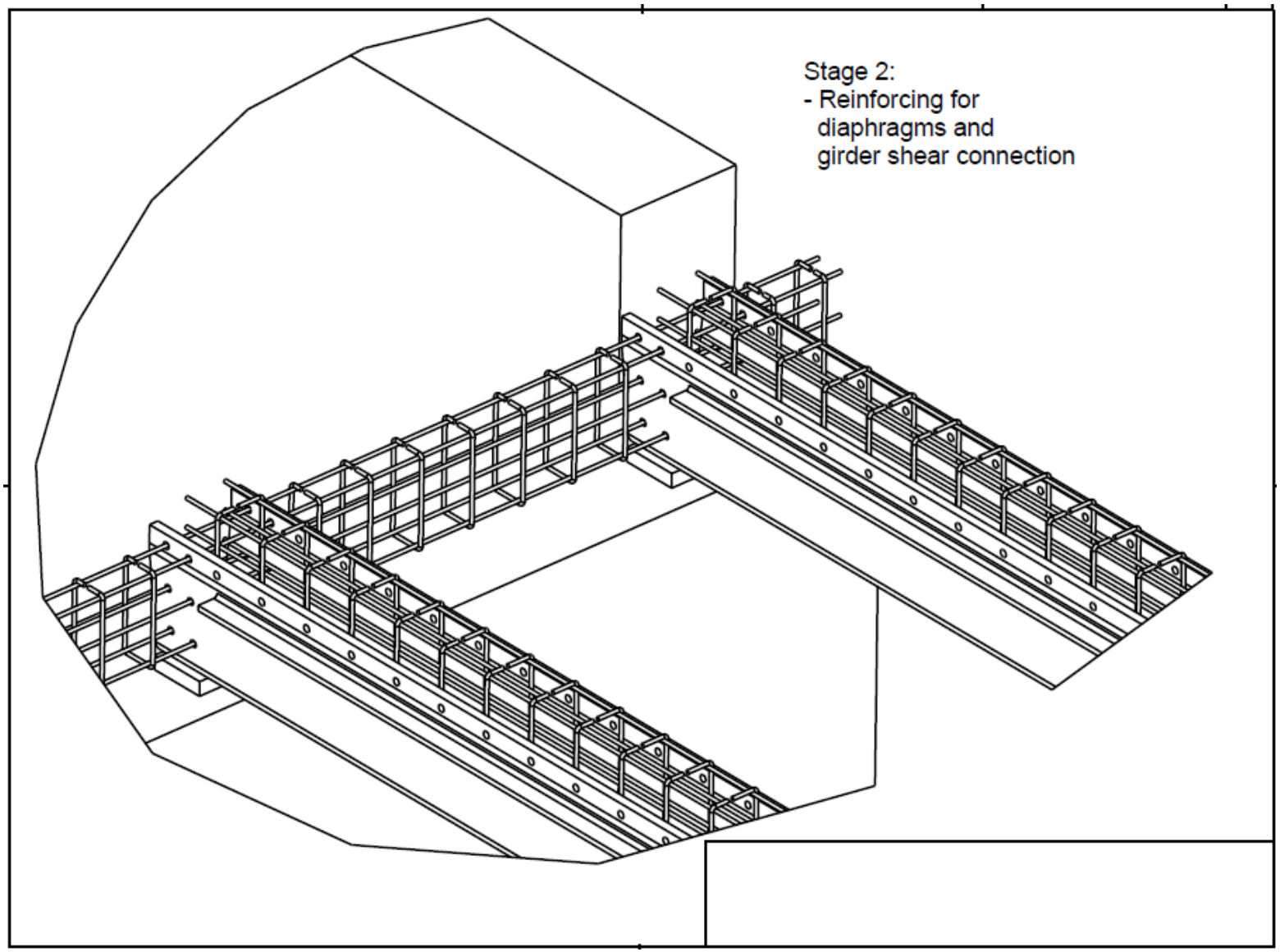

Figure 114. Reinforcement for diaphragms and concrete inside U-girder

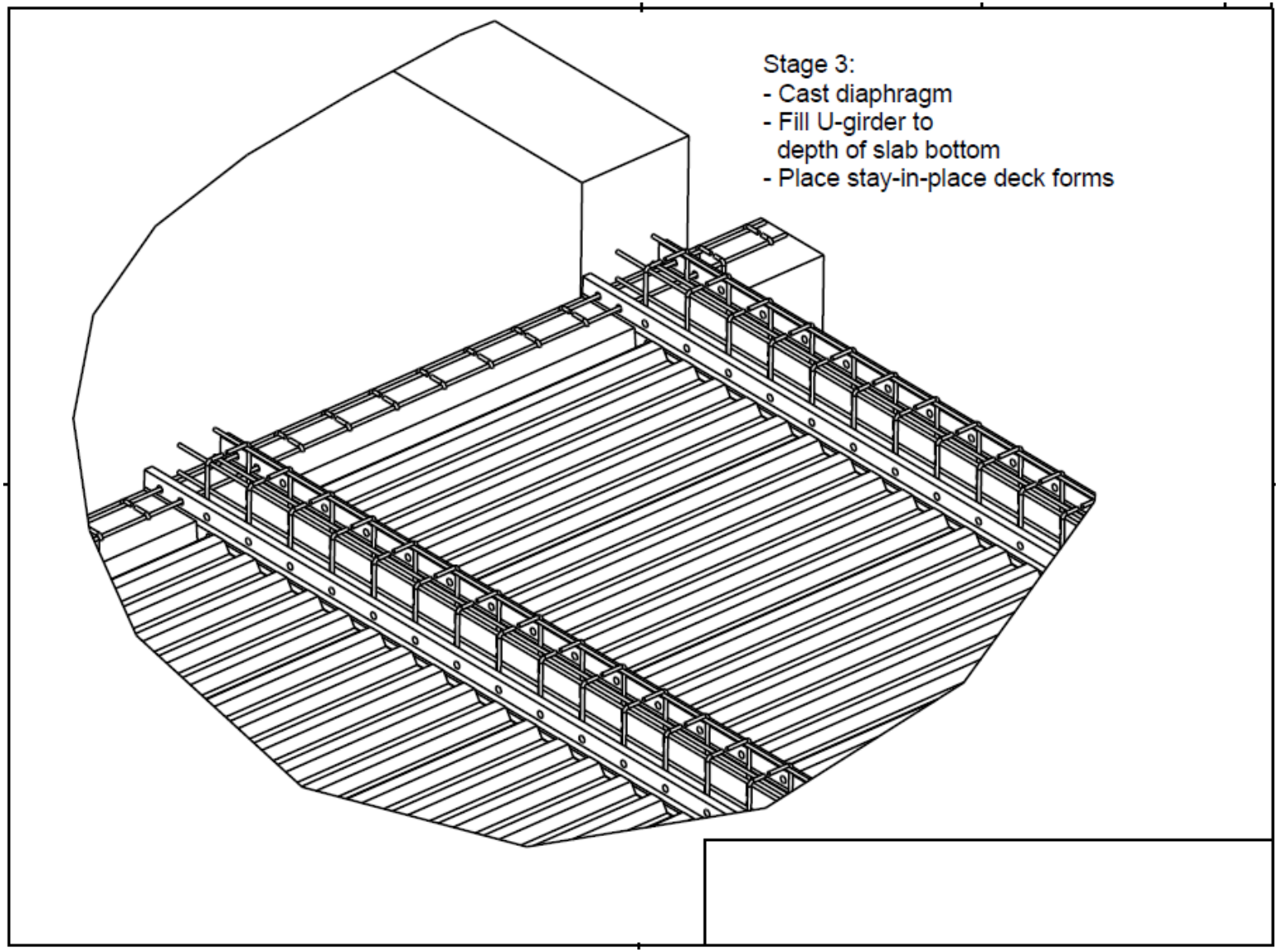

Figure 115. Casting diaphragms, filling U-girders, and placing formwork for cast-in-place deck.

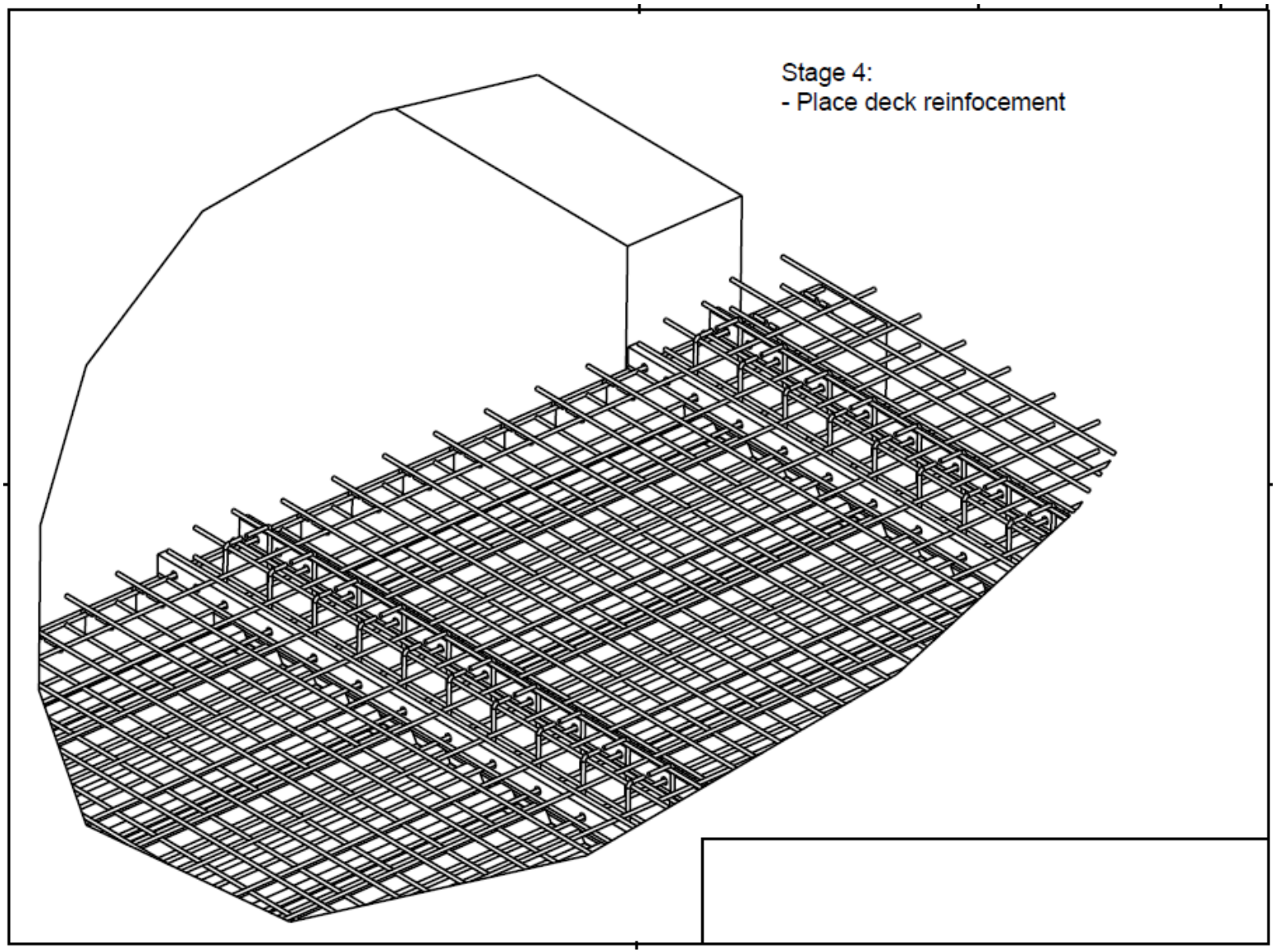

Figure 116. Placing deck reinforcement

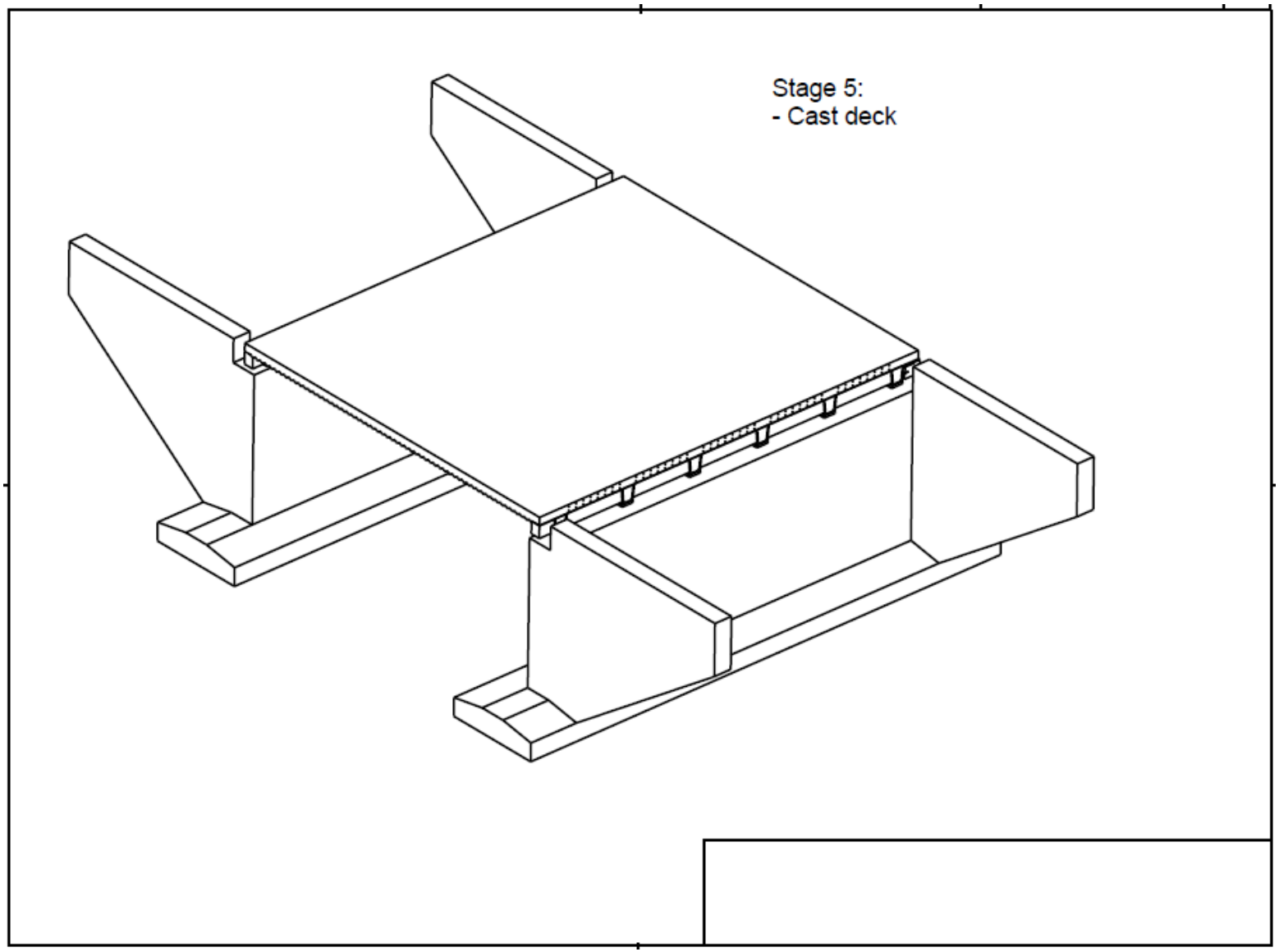

Figure 117. Cast deck

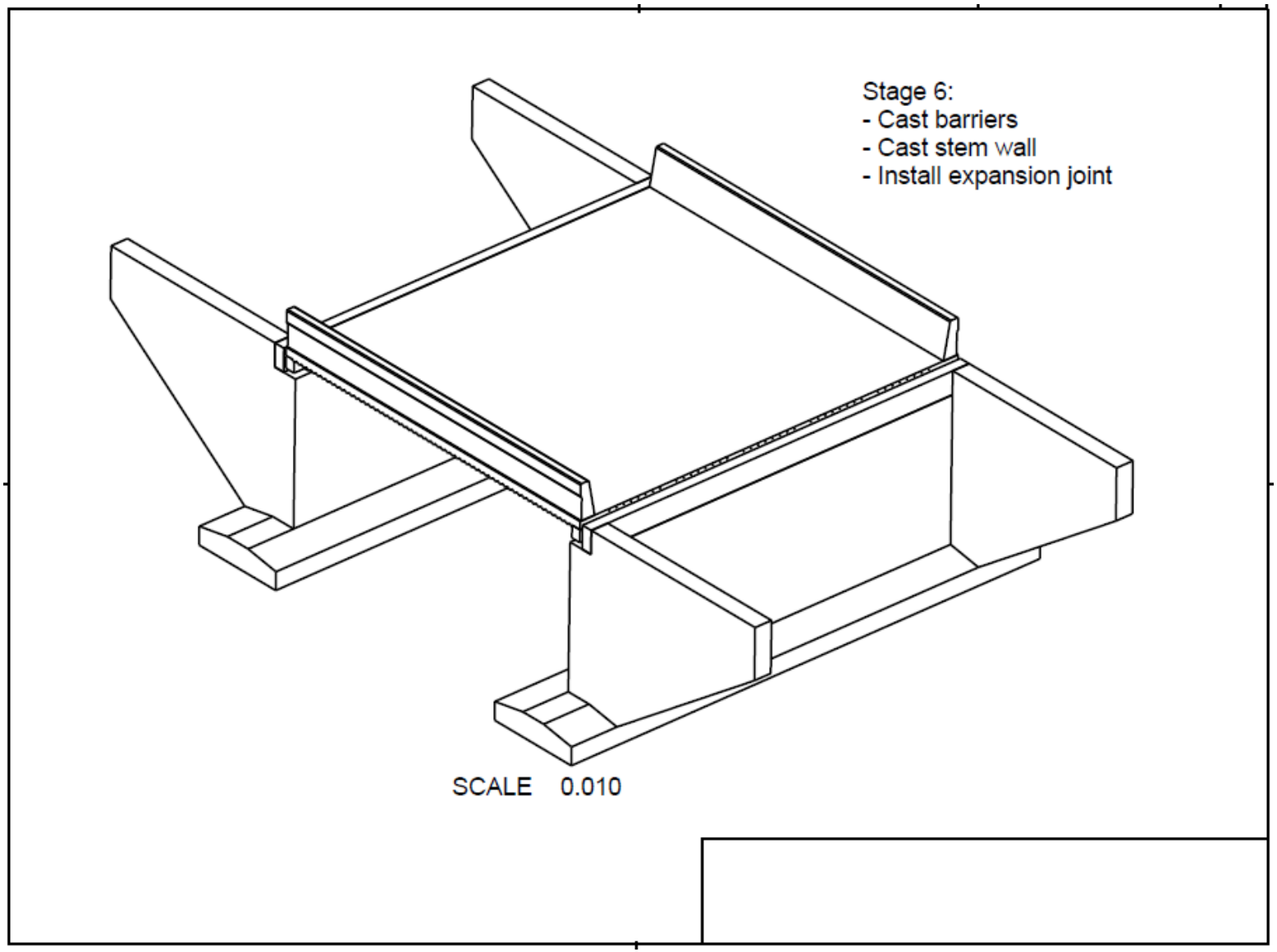

Figure 118. Cast-in-place barriers, complete stem wall, and install expansion joint

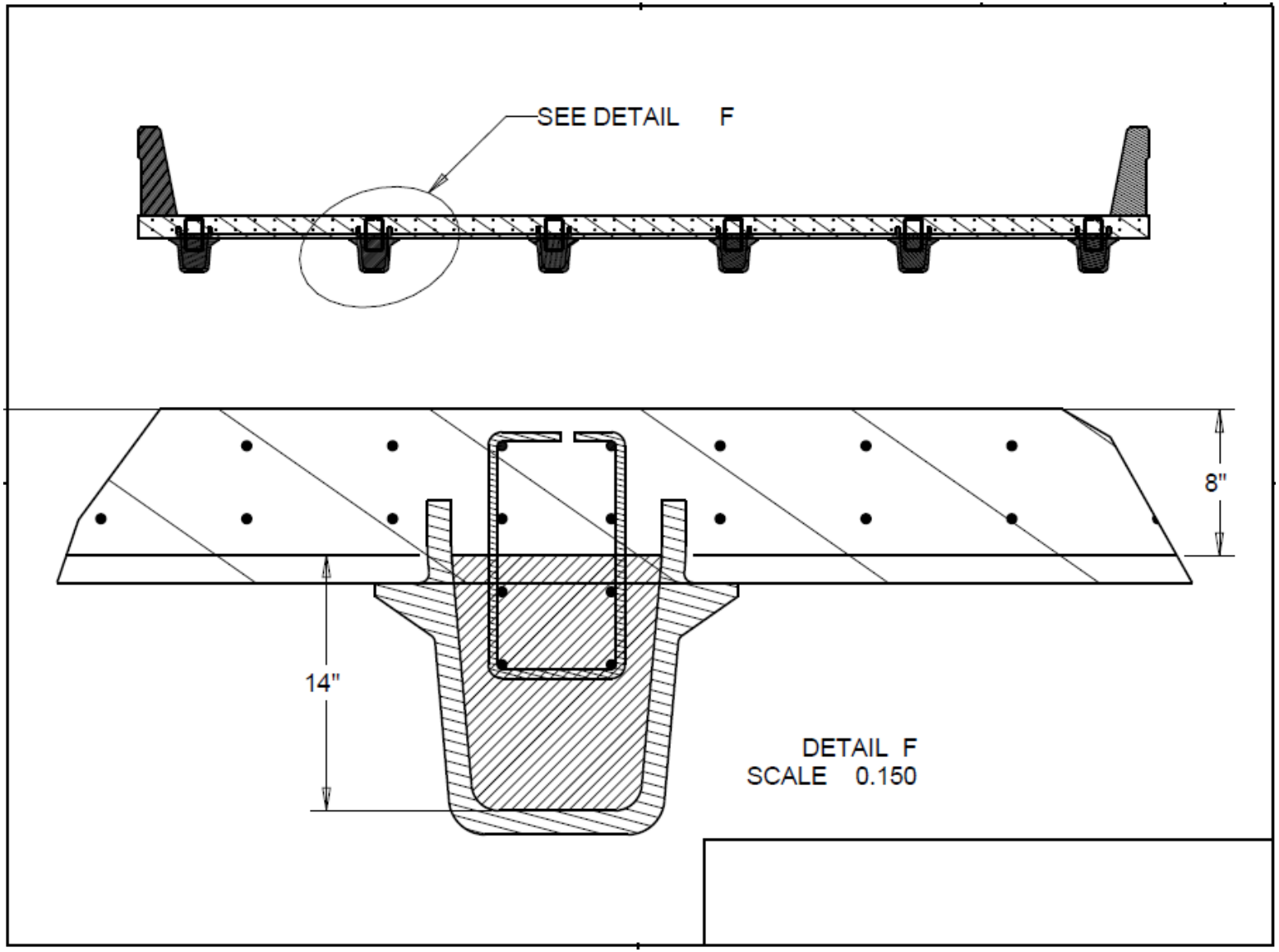

Figure 119. Final cross-section for 30-ft span length bridge designed using AASHTO distribution factor method

12.2.2 CFFT

Construction sequencing for the CFFT is similar to what is provided for the FRP U-girder. In the traditional Concrete Arch Bridge System (CABS), the stay-in-place FRP forms span the CFFTs continuously. This may not be possible if a fully developed shear connection is desired between the CFFT and the cast-in-place concrete deck. The King's Stormwater Channel bridge included an uninterrupted polymer concrete shear key that was formed on top of the CFFT and connected the FRP bridge deck to the girders (Figure 120).

If an infusion process is used to manufacture the CFFTs, it may be possible to form an additional integrated ledge that would facilitate establishing the connection between the girder and the deck. Nonetheless, establishing the shear connection for the CFFT will be a more difficult than what is required for the FRP U-girder. The cast-in-place diaphragm would also require a more sophisticated formwork system than the FRP U-girder due to the curved ends in each formwork section. It should be noted that the King's Stormwater Channel bridge originally omitted the cast-in-place diaphragm, which ultimately lead to premature damage issues in the FRP deck.

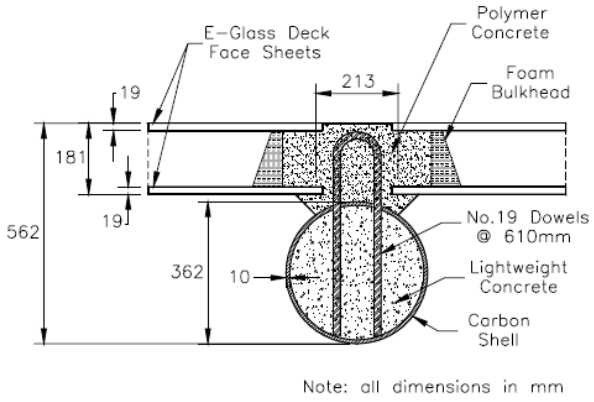

Figure 120. Kings Stormwater Channel bridge near the Salton Sea on California S.R. 86 [58]

12.2.3 Pultruded FRP Girder

Construction sequencing for the pultruded FRP sections is similar to what might be encountered in steel I-beams. One major difference, however, is that steel shear studs cannot be welded to the FRP flanges. The FRP bridge girders used in Poland relied on galvanized steel shear connectors that passed through drilled holes in the flanges and then anchored in the concrete slab above. The pultruded girder bridges in Virginia relied on a sophisticated clipping system to connect the FRP girders to the laminated timber deck. This bridge was designed assuming no composite action between the timber deck and the pultruded girder, which results in compression in the top flange. Because buckling/shear delamination in the top flange was cited as a primary failure mode for these beams in flexure (see Figure 106), there was likely some hesitancy to drill through the top flange to make the deck connection (Figure 122A).

As long as a positive shear connection can be maintained between the FRP flanges and the cast-in-place deck, concerns over compression flange buckling should be minimized. Proper detailing of these shear connectors would require additional design work and would also need to be validated through

full-scale testing before deployment in the field. One final issue that would need to be addressed during construction is the installation of cross-bracing (Figure 122B).

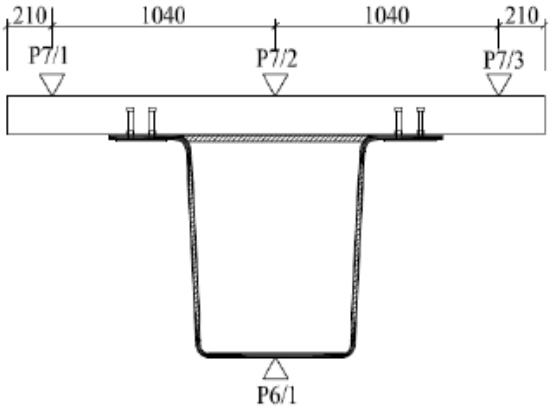

Figure 121. Shear connection for FRP bridge in Poland [132]

Figure 122. Photos of Dickey Creek bridge, Route 601, Sugar Grove, VA. (A) Deck connectors for pultruded FRP bridge girders. (B) Galvanized steel cross-bracing. Photos courtesy of Dr. Brandon Ross, Clemson University.

12.3 Maintenance

Long-term maintenance requirements for FRP bridge girders are not well defined. There are, however, several general durability concerns for FRP materials that have been identified as relevant to FRP composites in bridge applications [133]:

- Chalking
- Cracking
- Blistering
- Flaking
- Discoloration
- Damage from exposure to the following:
  - UV radiation
  - Chemicals
  - Fire
- Fatigue damage due to normal loading conditions
- Impact damage due to vehicle strikes
- Damage during routine or non-routine maintenance operations (e.g., deck replacement or repair of corrosion damage)

Discussions with one prominent resin manufacturer indicated that the application of a protective gelcoat during manufacturing would be critical to the long-term durability of the FRP composite. Over time, the gelcoat is expected to discolor and eventually begin to exhibit signs of oxidation/chalking. Most of the concerns associated with this behavior are aesthetic and should not affect the structural performance of the composite. Once discoloration and chalking have exceeded some acceptable threshold, the surface can be refinished to provide additional gelcoat thickness and to restore the original color and shine. If the surface is left without refinishing, the gelcoat will continue to erode until the fibers are exposed.

Researchers in Japan completed a life-cycle analysis (LCA) study that compared the total lifecycle costs for an FRP pedestrian bridge to steel and prestressed concrete alternatives in an extremely aggressive coastal environment [134,135]. The author draws the now-typical conclusion that FRP composite structures can be cost-competitive with traditional materials if the overall lifecycle costs are properly accounted for. This is especially true for extremely corrosive environments. Repainting was cited as the primary maintenance cost associated with FRP bridges. The repair interval used in the LCA for the repainting operation was 120 years based on a 75µm thick fluorine resin paint.

One important point identified in the Japanese study is that the assumed maintenance costs for FRP structures (generally very low) may not always be accurate. One specific area noted by the author relates to corrosion in metallic fasteners and their need for replacement. One pedestrian bridge cited in the study required new stainless steel bolts after five years of service in an extremely aggressive environment.

These observations related to metal fasteners are confirmed based on recent images obtained for the pultruded FRP girder bridge in Sugar Grove, VA (4.2.1.2). Photos taken on December 26, 2016—15 years after the bridge was constructed—indicate that many of the metallic fasteners used to secure the FRP girders to the laminated timber bridge deck have started to corrode (Figure 123). It is

unknown if this corrosion resulted from the use of deicing salts in the winter months or if it was caused by ambient environmental conditions. In any case, the use of such fasteners in an extremely aggressive marine environment would likely yield similar results and should be avoided.

Another study investigating the long-term durability of an FRP pedestrian bridge in Switzerland [136] found that the pultruded FRP material itself performed well and did not pose any significant durability concerns. Nonetheless, considerable damage was noted after eight years of service due to mishandling of the bridge structure during installation and subsequent removals (Figure 124). This bridge was only used during the winter months and moved to higher ground every year during the summer to avoid high water levels in the stream. Some fiber blooming—locations where glass fibers are exposed—was also observed, but these areas coincided with locations where the surface veil intended to protect the composite had been misplaced.

Figure 123. Corrosion of metallic components on pultruded FRP girder bridge (Dickey Creek bridge, Route 601, Sugar Grove, VA) Photos taken December 26, 2016. Photos courtesy of Dr. Brandon Ross, Clemson University.

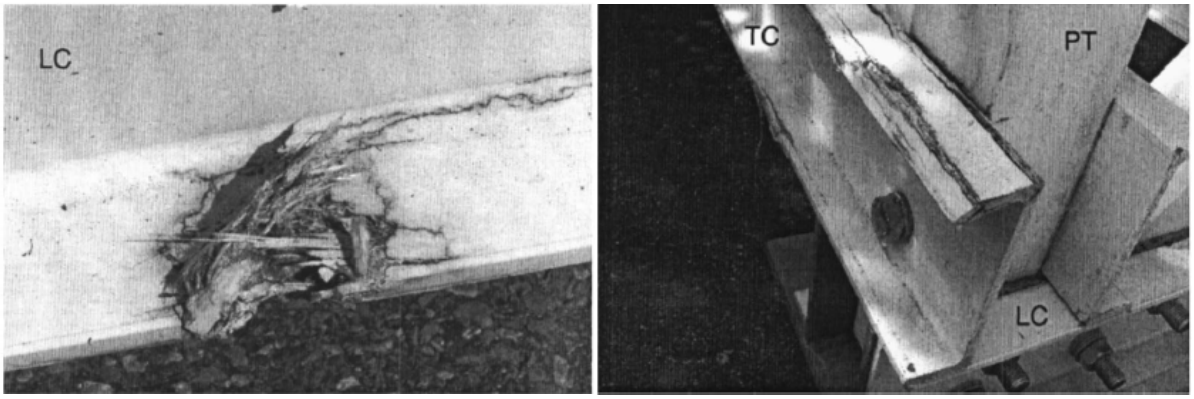

Figure 124. Observed damage in FRP pedestrian bridge in Switzerland [136].

12.4 Service Life

The University of Maine and Advanced Infrastructure Technologies published a report in January 2016 that evaluated the 100-year service life criteria for the CFFTs used in the concrete arch bridge system (CABS). The CFFT tubes they were attempting to validate for the 100-year service life were described as consisting of "braided glass fiber material within a vinylester resin." The report summarized research from several sources and used an Arrhenius relationship to estimate the actual environmental reduction factor, C_E, at a 100-year service life for cities around the US. The ultimate conclusion drawn by these researchers was that the C_E value of 0.65 (GFRP in a normal environment) is overly conservative for a 100 year design life (Figure 125).

Table 25: Summary of C_E environmental degradation factors at 100-year design life

Source	Conditioning	Mechanical Property	T1 (°C)	T2 (°C)	C_E				
					Portland, ME	Saint Louis, MO	San Diego, CA	Brownsville, TX	Miami, FL
Montaigu et al [3]	Alkaline Solution	VE35 Transverse Shear	23	50	0.93	0.92	0.92	0.91	0.91
			23	60	0.93	0.92	0.92	0.91	0.91
		VE38 Transverse Shear	23	50	1.00	0.99	0.99	0.98	0.98
			23	60	1.00	0.99	0.99	0.98	0.98
		VE35 Flexural	23	50	0.96	0.95	0.95	0.95	0.95
		VE38 Flexural	50	60	0.98	0.97	0.97	0.96	0.96
Karbahari [46]	Deionized Water	CM-Warp Shear	5	23	0.75	0.75	0.76	0.76	0.76
			23	40	0.79	0.78	0.77	0.76	0.76
			5	40	0.74	0.73	0.73	0.72	0.72
		CM-Fill Shear	5	23	0.75	0.75	0.75	0.75	0.75
			23	40	0.78	0.77	0.76	0.75	0.75
			5	40	0.74	0.73	0.73	0.71	0.71
Robert and Benmokrane [8]	Alkaline Solution	Tensile	23	40	0.97	0.92	0.94	0.89	0.89
			40	50	0.72	0.71	0.71	0.70	0.70
			23	50	0.95	0.93	0.93	0.90	0.90

Figure 125. Environmental knockdown factors for GFRP at 100-year service. From AIT Composite Arch Durability Report 137.

These results suggest that the GFRP composites evaluated in the current study are capable of achieving the 75-year required design. A major difference that must be kept in mind, however, is that the CABS bridges are not subjected to any long-term tensile stress due to bending. The research cited in the AIT study relied primarily on exposure to chemical weathering followed by assessment of the test specimens' mechanical properties. Some studies applied load before exposure to the chemical

weathering, but none of the studies explicitly state that loading was maintained during the weathering.

Dr. El-Safty's (University of North Florida) ongoing work related to FRP durability under sustained loading(BDV34 977-05) should provide additional insight into the anticipated service life of FRP bridge girders. It must also be noted, however, that the girders designed for the present study assume a maximum tensile stress under service loads of only 10% of the manufacturer's specified strength.

12.5 Overall Summary and Side-by-Side Comparison

Table 74. Pros and cons associated with each alternative: Design

	Design	
	Pros	Cons
General FRP	• Assumed linear relationship between stress and strain to failure • Fiber orientation can be tailored to meet strength demands in different regions of the girder. • Classical laminate theory (CLT) can be used to determine the strength and stiffness properties of FRP laminates. • AASHTO LRFD codes for internal reinforcement and CFFT bridge elements (along with ACI 440) have established a fundamental framework for characterizing the FRP material properties needed for bridge design applications.	• Material strength and stiffness properties are dependent on laminate architecture. Changes in the fiber orientation angle for a specific fiber ply will impact the overall laminate strength and stiffness. • Variability in available matrix materials can lead to variations in strength and stiffness. • Bridge designers are familiar with non-homogeneous materials (e.g. concrete), but the transition to composites design with five required lamina strength parameters, four stiffness properties, and an array of failure criteria (e.g. maximum stress, maximum strain, Tsai-Hill/Wu) will be challenging. • For GFRP in an extremely aggressive environment, the strength resistance factor, Φ, combined with the environmental reduction factor, C_E, limits the allowable stress in the FRP at the strength limit state to 27.5% of the ultimate tensile strength. The allowable stress for the fatigue and creep rupture limit state is only 10% of the ultimate tensile strength. These values may be overly conservative.

Table 74. Pros and cons associated with each alternative: Design (continued)

	Design (continued)	
	Pros	Cons
General FRP (continued)		• Actual failure modes in FRP bridge girders at the strength limit state are difficult to predict. • The modulus of elasticity of GFRP ranges from 10% to 20% of the modulus for steel.
Alternatives		
FRP U-Girder	AASHTO distribution factors appear to be suitable for determining girder demand based on single lane loading	• No accepted standards for evaluating shear strength and flexural strength at limit state • No accepted details for establishing shear connection between FRP and cast-in-place RC deck • Development of moment-curvature diagrams for a proposed cross-section requires an iterative/trial and error approach •
CFFT	AASHTO LRFD-FRP provides a closed-form solution for evaluating the moment capacity of a proposed cross-section. The method does not incorporate the strength contribution of a cast-in-place deck.	• The shear-strength model proposed in AASHTO LRFD-FRP favors laminates with fibers running primarily in the hoop direction. The shear-strength predicted for CFFT girders with +/- 45-degree laminates is considerably lower than predictions made for 0/90 laminates. See section 8.1.5.8. • A circular tube is not the most efficient structural shape for resisting bending moment or shear. If composite action with a RC deck is desired, much of the composite will be close to the neutral axis and will not experience large stresses.

Table 74. Pros and cons associated with each alternative: Design (continued)

	Design (continued)	
	Pros	Cons
Alternatives (continued)		
Pultruded Shape	• Considerable research was completed in the late 1990's through early 2000's on bridge girder design for the DWB8 and DWB36. Strongwell has produced a design manual for these shapes.	• The DWB shape geometry and laminate architecture are considered proprietary. • Standard FRP pultruded shapes are typically too small to be considered for bridge girder applications. For steel bridge girders, designers typically have access to a wide variety of W-shapes or the ability to specify custom plate girder cross-sections to meet the requirements of a specific bridge. It may be possible to join smaller pultruded shapes together using glue or other shear connectors.

Table 75. Pros and cons associated with each alternative: Manufacturing and fabrication

	Manufacturing and Fabrication	
	Pros	Cons
General FRP	• Complete curing of the FRP composite can be achieved in 24 hours at room temperature and as little as 2 hours at 250 °F (120 °C). • Components are relatively light compared to reinforced concrete or steel. • Manufacturing of large-scale composite parts using resin infusion has increased considerably in the past decade. Utility scale wind turbine blades can approach 250 feet in length and possess complex geometries.	• Manufacturing involves hazardous materials • Composites production facilities typically operate in an indoor environment.

Table 75. Pros and cons associated with each alternative: Manufacturing and fabrication (cont.)

	Manufacturing and Fabrication (continued)	
	Pros	Cons
Alternatives		
FRP U-Girder – resin infusion	• Fiber orientation can be tailored to match localized structural demands • Male or female mold can be used • Minimal capital investment needed for tooling and molds. •	• Some degree of standardization regarding section depth and width is needed to reuse molds. • Fabrics must be woven or stitched to maintain their shape and directionality during laminate stacking (increased cost compared to basic tows). This adds cost to the fiber material. • Each fabric layer must be cut to specified length • Depending on the size of the fabric roll, there may be considerable waste • Overlap shear splices may be necessary depending on the size of the girder • Lower fiber volume fraction than other alternatives
CFFT – filament wound	• Rapid production once winding begins • Standardized shape and repeatable material properties • Continuous fiber for entire part (no overlap splices needed) • Higher fiber-volume fraction than other alternatives • Fiber tows are the least expensive form of fiber material	• The winding angle for a given ply is limited to ~10 degrees. For CFFT bridge girders subjected to flexure, it is advantageous to have true 0-degree plies to increase stiffness and strength in the longitudinal direction. • Overall winding speed is reduced for low-angle plies (e.g. 10°). • The total length of filament wound tubes may be limited. Larger mandrels become more expensive
CFFT – resin infused	• An inflatable tube can be used as the mold • Fiber orientation can be tailored to match localized structural demands	•

Table 75. Pros and cons associated with each alternative: Manufacturing and fabrication (cont.)

	Manufacturing and Fabrication (continued)	
	Pros	Cons
Alternatives (continued)		
Pultruded Shape	• Fibers are predominantly oriented in the longitudinal direction. • Rapid production • Standardized shape and repeatable material properties	• Obtaining off-axis fiber orientation is more difficult. This limits the shear strength of pultrusions—especially near flange/web interfaces. • Large capital costs for pultruding equipment • High cost of pultrusion dies that are unique for each cross-section

Table 76. Pros and cons associated with each alternative: Construction

	Construction	
	Pros	Cons
General FRP	• Lightweight compared to steel and concrete components • Smaller cranes required on site • More girders can be delivered on a single truck	• FRP components are easily damaged during movement and placing • Additional care is needed to avoid damaging girder when placing reinforcement for cast-in-place deck
Alternatives		
FRP U-Girder	• Girder will act as stay-in-place form to support deck formwork and reinforcement for deck casting •	•
CFFT	•	• Formwork for cast-in-place shear key is complex
Pultruded Shape	•	• Difficult to establish shear connection with RC deck without using metal fasteners

Table 77. Pros and cons associated with each alternative: Maintenance

	Maintenance	
	Pros	Cons
General FRP	• Highly corrosion resistant • Thermal imaging is an effective NDE technique for identifying delaminations/voids within ~0.02 in (5 mm) of the surface. This could help to identify environmentally induced damage (temperature/moisture, etc…) before it becomes a serious problem.	• Gel coat may require painting/refurbishing • Internal damage to the composite > 0.02 in (5mm) from the surface is more difficult to detect with thermal imaging. Large delaminations might be detected through sounding methods (e.g. coin tap)
FRP U-Girder		
CFFT		
Pultruded Shape		• If metallic fasteners are used, they will eventually corrode in an extremely aggressive environment.

Table 78. Cost comparison (including traditional girder options)

	Cost	
	Material Cost	**Girder cost per SF of deck (50ft Span)**
FRP U-Girder	~$5.25 per pound for resin infused GFRP	$62
CFFT	~$4.00 per pound for filament wound GFRP	$75
Pultruded Shape	~$5.25 per pound for GFRP ~$8.50 per pound GFRP/CFRP hybrid	$112
Florida Slab Beam (12”x60”)**		$52*
Florida Slab Beam (15”x60”)**		$54*
Florida Slab Beam (18”x60”)**		$62*
AASHTO Type 2***		$21*
FL I-Beam 36”***		$41*

*Per foot costs obtained from 2017 FDOT Structures Guidelines Section 9.2.2.

**Cost does not include topping concrete

**Assumes six girders are required for 32-ft-wide bridge deck to span 50 ft.

A summary ranking matrix for the three alternatives evaluated in the current study is provided in Table 79. A distinction is made for the CFFT option between resin infusion and filament winding due to some variability in performance regarding fiber orientation flexibility and other manufacturing costs. The ranking process involved assigning a numeric value between one and four for each criteria, with one being the best and four being the worst. If two or more alternatives are considered to be roughly equivalent, the total points available for the tied rankings are split evenly amongst the contenders for those positions. For example, the manufacturing facility capital costs for the resin infused U-girder and the resin infused CFFT are considered to be equivalent (and the lowest), followed

by the filament wound CFFT (the next lowest), and the pultruded DWB. The two resin infused options split evenly a total of three points that are available for first and second place and the filament wound tube and the pultruded DWB are awarded three and four points, respectively.

The FRP U-girder received the lowest total points (best ranking). It should be noted, however, that this ranking system applies equal weight to each criterion. There may be circumstances for a specific bridge application where the influence of one criterion could be magnified (or diminished) that will lead to a different ranking outcome. Nonetheless, the ranking matrix in Table 79 does provide a reasonable snapshot of the relative strengths and weaknesses for each alternative.

Table 79. Alternatives ranking

		FRP U-Girder (resin infused)	CFFT (resin infused)	CFFT (filament wound)	Pultruded DWB
Design	Analysis	3	3	3	1
	X-section shape flexibility	1	2.5	2.5	4
	Fiber-orientation flexibility	1	2	3	4
Manufacturing	Facility capital costs	1.5	1.5	3	4
	Labor intensive	3.5	3.5	2	1
	Economy of scale	3.5	3.5	2	1
Construction	Girder placement	2	3	3	2
	Diaphragm/ bracing	1	3.5	3.5	2
	Deck forming	1	3	3	3
Maintenance		2	2	2	4
Service life		2	2	2	4
Cost		1	2	3	4
Total		**22.5**	**31.5**	**32**	**34**

13. Recommendations for Future Research

The primary objective of this research was to evaluate different, non-proprietary, bridge girder alternatives for extremely aggressive environments that are suitable for span lengths between 30 ft and 75 ft. During the literature review phase, four bridges in the U.S. meeting the span length criteria were identified that utilized all FRP or hybrid FRP/concrete bridge girders. Once it was determined that the girders for these bridges have performed well with no required maintenance since their construction between 2001 and 2007 (three of the four bridges are still in service—one of the bridges was removed due to maintenance concerns with the FRP bridge deck), the question that naturally followed was "why haven't more FRP bridge girders been implemented since the initial flurry of interest in the late 1990's and early 2000's?"

The answer that we received from officials responsible for maintaining these FRP girder bridges focused primarily on cost. With the long-term durability (i.e. > 75 years) of these materials still unproven in vehicle bridge applications, anticipated savings resulting from reduced maintenance costs or an extended service-life are difficult to justify. On the one hand, two existing proprietary FRP bridge systems (Advanced Infrastructure Technology's "Bridge-in-a-Backpack" and Hillman Composite Beams) are claiming that a 100-year service life is possible for bridges incorporating FRP materials. On the other hand, some negative experiences with FRP bridge decks have left certain DOTs leery of utilizing FRP in primary load-bearing members. If these structural elements fail to perform as intended for 75+ years, the early replacement costs would be difficult to bear.

Another challenge facing the broader adoption of FRP materials for bridge girder applications is that design criteria for all-FRP or hybrid FRP/concrete bridge girders in pure shear/flexure are still in the early phases of development. AASHTO's LRFD Guide Specifications for Design of Concrete-Filled FRP Tubes provides guidance for the CFFT option, but the FRP U-girder and pultruded DWB options evaluated in this study would still be considered experimental. This research identified four basic limit states that can be used to evaluate the suitability of a proposed FRP cross-section:

- LS-1: Concrete compressive stresses
- LS-2: Displacements
- LS-3: Fatigue and creep rupture
- LS-4: Strength

With the exception of LS-1 (concrete compressive stresses), there are still unanswered questions related to the application of each limit state. The following sections describe additional research work that would support the broader application of FRP bridge girders in extremely aggressive environments.

13.1 Questions Related to Limit States

13.1.1 LS-2: Displacements

The current research evaluated the impacts that different assumptions about boundary conditions, the presence/absence of barriers, and the stiffness contribution of concrete placed inside an FRP U-girder have on the overall FRP material requirements for a specific span length. Specific questions that need to be addressed include:

- Is the increased stiffness that results from filling the U-girder with concrete realized throughout the entire range of typical service loads? In other words, if service loads result in concrete cracking, how should the stiffness of the cracked/transformed cross-section be applied in deflection calculations?
- When using refined methods of analysis (i.e. finite element modeling) for the entire bridge structure, the specified boundary conditions have significant influence on the resulting deformations and the amount of FRP required for a specific application. Previous research by Chen et al (2009) indicates that basic simply-supported end conditions may be overly conservative for hybrid FRP/concrete U-girders with a cast-in-place RC deck, end diaphragms, and cast-in-place concrete barriers. Furthermore, this type of modeling also violates the "all girders deform equally" principle outlined in AASHTO LRFD-7 S2.5.2.6.2. If finite element models are used to evaluate deflection criteria, should the loads be applied such that the resulting deformations are uniform for all bridge girders?

13.1.2 LS-3: Fatigue and Creep Rupture

In the current study, the tensile stress limit for GFRP in an extreme environment was limited to 10% of the manufacturer's specified tensile strength. This may be overly conservative. While marine environments in Florida are certainly extreme from the perspective of corrosion damage in reinforcing steel, the harsh chemical environments that GFRP materials are subjected to in the chemical processing industry are far more demanding. For example, GFRP tanks (with an appropriate resin-rich liner) are commonly used to store sodium hydroxide (pH=13). The study by AIT suggests that an environmental knockdown factor of 0.7 through 0.98 is appropriate for a 100-year service life in Florida environments. The value used in the current study was 0.5. Unfortunately, none of the literature cited in the AIT study appears to have investigated the synergistic effects of load, temperature, and alkalinity on the creep rupture process for GFRP. It is also unclear how this combined degradation mechanism will affect GFRP laminates with thicknesses on the order of 0.75 to 1.5 in.

Another potential modification to this limit state would be the decoupling of fatigue and creep rupture. It is not clear that these mechanisms are interdependent for the load durations associated with vehicle live load reversals. This is further complicated by the fact that creep rupture behavior is based on extrapolated test data obtained from relatively short duration experiments.

13.1.3 LS-4a: Strength – Flexure

The flexural strength limit state was never a controlling factor for the span lengths investigated in the current study. Nonetheless, this was all based on the assumption of perfect composite action with the reinforced concrete deck. Previous work by others that included full-scale load testing of FRP U-girders concluded that an adequate shear connection can be established using metal shear connectors. Due to the high cost of stainless steel and the ultimate susceptibility to corrosion of these metal connectors, the conceptual design for the proposed hybrid FRP/concrete U-girder involves grouted GFRP bars that pass through holes in the U-girder. These holes are drilled through a flange that protrudes several inches vertically into the cast-in-place deck. It is also recommended that concrete should be cast throughout the depth of the U-girder. With appropriate surface treatment of the girder's interior surface, it should be possible to provide a strong mechanical interlock between the FRP and the cast-in-place concrete. Some degree of experimental testing will be needed to validate this proposed shear transfer mechanism.

Another outstanding issue relates to the computation of the strength reduction factor, Φ, when evaluating the flexural strength of hybrid FRP/concrete girders. The relationships provided in LRFD-FRP for CFFT bridge girders are based on a "balanced" reinforcement ratio, ρ_b, that results in simultaneous concrete crushing and FRP rupture. For traditional reinforced concrete sections, limits on the reinforcement ratio serve to ensure that if the flexural capacity of a member is ever exceeded, the failure will be ductile. For the case of CFFTs, preference (i.e. a higher Φ–factor) is given to over-reinforced sections that will result in concrete crushing before the FRP ruptures. When sections include the cast-in-place RC deck as part of the compression flange, the amount of FRP needed to ensure a balanced failure mode will be high. In the current study, the FRP was assumed to have "ruptured" when the maximum tensile stress in the cross-section reaches the design tensile strength of the FRP. This design tensile strength is determined by multiplying the manufacturer's specified tensile strength by the appropriate environmental knockdown factor, C_E. For GFRP in an aggressive environment, the C_E value is 0.5. For the purposes of determining whether or not a section is "balanced", it might be more appropriate to assume that the entire manufacturer's specified tensile strength is available.

13.1.4 LS-4b Strength: – Shear

There is significant divergence between proposed models for determining the shear strength contribution of FRP tubes. We were not able to locate any proposed models for evaluating the shear strength of a hybrid FRP/concrete U-girder. The model proposed in the current study is based on the ultimate shear strength of the GFRP laminate. How this GFRP laminate strength might combine with the shear strength contribution of concrete at the strength limit state is not well defined. Additional experimental testing to validate the proposed model is warranted.

13.2 Advancing Design Practice

The preliminary design work completed in this study establishes a basic framework for the analysis and design of hybrid FRP/concrete U-girders. Different laminate architectures were evaluated over the range of desired span lengths, but further optimization could be achieved by tailoring the laminate architectures over specific regions of the girder. For example, regions of high shear near the supports could contain layers of +/- 45 degree fibers while the tension flange consists of additional unidirectional fibers oriented in the primary direction of the girder. Adding additional unidirectional layers in the tension flange was shown to result in a reduction in total FRP weight for spans longer than 50 ft. For shorter span lengths, where shear strength is a controlling limit state, a decision was made to rely on conservative shear strength values for 0-90 biaxial laminates. Additional research is needed to establish a reliable method for detailing the laminate architecture in high shear regions. Further research into appropriate detailing for transition regions would also help to ensure that the GFRP material is being utilized efficiently throughout the bridge girder.

To make the design process more accessible to current bridge designers, it might be beneficial to establish pre-defined laminate architectures for use in specific regions of a bridge girder. As long as the percentage of fibers specified in each direction is held constant, the strength and stiffness properties for the laminate would be known. The overall girder dimensions (i.e. width, depth, web thickness, and flange thickness) would still be variable and could be tailored for a particular design scenario. A library of standard laminate architectures that have been validated through laboratory testing would work to keep the number of unknowns to a manageable level for the designers and also

provide DOTs with confidence that a specified laminate architecture will meet some minimum performance standard. One practical approach for establishing this laminate architecture database and identifying specific regions of a girder where each laminate type is applicable would be to complete a detailed design and optimization study for a fixed-length bridge.

Finally, additional research is needed to develop laminate architectures that provide some indication that a certain load threshold has been exceeded. The general concept involves strategic placement of unidirectional carbon fiber tows in the tension flange and webs of high shear regions. These high stiffness fibers would rupture first in the case of overloading and provide a visual cue that the girder may have been damaged. Other ideas include the strategic placement of 90-degree lamina in regions experiencing high tension. These off-axis can be designed to fail and delaminate at a specified load threshold. This layer could be located close to the surface such that the resulting delamination could be detected with acoustic sounding methods (e.g. coin tap), infrared thermography, or acoustic emissions during load testing.

References

1. Florida Department of Transportation (FDOT). (2017). *FDOT Structures Manual, Vol. 4 – Fiber-Reinforced Polymer Guidelines*. Tallahassee, FL: FDOT. http://www.fdot.gov/structures/StructuresManual/CurrentRelease/Vol4FRPG.pdf.

2. American Association of State Highway and Transportation Officials (AASHTO). (2014). AASHTO *LRFD Bridge Design Specifications*, 7th Edition. Washington, D.C.: AASHTO.

3. American Association of State Highway and Transportation Officials (AASHTO). (2012). *LRFD Design Specifications for Concrete-Filled FRP Tubes for Flexural and Axial Members*, 1st Edition. Washington, D.C.: AASHTO.

4. American Society of Civil Engineers (ASCE). (2010). *Pre-Standard for Load and Resistance Factor Design (LRFD) of Pultruded Fiber Reinforced Polymer Structures*. Arlington, VA; American Composites Manufacturers Association.

5. Florida Department of Transportation (FDOT). (2015). *FDOT Standard Specifications for Road and Bridge Construction*. Tallahassee, FL: FDOT.

6. Cessna. *Materials and Process Specifications Index*. Webpage: https://supplier.cessna.com/cgi-bin/technical/mtl_specs.pl. Accessed Nov. 28, 2017.

7. Morgan, P. (2005). *Carbon fibers and their composites*. Boca Raton, FL: Taylor & Francis Group, LLC.

8. Harris, B. (1999). *Engineering Composite Materials*. London: The Institute of Materials.

9. Peters, S. T. (1998). *Handbook of Composites,* 2nd ed. London: Chapman & Hall.

10. Baker, A. A., Dutton, S., & Kelly, D. (2004). *Composite materials for aircraft structures*, 2nd ed. Reston, VA: American Institute of Aeronautics and Astronautics.

11. Campbell, F.C. (2006). *Manufacturing Technology for Aerospace Structural Materials*. Oxford: Elsevier Science.

12. Campbell, F.C. (2010), *Structural Composite Materials*. Materials Park, OH: ASM International.

13. Mazumdar, S.K. (2002). *Composites Manufacturing: Materials, Product, and Process Engineering*. Boca Raton, FL: CRC Press.

14. Zhou, Y. Z., Yang, L., & Huang, Y. (2013). Mechanical properties of Composite materials. *Micro- and macromechanical properties of materials* (1st ed., pp. 535-564) CRC Press.

15. McCauley, R.A. (2013). Composite Materials. *Corrosion of Ceramic Materials* (3rd ed., pp. 315-356) CRC Press.

16. Maguire, J., Weed, D., & Rose, T. (2006). Composite manufacturing. In R. Crowson (Ed.), *Parts fabrication: Principles and process* (pp. 229-273). Boca Raton, FL: Taylor & Francis Group.

17. Gay, D., Hoa, S.V., & Tsai, S.W. (2002). *Composite Materials: Design and Applications*. Boca Raton, FL: CRC Press.

18. Advani, S.G. & T. Hsiao, K.T. (2012). *Manufacturing Techniques for Polymer Matrix Composites (PMCs)* Cambridge, United Kingdom: Woodhead Publishing.

19. Hexcel (2013). *HexPly Prepreg Technology Manual*. Retrieved Nov. 28, 2017 from http://www.hexcel.com/user_area/content_media/raw/Prepreg_Technology.pdf.

20. A. Velicki, A., Yovanof, N., Baraja, J., Linton, K., Li, V., Hawley, A., Thrash, P., DeCoux, S., & Pickell, R. (2011). *Damage Arresting Composites for Shaped Vehicles - Phase II Final Report*. NASA Langley Research Center, NASA/CR-2011-216880, NF1676L-11864.

21. Uddin, N. (2013). *Developments in Fiber-Reinforced Polymer (FRP) Composites for Civil Engineering*. Cambridge, UK: Woodhead Publishing.

22. Velicki, A., & Thrash, P. (2008). Advanced structural concept development using stitched composites. *49th AIAA/ASME/ASCE/AHS/ASC Structures, Structural Dynamics, and Materials Conference*.

23. Biron, M. (2013). *Thermosets and composites: Material selection, applications, manufacturing and cost analysis* (2nd ed.) Elsevier.

24. Plastics news. *Current resin pricing - thermoset.* Retrieved Nov. 28, 2017, from http://www.plasticsnews.com/resin/thermosets/current-pricing

25. Fiber Glast Developments Corp. *Resins and Gel Coats*. Retrieved Nov. 28, 2017, from http://www.fibreglast.com/category/Resins.

26. McConnell, V.P. (2009). *Resins for the Hot Zone, Part II: BMIs, CEs, benzoxazines and phthalonitriles*. Retrieved Nov. 28, 2017, from https://www.compositesworld.com/articles/resins-for-the-hot-zone-part-ii-bmis-ces-benzoxazines-and-phthalonitriles.

27. Balasubramanian, M. (2014), *Composite Materials and Processing*. Boca Raton, FL: CRC Press.

28. Strong, A.B. (2007). *Fundamentals of Composites Manufacturing: Materials, Methods and Applications, 2nd ed*. Society of Manufacturing Engineers.

29. Molded Fiber Glass Companies. *Technical Design Guide for FRP Composite Products and Parts* Retrieved Nov. 28, 2017, from http://www.moldedfiberglass.com/sites/default/files/docs/MFG_Technical_Design_Guide_FRP_Composite_0.pdf

30. Advani, S.G. & Sozer, E.M. (2010). *Process Modeling in Composites Manufacturing, 2nd ed.* CRC Press.

31. D. Heider, D. & Gillespie, J. W. (20010). VARTM Variability and Substantiation. *Joint Advanced Materials & Structures Center of Excellence 2010 Conference*. Retrieved Nov. 28, 2017, from https://depts.washington.edu/amtas/events/jams_10/pap10-Heider.pdf.

32. Molded Fiber Glass Companies. *Vacuum Infusion Processing (VIP), RTM Light (LRTM, Resin Infusion, VARTM, SCRIMP)*. Retrieved Nov. 28, 2017, from http://www.moldedfiberglass.com/processes/processes/closed-molding-processes/vacuum-infusion-molding.

33. Irving, P.E. & Soutis, C. (2014). *Polymer Composites in the Aerospace Industry.* Elsevier Science.

34. Velicki, A. (2009). *Damage Arresting Composites for Shaped Vehicles*. NASA Langley Research Center, NASA/CR-2009-215932, LF99-8391. Retrieved Nov. 28, 2017, from https://ntrs.nasa.gov/search.jsp?R=20090034167.

35. Strongwell (2017). *Why Choose Strongwell?.* Retrieved Nov. 28, 2017, from https://www.linkedin.com/pulse/why-choose-strongwell-strongwell-corporation.

36. O'Connor, J.S. (2013). *Composite Bridge Decking: Final Report.* Federal Highway Administration Report: FHWA-HIF-13-029. Retrieved Nov. 28, 2017, from https://www.fhwa.dot.gov/hfl/partnerships/hif13029/fhwahif13029.pdf.

37. Transportation Research Board. *NCHRP IDEA 20-30/IDEA 030*. Retrieved April 4, 2016, from http://apps.trb.org/cmsfeed/trbnetprojectdisplay.asp?projectid=2005.

38. Plunkett, J.D (1997). *Fiber-Reinforced Polymer Honeycomb Short Span Bridge for Rapid Installation*. IDEA Project Final Report, Contract NCHPR-96-IDO30. Retrieved Nov. 28, 2017, from http://onlinepubs.trb.org/onlinepubs/archive/studies/idea/finalreports/highway/NCHRP030_Final_Report.pdf..

39. Zhou, E., Wang, Y., Meggers, D., & Plunkett, J. (2007). Field tests to determine static and dynamic response to traffic loads of fiber-reinforced polyester no-name creek bridge. *Transportation Research Record: Journal of the Transportation Research Board,* (2028), 231-237.

40. Liu, W., Zhou, E., & Wang, Y. (2012). *Response of No-Name Creek FRP Bridge to Local Weather*. Federal Highway Administration Report: FHWA-KS-12-6. Retrieved Nov. 28, 2017, from http://www.ksdot.org/PDF_Files/FHWAKS126_Final.pdf.

41. Bridgehunter.com – *Historical and Notable Bridges of the U.S.*-Plastic Bridge, Russell County, Kansas. Retrieved August 26, 2017 from https://bridgehunter.com/ks/russell/plastic/.

42. Nystromm H., Watkins, S., Stone, D., & Nanni, A. (2002). *Laboratory and Field Testing of FRP Composite Bridge Decks and FRP-Reinforced Concrete Bridge for the City of St. James, Phelps County, MO*. Federal Highway Administration Report:. RDT02-012. Retrieved Nov. 28, 2017, from https://library.modot.mo.gov/rdt/reports/ri00021/rdt02012.pdf.

43. Holdener, D., Myers, J., & Kleinhans, D. (2007). Six Year Performance Evaluation of St. James, Missouri, Composite Bridges. *Transportation Research Board, 87th Annual Meeting*. January 13-17, 2008, Washington, D.C. Retrieved Nov. 28, 2017, from http://transportation.mst.edu/media/research/transportation/documents/C65_2008_Myers.pdf.

44. Nims, D. (2013). *Huron County Ohio Innovative Bridge Construction Evaluation for Bridge FA-114-01.64*. Final Report for the Huron County, Ohio, Engineer. Retrieved Nov. 28, 2017, from http://www.dot.state.oh.us/Divisions/Planning/SPR/Research/reportsandplans/Reports/2013/Structures/.

45. Nystrom, H., Watkins, S., Nanni, A., & Murray, S. (2003). Financial viability of fiber-reinforced polymer (FRP) bridges. *Journal of Management in Engineering,* 19(1), 2-8. Retrieved Nov. 28, 2017, from http://transportation.mst.edu/media/research/transportation/documents/j6.pdf.

46. Barker, M., Staebler, J., & Barth, K. (2011). *Serviceability limits and Economical Steel Bridge Design*. Federal Highway Administration Report: FHWA-HIF-11-044. Retrieved Nov. 28, 2017 from https://www.fhwa.dot.gov/bridge/steel/pubs/hif11044/hif11044.pdf.

47. Neely, W., Cousins, T., Phifer, S., Senne, J., Case, S., Lesko, J., & Gomez, J. (2003). *Evaluation of the In-Service Performance of the Tom's Creek Bridge Fiber-Reinforced Polymer Superstructure*. Virginia Transportation Research Council Report: 04-CR5. Retrieved Nov. 28, 2017, from http://vtrc.virginiadot.org/PubDetails.aspx?PubNo=04-CR5.

48. Cousins. T. & Lesko, J. (2005). *Construction of a Virginia Short-span Bridge with the Strongwell 36-inch Double-web I-Beam*. Virginia Transportation Research Council Report: 06-CR5. Retrieved Nov. 28, 2017, from http://www.virginiadot.org/vtrc/main/online_reports/pdf/06-cr5.pdf.

49. Cousins. T. & Lesko, J. (2003). *EXTREN DWB Design Guide*. Retrieved Nov. 28, 2017, from http://www.strongwell.com/wp-content/uploads/2013/03/EXTREN-DWB-Design-Guide.pdf.

50. Fyfe (2015). *Tyfo SCH-41 Composite Data Sheet*. Retrieved Nov. 28, 2017, from http://www.fyfeco.com/-/media/Files/Fyfe/2013-Products/Tyfo%20SCH%2041.ashx?la=en.

51. Ulloa, F.V. & Fowler, T.J. (2002). *Composite Structural Members for Short Span Highway Bridges*. Texas Department of Transportation Research Project 0-1773. Retrieved Nov. 28, 2017, from https://fsel.engr.utexas.edu/pdfs/1773-1.pdf.

52. Reitmann, B. (2007). San Patricio Fiber Reinforced Polymer (FRP) Bridge. *2007 Design and Bridge Conference, Texas Department of Transportation*. August 15, 2007. Retrieved Nov. 28, 2017, from ftp://ftp.dot.state.tx.us/pub/txdot-info/des/presentations/desbrgconf07/reitmann%20frp_bridge.pdf.

53. Ramirez, G., Ziehl, P, & Fowler, T. (2009). Nondestructive Evaluation of Full-Scale FRP Bridge Beams Prior to Construction. *Research in Nondestructive Evaluation,* 20(1): 32-50. Retrieved Nov. 28, 2017, from https://www.researchgate.net/publication/233437227_Nondestructive_Evaluation_of_Full-Scale_FRP_Bridge_Beams_Prior_to_Construction.

54. Chen, Y., Ziehl, P., & Harrison, K. (2009). Experimental Characterization and Optimization of Hybrid FRP/RC Bridge Superstructure System. *Journal of Bridge Engineering,* 14(1), 45-54. Retrieved Nov. 28, 2017, from http://ascelibrary.org/doi/pdf/10.1061/%28ASCE%291084-0702%282009%2914:1%2845%29.

55. Williams, J. (2008). The Ongoing Evolution of FRP Bridges. *Public Roads (FHWA-HRT-08-006)*, 72(2), Sept/Oct 2008. Retrieved Nov. 28, 2017, from https://www.fhwa.dot.gov/publications/publicroads/08sep/03.cfm.

56. NetComposites (2008). *TxDOT Advances Viability of Custom FRP Bridge Beams*. Retrieved Nov. 28, 2017, from https://netcomposites.com/news/2008/march/28/txdot-advances-viability-of-custom-frp-bridge-beams/.

57. Maine Department of Transportation. *Research Reports and Publications: Bridge Research Reports.* Retrieved Nov. 28, 2017, from http://www.maine.gov/mdot/tr/rrp/.

58. Zhao, L., Burgueno, R., La Rovere, H., Seible, F., & Karbhari, V. (2000). *Preliminary Evaluation of the Hybrid Tube Bridge System*. California Department of Transportation Report: TR-2000/04. Retrieved Nov. 28, 2017, from http://www.dot.ca.gov/hq/esc/earthquake_engineering/Research/modgirde.pdf.

59. Van Den Einde, L., Zhao. L., & Seible,L. (2003). Use of FRP composites in civil structural applications. *Construction and Building Materials*, 17(6), 389-403.

60. Hillman, J. (2006). U.S. Patent #7562499 B2. Filing date January 13, 2006.

61. Aboelseoud, M. & Myers, J. (2015). Finite-Element Modeling of Hybrid Composite Beam Bridges in Missouri. *Journal of Bridge Engineering*, 20(1).

62. Hillman Bridge Company. Retrieved May 7, 2015, from. http://www.hcbridge.com/portfolio-single/2010-mo-b0439.

63. Gutírrez, E., Primi, S., Mieres, J. M., & Calvo, I. (2008). Structural testing of a vehicular carbon fiber bridge: Quasi-static and short-term behavior. *Journal of Bridge Engineering*, 13(3), 271-281.

64. Paulotto, C., Areiza Hurtado, M., Bansal, A., & Primi, S. (2012). FRP girder bridges: Lessons learned in spain in the last decade. *Proceedings of the 6th International Conference on FRP Composites in Civil Engineering, CICE 2012*.

65. Florida Department of Transportation (2009) *Temporary Design Bulletin C09-01.* Retrieved Nov. 28, 2017, from http://www.fdot.gov/structures/Bulletins/2009/TemporaryDesignBulletinC09-01.pdf.

66. Chawla, K. K. (2012). *Composite Materials: Science and Engineering, 3rd Edition.* Springer.

67. Bashtannik, T. I. (1998). Regulation of the mechanical properties of thermoplastic carbon fiber-reinforced plastics by changing their production conditions and surface treatment of the fibers. *Mechanics of Composites Materials*, 34(5), 483–488.

68. Hine, P. J., Brew, B., & Duckett, R. A. (1991). Failure mechanisms in carbon fibre reinforced poly (etheretherketone). *Composites Science Technology*, 40, 47–67.

69. Prandy, J. M., & Hahn H. T.(1990), "Advanced Materials: The Challenge of the Next Decade. *Proceedings of International SAMPE Symposium.* Edited by G. Janicki, V. Bailey, and H. Schjelderup, pp. 1657-1670.

70. Camponeschi, E. T. (1991). Compression of Composite Materials: A Review. *Composite Materials: Fatigue and Fracture*, 550(3), ASTM International.

71. Welsh, J. S., & Adams, D. F (1997). Current status of compression test methods for composite materials. *SAMPE journal*, 33(1), 35-43.

72. Dufner, E. (2014). *Boeing orders checks of 787 Dreamliners on fuselage delamination.* Retrieved August 01, 2015, from The Wichita Eagle: http://www.kansas.com/news/business/aviation/article1085788.html.

73. Whitney, J. M. (1973). *Analysis of the test methods for high modulus fibers and composites.* West Conshohocken, PA: ASTM International. Retrieved August 15, 2015, from https://doi.org/10.1520/STP521-EB.

74. Bergmann, H. (1985). *Carbon fibres and their composites.* (E. Filtzer, Ed.) Berlin: Springer Berlin Heidelberg.

75. Jegley, D. C, & Velicki, A. (2013). Status of advanced stitched unitized composite aircraft structures. *51st AIAA Aerospace Sciences Meeting.* Grapevine, TX, United States, Jan 07, 2013.

76. Jegley, D. C. (2013). Behavior of Frame-Stiffened Composite Panels with Damage. *54th AIAA/ASME/ASCE/AHS/ASC, Structures, Structural Dynamics, and Materials Conference.* Boston, MA, United States, Apr 08, 2013.

77. Eastep, F.E, Tischler, V.A., Venkayya, V.B. & Khot, N.S. (1999). Aeroelastic tailoring of composite structures. *Journal of Aircraft, 36*(6), 1041-1047.

78. Alyanak, E., & Pendleton, E. (2014). A Design Study Employing Aeroelastic Tailoring and an Active Aeroelastic Wing Design Approach on a Tailless Lambda Wing Configuration. *15th AIAA/ISSMO Multidisciplinary Analysis and Optimization Conference, AIAA AVIATION Forum.* Atlanta, GA, 16-20 June, 2014.

79. Cesnik, C., Hodgesy, H., & Patilz, J(1996). Aeroelastic Analysis of Composite Wings. *37th Structural Dynamics and Materials Conference.* Salt Lake City, Utah, April 15-17, 1996.

80. Prananta, B. B, Hounjet, M., & Eussen, B. (2009). *Flutter analyses of fighter aircraft with metallic and hybrid metal-composite wings.* National Aerospace Laboratory NLR.

81. Hollowell, S. J. (1981). *Aeroelastic flutter and divergence of graphite/epoxy cantilevered plates with bending-torsion stiffness coupling.* (Doctoral Dissertation) Massachusetts Institute of Technology.

82. Tenney, D. R., Davis, J. G., Pipes, R. B., Bray, J. L., & Johnston, N. (2009). *NASA Composite Materials Development: Lessons Learned and Future Challenges.* NATO Research and Technology Agency.

83. Curtis, P. T. (1987). An Investigation of the Tensile Fatigue Behaviour of Improved Carbon Fibre Composite Materials. *ICCM*, 6, 54-64.

84. Reifsnider, K. L., & Highsmith, A. L. (1981). Characteristic damage states: A new approach to representing fatigue damage in composite laminates. *Experimentation and Design in Fatigue*, 246-260.

85. Reifsnider, K. (1991). Damage and damage mechanics. In *Fatigue of Composite Materials.* BV, Amsterdam: Elsevier Science Publishers.

86. Scott, A. & Hepher, T. (2014). *Boeing reports wing cracks on 787 Dreamliners in production.* (2014). Retrieved June 15, 2015, from Reuters.com: http://www.reuters.com/article/2014/03/08/us-boeing-cracks-idUSBREA261QG20140308.

87. Scott, L. G., & Scala, C. M. (1982). A review of nondestructive testing of composite materials. *NDT International*, *15*(2), 75-86.

88. Reynolds, W. N. (1985). Nondestructive testing (NDT) of fiber-reinforced composite materials. *SAMPE Q, 16*(4), 1-16.

89. Hill, S. (1996). Rapid non-destructive testing of carbon fibre reinforced plastics. *Materials World, 4*(8).

90. Novel, P. K. (2008). Fiber-optic sensors. *Encyclopedia of structural health monitoring*, edited by Boller C., Chang F.K., and Fujino, Y.. Wiley.

91. Murayama, H., Kageyama, K., Naruse, H., Shimada, A., & Uzawa, K. (2003). Application of fiber-optic distributed sensors to health monitoring for full-scale composite structures. *Journal of Intelligent Material Systems and Structures, 14*(1), 3-13.

92. Daniel, I. M. & Ishai, O. (2006). *Engineering Mechanics of Composite Materials.* New York: Oxford University Press.

93. Staab, G. H. (1999). *Laminar Composites.* Oxford, UK: Butterworth-Heinemann.

94. Brunner, A. J. (2015). Fracture mechanics of polymer composites for aerospace industry. In *Polymer composites in the aerospace industry.* Cambridge: Woodhead Publishing Limited.

95. Larve, E. V., Mollenhauer, D., Whitney, T. J., & Kim, R. (2006). Strength prediction in composites with stress concentrations: classical Weibull and critical failure volume methods with micromechanical considerations. *Journal of Material Sciences*, *41*(20), 6610-6621.

96. Larve, E. V., Gurvich, M. R., Mollenhauer, D.H., Rose, C. A., & Davila, C. G., (2011). Mesh-independent matrix cracking and delamination modeling in laminated composites. *International Journal for Numerical Methods in Engineering*, *88*(8), 749-783.

97. Credeur, M. & Schlangenstein, M. (2013). *Engineering advances and better airline procedures have made crashes less deadly*. (2013). Retrieved June 10, 2015, from Bloomberg: http://www.bloomberg.com/bw/articles/2013-07-11/asiana-flight-214s-crash-shows-airline-safety-progress.

98. NASA (2017). *What's Next for NASA?* Retrieved Dec. 2, 2017, from https://www.nasa.gov/about/whats_next.html.

99. Renton, W. J., Olcott, D., Roeseler, W., Batzer, R., Baron, W., & Velicki, A. (2004). Future of Flight Vehicle Structures (2000-2023). *Journal of Aircraft, 41*(5), 986-998.

100. Velicki, A. & Jegley, D. (2014). PRSEUS structural concept development. *52nd AIAA Aerospace Sciences Meeting.* National Harbor, MD, January 13-17, 2014.

101. Bergan, A. C., Bakuckas, Jr J.G., Lovejoy, A. E., Jegley, D. C., Awerbuch, J., & Tan, T. M (2010). Assessment of Damage Containment Features of a Full-Scale PRSEUS Fuselage Panel through Test and Teardown. *American Society for Composites 27th Technical Conference.* Arlington, TX, Oct 01, 2012.

102. Gould, K., Lovejoy, A. E., Jegley, D. C., Neal, A. L., Linton, K. A., Bergan, A. C., & Bakuckas Jr J. G. (2014). Nonlinear Analysis and Post-Test Correlation for a Curved PRSEUS Panel. *Journal of Aircraft, 52*(2), 628-637.

103. Jegley, D. C., Velicki, A., & Hansen, D. A. (2008). Structural Efficiency Of Stitched Rod-Stiffened Composite Panels With Stiffener Crippling. *49th AIAA/ASME/ASCE/AHS/ASC Structures, Structural Dynamics, and Materials Conference.* Schaumburg, IL, April 7-10, 2008.

104. Yovanof, N., Lovejoy, A. E., Baraja, J., & Gould, K. (2012). Design, Analysis and Testing of a PRSEUS Pressure Cube to Investigate Assembly Joints. *Airworthiness and Sustainment Conference.* Baltimore, MD, April 2-5, 2012.

105. Jegley, D. C. (2009). *Experimental behavior of fatigued single stiffener PRSEUS specimens.* Hampton, VA: NASA Langley Research Center; NASA/TM-2009-215955.

106. Yovanof, N. P., & Jegley, D. (2011). Compressive behavior of frame-stiffened composite panels. *52nd AIAA Structures Dynamics and Materials Conference, AIAA.* Denver, CO, April 4-7, 2011.

107. Johnston, P. H. (2013). *Ultrasonic Nondestructive Evaluation of PRSEUS Pressure Cube Article in Support of Load Test to Failure.* Hampton, VA: NASA Langley Research Center; NASA/TM-2013-217799.

108. Wang, J. T., Grenoble R. W., & Pickell R. D. (2012). Structural Integrity Testing Method for PRSEUS Rod-Wrap Stringer Design. *53rd AIAA/ASME/ASCE/AHS/ASC Structures, Structural Dynamics and Materials Conference.* Honolulu, HI, April 23-26, 1012.

109. Jegley, D. (2012). Failure at Frame--Stringer Intersections in PRSEUS Panels. *American Society for Composites 27th Technical Conference.* Arlington, VA, October 1-3, 2012.

110. Young, R. (2009). NASA Perspectives on Airframe Structural Substantiation: Past Support and Future Developments. *FAA/EASA/Industry Composite Damage Tolerance and Maintenance Workshop.* Tokyo, Japan, June 4-5, 2009.

111. Li, V. & Velicki, A. (2008). Advanced PRSEUS Structural Concept Design and Optimization. *12th AIAA/ISSMO Multidisciplinary Analysis and Optimization Conference.* Victoria, British Columbia Canada, September 10-12, 2008.

112. American Association of State Highway and Transportation Officials (AASHTO). (2012). *AASHTO LRFD Guide Specifications for Design of Concrete-Filled FRP Tubes*, 1st Edition. Washington, D.C.: AASHTO.

113. Nolan, S. & McDaniel, G. (2013). Short-Medium Span Bridge Beams "Fill the Gap". Presentation at the *2013 FDOT design Expo*. Retrieved Mar. 4, 2016, from http://www.fdot.gov/design/training/DesignExpo/2013/Presentations/McDaniel_Nolan-Short-MediumSpanBridgeBeams.pdf.

114. Florida Department of Transportation (2016). *FDOT Index D20450 Series Florida Slab Beams*. Retrieved Mar. 4, 2017 from http://www.fdot.gov/roadway/DS/Dev/IDDS/IDDS-D20450.pdf.

115. Gibson, R.F. (2012). *Principles of Composite Materials Mechanics.* CRC Press.

116. Burgueno, R. (1999). *System Characterization and design of Modular Fiber Reinforced Polymer Short- and Medium-Span Bridges.* Dissertation completed at the University of California-San Diego.

117. Burgueno, R. & Bhide, K. (2006). Shear response of concrete-filled FRP composite cylindrical shells. *Journal of Structural Engineering,* 132(6), 949-60.

118. Vectorply (2017). *Vectorlam on-line laminate property calculator*. Retrieved Nov. 29, 2017, from http://vectorlamcirrus.cloudapp.net/#/.

119. Fyfe (2015). *Tyfo SEH-51A Composite Data Sheet*. Retrieved May 24, 2017, from http://www.fyfeco.com/-/media/Files/Fyfe/2013-Products/Tyfo-SEH-51A-Composite.ashx.

120. Vectorply (2015). *E-T 2200 Material Properties Data Sheet.* Retrieved May 24, 2017, from http://vectorply.com/wp-content/uploads/2015/06/E-T-22001.pdf.

121. Fiber Glast (2017). Retrieved Aug. 11, 2017 from http://www.fibreglast.com/product/Continuous_Strand_Mat_251/Fiberglass_Mat.

122. Ziehl, P., Engelhardt, M., Fowler, T., Ulloa, F., Medlock, R., & Schell, E. (2009). Design and field evaluation of hybrid FRP/Reinforced concrete superstructure system. *Journal of Bridge Engineering,* 14(5),309-18.

123. Hillman, J. R. (2012). *Hybrid-Composite Beam (HCB®) Design Manual*." Retrieved Mar. 10, 2017, from http://aii.transportation.org/Documents/BMDO/HCB-design-maint-manual.pdf.

124. Hillman, J. R. (2003). *Investigation of a Hybrid-Composite Beam System*. Final report for High-Speed Rail IDEA Project 23. Retrieved Mar. 10, 2017, from http://citeseerx.ist.psu.edu/viewdoc/download?doi=10.1.1.603.4896&rep=rep1&type=pdf.

125. Priestley, M.J.N., Seible, F., & Calvi, G.N. (1996). *Seismic Design and Retrofit of Bridges.* New York, NY: Wiley & Sons.

126. Ahmad, I, Zhu, Z., Mirmiran, A., & Fam, A. (2005). Shear Strength Prediction of Deep CFFT Beams. *ACI Special Publication 230*. Retrieved Nov. 29, 2018 from http://www.quakewrap.com/frp%20papers/ShearStrengthPredictionofDeepCFFTBeams.pdf. .

127. Yu, T. & Teng, J. (2011). Design of Concrete-Filled FRP Tubular Columns: Provisions in the Chinese Technical Code for Infrastructure Application of FRP Composites. *Journal of Composites for Construction,* 15(3), 451-61.

128. Neely, W. D. (2000). *Evaluation of the in-service performance of the Tom's Creek bridge*. Master's Thesis at Virginia Tech. Retrieved Nov. 29, 2017, from http://scholar.lib.vt.edu/theses/available/etd-05262000-09210036.

129. Restrepo, E. S. (2002). *Determination of AASHTO bridge design parameters through field evaluation of the Rt. 601 bridge: A bridge utilizing strongwell 36 in. fiber-reinforced polymer*

double web beams as the main load carrying members. Master's Thesis at Virginia Tech. Retrieved Nov. 29, 2017, from http://hdl.handle.net/10919/36182.

130. Siwowski, T., Kaleta, D., & Rajchel, M. (2015). Design and research on the first polish FRP composite road bridge. *Romanian Journal of Transport Infrastructure*, 4(2), 62-74.

131. Metal Dek Group. *Stay Ahead with Stay-In-Place: Rhino-Dek, Bridge Forms for Aggressive Environments.* Retrieved Nov. 29, 2017, from http://www.metaldek.com/UserFiles/File/eBinder/brochures/Rhino-Dek%20brochure.pdf.

132. Siwowski, T. & Rajchel, M. (2015). Design and research on the first polish FRP composite road bridge. *International Scientific Conference: Road Research and Administration, "CAR 2015".* Bucharest, Hungary, July 9-11, 2015. Retrieved July 25, 2017, from : https://www.researchgate.net/publication/284347096_Design_and_research_on_the_first_polish_FRP_composite_road_bridge.

133. Telang, N., Dumlao, C., Mehrabi, A., Ciolko, A., & Gutierrez, J. (2006). *Field Inspection of In-Service FRP Bridge Decks*. NCHRP Report No. 564. Retrieved Nov. 29, 2017, from https://www.nap.edu/download/23284.

134. Nishizaki, I. (2009). Life-Cycle Cost Assessment for FRP Structures. *Proceedings of US-Japan Workshop on Life Cycle Assessment of Sustainable Infrastructure Materials*. Sapporo, Japan, October 21-22, 2009.

135. Nishizaki, I. et al. (2006). A Case Study of Life Cycle Cost based on a Real FRP Bridge. *Third International Conference on FRP Composites in Civil Engineering (CICE 2006)*. December 13-15 2006, Miami, Florida, USA.

136 Keller, T., Bai, Y., & Vallee, T. (2007). Long-Term Performance of a Glass Fiber-Reinforced Polymer Truss Bridge. *Journal of Composites for Construction*, 11(1), 99-108.

137. Tomlinson, S. (2016). *AIT Long-Term Composite Arch System Durability Evaluation Report*. University of Maine – Advanced Structures and Composites Center: Report No. 16-20-267.

Appendix A – Optimization Curves for AASHTO Distribution Factor Method

The graphs provided in this appendix summarize two basic results that were determined using the AASHTO distribution factor method for FRP U-Girders and concrete-filled FRP tubes (CFFTs):

1. **Total girder cost vs. girder depth** for span lengths = 30 ft, 40 ft, 50 ft, 60 ft, and 75 ft. These are referred to as "cost optimization curves". For the FRP U-girders, two graphs are provided for each span length. The first graph is based on the LS-2a displacement criteria and the second graph is based on the LS-2c displacement criteria. For LS-2a, the concrete below the slab **does not** contribute to the overall flexural stiffness of the bridge. For LS-2c, 100% of the concrete below the slab is assumed to contribute to the overall flexural stiffness. For the CFFTs, only results for LS-2c are provided. For both of these cases, the stiffness contribution of the cast-in-place barriers are ignored. Finally, each graph contains the curve for a six-girder bridge (N_b = 6) and an eight-girder bridge (N_b = 8). These results are summarized in Figure A-1 through Figure A-5 for the FRP U-girders and Figure A-16 through Figure A-20 for the CFFTs.
2. **Minimum required FRP thickness vs. girder depth** for each limit state (also for span lengths = 30 ft, 40 ft, 50 ft, 60 ft, and 75 ft). These are referred to as "required thickness curves". For the FRP U-girders, a total of four graphs are provided for each span length. Results based on LS-2a (0% concrete stiffness below slab) are provided in Figure A-6 through Figure A-10. Results based on LS-2c (100% concrete stiffness below slab) are provided in Figure A-11 through Figure A-15. Two graphs are provided for each span length (one for N_b = 6 and one for N_b = 8) and each graph contains a required thickness curve corresponding to each of the following five limit states:
    i. LS-1: Concrete compressive stresses
    ii. LS-2: Displacements
        a. LS-2a = 0% concrete stiffness below the slab
        b. LS-2c = 100% concrete stiffness below the slab
    iii. LS-3: Fatigue and creep rupture
    iv. LS-4a: Strength in flexure
    v. LS-4b: Strength in shear

    For the CFFTs, only two graphs are provided for each span length (one for N_b = 6 and one for N_b = 8). These graphs are provided in Figure A-21 through Figure A-25. All results for the CFFTs assume a 100% stiffness contribution for the concrete below the slab.

A reference guide that summarizes the location for each result is provided in Table A- 1.

Table A- 1. Quick reference guide for AASHTO distribution factor optimization and required thickness curves

Span length (ft)	Girder type	Result type	Displacement limit state criteria	Figure ID
30	U	Optimization curve	2a & 2c	Figure A-1
40	U	Optimization curve	2a & 2c	Figure A-2
50	U	Optimization curve	2a & 2c	Figure A-3
60	U	Optimization curve	2a & 2c	Figure A-4
75	U	Optimization curve	2a & 2c	Figure A-5
30	U	Required thickness	2a	Figure A-6
40	U	Required thickness	2a	Figure A-7
50	U	Required thickness	2a	Figure A-8
60	U	Required thickness	2a	Figure A-9
75	U	Required thickness	2a	Figure A-10
30	U	Required thickness	2c	Figure A-11
40	U	Required thickness	2c	Figure A-12
50	U	Required thickness	2c	Figure A-13
60	U	Required thickness	2c	Figure A-14
75	U	Required thickness	2c	Figure A-15
30	CFFT	Optimization curve	2c	Figure A-16
40	CFFT	Optimization curve	2c	Figure A-17
50	CFFT	Optimization curve	2c	Figure A-18
60	CFFT	Optimization curve	2c	Figure A-19
75	CFFT	Optimization curve	2c	Figure A-20
30	CFFT	Required thickness	2c	Figure A-21
40	CFFT	Required thickness	2c	Figure A-22
50	CFFT	Required thickness	2c	Figure A-23
60	CFFT	Required thickness	2c	Figure A-24
75	CFFT	Required thickness	2c	Figure A-25

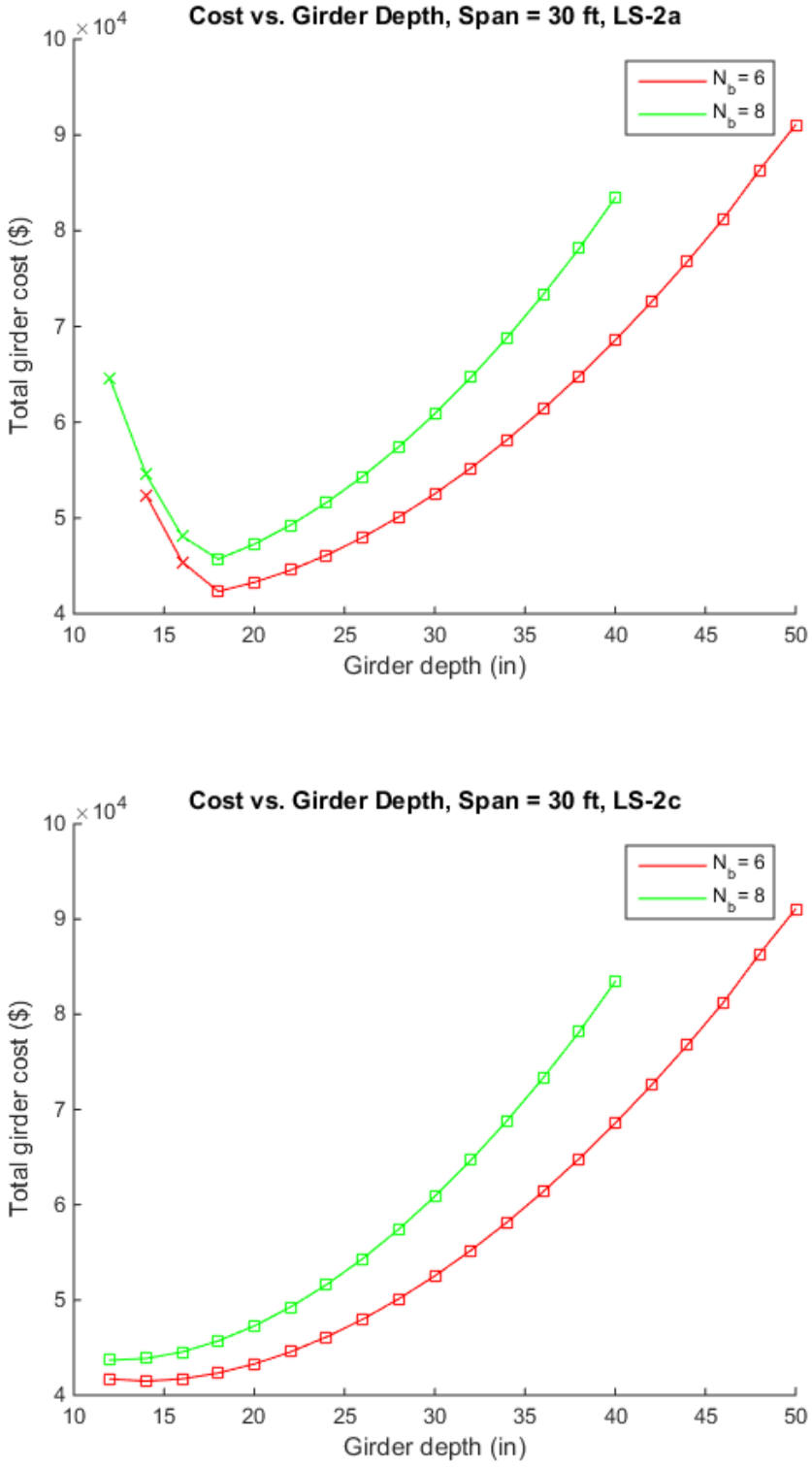

Figure A-1. FRP U-girder cost optimization curves for span length = 30 ft (return to Table A- 1)

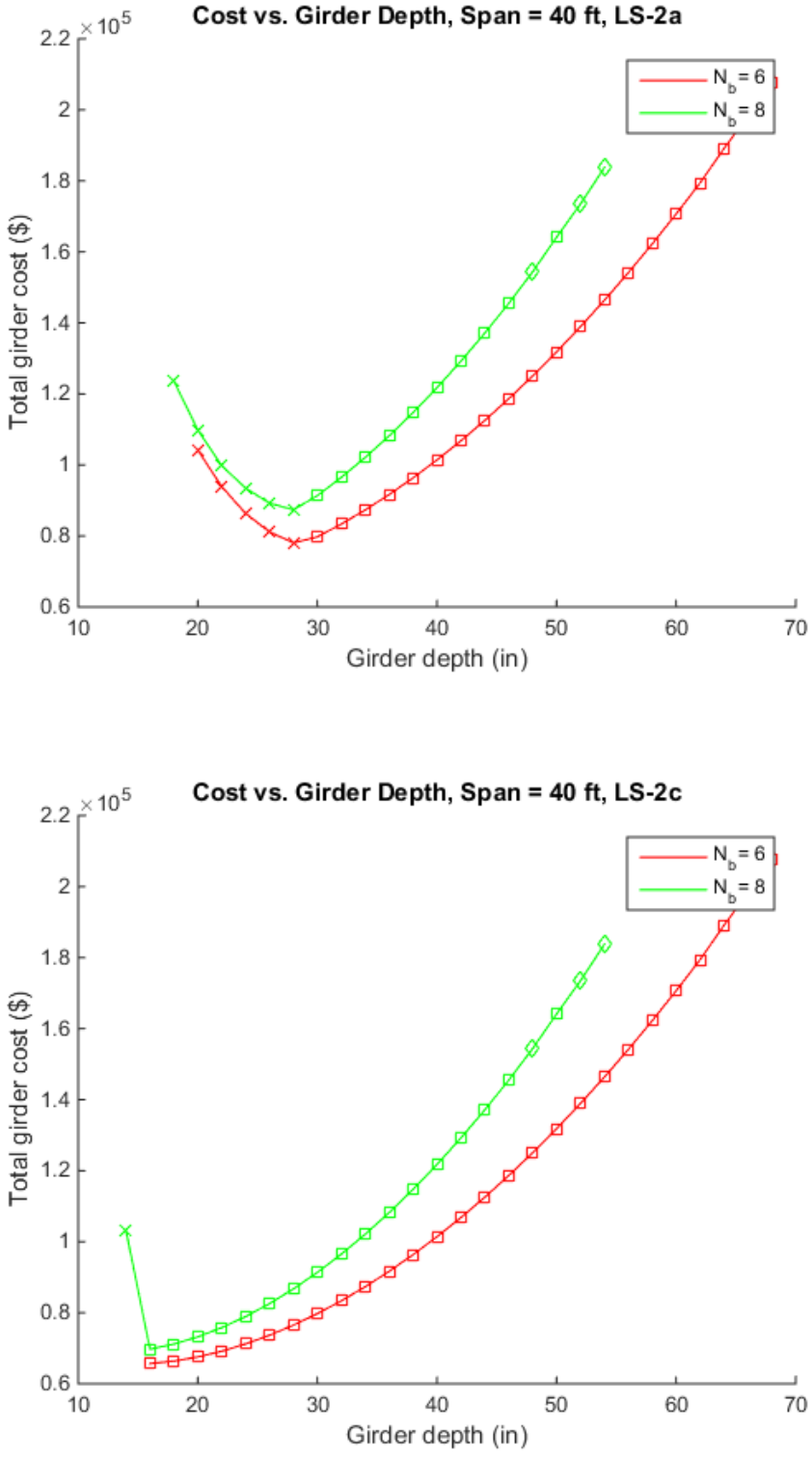

Figure A-2. FRP U-girder cost optimization curves for span length = 40 ft (return to Table A- 1)

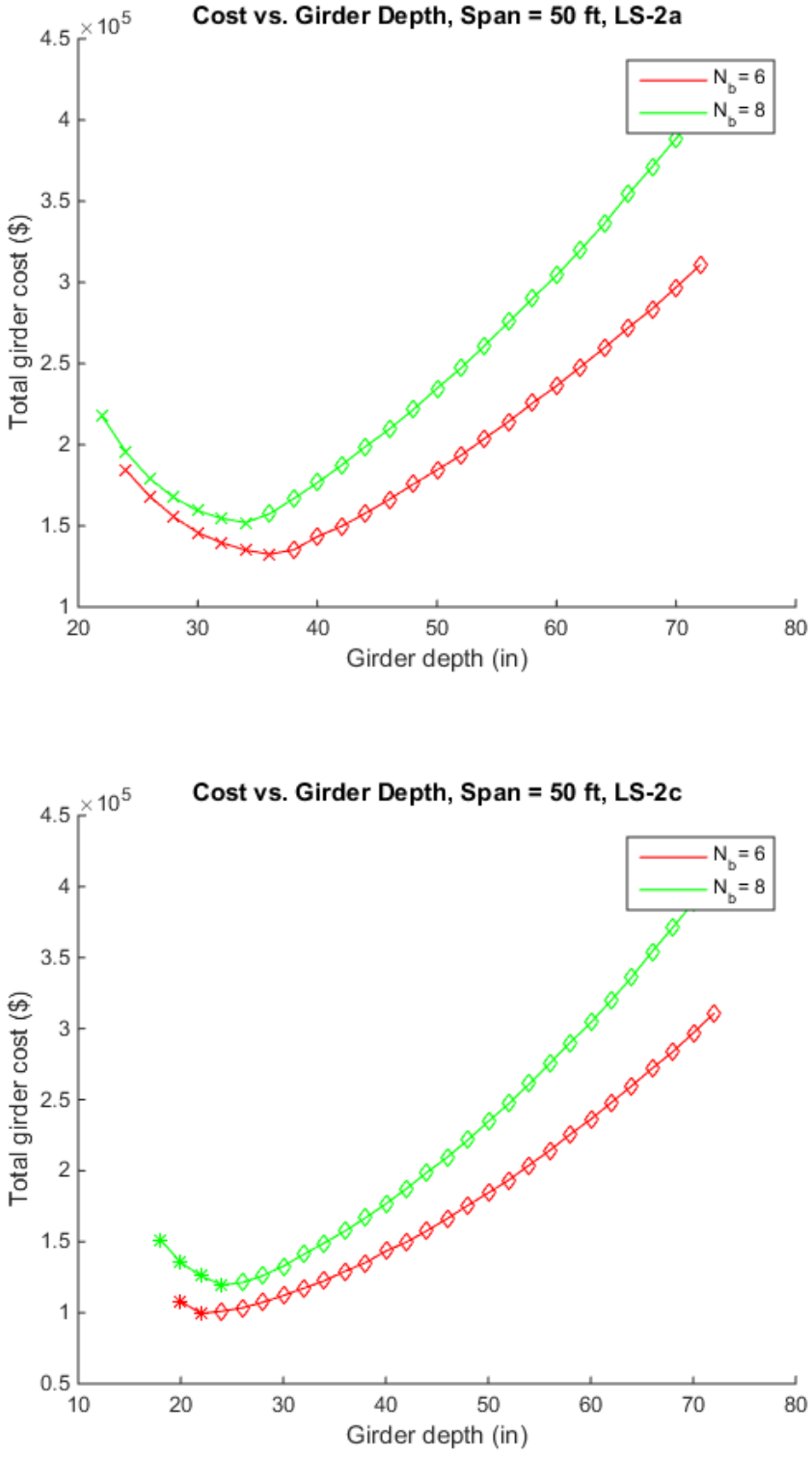

Figure A-3. FRP U-girder cost optimization curves for span length = 50 ft (return to Table A- 1)

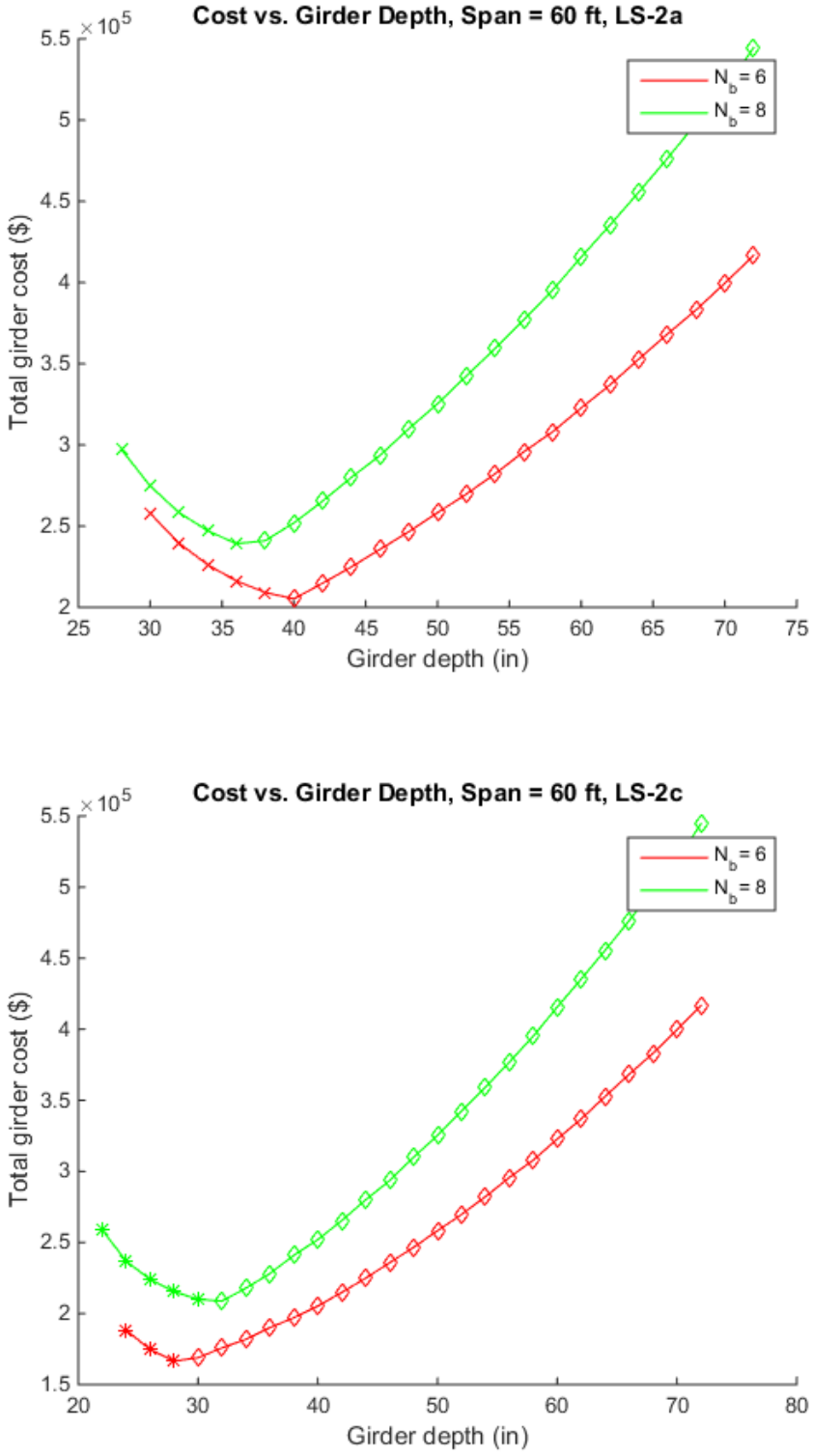

Figure A-4. FRP U-girder cost optimization curves for span length = 60 ft (return to Table A- 1)

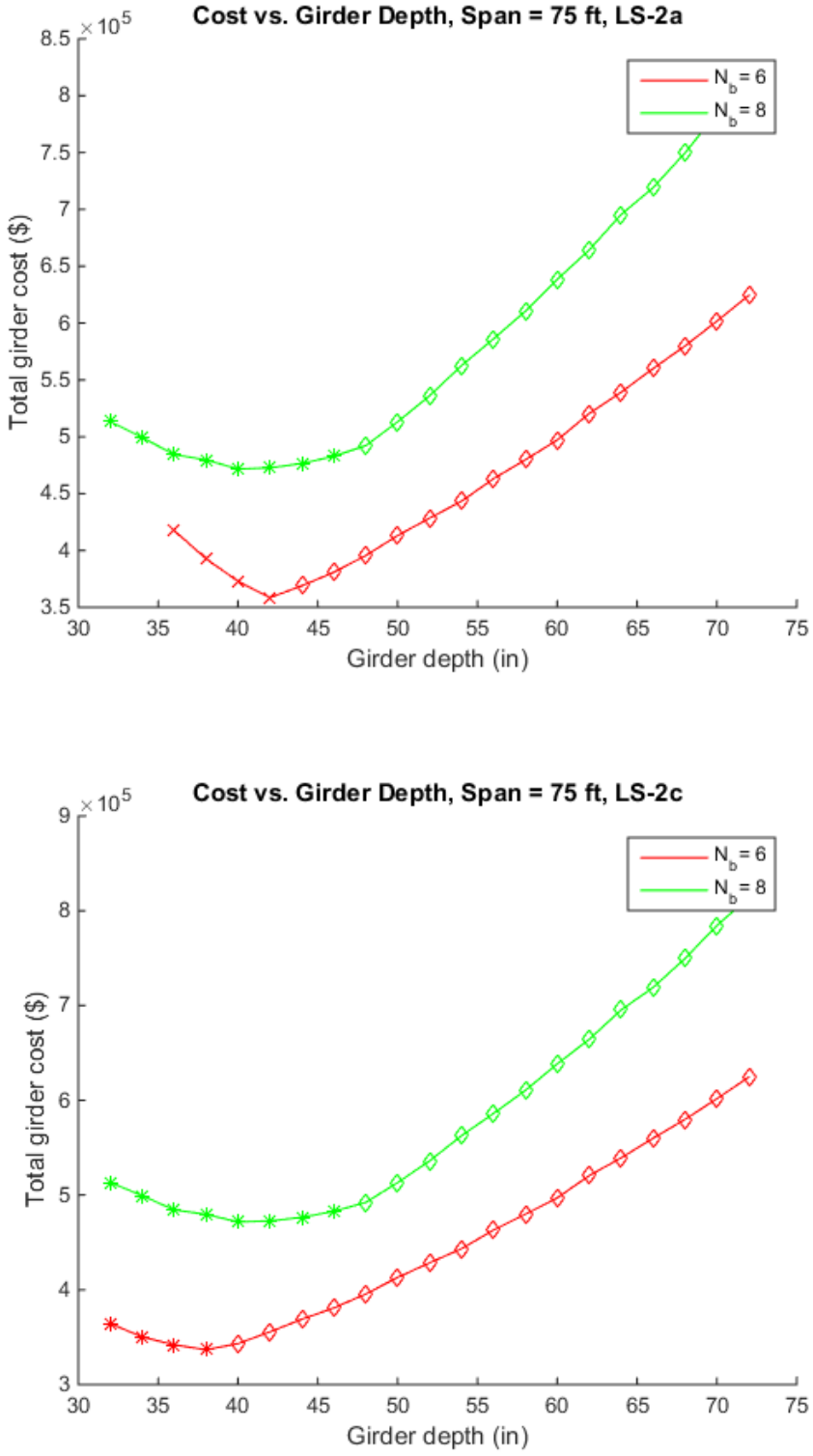

Figure A-5. FRP U-girder cost optimization curves for span length = 75 ft (return to Table A- 1)

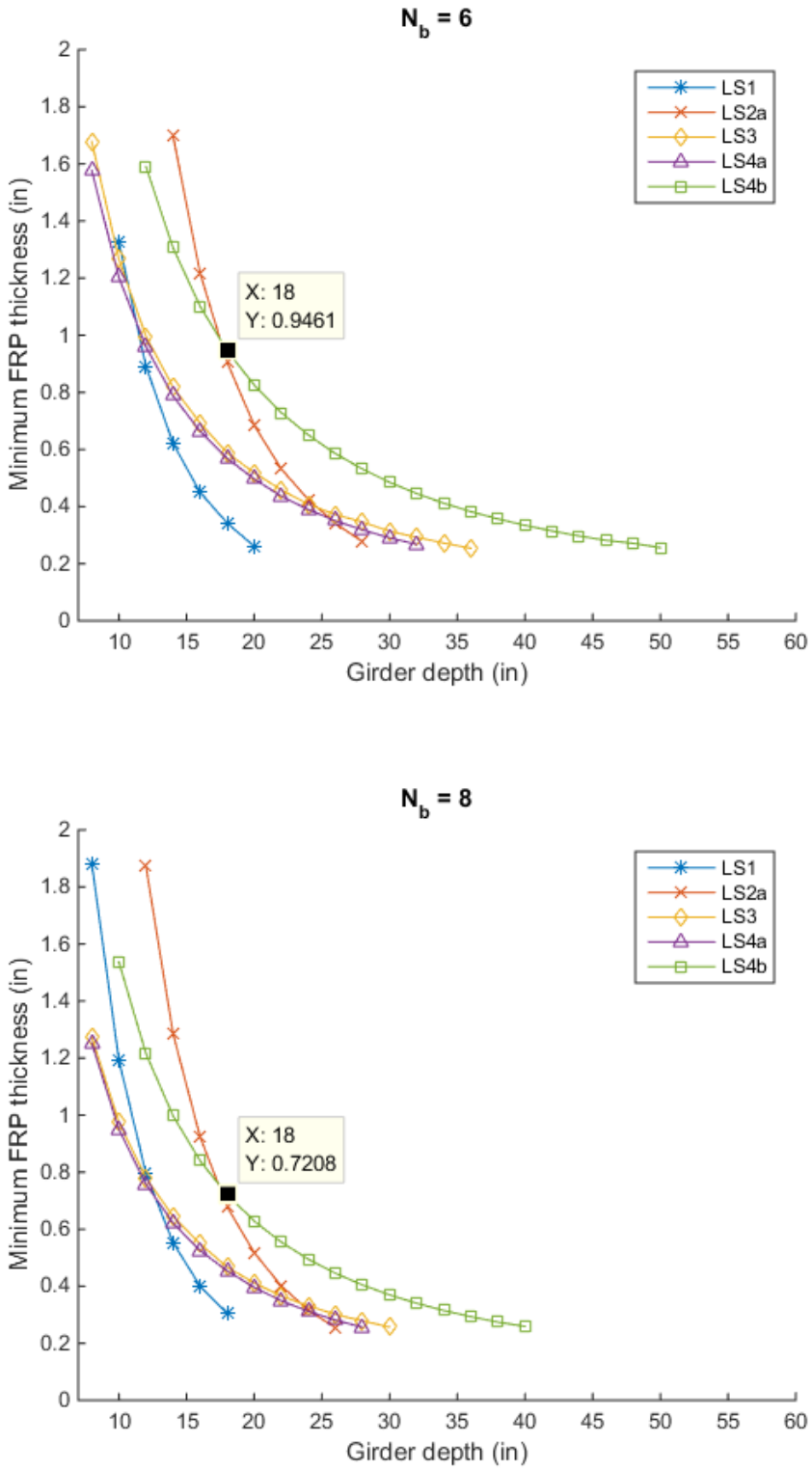

Figure A-6. FRP U-girder required thickness curves for span length = 30 ft, LS-2a (return to Table A- 1)

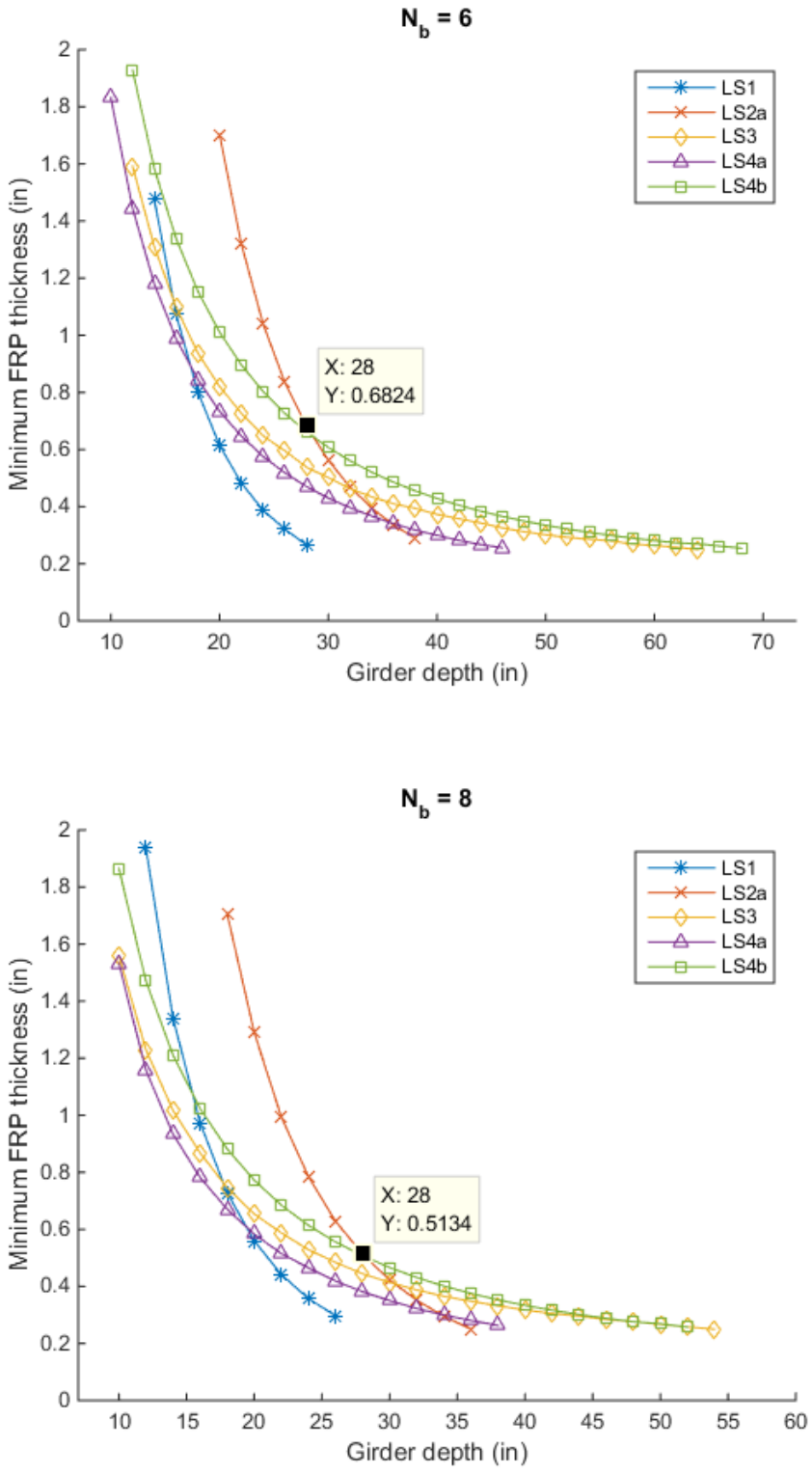

Figure A-7. FRP U-girder required thickness curves for span length = 40 ft, LS-2a (return to Table A- 1)

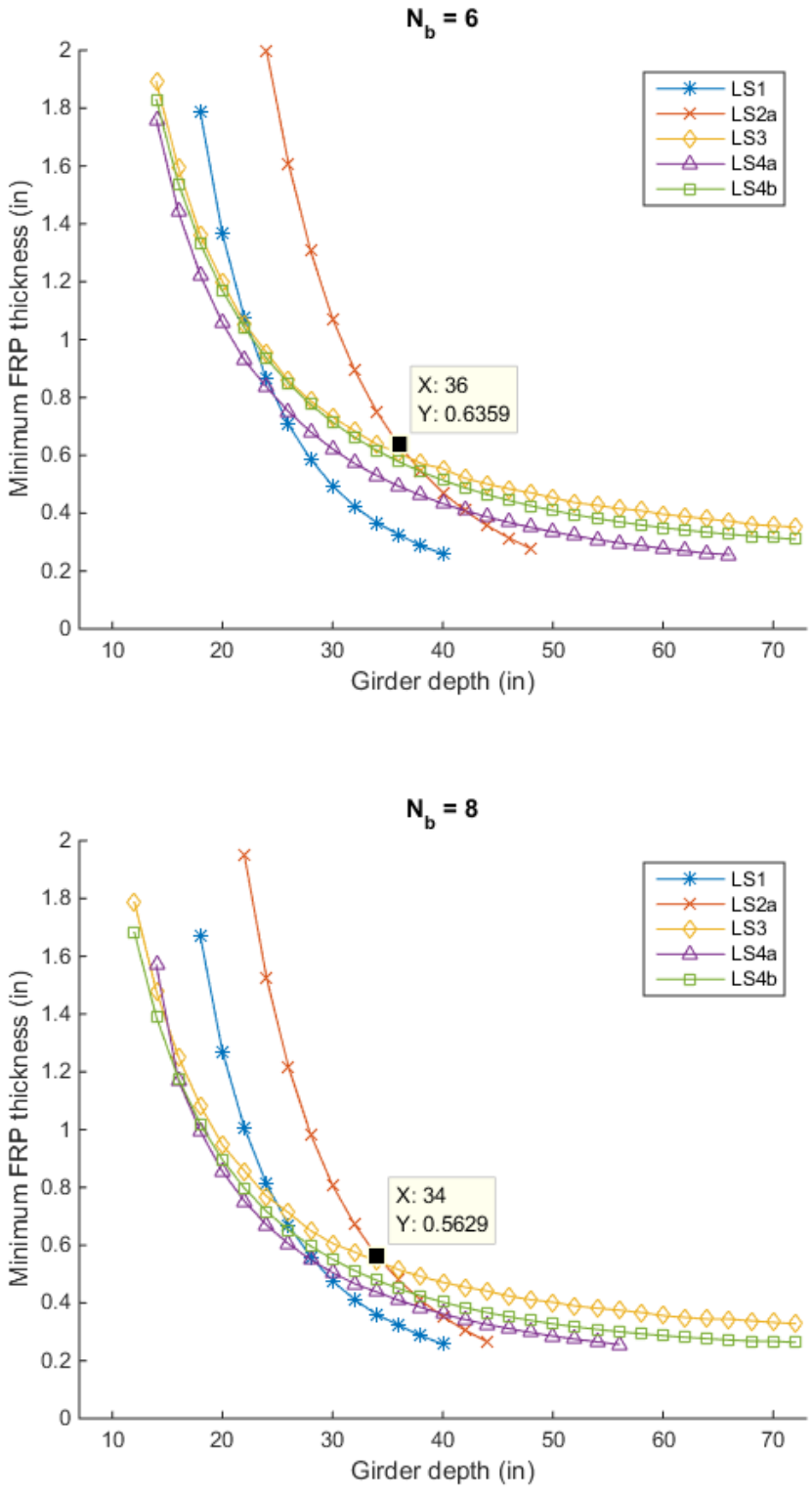

Figure A-8. FRP U-girder required thickness curves for span length = 50 ft, LS-2a (return to Table A- 1)

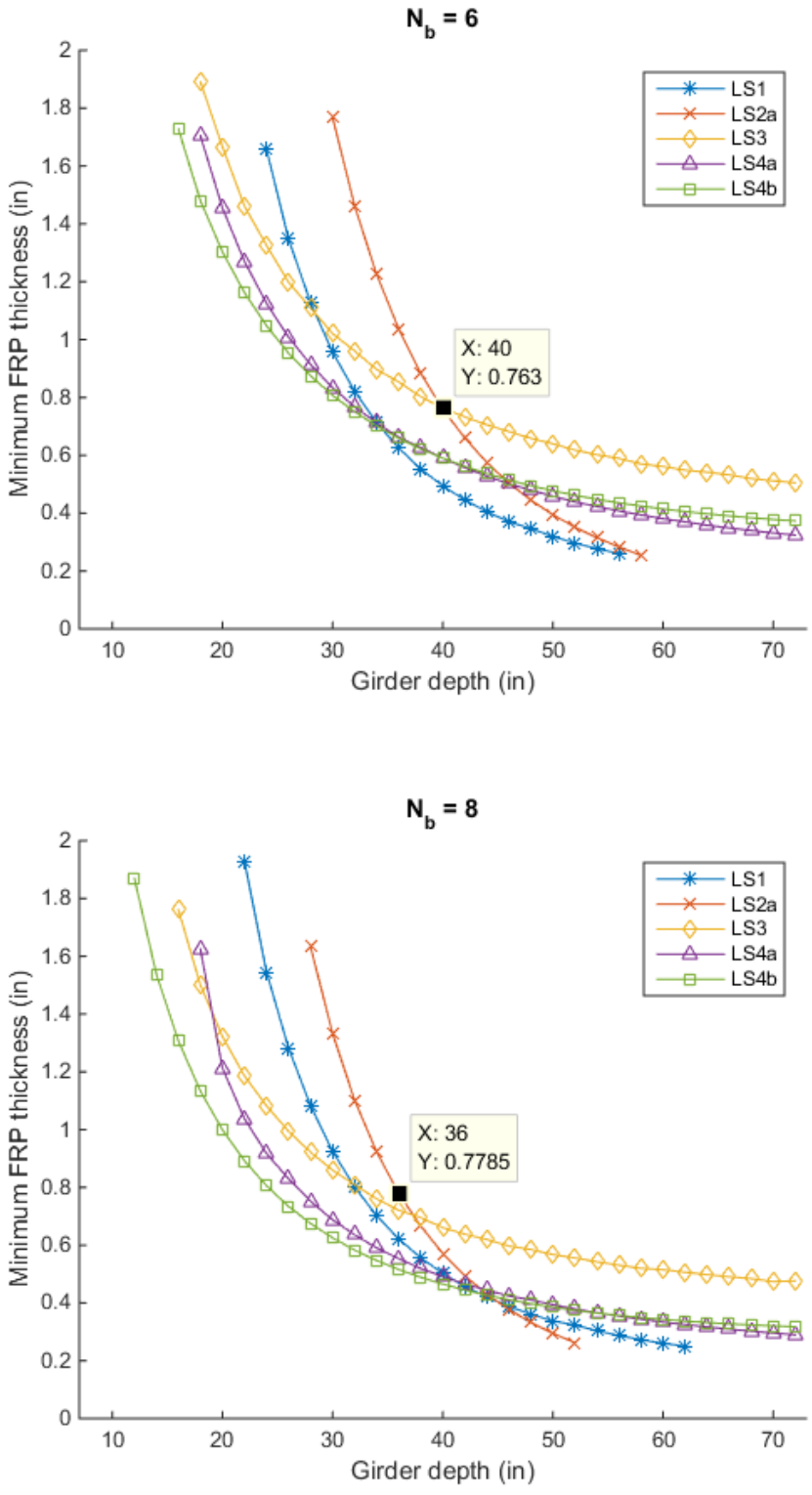

Figure A-9. FRP U-girder required thickness curves for span length = 60 ft, LS-2a (return to Table A- 1)

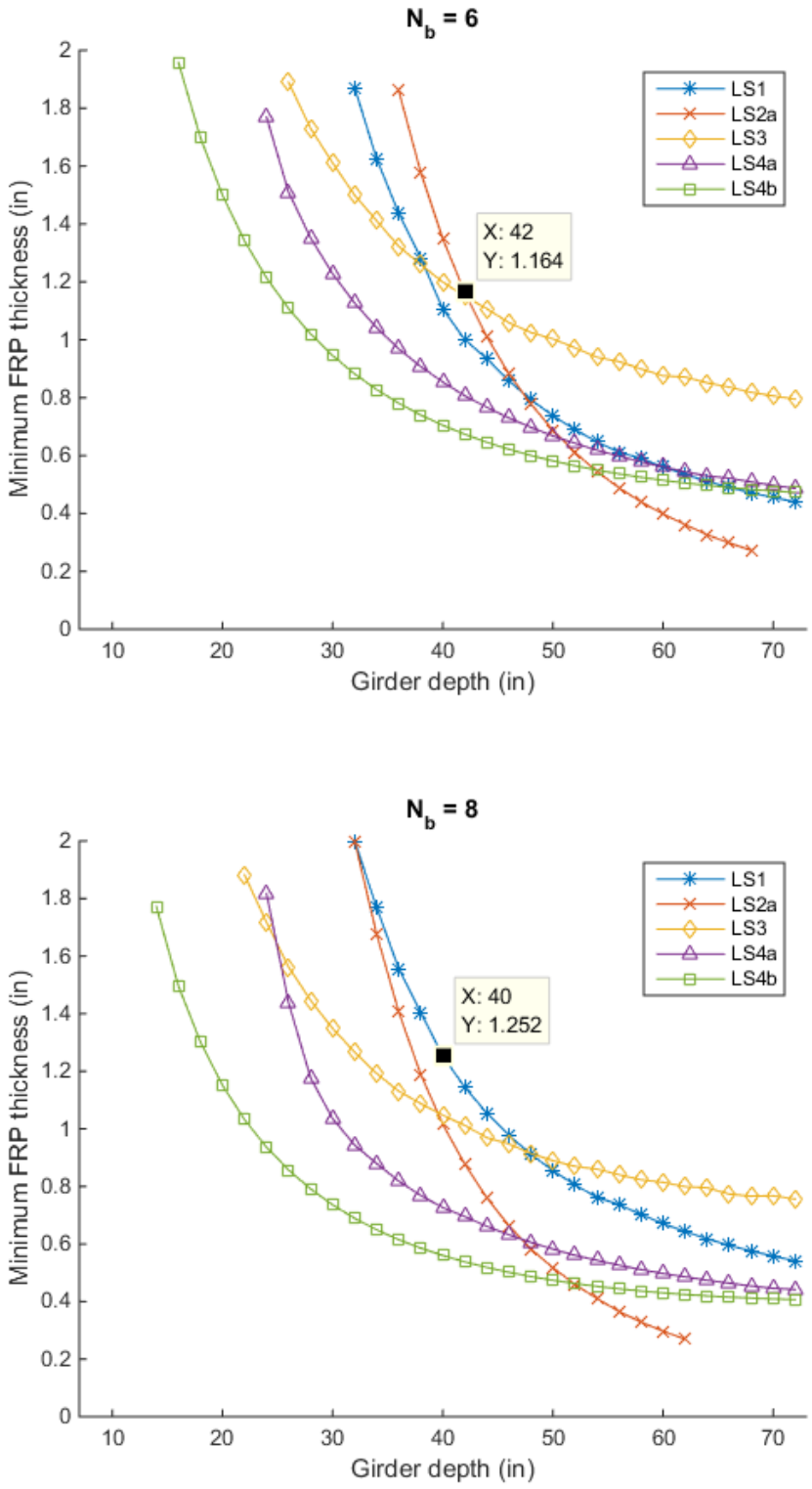

Figure A-10. FRP U-girder required thickness curves for span length = 75 ft, LS-2a (return to Table A- 1)

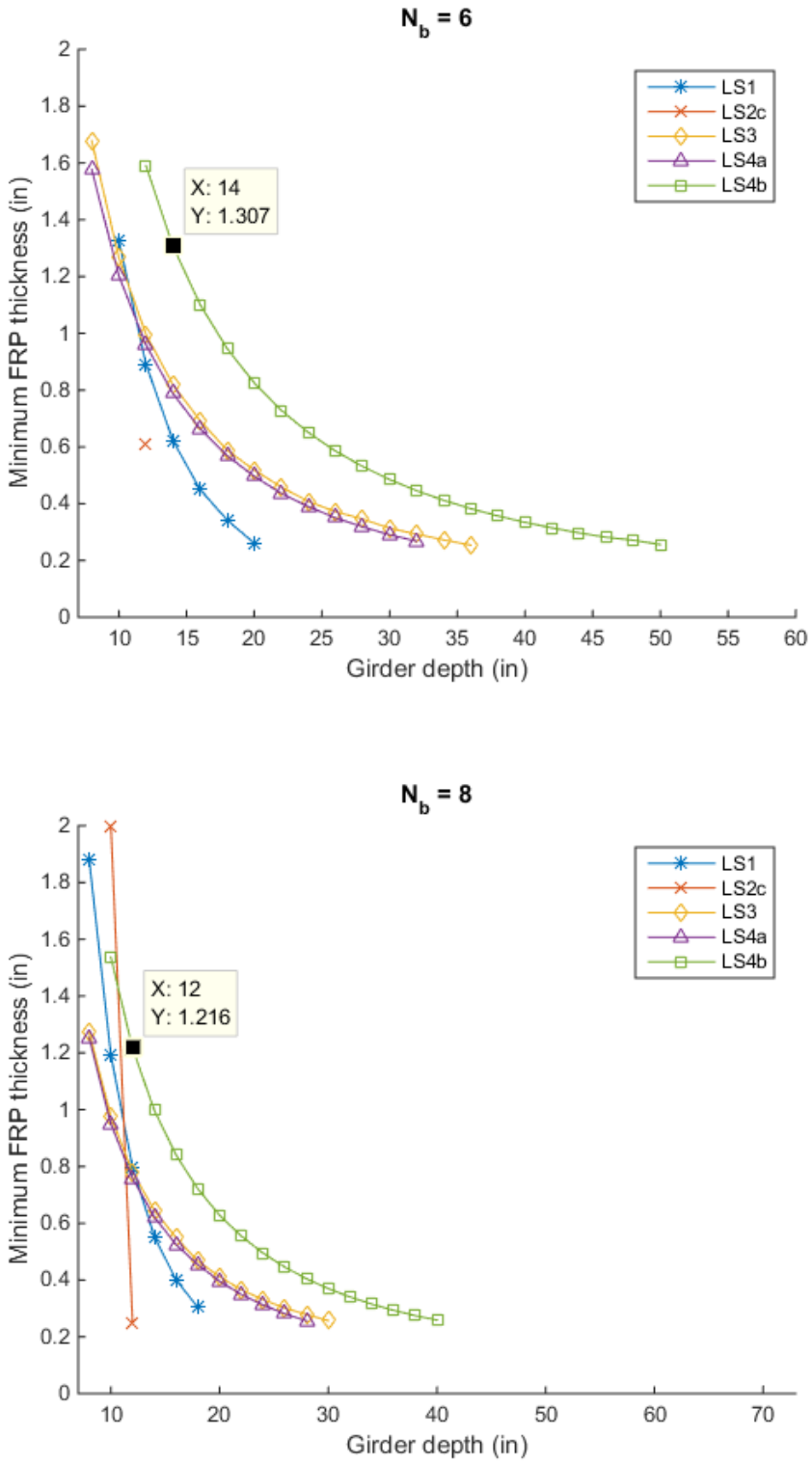

Figure A-11. FRP U-girder required thickness curves for span length = 30 ft, LS-2c (return to Table A- 1)

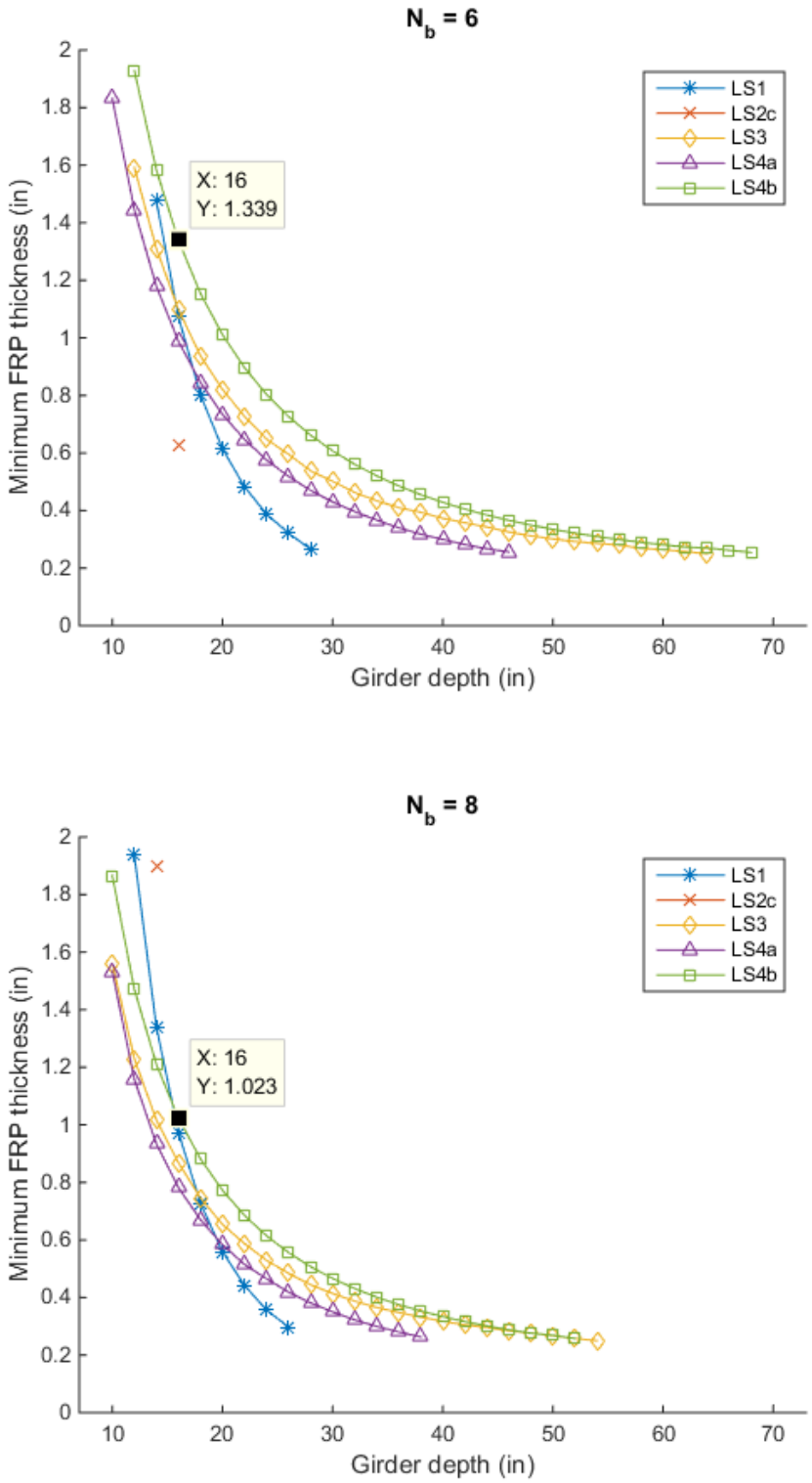

Figure A-12. FRP U-girder required thickness curves for span length = 40 ft, LS-2c (return to Table A- 1)

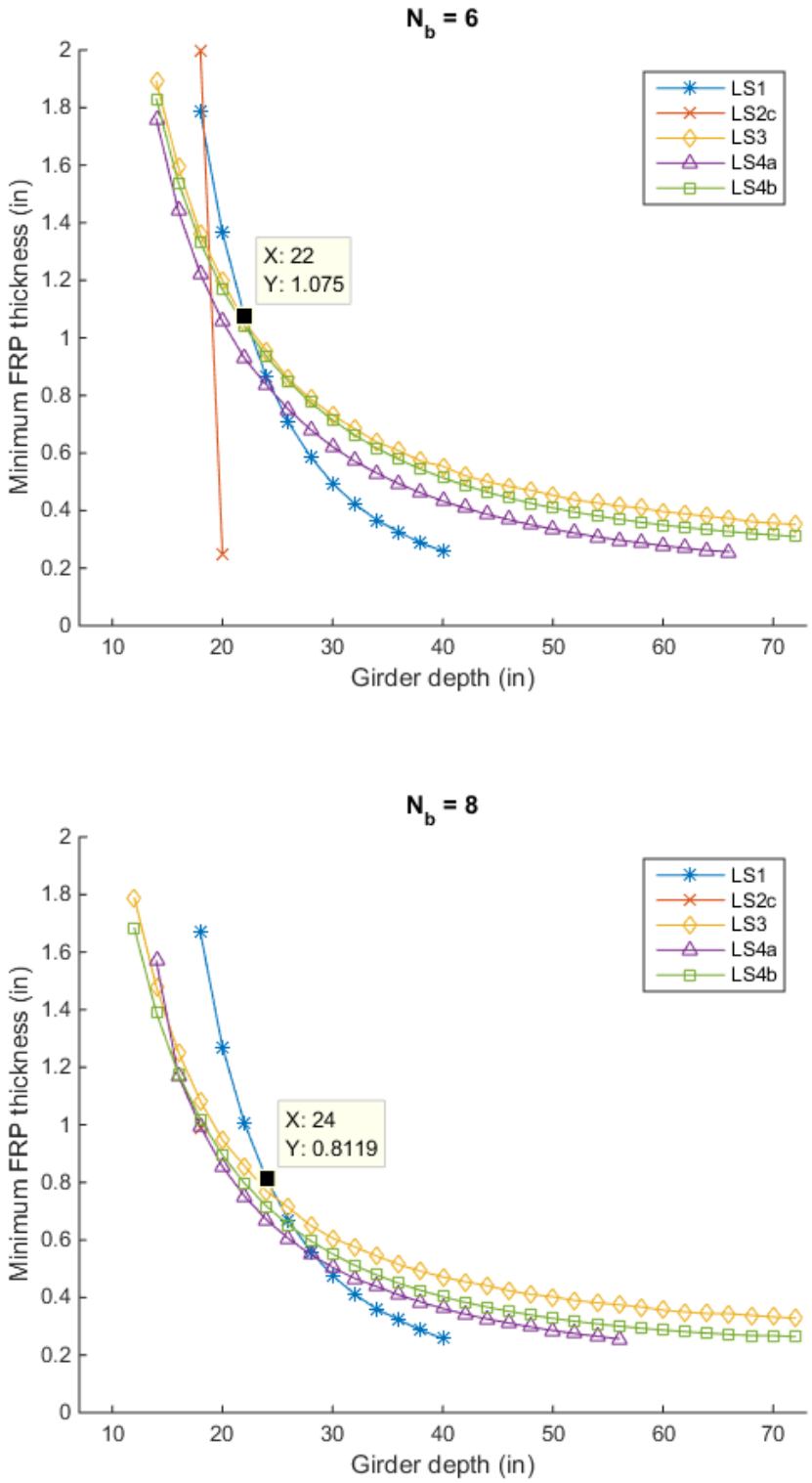

Figure A-13. FRP U-girder required thickness curves for span length = 50 ft, LS-2 (return to Table A- 1)

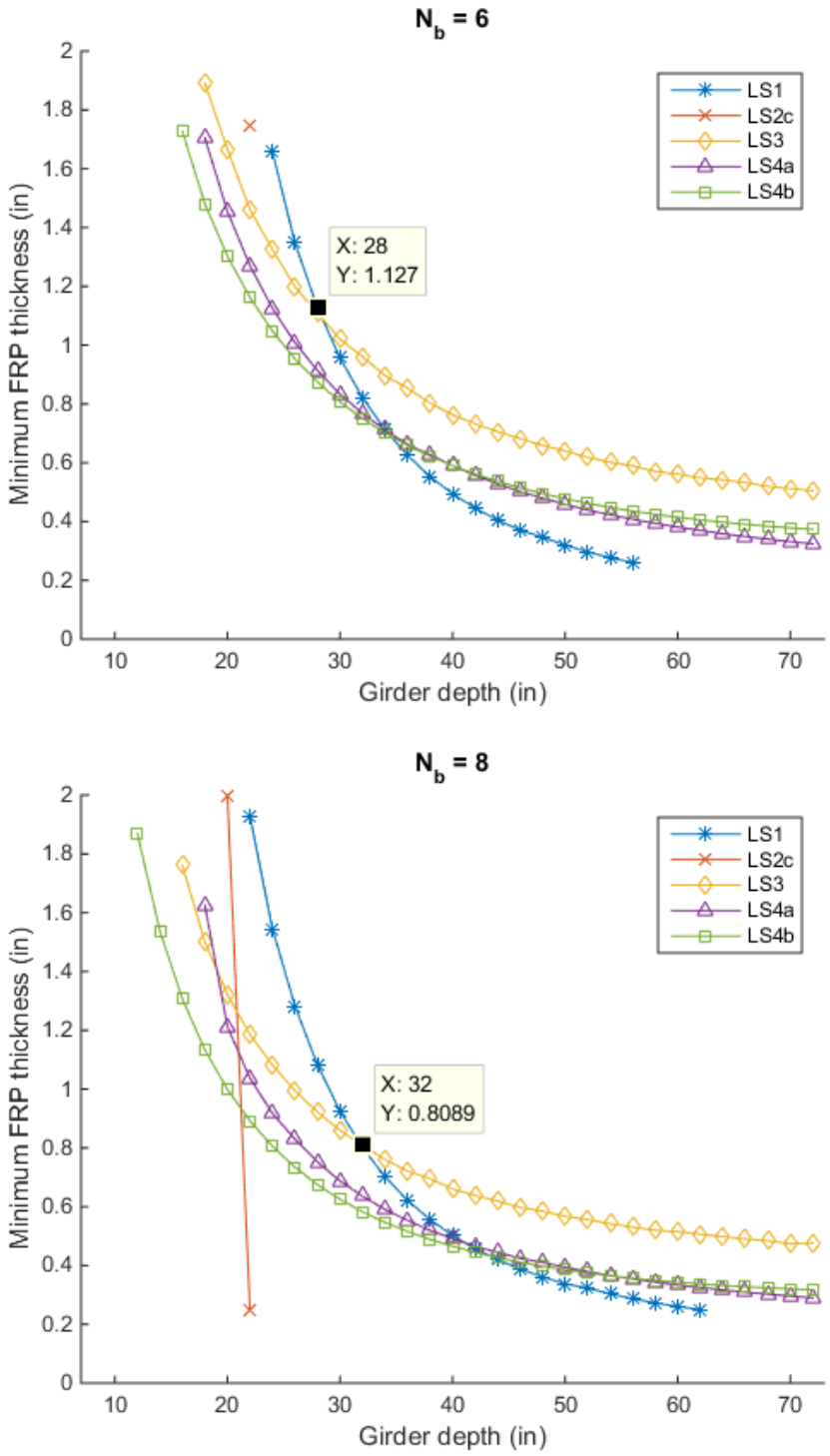

Figure A-14. FRP U-girder required thickness curves for span length = 60 ft, LS-2c (return to Table A- 1)

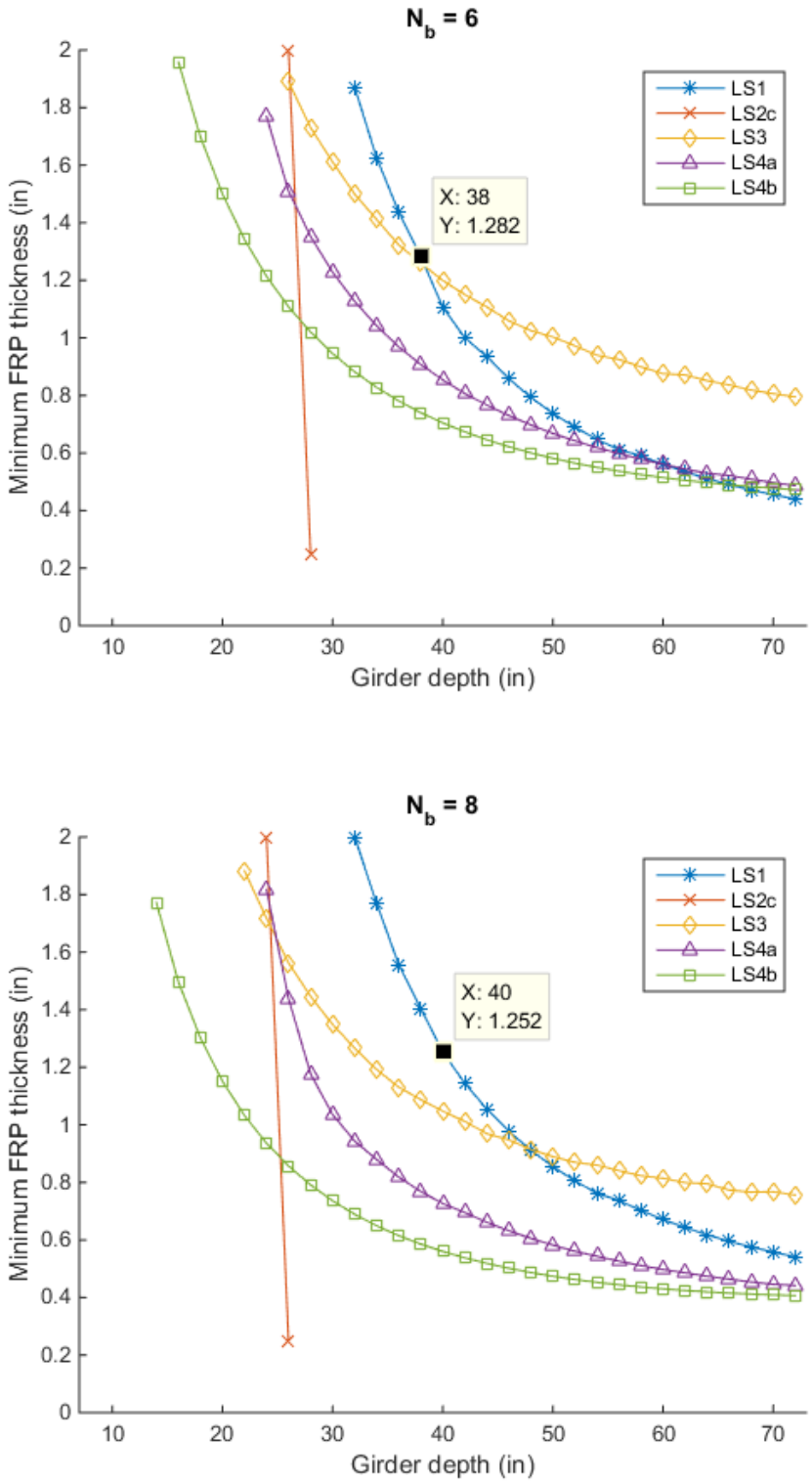

Figure A-15. FRP U-girder required thickness curves for span length = 75 ft, LS-2c (return to Table A- 1)

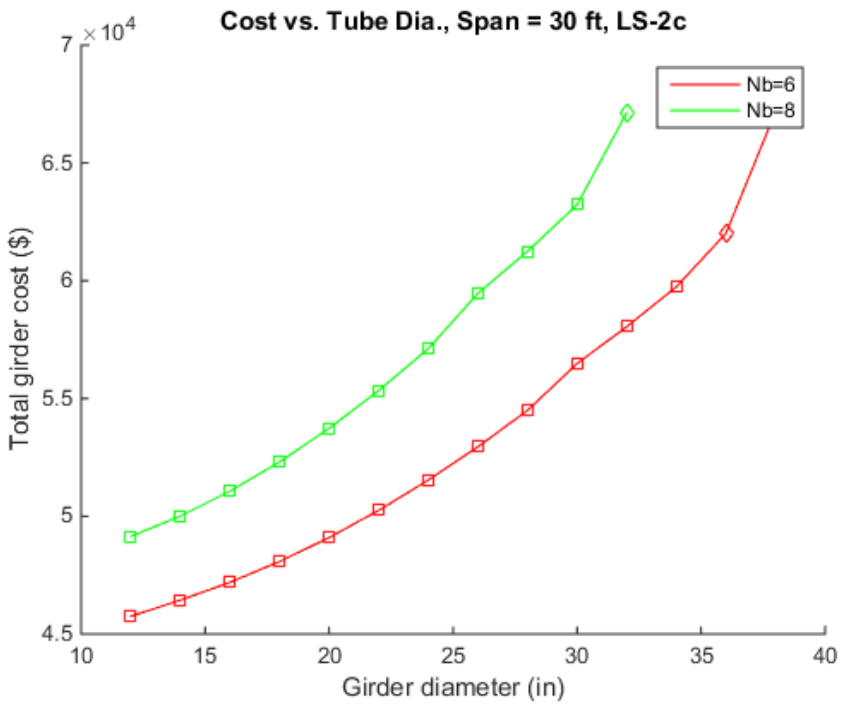

Figure A-16. CFFT cost optimization curves for span length = 30 ft (return to Table A- 1)

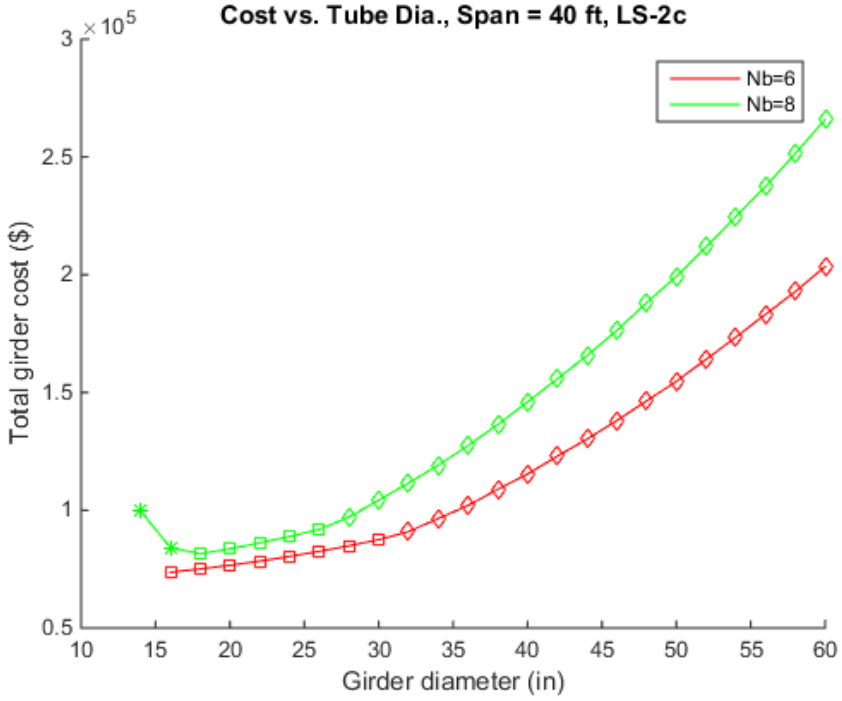

Figure A-17. CFFT cost optimization curves for span length = 40 ft (return to Table A- 1)

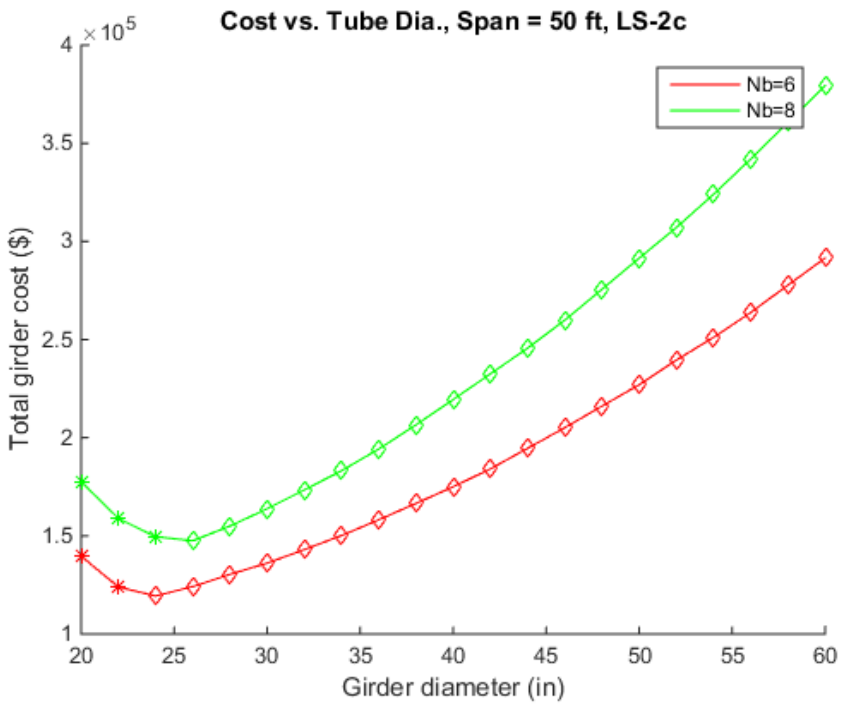

Figure A-18. CFFT cost optimization curves for span length = 50 ft (return to Table A- 1)

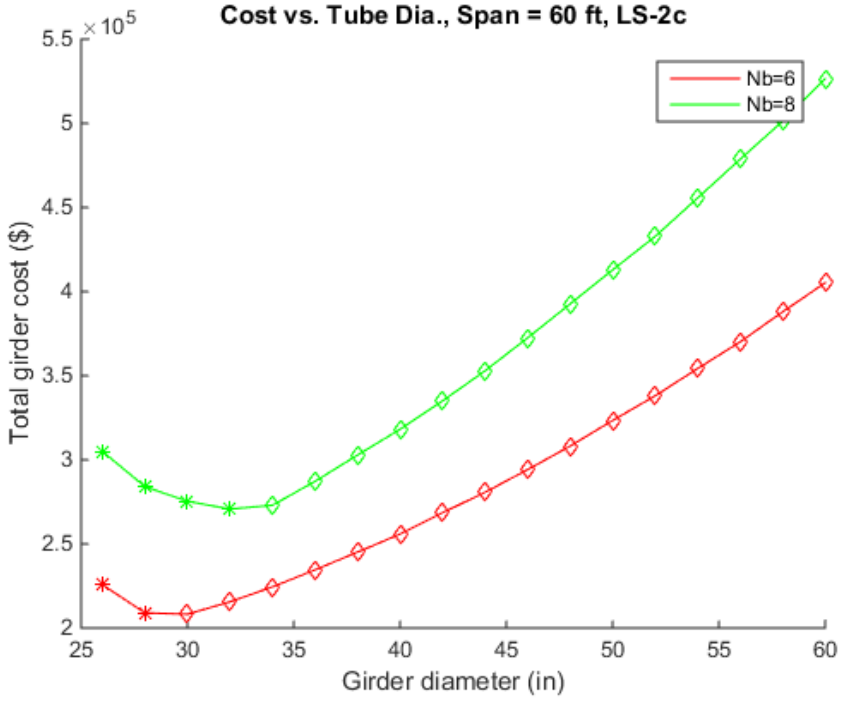

Figure A-19. CFFT cost optimization curves for span length = 60 ft (return to Table A- 1)

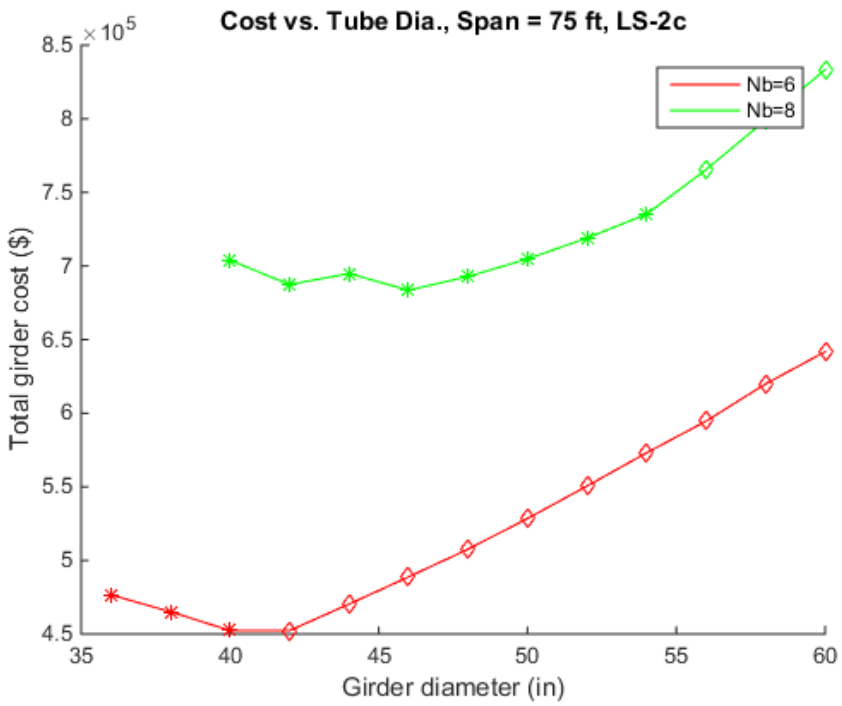

Figure A-20. CFFT cost optimization curves for span length = 75 ft (return to Table A- 1)

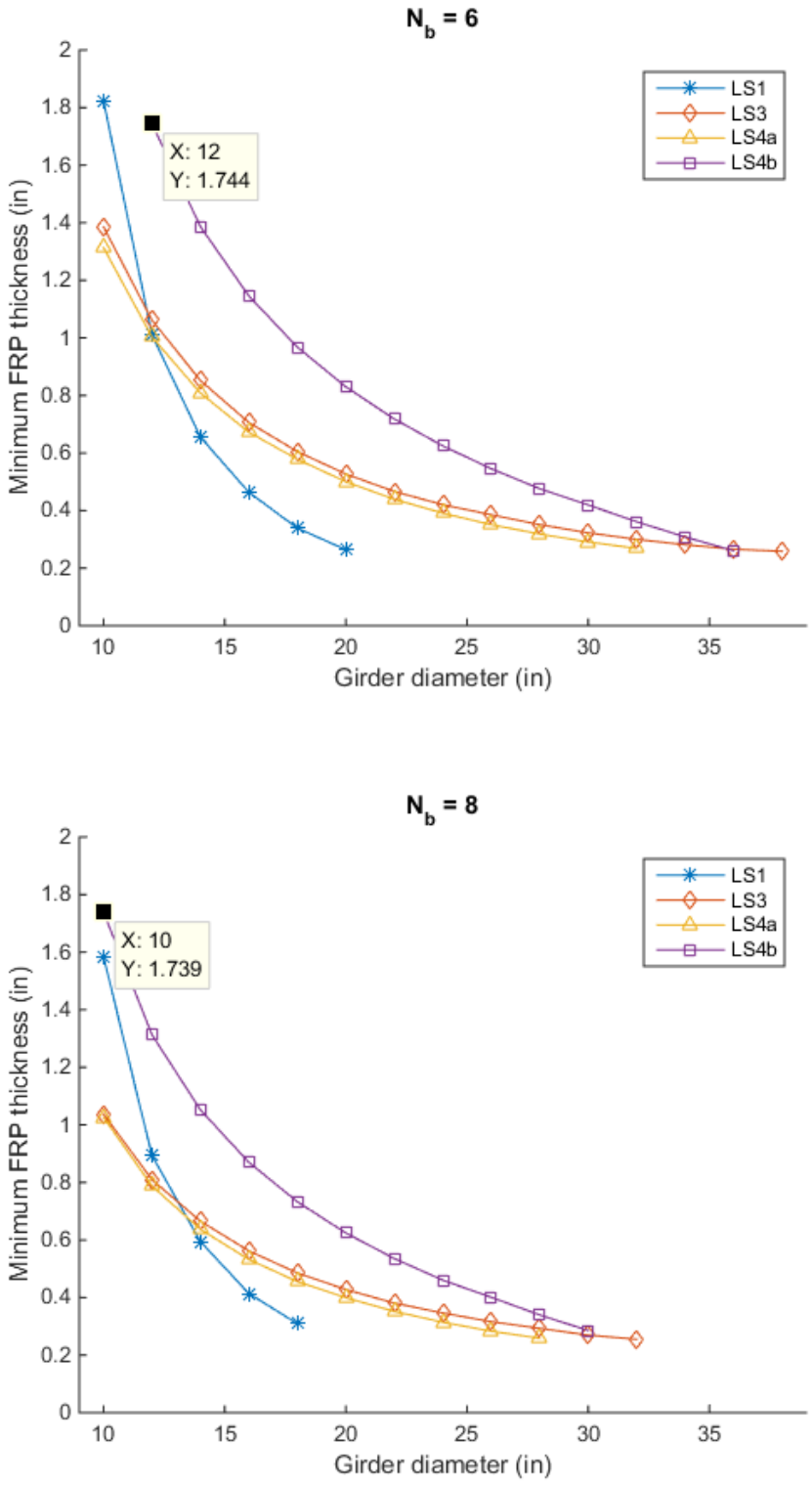

Figure A-21. CFFT required thickness curves for span length = 30 ft, LS-2c

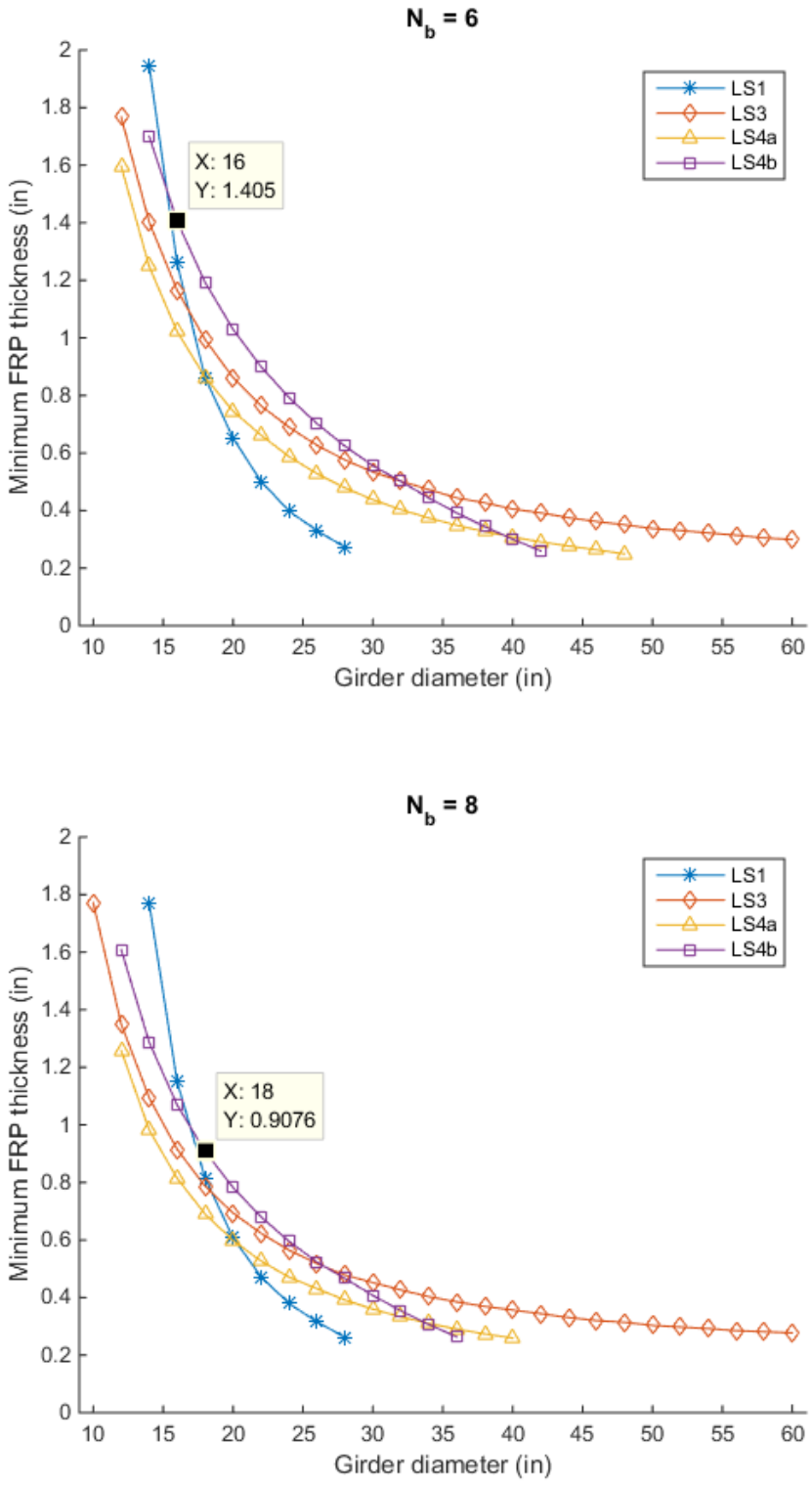

Figure A-22. CFFT required thickness curves for span length = 40 ft, LS-2c

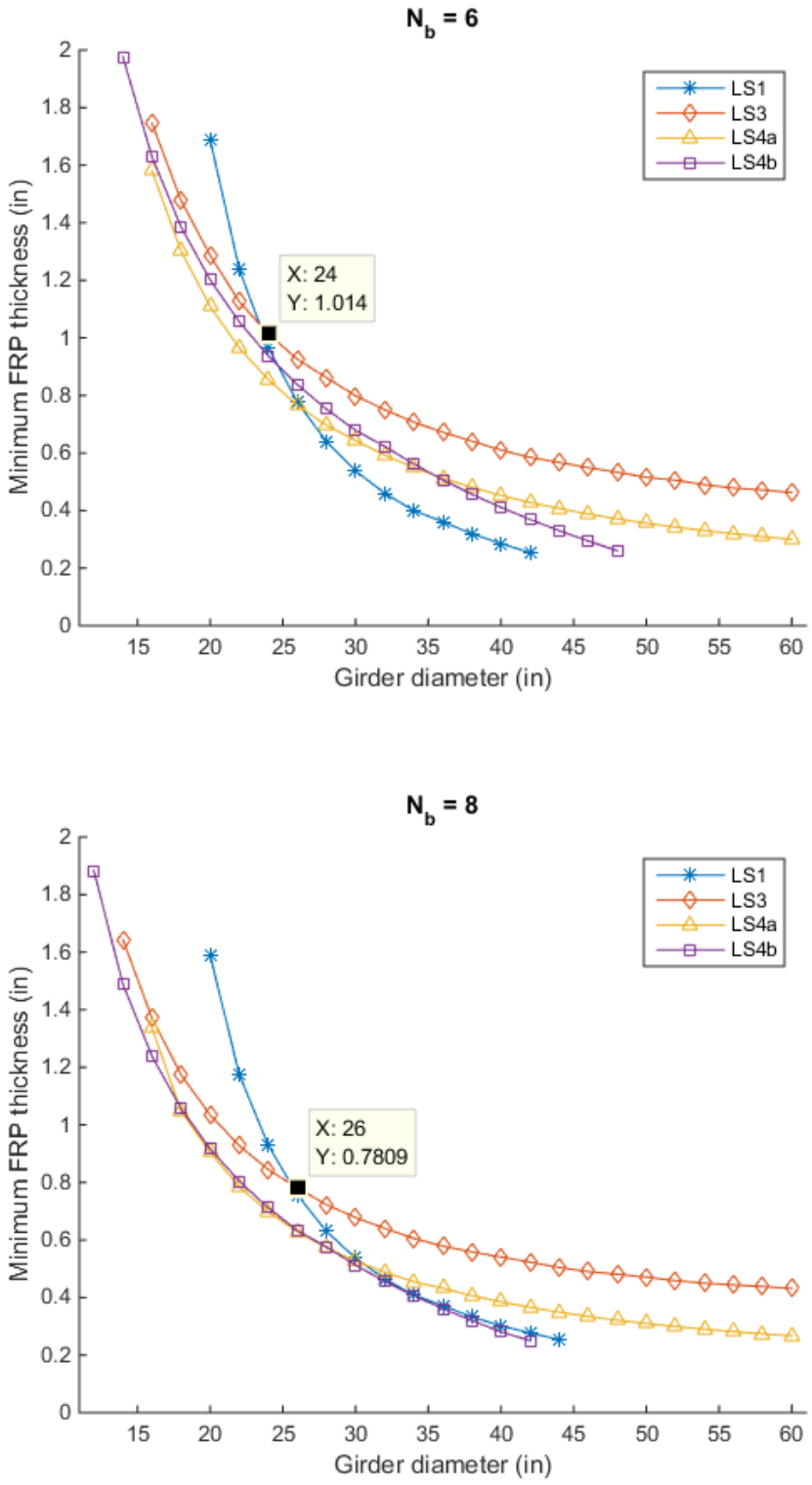

Figure A-23. CFFT required thickness curves for span length = 50 ft, LS-2c

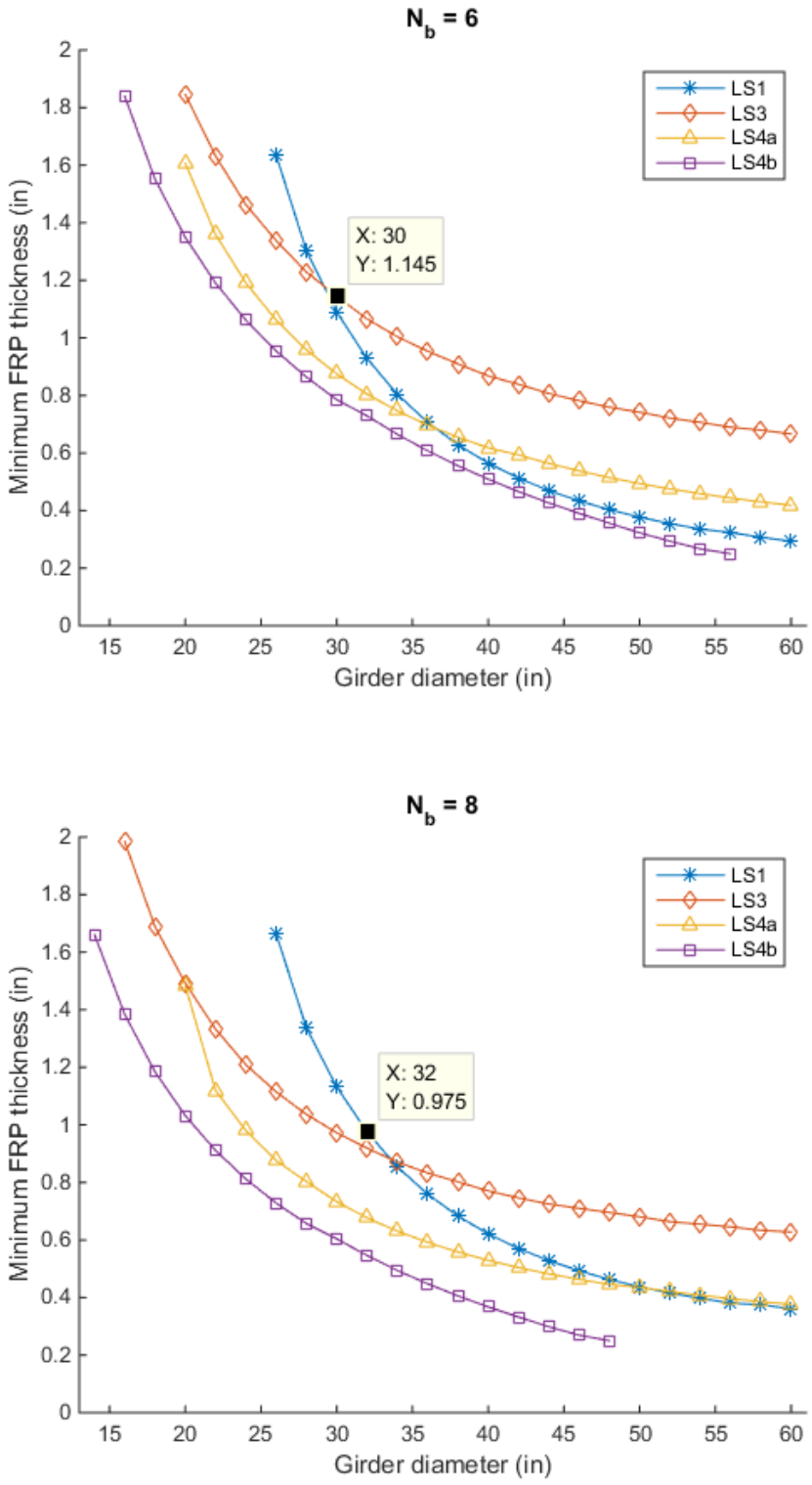

Figure A-24. CFFT required thickness curves for span length = 60 ft, LS-2c

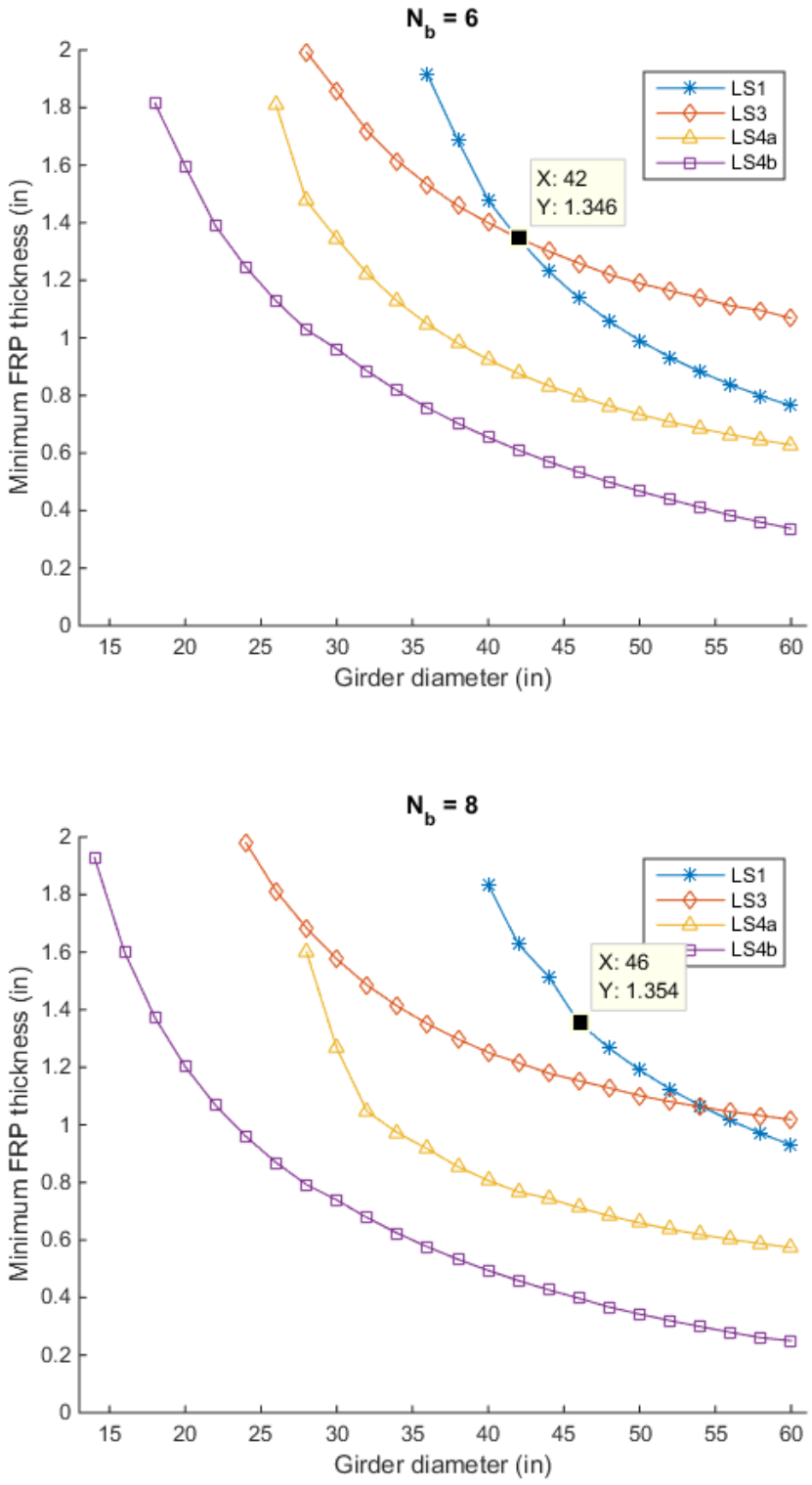

Figure A-25. CFFT required thickness curves for span length = 75 ft, LS-2c

Appendix B

Bridge Girder Alternatives for Extremely Aggressive Environments (BDV22-977-01)

Hand Calculations for 50' Span Length

Objective: The purpose of these hand calculations is to validate the results generated by the software "FRP_BGAT" that was developed for the present study. This software determines the required FRP thickness to satisfy the four limit states over a range of girder depths. The resulting total girder cost for the bridge is determined assuming a material cost for FRP of $5.25 per pound and cast-in-place concrete cost to fill the U-girders of $0.21 per pound. The resulting series of cost curves can be used to determine the girder depth corresponding to the least cost. Once the girder depth is known, the required FRP thickness can be determined.

Summary of Results from FRP_BGAT described in Section 9.1.3.3 for 50' span

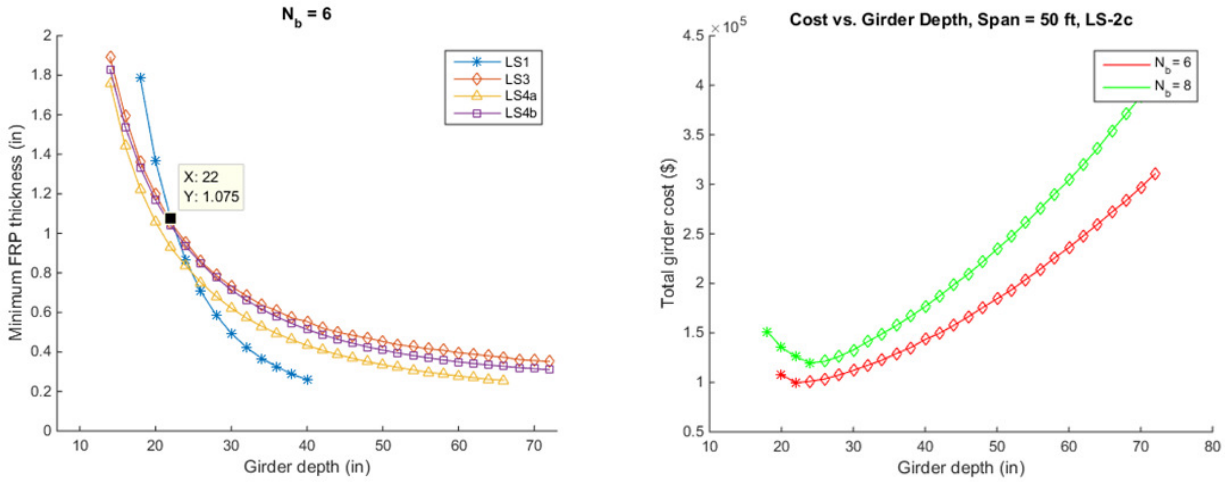

These results were obtained for a bridge with six girders (Nb = 6) and 100% of the girder was filled with concrete. For deflection calculations, the concrete inside the U-girder contributed to the overall stiffness and the cast-in-place barriers were not included in the stiffness of the bridge (LS-2c in Table 25 in Section 8.1.2).

The minimum girder cost is obtained at a girder depth of 22". The corresponding FRP thickness required to satisfy all limit states at this girder depth is 1.075".

The MathCAD worksheet contained in this appendix requires that the overall bridge geometry, girder dimensions, and material properties are fully specified. The input values used in the worksheet are described in Section 9.1 of the report.

Basic Bridge Geometry
(Inputs)

$L := 50\ ft$ Bridge span length

$W_{lane} := 12\ ft$ Lane width

$N_{lane} := 2$ Number of lanes

$W_{shoulder} := 4\ ft$ Shoulder width

$N_{shoulder} := 2$ Number of shoulders

$W_{barrier} := 16\ in$ Traffic barrier width at base

$N_{barrier} := 2$ Number of barriers

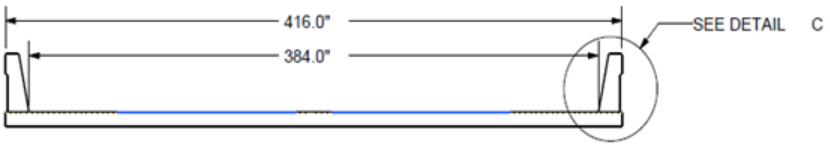

Roadway/deck cross-section

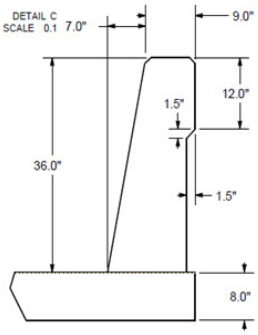

Type "F" traffic barrier/railing

Basic Bridge Geometry
(Calculated)

$W := W_{lane} \cdot N_{lane} + W_{shoulder} \cdot N_{shoulder} = 32\ ft$ Clear distance between barriers

$W_{slab} := W + W_{barrier} \cdot N_{barrier} = 34.667\ ft$ Total slab width

Bridge Cross-section
(Inputs)

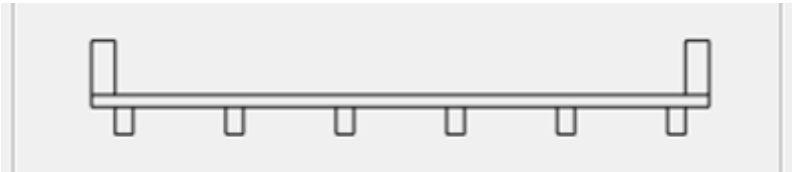

$N_b := 6$ Number of Girders

$t_s := 8\ in$ Reinforced concrete slab thickness

Girder Cross-section
(Inputs)

$h_{web} := 22\ in$ Height of web beneath slab

$Ratio_{web\_height\_to\_flange\_width} := 1.5$

$t_{flan} := 1.08\ in$ FRP flange thickness

$Ratio_{web\_thickness\_to\_flange\_thickness} := 1.0$

$Ratio_{depth\_of\_concrete\_below\_slab\_to\_web\_height} := 1.0$

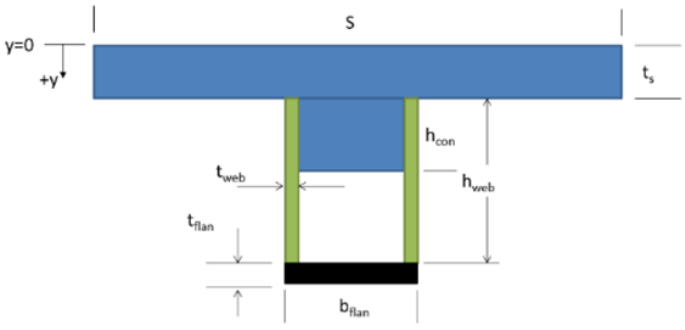

Girder Cross-section
(Calculated)

$b_{flan} := \frac{h_{web}}{Ratio_{web\_height\_to\_flange\_width}} = 14.667\ in$ Width of flange

$t_{web} := t_{flan} \cdot Ratio_{web\_thickness\_to\_flange\_thickness} = 1.08\ in$ FRP web thickness

$h_{con} := h_{web} \cdot Ratio_{depth\_of\_concrete\_below\_slab\_to\_web\_height} = 22\ in$ Depth of concrete below slab

$b_{con} := b_{flan} - 2 \cdot t_{web} = 12.507\ in$ Width of concrete below slab

Girder Spacing

$S := \frac{W - b_{flan}}{N_b - 1} = 6.156\ ft$

Material Properties
(Inputs)

Concrete:

$f'_c := 5500\ psi$ Concrete Compressive Strength

$\gamma_{con} := 150\ pcf$ Unit weight of concrete

$\varepsilon_{ult} := 0.003\ \frac{in}{in}$ Ultimate compressive strain of concrete

FRP:

$f'_{fu\_flan} := 73.8\ ksi$ Manufacturer's specified FRP tensile strength (flange)

$E_{flan} := 3.9 \cdot 10^3\ ksi$ Manufacturer's specified FRP tensile modulus (flange)

$f'_{fu\_web} := 73.8\ ksi$ Manufacturer's specified FRP tensile strength (web)

$E_{web} := 3.9 \cdot 10^3\ ksi$ Manufacturer's specified FRP tensile modulus (web)

$\gamma_{frp} := 118\ pcf$ Unit weight of FRP

$\tau'_{fu} := 10\ ksi$ Manufacturer's specified FRP shear strength

Material knock-down factors

$C_E := 0.5$ Environmental knock-down factor (0.5 for GFRP in aggressive environment)

$C_{fatigue\_rupture} := 0.2$ Strength reduction for fatigue and creep rupture

Material Properties
(Calculated)

$E_{con} := 1820 \cdot \sqrt{\frac{f'_c}{ksi}} \cdot ksi = (4.268 \cdot 10^3)\ ksi$ Modulus of elasticity of concrete

$f_r := 0.2 \cdot \sqrt{\frac{f'_c}{ksi}} \cdot ksi = 0.469\ ksi$ Modulus of rupture of concrete

$f_{fu\_flan} := C_E \cdot f'_{fu\_flan} = 36.9\ ksi$ Design tensile strength of FRP (flange)

$f_{fu\_web} := C_E \cdot f'_{fu\_web} = 36.9\ ksi$ Design tensile strength of FRP (web)

$\tau_{fu} := C_E \cdot \tau'_{fu} = 5\ ksi$ Design shear strength of FRP

Loading Parameters

Dead Loads:

$W_{fws} := 15\ psf$ Allowance for future wearing surface

$w_{barrier} := 0.432\ klf$ Uniform distributed load for single barrier

Live Loads:

$w_{lane} := 0.64\ klf$

$P_{truck} := \begin{bmatrix} 8\ kip \\ 32\ kip \\ 32\ kip \end{bmatrix}$ Axle loads for HL-93 design truck

$S_{truck} := \begin{bmatrix} 14\ ft \\ 14\ ft \end{bmatrix}$ Axle spacing for LS-1, LS-2, and LS-4

$S_{truck\_fatigue} := \begin{bmatrix} 14\ ft \\ 30\ ft \end{bmatrix}$ Axle spacing for LS-3 (fatigue and creep rupture)

$P_{tandem} := \begin{bmatrix} 25\ kip \\ 25\ kip \end{bmatrix}$ Axle loads for design tandem

$S_{tandem} := 4\ ft$ Axle spacing for design tandem

Interior Girder using AASHTO Distribution Factors

Distribution Factor Calculations: General process is to transform girder below slab into equivalent concrete cross-section and then compute moment of inertia of girder around its own centroid.

$n_{web} := \frac{E_{web}}{E_{con}} = 0.914$ Modulus ratio for FRP in web to concrete

$n_{flan} := \frac{E_{flan}}{E_{con}} = 0.914$ Modulus ratio for FRP in flange to concrete

Transformed Section Dimensions

$t_{web\_tr} := t_{web} \cdot n_{web} = 0.987\ in$

$b_{flan\_tr} := b_{flan} \cdot n_{flan} = 13.401\ in$

Girder dimensions below slab – transformed to concrete

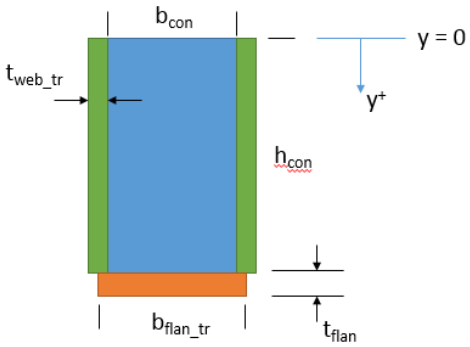

Build arrays with "b" and "h" for:

1. Concrete below slab
2. FRP webs
3. FRP flange

$b := \begin{bmatrix} b_{con} \\ 2 \cdot t_{web\_tr} \\ b_{flan\_tr} \end{bmatrix} = \begin{bmatrix} 12.507 \\ 1.974 \\ 13.401 \end{bmatrix} in$ $h := \begin{bmatrix} h_{con} \\ h_{web} \\ t_{flan} \end{bmatrix} = \begin{bmatrix} 22 \\ 22 \\ 1.08 \end{bmatrix} in$ $y_{bar} := \begin{bmatrix} \frac{h_{con}}{2} \\ \frac{h_{web}}{2} \\ h_{web} + \frac{t_{flan}}{2} \end{bmatrix} = \begin{bmatrix} 11 \\ 11 \\ 22.54 \end{bmatrix} in$

Locate centroid of transformed section

$Y_{bar} := \frac{\sum_{i=1}^{3} b_i \cdot h_i \cdot y_{bar_i}}{\sum_{i=1}^{3} b_i \cdot h_i} = 11.502\ in$

Distance to centroid of transformed girder measured from the bottom of the slab.
Note: array origin == 1

Determine moment of inertia of transformed section about its own centroid

$I_{girder} := \sum_{i=1}^{3} \left(\frac{b_i \cdot h_i^{\,3}}{12} + b_i \cdot h_i \cdot \left(y_{bar_i} - Y_{bar} \right)^2 \right) = 14694\ in^4$

Determine Kg

$n := 1$ (already transformed girder to concrete)

$A := \sum_{i=1}^{3} b_i \cdot h_i = 333.04\ in^2$ Area of girder below slab

$e_g := \frac{t_s}{2} + Y_{bar} = 15.502\ in$ Distance between centroid of slab and centroid of girder

$K_g := n \cdot \left(I_{girder} + A \cdot {e_g}^2\right) = 94722\ in^4$ AASHTO distribution factors are valid for $10000\ in^4 \le K_g \le 7000000\ in^4$

Compute distribution factor for bending moment:

$$DF_{2LL} := 0.075 + \left(\frac{\frac{S}{ft}}{9.5}\right)^{0.6} \cdot \left(\frac{S}{L}\right)^{0.2} \cdot \left(\frac{K_g}{12\ in \cdot \frac{L}{ft} \cdot {t_s}^3}\right)^{.1} = 0.526$$ Two lanes loaded

$$DF_{1LL} := 0.06 + \left(\frac{\frac{S}{ft}}{14}\right)^{0.4} \cdot \left(\frac{S}{L}\right)^{0.3} \cdot \left(\frac{K_g}{12\ in \cdot \frac{L}{ft} \cdot {t_s}^3}\right)^{.1} = 0.401$$ One lane loaded

$DF_{Mom} := \max\left(DF_{2LL}, DF_{1LL}\right) = 0.526$ Select maximum of 1-lane and 2-lanes loaded

Compute distribution factor for shear:

$$DF_{shear\_1LL} := 0.36 + \frac{\frac{S}{ft}}{25} = 0.606$$

$$DF_{shear\_2LL} := 0.2 + \frac{\frac{S}{ft}}{12} - \left(\frac{\frac{S}{ft}}{30}\right)^2 = 0.671$$

$DF_{Shear} := \max\left(DF_{shear\_1LL}, DF_{shear\_2LL}\right) = 0.671$ Select maximum of 1-lane and 2-lanes loaded

Uniform Distributed Loading for single girder (Dead Loads)

$$w_{DL\_slab} := S \cdot t_s \cdot \gamma_{con} = 0.616 \ \frac{kip}{ft}$$

$$w_{DL\_frp} := 2 \cdot h_{web} \cdot t_{web} \cdot \gamma_{frp} + b_{flan} \cdot t_{flan} \cdot \gamma_{frp} = 0.052 \ \frac{kip}{ft}$$

$$w_{DL\_con\_bs} := h_{con} \cdot \left(b_{flan} - 2 \cdot t_{web}\right) \cdot \gamma_{con} = 0.287 \ \frac{kip}{ft}$$

$$w_{DL\_barrier} := \frac{2 \cdot w_{barrier}}{N_b} = 0.144 \ \frac{kip}{ft}$$

$$w_{DL} := w_{DL\_slab} + w_{DL\_frp} + w_{DL\_con\_bs} + w_{DL\_barrier} = 1.098 \ \frac{kip}{ft}$$

Total DL (excluding future wearing surface)

$$w_{DL\_fws} := W_{fws} \cdot S = 0.092 \ \frac{kip}{ft}$$

Live Loads w/ Distribution Factors

$$w_{LL\_Moment} := w_{lane} \cdot DF_{Mom} = 0.336 \ \frac{kip}{ft}$$

$$w_{LL\_Shear} := w_{lane} \cdot DF_{Shear} = 0.429 \ \frac{kip}{ft}$$

These values will later be multiplied by the appropriate load factor for each limit state. The results will then serve as input for a separate shear and moment envelope generator.

$$P_{truck\_Mom} := P_{truck} \cdot DF_{Mom} = \begin{bmatrix} 4.206 \\ 16.822 \\ 16.822 \end{bmatrix} kip$$

$$P_{truck\_Shear} := P_{truck} \cdot DF_{Shear} = \begin{bmatrix} 5.367 \\ 21.468 \\ 21.468 \end{bmatrix} kip$$

$$P_{tandem\_Mom} := P_{tandem} \cdot DF_{Mom} = \begin{bmatrix} 13.143 \\ 13.143 \end{bmatrix} kip$$

$$P_{tandem\_Shear} := P_{tandem} \cdot DF_{Shear} = \begin{bmatrix} 16.772 \\ 16.772 \end{bmatrix} kip$$

Load Factors

	IM	LL-Trk/Tan	LL-Lane	DL	DL-FWS
LS-1: Concrete Compressive Stresses	1.3300	1	1	1	1
LS-2: Displacements	1.3300	1	0	0	0
LS-3: Fatigue/Creep Rupture	1.3300	0.7500	0	1	1
LS-4: Strength	1.3300	1.7500	1.7500	1.2500	1.5000

Limit State 1 - Concrete Compressive Stresses - Need factored design moment, M_u

Define Load Factors:

$IM := 1.33$	Impact
$LL_{vehicle} := 1$	Live load for truck/tandem
$LL_{lane} := 1$	Live load for lane loading
$DL := 1$	Dead load
$DL_{fws} := 1$	Dead load - future wearing surface

Factored loads (includes distribution factors for live loads):

$$w_{u\_LS1} := w_{LL\_Moment} \cdot LL_{lane} + w_{DL} \cdot DL + w_{DL\_fws} \cdot DL_{fws} = 1.527 \ \frac{kip}{ft}$$

$$w_{u\_LS1} = 0.127 \ \frac{kip}{in}$$

$$P_{u\_truck\_LS1} := P_{truck\_Mom} \cdot LL_{vehicle} \cdot IM = \begin{bmatrix} 5.593 \\ 22.374 \\ 22.374 \end{bmatrix} kip$$

$$P_{u\_tandem\_LS1} := P_{tandem\_Mom} \cdot LL_{vehicle} \cdot IM = \begin{bmatrix} 17.48 \\ 17.48 \end{bmatrix} kip$$

Shear and Moment Envelope Results:

$$M_{u\_truck\_LS1} := 10953 \ kip \cdot in = 912.75 \ kip \cdot ft \qquad M_{u\_tandem\_LS1} := 10543 \ kip \cdot in = 878.583 \ kip \cdot ft$$

$$M_{u\_LS1} := \max\left(M_{u\_truck\_LS1}, M_{u\_tandem\_LS1}\right) = 10953 \ kip \cdot in$$

V_M_Envelopes Program Output for LS-1, Concrete Compressive Stresses
Truck Loading

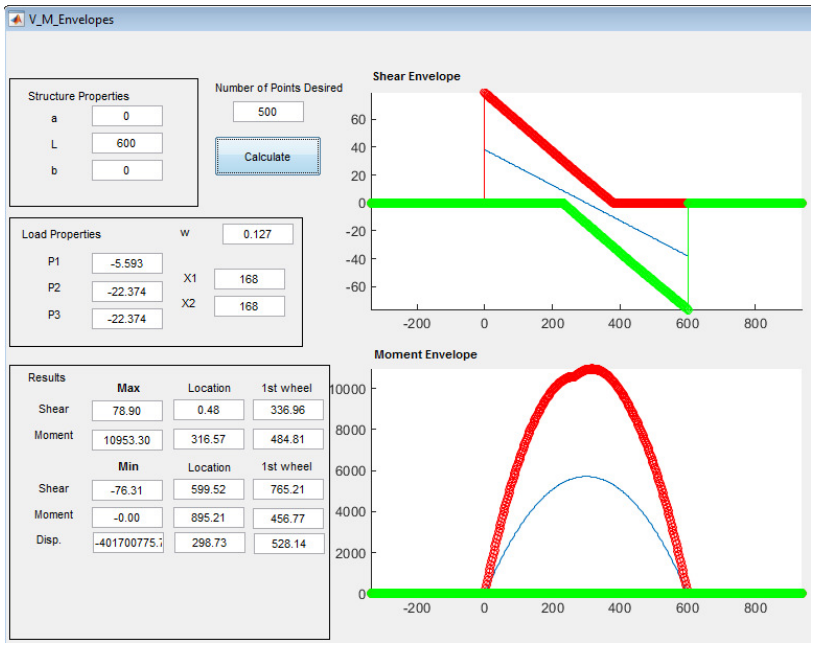

All units are kips & inches

Tandem Loading

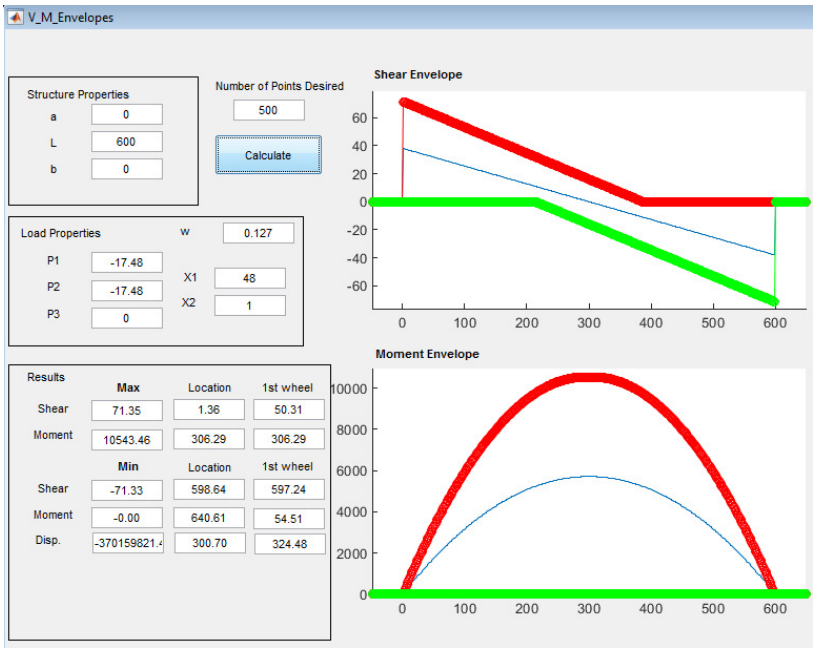

All units are kips & inches

Limit State 2 - Displacements

Generate displacement envelope for simply supported beam with EI = 1. Truck load includes impact and the number of trucks applied equals the number of lanes in the bridge.

Define Load Factors:

$IM := 1.33$	Impact
$LL_{vehicle} := 1$	Live load for truck/tandem
$LL_{lane} := 0$	Live load for lane loading
$DL := 0$	Dead load
$DL_{fws} := 0$	Dead load - future wearing surface

Factored loads (includes distribution factors for live loads):

$$w_{u\_LS2} := w_{LL\_Moment} \cdot LL_{lane} + w_{DL} \cdot DL + w_{DL\_fws} \cdot DL_{fws} = 0 \ \frac{kip}{ft}$$

$$w_{u\_LS2} = 0 \ \frac{kip}{in}$$

Multiple Presence Factor:

$$m := \begin{cases} \text{if } N_{lane} = 1 \\ \quad \text{return } 1.2 \\ \text{else if } N_{lane} = 2 \\ \quad \text{return } 1.0 \\ \text{else if } N_{lane} = 3 \\ \quad \text{return } 0.85 \\ \text{else} \\ \quad \text{return } 0.65 \end{cases} \qquad m = 1$$

$$14 \ ft = 168 \ in$$

$$P_{u\_truck\_LS2} := P_{truck} \cdot LL_{vehicle} \cdot IM \cdot N_{lane} \cdot m = \begin{bmatrix} 21.28 \\ 85.12 \\ 85.12 \end{bmatrix} kip$$

note: P_{truck} does not include distribution factor

Displacement envelope results:

$$\Delta_{max} = \frac{-712923596 \cdot kip \cdot in^3}{EI_{total}}$$

EI_{total} = total bridge flexural stiffness in $kip \cdot in^2$ assuming that all elements of the bridge deflect uniformly. EI_{total} should not include cast-in-place barriers or sidewalks-- only the bridge deck and supporting girders.

V_M_Envelopes Program Output for LS-2, Displacements

Truck Loading (for deflection calculations)

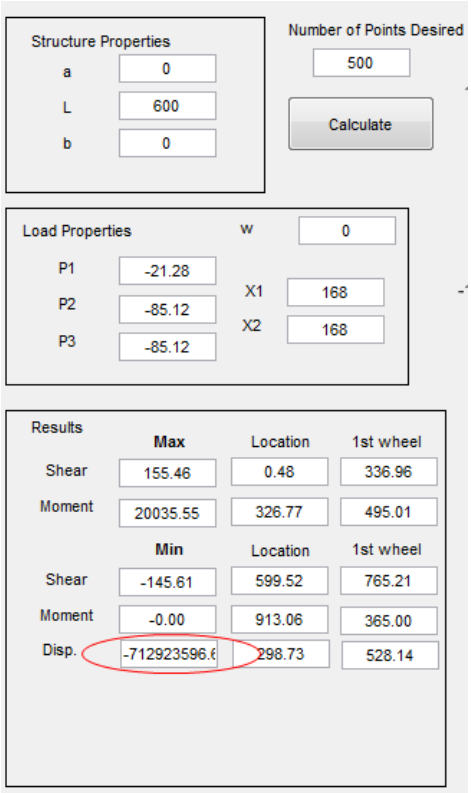

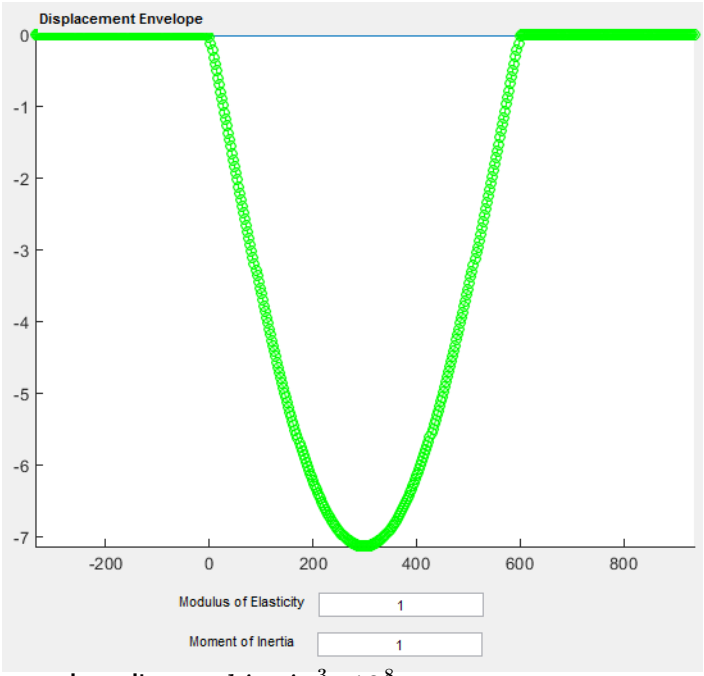

y-axis units are $kip \cdot in^3 \cdot 10^8$
x-axis units are in

Vehicle positioning to generate maximum displacement:

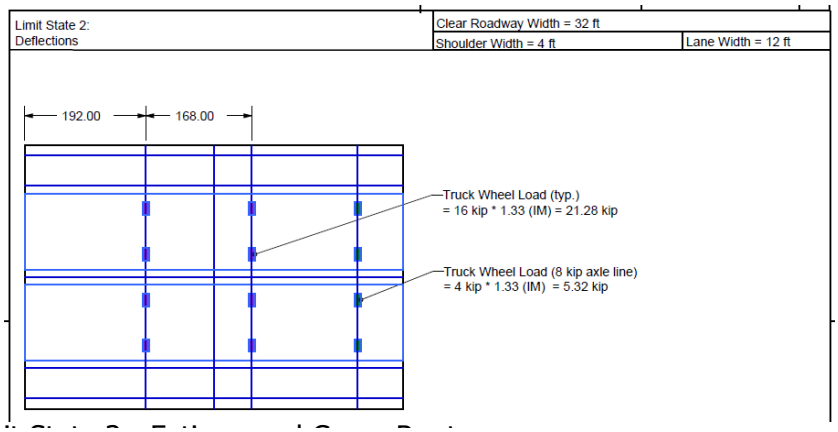

Limit State 3 - Fatigue and Creep Rupture

Require moment envelope for fatigue truck with 1.33 factor for impact and 0.75 factor for fatigue and creep rupture limit state. Also includes dead load and future wearing surface.

Define Load Factors:

$IM := 1.33$	Impact
$LL_{vehicle} := 0.75$	Live load for truck/tandem
$LL_{lane} := 0$	Live load for lane loading
$DL := 1$	Dead load
$DL_{fws} := 1$	Dead load - future wearing surface

Factored loads (includes distribution factors for live loads):

$$w_{u\_LS3} := w_{LL\_Moment} \cdot LL_{lane} + w_{DL} \cdot DL + w_{DL\_fws} \cdot DL_{fws} = 1.19 \ \frac{kip}{ft}$$

$$w_{u\_LS3} = 0.099 \ \frac{kip}{in}$$

$$P_{u\_truck\_LS3} := P_{truck\_Mom} \cdot LL_{vehicle} \cdot IM = \begin{bmatrix} 4.195 \\ 16.78 \\ 16.78 \end{bmatrix} kip$$

note: P_{truck_Mom} includes distribution factor

$$S_{truck\_fatigue} = \begin{bmatrix} 168 \\ 360 \end{bmatrix} in$$

Axle spacing for LS-3 (fatigue and creep rupture)

Shear and Moment Envelope Results:

$$M_{u\_LS3} := 7249 \ kip \cdot in = 604.083 \ kip \cdot ft$$

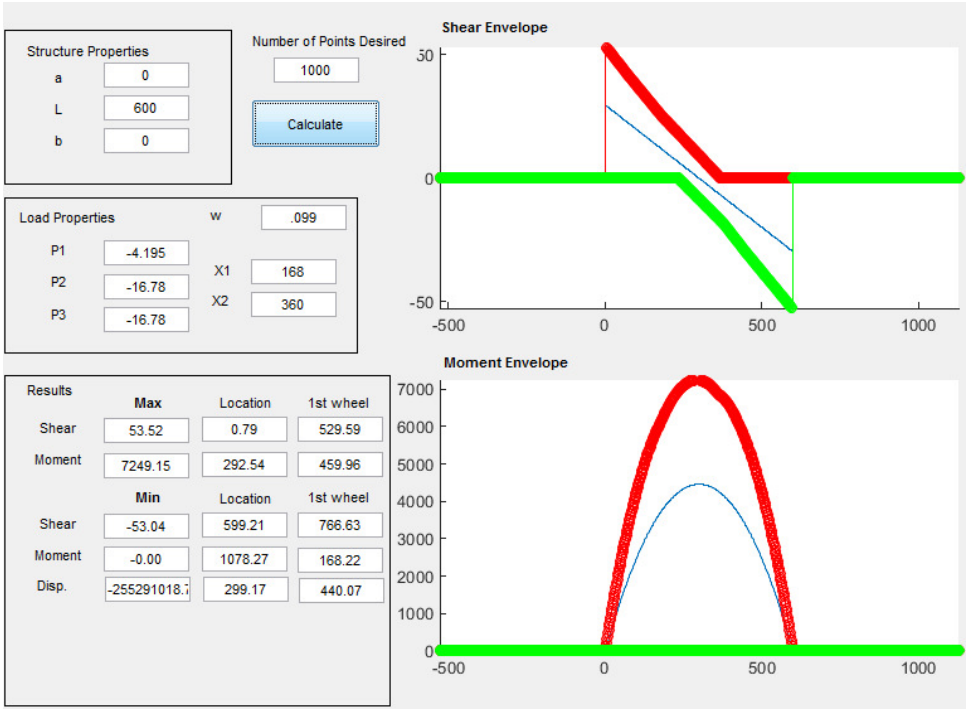

Limit State 4a - Flexural Strength

Require moment envelope for standard truck and tandem, lane loading, and dead loads.

Define Load Factors:

$S = 73.867\ in$

$IM := 1.33$	Impact
$LL_{vehicle} := 1.75$	Live load for truck/tandem
$LL_{lane} := 1.75$	Live load for lane loading
$DL := 1.25$	Dead load
$DL_{fws} := 1.5$	Dead load - future wearing surface

Factored loads (includes distribution factors for live loads):

$$w_{u\_LS4a} := w_{LL\_Moment} \cdot LL_{lane} + w_{DL} \cdot DL + w_{DL\_fws} \cdot DL_{fws} = 2.1\ \frac{kip}{ft}$$

$$w_{u\_LS4a} = 0.175\ \frac{kip}{in}$$

$18.6 \cdot DF_{Mom} = 9.778$

$$P_{u\_truck\_LS4a} := P_{truck\_Mom} \cdot LL_{vehicle} \cdot IM = \begin{bmatrix} 9.789 \\ 39.154 \\ 39.154 \end{bmatrix} kip$$

note: P_{truck_Mom} and P_{tandem_Mom} includes distribution factor

$$P_{u\_tandem\_LS4a} := P_{tandem\_Mom} \cdot LL_{vehicle} \cdot IM = \begin{bmatrix} 30.589 \\ 30.589 \end{bmatrix} kip$$

Shear and Moment Envelope Results:

$$M_{u\_truck\_LS4a} := 17048.5\ kip \cdot in = 1421\ kip \cdot ft$$

$$M_{u\_tandem\_LS4a} := 16325\ kip \cdot in = 1360\ kip \cdot ft$$

$$M_{u\_LS4a} := \max\left(M_{u\_truck\_LS4a}, M_{u\_tandem\_LS4a}\right) = 17049\ kip \cdot in$$

V and M Envelopes for truck:

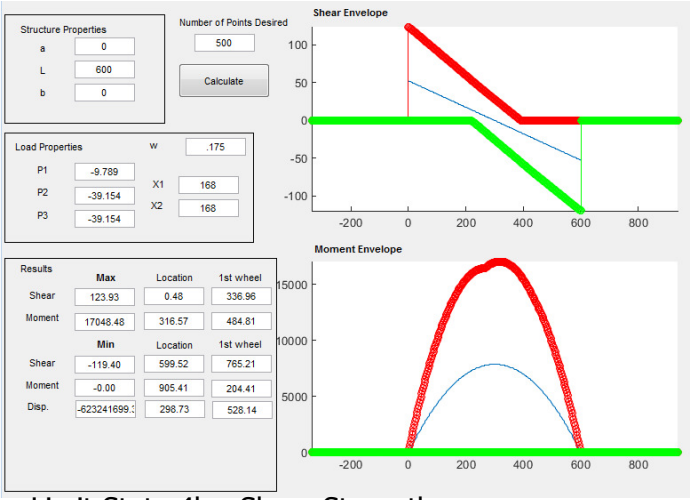

V and M Envelopes for Tandem:

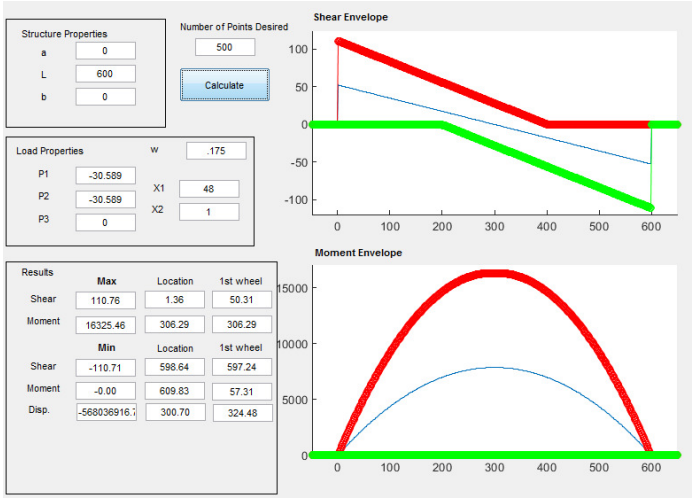

Limit State 4b - Shear Strength

Require shear envelope for standard truck and tandem, lane loading, and dead loads.

Define Load Factors:

$IM := 1.33$	Impact
$LL_{vehicle} := 1.75$	Live load for truck/tandem
$LL_{lane} := 1.75$	Live load for lane loading
$DL := 1.25$	Dead load
$DL_{fws} := 1.5$	Dead load - future wearing surface

Factored loads (includes distribution factors for live loads):

$$w_{u\_LS4b} := w_{LL\_Shear} \cdot LL_{lane} + w_{DL} \cdot DL + w_{DL\_fws} \cdot DL_{fws} = 2.262 \ \frac{kip}{ft}$$

$$w_{u\_LS4b} = 0.189 \ \frac{kip}{in}$$

$$w_{u\_LS4b} \cdot \frac{L}{2} = 56.562 \ kip$$

$$S_{truck} = \begin{bmatrix} 168 \\ 168 \end{bmatrix} in$$

$$P_{u\_truck\_LS4b} := P_{truck\_Shear} \cdot LL_{vehicle} \cdot IM = \begin{bmatrix} 12.491 \\ 49.966 \\ 49.966 \end{bmatrix} kip$$

note: P_{truck_Shear} and P_{tandem_Shear} includes distribution factor

$$P_{u\_tandem\_LS4b} := P_{tandem\_Shear} \cdot LL_{vehicle} \cdot IM = \begin{bmatrix} 39.036 \\ 39.036 \end{bmatrix} kip$$

Shear and Moment Envelope Results:

$$V_{u\_truck\_LS4b} := 147.9 \ kip$$

$$V_{u\_tandem\_LS4b} := 131.04 \ kip$$

$$V_{u\_LS4b} := \max\left(V_{u\_truck\_LS4b}, V_{u\_tandem\_LS4b}\right) = 148 \ kip$$

V and M Envelopes for truck:

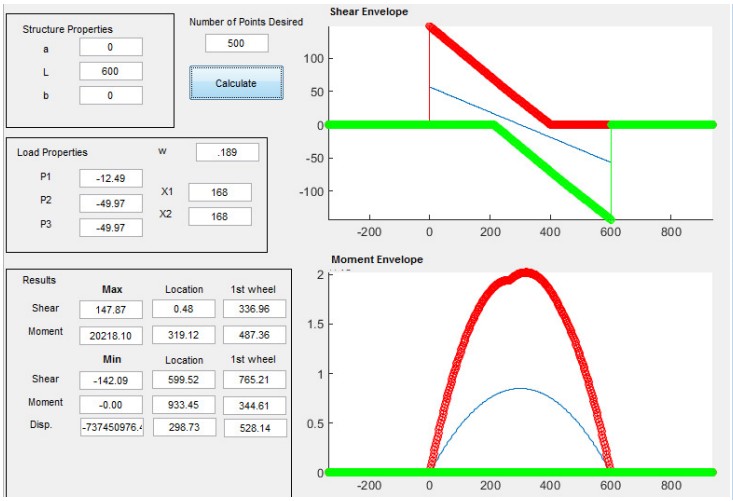

V and M Envelopes for Tandem:

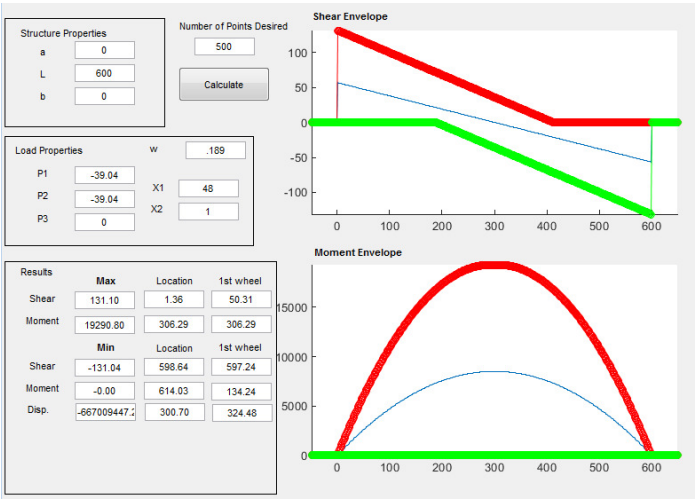

Summary of Factored Structural Demands and Limit State Criteria:

LS-1: Concrete Compressive Stresses

$M_{u\_LS1} = 10953\ kip \cdot in$

$M_{u\_LS1} = 912.8\ kip \cdot ft$

Criteria:
Maximum concrete compressive stress less than 45% of concrete compressive strength

$$f_c \le 0.45\ f'_c$$

LS-2: Displacements

$$\Delta_{max} = \frac{-712923596 \cdot kip \cdot in^3}{EI_{total}}$$

In the section on Capacity Analysis for LS-2, the EI_{total} for the entire bridge will be calculated. This value will then be used to compute the maximum displacement assuming the that all girders deflect uniformly.

Criteria:

$$\Delta_{max} \le \frac{L}{1000}$$

LS-3: Fatigue and Creep Rupture

$M_{u\_LS3} = 7249\ kip \cdot in$

$M_{u\_LS3} = 604.1\ kip \cdot ft$

Criteria:
Maximum tensile stress in FRP is limited by the following:

$$f_{frp\_max} \le f'_{fu\_flan} \cdot C_E \cdot C_{fatigue\_rupture}$$

where:
f_{frp_max} = maximum FRP stress that develops under LS-3 loading conditions
f'_{fu_flan} = manufacturer's specified tensile strength
C_E = enviromental knockdown factor
$C_{fatigue\_rupture}$ = knockdown factor for fatigue and creep rupture

LS-4a: Flexural Strength

$M_{u\_LS4a} = 17048.5\ kip \cdot in$

$M_{u\_LS4a} = 1420.708\ kip \cdot ft$

Criteria:

$$M_{u\_LS4a} \le \Phi \cdot M_n$$

LS-4b: Shear Strength

$V_{u\_LS4b} = 147.9\ kip$

Criteria:

$$V_{u\_LS4b} \le \Phi \cdot V_n$$

Establish function for concrete stress as a function of strain using Thorenfeldt, Tomaszewicz, and Jensen Model. (pg. 71 of Wight text on Reinforced Concrete)

Summary of input material properties:

$f_r = 0.469\ ksi$ Max tensile stress

$f'_c = 5.5\ ksi$ Max compressive stress

$\varepsilon_{ult} = 0.003$ Max compressive strain of concrete

$E_{con} = 4268\ ksi$ Modulus of elasticity of concrete in linear region

Other factors needed to develop function:

$\varepsilon_{ult\_tension} := \frac{-f_r}{E_{con}} = -1.099 \cdot 10^{-4}$ Ultimate tensile strain

$cf := 0.8 + \frac{f'_c}{2.5 \cdot ksi} = 3$ Curve fitting factor

$\varepsilon_o := \frac{f'_c}{E_{con}} \cdot \left(\frac{cf}{cf - 1}\right) = 0.002$ compressive strain corresponding to maximum tensile stress

Define concrete stress, f_c , as a function of concrete strain, ε_c

$f_c(\varepsilon_c) :=$ if $\varepsilon_c < \varepsilon_{ult\_tension}$ — Concrete cracked

  return $0 \cdot ksi$

else if $\varepsilon_c < 0$ — Concrete in tension

  return $\varepsilon_c \cdot E_{con}$

else if $\varepsilon_c \le \varepsilon_o$ — Concrete in compression with $\varepsilon_c \le \varepsilon_o$

  $k \leftarrow 1$

  return $f'_c \cdot \left(\frac{cf \cdot \frac{\varepsilon_c}{\varepsilon_o}}{cf - 1 + \left(\frac{\varepsilon_c}{\varepsilon_o}\right)^{cf \cdot k}}\right)$

else if $\varepsilon_c \le \varepsilon_{ult}$ — Concrete in compression with $\varepsilon_c \le \varepsilon_{ult}$

  $k \leftarrow \max\left(1, 0.67 + \frac{f'_c}{9 \cdot ksi}\right)$

  return $f'_c \cdot \left(\frac{cf \cdot \frac{\varepsilon_c}{\varepsilon_o}}{cf - 1 + \left(\frac{\varepsilon_c}{\varepsilon_o}\right)^{cf \cdot k}}\right)$

$\max\left(1, 0.67 + \frac{f'_c}{9 \cdot ksi}\right) = 1.281$

Plot of stress vs. strain for concrete

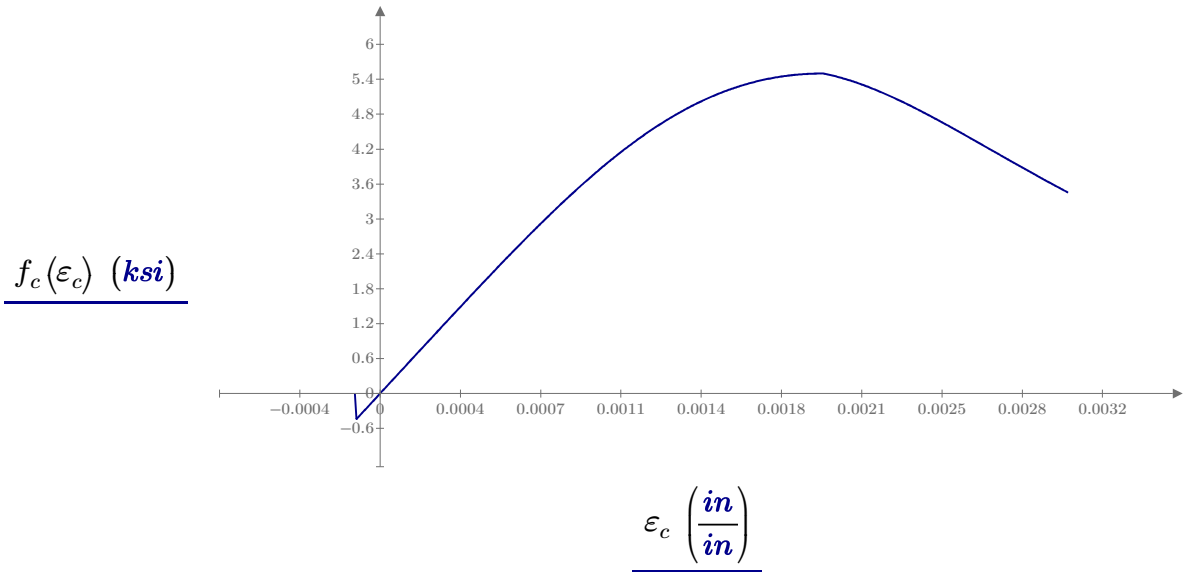

LS-1: Concrete Compressive Stress

Two methods for computing the moment capacity for LS-1 will be investigated:

Method 1: Moment-curvature analysis that incorporates non-linear stress-vs-strain relationship for concrete.

Method 2: Simplified cracked-section analysis that assumes linear stress-vs-strain relationship for concrete and transformed width properties for FRP.

Method 1 - Moment-curvature analysis

1. Find concrete strain corresponding to $0.45 \cdot f'_c$

Guess Values

$\varepsilon_{c\_max} := 0.45 \cdot \varepsilon_o$ initial guess required by solver

Constraints

$f_c(\varepsilon_{c\_max}) = 0.45\ f'_c$

Solver

$\varepsilon_{c\_max} := \text{find}(\varepsilon_{c\_max})$ $\varepsilon_{c\_max} = 5.88 \cdot 10^{-4}$ max concrete strain

$f_c(\varepsilon_{c\_max}) = 2.475$ ksi

$0.45\ f'_c = 2.475$ ksi

2. Establish strain profile as a function of known strain and depth to NA

$$\varepsilon\left(\varepsilon_{known}, y_{known}, y_{NA}, y\right) := \left\| \begin{array}{l} m \leftarrow \dfrac{\varepsilon_{known}}{y_{known} - y_{NA}} \\ \text{return } m \cdot \left(y - y_{NA}\right) \end{array} \right\|$$

$$f_{frp\_flan}\left(\varepsilon_{frp}\right) := E_{flan} \cdot \varepsilon_{frp}$$

$$f_{frp\_web}\left(\varepsilon_{frp}\right) := E_{web} \cdot \varepsilon_{frp}$$

For Limit State 1, $\varepsilon_{known} = \varepsilon_{c\_max}$
where
ε_{c_max} is the strain in concrete corresponding to $0.45\ f'_c$ (determined in Step 1)
y_{known} = 0 because this strain occurs at the top of the slab

2. Determine the depth of the neutral axis through force equilibrium. The stress profile is integrated over the depth of the section. The neutral axis occurs where the sum of the forces is equal to zero. The "solve block" feature in MathCAD is used to determine the depth of the neutral axis.

Guess Values

$y_{NA} := 4\ in$
$F_{ff} := 1\ kip$
$F_{fw} := 1\ kip$
$F_{cbs} := 1\ kip$
$F_s := 1\ kip$

Constraints

$$F_{ff} = \int_{t_s + h_{web}}^{t_s + h_{web} + t_{flan}} f_{frp\_flan}\left(\varepsilon\left(\varepsilon_{c\_max}, 0, y_{NA}, y\right)\right) \cdot \left(b_{flan}\right) \mathrm{d}y \qquad F_{ff} \text{ = force in FRP flange}$$

$$F_{fw} = \int_{t_s}^{t_s + h_{web}} f_{frp\_web}\left(\varepsilon\left(\varepsilon_{c\_max}, 0, y_{NA}, y\right)\right) \cdot \left(2 \cdot t_{web}\right) \mathrm{d}y \qquad F_{fw} \text{ = force in FRP web}$$

$$F_{cbs} = \int_{t_s}^{t_s + h_{web}} f_c\left(\varepsilon\left(\varepsilon_{c\_max}, 0, y_{NA}, y\right)\right) \cdot \left(b_{flan} - 2 \cdot t_{web}\right) \mathrm{d}y \qquad F_{cbs} \text{ = force in concrete below slab}$$

$$F_s = \int_{0\ in}^{t_s} f_c\left(\varepsilon\left(\varepsilon_{c\_max}, 0, y_{NA}, y\right)\right) \cdot \left(S\right) \mathrm{d}y \qquad F_s \text{ = force in slab}$$

$F_{ff} + F_{fw} + F_{cbs} + F_s = 0$ The sum of the forces = 0 when the correct depth to the neutral axis has been identified.

Solver

$$\begin{bmatrix} y_{NA} \\ F_{ff} \\ F_{fw} \\ F_{cbs} \\ F_s \end{bmatrix} := \text{find}\left(y_{NA}, F_{ff}, F_{fw}, F_{cbs}, F_s\right)$$

"find" is MathCAD's solve function that determines the depth to the neutral axis numerically.

$$\begin{bmatrix} \quad \\ \quad \end{bmatrix} \begin{bmatrix} \quad 0.434\ ft \quad \end{bmatrix}$$

$$\begin{bmatrix} y_{NA} \\ F_{ff} \\ F_{fw} \\ F_{cbs} \\ F_s \end{bmatrix} = \begin{bmatrix} 0.434\ ft \\ -1.765 \cdot 10^5\ lbf \\ -2.883 \cdot 10^5\ lbf \\ \left(4.704 \cdot 10^{-27}\right) lbf \\ \left(4.649 \cdot 10^5\right) lbf \end{bmatrix}$$

Note: Compression is positive, Tension is negative

$y_{NA} = 5.211\ in$ $F_s = 464.877\ kip$ $F_{ff} = -176.547\ kip$ $F_{cbs} = 0\ kip$

$F_{fw} = -288.33\ kip$

3. Determine the moment generated by each component using the depth to the neutral axis obtained in Step 2.

$$M_{ff} := \int_{t_s + h_{web}}^{t_s + h_{web} + t_{flan}} f_{frp\_flan}\left(\varepsilon\left(\varepsilon_{c\_max}, 0, y_{NA}, y\right)\right) \cdot \left(b_{flan}\right) \cdot \left(y_{NA} - y\right) \mathrm{d}y = \left(4.472 \cdot 10^3\right)\ kip \cdot in$$

$$M_{fw} := \int_{t_s}^{t_s + h_{web}} f_{frp\_web}\left(\varepsilon\left(\varepsilon_{c\_max}, 0, y_{NA}, y\right)\right) \cdot \left(2 \cdot t_{web}\right) \cdot \left(y_{NA} - y\right) \mathrm{d}y = \left(4.819 \cdot 10^3\right)\ kip \cdot in$$

$$M_{cbs} := \int_{t_s}^{t_s + h_{web}} f_c\left(\varepsilon\left(\varepsilon_{c\_max}, 0, y_{NA}, y\right)\right) \cdot \left(b_{flan} - 2 \cdot t_{web}\right) \cdot \left(y_{NA} - y\right) \mathrm{d}y = 0\ kip \cdot in$$

$$M_s := \int_{0\ in}^{t_s} f_c\left(\varepsilon\left(\varepsilon_{c\_max}, 0, y_{NA}, y\right)\right) \cdot (S) \cdot \left(y_{NA} - y\right) \mathrm{d}y = \left(1.676 \cdot 10^3\right)\ kip \cdot in$$

4. Determine the total moment capacity of the cross-section for Limit State 1 by summing the moment contributions from each component

$$M_{n\_LS1} := M_{ff} + M_{fw} + M_{cbs} + M_s = \left(1.097 \cdot 10^4\right)\ kip \cdot in$$

5. Compare the moment capacity with the factored demand for the current limit state

$$M_{u\_LS1} = \left(1.095 \cdot 10^4\right)\ kip \cdot in$$

$M_{n\_LS1} \geq M_{u\_LS1} = 1$ "ok"

Method 2 - Simplified cracked-section analysis

Step 1: Determine transformed section properties

Modulus ratio for FRP in web to concrete

$$n_{web} := \frac{E_{web}}{E_{con}} = 0.914$$

Modulus ratio for FRP in flange to concrete

$$n_{flan} := \frac{E_{flan}}{E_{con}} = 0.914$$

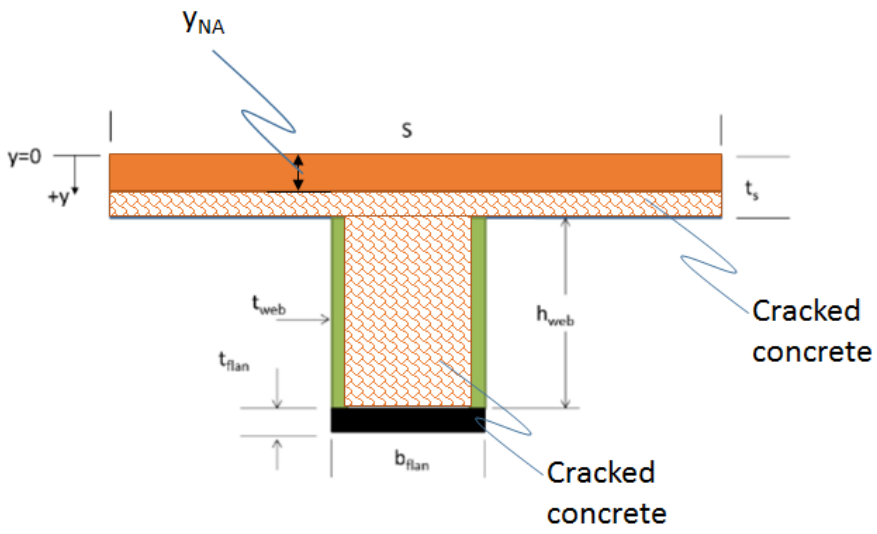

Transformed Section Dimensions:

$$t_{web\_tr} := t_{web} \cdot n_{web} = 0.987 \ in$$

$$b_{flan\_tr} := b_{flan} \cdot n_{flan} = 13.401 \ in$$

Step 2: Determine location of neutral axis

First moment of area for regions above the Neutral Axis must equal first moment of area for regions below the Neutral Axis. Use solve block to solve for y_{NA}:

Given

$y_{NA} := 4 \ in$ initial guess value required by solver

$$S \cdot y_{NA} \cdot \frac{y_{NA}}{2} = b_{flan\_tr} \cdot t_{flan} \cdot \left(\left(t_s + h_{web} + \frac{t_{flan}}{2} \right) - y_{NA} \right) + 2 \cdot t_{web\_tr} \cdot h_{web} \cdot \left(\left(t_s + \frac{h_{web}}{2} \right) - y_{NA} \right)$$

$y_{NA} := \text{find}(y_{NA})$

$y_{NA} = 5.125 \ in$ Distance to neutral axis for cracked concrete section measured from the top of slab. Note this value must be less than the slab thickness in order for the constraint equation defined above to be valid.

$y_{NA\_cr\_tr} := y_{NA}$ Use this value below for LS-3.

Step 3: Determine moment of inertia of cracked/transformed section about the neutral axis

$$b := \begin{bmatrix} S \\ 2 \cdot t_{web\_tr} \\ b_{flan\_tr} \end{bmatrix}$$

b_1 = width of concrete slab

b_2 = transformed width of FRP web

b_3 = transformed width of FRP flange

$$h := \begin{bmatrix} y_{NA} \\ h_{web} \\ t_{flan} \end{bmatrix}$$

h_1 = height of concrete slab in compression

h_2 = height of FRP web

h_3 = height of FRP flange

$$d := \begin{bmatrix} \frac{y_{NA}}{2} \\ \left(t_s + \frac{h_{web}}{2}\right) - y_{NA} \\ \left(t_s + h_{web} + \frac{t_{flan}}{2}\right) - y_{NA} \end{bmatrix}$$

d_1 = distance from NA to centroid of concrete slab in compression

d_2 = distance from NA to centroid of FRP webs

d_3 = distance from NA to centroid FRP flange

$$I_{cr\_tr} := \sum_{i=1}^{3} \left(\frac{b_i \cdot h_i^{\,3}}{12} + \left(b_i \cdot h_i\right) \cdot d_i^{\,2} \right) = \left(2.277 \cdot 10^4\right)\ in^4$$

I_{cr_tr} = cracked/transformed moment of inertia

Step 4: Determine moment that results in concrete compressive stress equal to $0.45\ f'_c$

Basic relationship for normal stress due to bending:

$$\sigma = \frac{M \cdot y}{I} \qquad \text{or} \qquad M = \frac{\sigma \cdot I}{y}$$

$$M_{n\_LS1\_simplified} := \frac{0.45\ f'_c \cdot I_{cr\_tr}}{y_{NA}} = \left(1.0997 \cdot 10^4\right)\ kip \cdot in$$

This result is almost identical to the value obtained using the complete moment-curvature formulation. This makes sense because the stress-vs-strain curve for concrete is effectively linear up to the value of $f_c = 0.45\ f'_c$.

LS-2: Displacements

For $L = 50\ ft$, the displacement envelope for $N_{lane} = 2$ results in the following relationship for Δ_{max}:

$$\Delta_{max} = \frac{-712923596 \cdot kip \cdot in^3}{EI_{total}}$$

To determine the maximum displacment due to live loading, assuming that all elements deflect equally, the total flexural stiffness of the bridge, EI_{total}, is needed. Moment of intertia calculations do not include the cast-in-place concrete barriers. The modulus of elasticity used in these calculations will be the modulus of concrete. Therefore, the FRP material needs to be transformed to concrete.

$n_{web} := \frac{E_{web}}{E_{con}} = 0.914$ Modulus ratio for FRP in web to concrete

$n_{flan} := \frac{E_{flan}}{E_{con}} = 0.914$ Modulus ratio for FRP in flange to concrete

Transformed Section Dimensions:

$t_{web\_tr} := t_{web} \cdot n_{web} = 0.987\ in$

$b_{flan\_tr} := b_{flan} \cdot n_{flan} = 13.401\ in$

Width of concrete in compression zone:

$b_w := b_{flan} - 2 \cdot t_{web} = 12.507\ in$

Define vectors for each component in bridge: Array indices:

$$b := \begin{bmatrix} W_{slab} \\ N_b \cdot b_w \\ N_b \cdot 2 \cdot t_{web\_tr} \\ N_b \cdot b_{flan\_tr} \end{bmatrix} = \begin{bmatrix} 416 \\ 75.04 \\ 11.842 \\ 80.407 \end{bmatrix} in$$

1. Concrete deck
2. Concrete below slab
3. FRP webs (transformed to concrete)
4. FRP bottom flanges (transformed to concrete)

$$h := \begin{bmatrix} t_s \\ h_{con} \\ h_{web} \\ t_{flan} \end{bmatrix} = \begin{bmatrix} 8 \\ 22 \\ 22 \\ 1.08 \end{bmatrix} in$$

Location of centroid with respect to top of slab:

$$y_{bar} := \begin{bmatrix} \frac{t_s}{2} \\ t_s + \frac{h_{con}}{2} \\ t_s + \frac{h_{web}}{2} \\ t_s + h_{web} + \frac{t_{flan}}{2} \end{bmatrix} = \begin{bmatrix} 4 \\ 19 \\ 19 \\ 30.54 \end{bmatrix} in$$

Locate centroid of transformed section

$$Y_{bar} := \frac{\sum_{i=1}^{4} b_i \cdot h_i \cdot y_{bar_i}}{\sum_{i=1}^{4} b_i \cdot h_i} = 9.816\ in$$

Distance to centroid of transformed girder measured from the top of the slab. Note: array origin == 1

Determine moment of inertia of transformed section about its own centroid

$$I_{bridge} := \sum_{i=1}^{4} \left(\frac{b_i \cdot h_i^{3}}{12} + b_i \cdot h_i \cdot \left(y_{bar_i} - Y_{bar} \right)^{2} \right) = 405938\ in^4$$

Multiply by modulus of concrete to obtain the flexural stiffness of the bridge:

$$EI_{total} := E_{con} \cdot I_{bridge} = \left(1.733 \cdot 10^{9}\right)\ kip \cdot in^2$$

Determine the maximum deflection using results from displacement envelope generated for $EI_{total} = 1$:

$$\Delta_{max} := \frac{712923596 \cdot kip \cdot in^3}{EI_{total}} = 0.411\ in$$

$$\Delta_{max\_LS2} := \frac{L}{1000} = 0.6\ in$$

LS-3: Fatigue and Creep Rupture

Similar to the calculations provided for LS-1, two methods for evaluating LS-3 will be explored:

Method 1 - Moment-curvature analysis

1. Find FRP strain corresponding to stress at fatigue and creep rupture limit.

$f'_{fu\_flan} = 73.8\ ksi$

$f_{f\_cr\_limit} := -f'_{fu\_flan} \cdot C_E \cdot C_{fatigue\_rupture} = -7.38\ ksi$

$\varepsilon_{frp\_max} := \frac{f_{f\_cr\_limit}}{E_{flan}} = -0.002$

2. Determine the depth of the neutral axis through force equilibrium. The stress profile is integrated over the depth of the section. The neutral axis occurs where the sum of the forces is equal to zero. The "solve block" feature in MathCAD is used to determine the depth of the neutral axis.

For Limit State 3, $\varepsilon_{known} = \varepsilon_{frp\_max}$

where

ε_{frp_max} is the strain in FRP corresponding to stress at fatigue and creep rupture limit (determined in Step 1)

$y_{known} = t_s + h_{web} + t_{flan}$ because this strain occurs at the bottom of the flange

Guess Values

$y_{NA} := 4\ in$

$F_{ff} := 1\ kip$

$F_{fw} := 1\ kip$

$F_{cbs} := 1\ kip$

$F_s := 1\ kip$

Constraints

$$F_{ff} = \int_{t_s + h_{web}}^{t_s + h_{web} + t_{flan}} f_{frp\_flan}\left(\varepsilon\left(\varepsilon_{frp\_max}, t_s + h_{web} + t_{flan}, y_{NA}, y\right)\right) \cdot \left(b_{flan}\right) \mathrm{d}y$$

$$F_{fw} = \int_{t_s}^{t_s + h_{web}} f_{frp\_web}\left(\varepsilon\left(\varepsilon_{frp\_max}, t_s + h_{web} + t_{flan}, y_{NA}, y\right)\right) \cdot \left(2 \cdot t_{web}\right) \mathrm{d}y$$

$$F_{cbs} = \int_{t_s}^{t_s + h_{web}} f_c\left(\varepsilon\left(\varepsilon_{frp\_max}, t_s + h_{web} + t_{flan}, y_{NA}, y\right)\right) \cdot \left(b_{flan} - 2 \cdot t_{web}\right) \mathrm{d}y$$

$$F_s = \int_{0\ in}^{t_s} f_c\left(\varepsilon\left(\varepsilon_{frp\_max}, t_s + h_{web} + t_{flan}, y_{NA}, y\right)\right) \cdot \left(S\right) \mathrm{d}y$$

$F_{ff} + F_{fw} + F_{cbs} + F_s = 0$

Solver

$$\begin{bmatrix} y_{NA} \\ F_{ff} \\ F_{fw} \\ F_{cbs} \\ F_s \end{bmatrix} := \mathbf{find}\left(y_{NA}, F_{ff}, F_{fw}, F_{cbs}, F_s\right)$$

$$\begin{bmatrix} y_{NA} \\ F_{ff} \\ F_{fw} \\ F_{cbs} \\ F_s \end{bmatrix} = \begin{bmatrix} 0.442\ ft \\ -1.144 \cdot 10^5\ lbf \\ -1.863 \cdot 10^5\ lbf \\ -3.565 \cdot 10^{-28}\ lbf \\ \left(3.008 \cdot 10^5\right)\ lbf \end{bmatrix}$$

$$y_{NA} = 5.309\ in$$

3. Determine the moment generated by each component using the depth to the neutral axis obtained in Step 2.

$$M_{ff} := \int_{t_s + h_{web}}^{t_s + h_{web} + t_{flan}} f_{frp\_flan}\left(\varepsilon\left(\varepsilon_{frp\_max}, t_s + h_{web} + t_{flan}, y_{NA}, y\right)\right) \cdot \left(b_{flan}\right) \cdot \left(y_{NA} - y\right) \mathrm{d}y = \left(2.888 \cdot 10^3\right)\ kip \cdot in$$

$$M_{fw} := \int_{t_s}^{t_s + h_{web}} f_{frp\_web}\left(\varepsilon\left(\varepsilon_{frp\_max}, t_s + h_{web} + t_{flan}, y_{NA}, y\right)\right) \cdot \left(2 \cdot t_{web}\right) \cdot \left(y_{NA} - y\right) \mathrm{d}y = \left(3.1 \cdot 10^3\right)\ kip \cdot in$$

$$M_{cbs} := \int_{t_s}^{t_s + h_{web}} f_c\left(\varepsilon\left(\varepsilon_{frp\_max}, t_s + h_{web} + t_{flan}, y_{NA}, y\right)\right) \cdot \left(b_{flan} - 2 \cdot t_{web}\right) \cdot \left(y_{NA} - y\right) \mathrm{d}y = 0\ kip \cdot in$$

$$M_s := \int_{0\ in}^{t_s} f_c\left(\varepsilon\left(\varepsilon_{frp\_max}, t_s + h_{web} + t_{flan}, y_{NA}, y\right)\right) \cdot (S) \cdot \left(y_{NA} - y\right) \mathrm{d}y = \left(1.174 \cdot 10^3\right)\ kip \cdot in$$

4. Determine the total moment capacity of the cross-section for Limit State 1 by summing the moment contributions from each component

$$M_{n\_LS3} := M_{ff} + M_{fw} + M_{cbs} + M_s = \left(7.162 \cdot 10^3\right)\ kip \cdot in$$

5. Compare the moment capacity with the factored demand for the current limit state

$$M_{u\_LS3} = \left(7.249 \cdot 10^3\right)\ kip \cdot in$$

Discussion: The moment capacity, M_{n_LS3} , is 1.2% less than the factored demand for LS-3. This is due to the fact that the moment-curvature routine used to determine the required thickness of 1.08 in for LS-3 assumes that the stress at the **centroid** of the FRP flange equals the stress at the fatigue and creep rupture limit. The value computed in the hand calculations above assumes that LS-3 is reached when the stress at the **bottom** of the FRP flange equals the stress at the fatigue and creep rupture limit. If the hand calculations are modified such that the FRP stress is evaluated at the centroid of the flange, the resulting M_{n_LS3} is $7.315 \cdot 10^3\ kip \cdot in$, which exceeds the required moment demand of $7.249 \cdot 10^3\ kip \cdot in$.

Method 2 - Simplified cracked-section analysis

The transformed section properties determined for LS-1 are applicable to LS-3 as long as the concrete has cracked and the stress-vs-strain response of the concrete is still approximately linear.

$$y_{NA\_cr\_tr} = 5.125\ in$$

$$I_{cr\_tr} = \left(2.277 \cdot 10^4\right)\ in^4$$

The equivalent stress in the transformed FRP flange is:

$$f_{frp\_tr} := \frac{-f_{f\_cr\_limit}}{n_{flan}} = 8.077\ ksi$$ negative sign has been neglected

The moment required to generate this level of stress at the bottom of the FRP flange is:

$$M_{n\_LS3\_simplified\_1} := \frac{f_{frp\_tr} \cdot I_{cr\_tr}}{\left(t_s + h_{web} + t_{flan}\right) - y_{NA\_cr\_tr}} = \left(7.087 \cdot 10^3\right)\ kip \cdot in$$

The moment required to generate this level of stress at the centroid of the FRP flange is:

$$M_{n\_LS3\_simplified\_2} := \frac{f_{frp\_tr} \cdot I_{cr\_tr}}{\left(t_s + h_{web} + \frac{t_{flan}}{2}\right) - y_{NA\_cr\_tr}} = \left(7.238 \cdot 10^3\right)\ kip \cdot in$$

Discussion: Both values for the moment capacity at Limit State 3 that were computed using the simplified method of cracked/transformed sections are in reasonable agreement with the result obtained from a complete moment-curvature analysis.

There is no appropriate/simplified closed-form solution for determining the flexural capacity at the strength limit state. The moment-curvature approach adopted below assumes that the section's capacity is reached when the stress in the FRP flange reaches the design tensile strength. This needs to be verified for each cross-section.

1. Find FRP strain corresponding to design tensile strength

$f'_{fu\_flan} = 73.8\ ksi$

$f_{f\_strength\_limit} := -f'_{fu\_flan} \cdot C_E = -36.9\ ksi$

$\varepsilon_{frp\_max} := \frac{f_{f\_strength\_limit}}{E_{flan}} = -0.009$

2. Find depth to the neutral axis. Assume maximum strain in FRP is achieved at the bottom of the FRP flange.

Guess Values

$y_{NA} := 4\ in$
$F_{ff} := 1\ kip$
$F_{fw} := 1\ kip$
$F_{cbs} := 1\ kip$
$F_s := 1\ kip$

Constraints

$$F_{ff} = \int_{t_s + h_{web}}^{t_s + h_{web} + t_{flan}} f_{frp\_flan}\left(\varepsilon\left(\varepsilon_{frp\_max}, t_s + h_{web} + t_{flan}, y_{NA}, y\right)\right) \cdot \left(b_{flan}\right) \mathrm{d}y$$

$$F_{fw} = \int_{t_s}^{t_s + h_{web}} f_{frp\_web}\left(\varepsilon\left(\varepsilon_{frp\_max}, t_s + h_{web} + t_{flan}, y_{NA}, y\right)\right) \cdot \left(2 \cdot t_{web}\right) \mathrm{d}y$$

$$F_{cbs} = \int_{t_s}^{t_s + h_{web}} f_c\left(\varepsilon\left(\varepsilon_{frp\_max}, t_s + h_{web} + t_{flan}, y_{NA}, y\right)\right) \cdot \left(b_{flan} - 2 \cdot t_{web}\right) \mathrm{d}y$$

$$F_s = \int_{0\,in}^{t_s} f_c\left(\varepsilon\left(\varepsilon_{frp\_max}, t_s + h_{web} + t_{flan}, y_{NA}, y\right)\right) \cdot \left(S\right) \mathrm{d}y$$

$$F_{ff} + F_{fw} + F_{cbs} + F_s = 0$$

Solver

$$\begin{bmatrix} y_{NA} \\ F_{ff} \\ F_{fw} \\ F_{cbs} \\ F_s \end{bmatrix} := \mathbf{find}\left(y_{NA}, F_{ff}, F_{fw}, F_{cbs}, \mathrm{F_s}\right)$$

$$\begin{bmatrix} y_{NA} \\ F_{ff} \\ F_{fw} \\ F_{cbs} \\ F_s \end{bmatrix} = \begin{bmatrix} 0.467\ ft \\ -5.721 \cdot 10^5\ lbf \\ -9.222 \cdot 10^5\ lbf \\ \left(1.116 \cdot 10^{-26}\right) lbf \\ \left(1.494 \cdot 10^6\right) lbf \end{bmatrix} \qquad y_{NA} = 5.599\ in$$

Determine if concrete crushes in compression:

$\varepsilon\left(\varepsilon_{frp\_max}, t_s + h_{web} + t_{flan}, y_{NA}, 0\right) = 0.002$ strain in concrete at top of slab (y = 0)

ε_{frp_max} = maximum strain in FRP corresponding to design tensile strength of FRP
$t_s + h_{web} + t_{flan}$ = Distance from top of slab to extreme FRP fiber in flange
y_{NA} = depth to neutral axis from the top of the slab
0 = location on cross section where strain is desired

Result:
Strain in concrete is less than .003 when FRP reaches design tensile strength, therefore FRP fails before concrete crushes. This is a tension controlled section. The strength reduction factor, Φ, is given as follows:

$\Phi := 0.55$

3. Compute factored moment capacity at strength limit state:

$$M_{ff} := \int_{t_s + h_{web}}^{t_s + h_{web} + t_{flan}} f_{frp\_flan}\left(\varepsilon\left(\varepsilon_{frp\_max}, t_s + h_{web} + t_{flan}, y_{NA}, y\right)\right) \cdot \left(b_{flan}\right) \cdot \left(y_{NA} - y\right) dy = \left(1.427 \cdot 10^4\right)\ kip \cdot in$$

$$M_{fw} := \int_{t_s}^{t_s + h_{web}} f_{frp\_web}\left(\varepsilon\left(\varepsilon_{frp\_max}, t_s + h_{web} + t_{flan}, y_{NA}, y\right)\right) \cdot \left(2 \cdot t_{web}\right) \cdot \left(y_{NA} - y\right) dy = \left(1.513 \cdot 10^4\right)\ kip \cdot in$$

$$M_{cbs} := \int_{t_s}^{t_s + h_{web}} f_c\left(\varepsilon\left(\varepsilon_{frp\_max}, t_s + h_{web} + t_{flan}, y_{NA}, y\right)\right) \cdot \left(b_{flan} - 2 \cdot t_{web}\right) \cdot \left(y_{NA} - y\right) dy = 0\ kip \cdot in$$

$$M_s := \int_{0\ in}^{t_s} f_c\left(\varepsilon\left(\varepsilon_{frp\_max}, t_s + h_{web} + t_{flan}, y_{NA}, y\right)\right) \cdot (S) \cdot \left(y_{NA} - y\right) dy = \left(5.316 \cdot 10^3\right)\ kip \cdot in$$

$M_{n\_LS4a} := M_{ff} + M_{fw} + M_{cbs} + M_s = \left(3.472 \cdot 10^4\right)\ kip \cdot in$

$\Phi \cdot M_{n\_LS4a} = \left(1.91 \cdot 10^4\right)\ kip \cdot in$

4. Compare factored resistance to factored demand

$M_{u\_LS4a} = \left(1.705 \cdot 10^4\right)\ kip \cdot in$ $\Phi \cdot M_{n\_LS4a} \geq M_{u\_LS4a} = 1$ "ok"

1. Determine depth to neutral axis for cracked concrete section

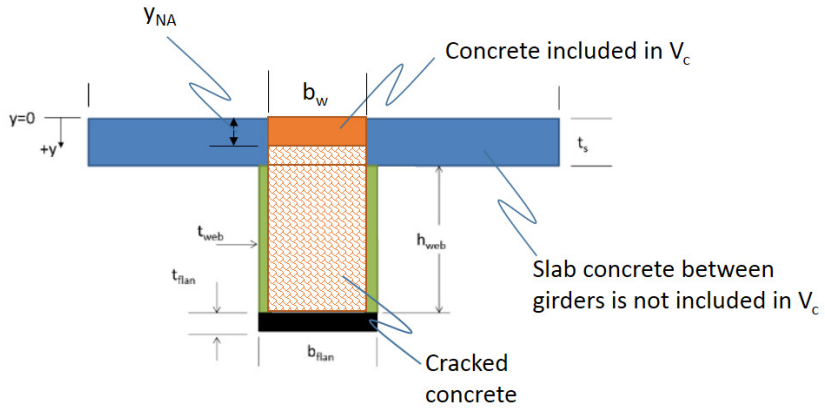

$n_{web} := \frac{E_{web}}{E_{con}} = 0.914$ Modulus ratio for FRP in web to concrete

$n_{flan} := \frac{E_{flan}}{E_{con}} = 0.914$ Modulus ratio for FRP in flange to concrete

Transformed Section Dimensions:

$t_{web\_tr} := t_{web} \cdot n_{web} = 0.987\ in$

$b_{flan\_tr} := b_{flan} \cdot n_{flan} = 13.401\ in$

Width of concrete in compression zone:

$b_w := b_{flan} - 2 \cdot t_{web} = 12.507\ in$

First moment of area for regions above the Neutral Axis must equal first moment of area for regions below the Neutral Axis. Use solve block to solve for y_{NA}:

Guess Values

$y_{NA} := 4\ in$ initial guess value required by solver

Constraints

$$b_w \cdot y_{NA} \cdot \frac{y_{NA}}{2} = b_{flan\_tr} \cdot t_{flan} \cdot \left(\left(t_s + h_{web} + \frac{t_{flan}}{2}\right) - y_{NA}\right) + 2 \cdot t_{web\_tr} \cdot h_{web} \cdot \left(\left(t_s + \frac{h_{web}}{2}\right) - y_{NA}\right)$$

Solver

$y_{NA} := \text{find}(y_{NA})$

$y_{NA} = 10.339\ in$ Distance to neutral axis for cracked concrete section measured from the top of slab

2. Determine area of concrete that participates in shear transfer

$$A_{con\_V} := b_w \cdot y_{NA} = 129.305\ in^2$$

3. Determine shear resistance provided by concrete

$$V_c := 0.158 \cdot \sqrt{\frac{f'_c}{ksi}} \cdot ksi \cdot A_{con\_V} = 47.913\ kip$$

4. Determine shear resistance provided by FRP

Basic relationship for shear stress in FRP webs:

$$\tau_{max} = \frac{3}{2} \cdot \frac{V_{FRP}}{A_{webs}}$$

$$A_{webs} := 2 \cdot t_{web} \cdot h_{web} = 47.52\ in^2$$

$$\tau_{fu} := C_E \cdot \tau'_{fu} = 5\ ksi$$

C_E = Environmental knockdown factor
τ'_{fu} = Manufacturer's specified shear strength for FRP in webs
τ_{fu} = Design shear strength for FRP in webs

Rearranging and solving for V_{FRP}

$$V_{FRP} := \frac{2}{3} \cdot \tau_{fu} \cdot A_{webs} = 158.4\ kip$$

4. Determine factored shear resistance

$$V_n := V_c + V_{FRP} = 206.313\ kip$$

$$\Phi_V := 0.75$$

$$\Phi_V \cdot V_n = 154.735\ kip$$

$$V_{u\_LS4b} = 147.9\ kip$$

5. Compare factored resistance to factored demand

$$\Phi_V \cdot V_n \geq V_{u\_LS4b} = 1 \qquad \text{"ok"}$$

Summary of Results

Limit State 1: Concrete compressive stress

$M_{n\_LS1} = 913.97\ kip \cdot ft$

$M_{u\_LS1} = 912.75\ kip \cdot ft$

Limit State 2: Displacements

$\Delta_{max} := \frac{712923596 \cdot kip \cdot in^3}{EI_{total}} = 0.411\ in$

$\Delta_{max\_LS2} := \frac{L}{1000} = 0.6\ in$

Limit State 3: Fatigue and creep rupture

$M_{n\_LS3} = 596.8\ kip \cdot ft$

$M_{u\_LS3} = 604.1\ kip \cdot ft$

Note: Discussion on why factored resistance is less than factored demand is provided on page 24.

Limit State 4a: Flexural strength

$\Phi \cdot M_{n\_LS4a} = 1591.4\ kip \cdot ft$

$M_{u\_LS4a} = 1420.7\ kip \cdot ft$

Limit State 4b: Shear strength

$\Phi_V \cdot V_n = 154.735\ kip$

$V_{u\_LS4b} = 147.9\ kip$

Appendix B

Bridge Girder Alternatives for Extremely Aggressive Environments (BDV22-977-01)

Hand Calculations for 50' Span Length

Objective: The purpose of these hand calculations is to validate the results generated by the software "FRP_BGAT" that was developed for the present study. This software determines the required FRP thickness to satisfy the four limit states over a range of girder depths. The resulting total girder cost for the bridge is determined assuming a material cost for FRP of $5.25 per pound and cast-in-place concrete cost to fill the U-girders of $0.21 per pound. The resulting series of cost curves can be used to determine the girder depth corresponding to the least cost. Once the girder depth is known, the required FRP thickness can be determined.

Summary of Results from FRP_BGAT described in Section 9.1.3.3 for 50' span

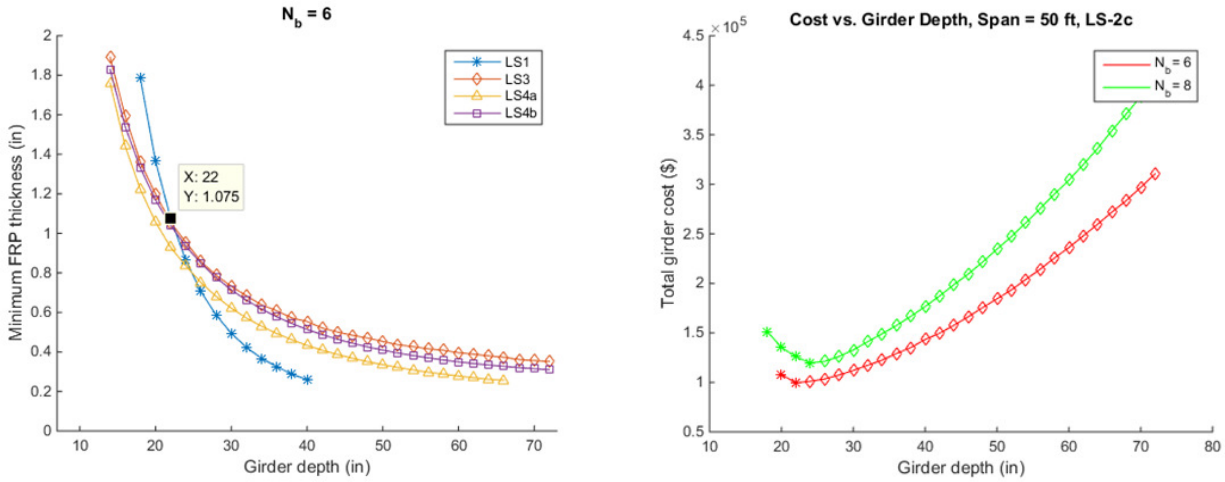

These results were obtained for a bridge with six girders (Nb = 6) and 100% of the girder was filled with concrete. For deflection calculations, the concrete inside the U-girder contributed to the overall stiffness and the cast-in-place barriers were not included in the stiffness of the bridge (LS-2c in Table 25 in Section 8.1.2).

The minimum girder cost is obtained at a girder depth of 22". The corresponding FRP thickness required to satisfy all limit states at this girder depth is 1.075".

The MathCAD worksheet contained in this appendix requires that the overall bridge geometry, girder dimensions, and material properties are fully specified. The input values used in the worksheet are described in Section 9.1 of the report.

Basic Bridge Geometry
(Inputs)

$L := 50\ ft$ Bridge span length

$W_{lane} := 12\ ft$ Lane width

$N_{lane} := 2$ Number of lanes

$W_{shoulder} := 4\ ft$ Shoulder width

$N_{shoulder} := 2$ Number of shoulders

$W_{barrier} := 16\ in$ Traffic barrier width at base

$N_{barrier} := 2$ Number of barriers

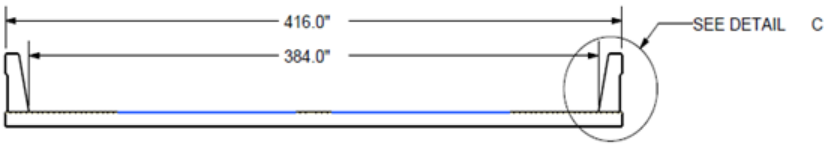

Roadway/deck cross-section

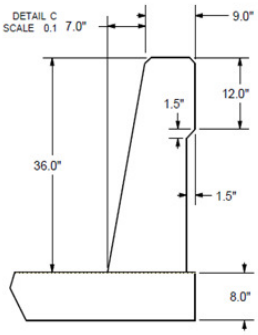

Type "F" traffic barrier/railing

Basic Bridge Geometry
(Calculated)

$W := W_{lane} \cdot N_{lane} + W_{shoulder} \cdot N_{shoulder} = 32\ ft$ Clear distance between barriers

$W_{slab} := W + W_{barrier} \cdot N_{barrier} = 34.667\ ft$ Total slab width

Bridge Cross-section
(Inputs)

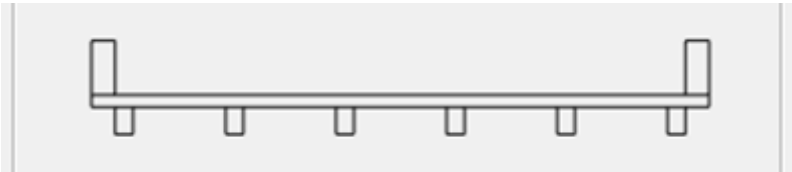

$N_b := 6$ Number of Girders

$t_s := 8\ in$ Reinforced concrete slab thickness

Girder Cross-section
(Inputs)

$h_{web} := 22\ in$ Height of web beneath slab

$Ratio_{web\_height\_to\_flange\_width} := 1.5$

$t_{flan} := 1.08\ in$ FRP flange thickness

$Ratio_{web\_thickness\_to\_flange\_thickness} := 1.0$

$Ratio_{depth\_of\_concrete\_below\_slab\_to\_web\_height} := 1.0$

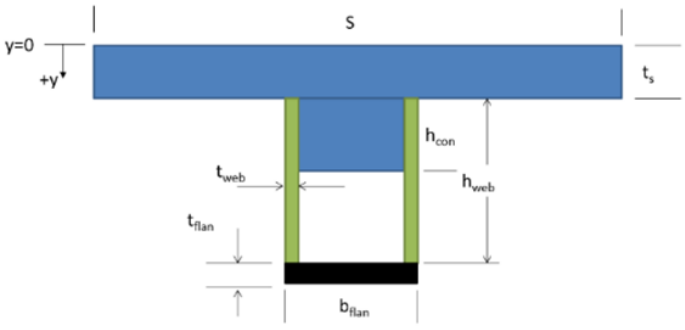

Girder Cross-section
(Calculated)

$b_{flan} := \frac{h_{web}}{Ratio_{web\_height\_to\_flange\_width}} = 14.667\ in$ Width of flange

$t_{web} := t_{flan} \cdot Ratio_{web\_thickness\_to\_flange\_thickness} = 1.08\ in$ FRP web thickness

$h_{con} := h_{web} \cdot Ratio_{depth\_of\_concrete\_below\_slab\_to\_web\_height} = 22\ in$ Depth of concrete below slab

$b_{con} := b_{flan} - 2 \cdot t_{web} = 12.507\ in$ Width of concrete below slab

Girder Spacing

$S := \frac{W - b_{flan}}{N_b - 1} = 6.156\ ft$

Material Properties
(Inputs)

Concrete:

$f'_c := 5500\ psi$ Concrete Compressive Strength

$\gamma_{con} := 150\ pcf$ Unit weight of concrete

$\varepsilon_{ult} := 0.003\ \frac{in}{in}$ Ultimate compressive strain of concrete

FRP:

$f'_{fu\_flan} := 73.8\ ksi$ Manufacturer's specified FRP tensile strength (flange)

$E_{flan} := 3.9 \cdot 10^3\ ksi$ Manufacturer's specified FRP tensile modulus (flange)

$f'_{fu\_web} := 73.8\ ksi$ Manufacturer's specified FRP tensile strength (web)

$E_{web} := 3.9 \cdot 10^3\ ksi$ Manufacturer's specified FRP tensile modulus (web)

$\gamma_{frp} := 118\ pcf$ Unit weight of FRP

$\tau'_{fu} := 10\ ksi$ Manufacturer's specified FRP shear strength

Material knock-down factors

$C_E := 0.5$ Environmental knock-down factor (0.5 for GFRP in aggressive environment)

$C_{fatigue\_rupture} := 0.2$ Strength reduction for fatigue and creep rupture

Material Properties
(Calculated)

$E_{con} := 1820 \cdot \sqrt{\frac{f'_c}{ksi}} \cdot ksi = (4.268 \cdot 10^3)\ ksi$ Modulus of elasticity of concrete

$f_r := 0.2 \cdot \sqrt{\frac{f'_c}{ksi}} \cdot ksi = 0.469\ ksi$ Modulus of rupture of concrete

$f_{fu\_flan} := C_E \cdot f'_{fu\_flan} = 36.9\ ksi$ Design tensile strength of FRP (flange)

$f_{fu\_web} := C_E \cdot f'_{fu\_web} = 36.9\ ksi$ Design tensile strength of FRP (web)

$\tau_{fu} := C_E \cdot \tau'_{fu} = 5\ ksi$ Design shear strength of FRP

Loading Parameters

Dead Loads:

$W_{fws} := 15\ psf$ Allowance for future wearing surface

$w_{barrier} := 0.432\ klf$ Uniform distributed load for single barrier

Live Loads:

$w_{lane} := 0.64\ klf$

$P_{truck} := \begin{bmatrix} 8\ kip \\ 32\ kip \\ 32\ kip \end{bmatrix}$ Axle loads for HL-93 design truck

$S_{truck} := \begin{bmatrix} 14\ ft \\ 14\ ft \end{bmatrix}$ Axle spacing for LS-1, LS-2, and LS-4

$S_{truck\_fatigue} := \begin{bmatrix} 14\ ft \\ 30\ ft \end{bmatrix}$ Axle spacing for LS-3 (fatigue and creep rupture)

$P_{tandem} := \begin{bmatrix} 25\ kip \\ 25\ kip \end{bmatrix}$ Axle loads for design tandem

$S_{tandem} := 4\ ft$ Axle spacing for design tandem

Interior Girder using AASHTO Distribution Factors

Distribution Factor Calculations: General process is to transform girder below slab into equivalent concrete cross-section and then compute moment of inertia of girder around its own centroid.

$n_{web} := \frac{E_{web}}{E_{con}} = 0.914$ Modulus ratio for FRP in web to concrete

$n_{flan} := \frac{E_{flan}}{E_{con}} = 0.914$ Modulus ratio for FRP in flange to concrete

Transformed Section Dimensions

$t_{web\_tr} := t_{web} \cdot n_{web} = 0.987\ in$

$b_{flan\_tr} := b_{flan} \cdot n_{flan} = 13.401\ in$

Girder dimensions below slab – transformed to concrete

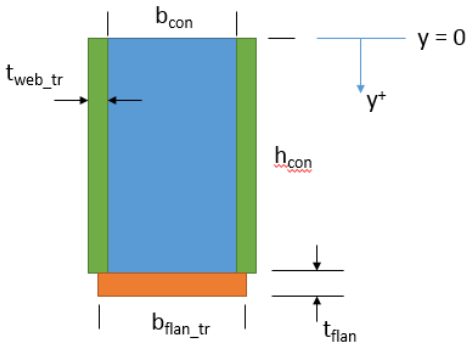

Build arrays with "b" and "h" for:

1. Concrete below slab
2. FRP webs
3. FRP flange

$b := \begin{bmatrix} b_{con} \\ 2 \cdot t_{web\_tr} \\ b_{flan\_tr} \end{bmatrix} = \begin{bmatrix} 12.507 \\ 1.974 \\ 13.401 \end{bmatrix} in$ $h := \begin{bmatrix} h_{con} \\ h_{web} \\ t_{flan} \end{bmatrix} = \begin{bmatrix} 22 \\ 22 \\ 1.08 \end{bmatrix} in$ $y_{bar} := \begin{bmatrix} \frac{h_{con}}{2} \\ \frac{h_{web}}{2} \\ h_{web} + \frac{t_{flan}}{2} \end{bmatrix} = \begin{bmatrix} 11 \\ 11 \\ 22.54 \end{bmatrix} in$

Locate centroid of transformed section

$Y_{bar} := \frac{\sum_{i=1}^{3} b_i \cdot h_i \cdot y_{bar_i}}{\sum_{i=1}^{3} b_i \cdot h_i} = 11.502\ in$

Distance to centroid of transformed girder measured from the bottom of the slab.
Note: array origin == 1

Determine moment of inertia of transformed section about its own centroid

$I_{girder} := \sum_{i=1}^{3} \left(\frac{b_i \cdot h_i^{\,3}}{12} + b_i \cdot h_i \cdot \left(y_{bar_i} - Y_{bar} \right)^2 \right) = 14694\ in^4$

Determine Kg

$n := 1$ (already transformed girder to concrete)

$A := \sum_{i=1}^{3} b_i \cdot h_i = 333.04\ in^2$ Area of girder below slab

$e_g := \frac{t_s}{2} + Y_{bar} = 15.502\ in$ Distance between centroid of slab and centroid of girder

$K_g := n \cdot \left(I_{girder} + A \cdot {e_g}^2\right) = 94722\ in^4$ AASHTO distribution factors are valid for $10000\ in^4 \le K_g \le 7000000\ in^4$

Compute distribution factor for bending moment:

$$DF_{2LL} := 0.075 + \left(\frac{\frac{S}{ft}}{9.5}\right)^{0.6} \cdot \left(\frac{S}{L}\right)^{0.2} \cdot \left(\frac{K_g}{12\ in \cdot \frac{L}{ft} \cdot {t_s}^3}\right)^{.1} = 0.526$$ Two lanes loaded

$$DF_{1LL} := 0.06 + \left(\frac{\frac{S}{ft}}{14}\right)^{0.4} \cdot \left(\frac{S}{L}\right)^{0.3} \cdot \left(\frac{K_g}{12\ in \cdot \frac{L}{ft} \cdot {t_s}^3}\right)^{.1} = 0.401$$ One lane loaded

$DF_{Mom} := \max\left(DF_{2LL}, DF_{1LL}\right) = 0.526$ Select maximum of 1-lane and 2-lanes loaded

Compute distribution factor for shear:

$$DF_{shear\_1LL} := 0.36 + \frac{\frac{S}{ft}}{25} = 0.606$$

$$DF_{shear\_2LL} := 0.2 + \frac{\frac{S}{ft}}{12} - \left(\frac{\frac{S}{ft}}{30}\right)^2 = 0.671$$

$DF_{Shear} := \max\left(DF_{shear\_1LL}, DF_{shear\_2LL}\right) = 0.671$ Select maximum of 1-lane and 2-lanes loaded

Uniform Distributed Loading for single girder (Dead Loads)

$$w_{DL\_slab} := S \cdot t_s \cdot \gamma_{con} = 0.616 \ \frac{kip}{ft}$$

$$w_{DL\_frp} := 2 \cdot h_{web} \cdot t_{web} \cdot \gamma_{frp} + b_{flan} \cdot t_{flan} \cdot \gamma_{frp} = 0.052 \ \frac{kip}{ft}$$

$$w_{DL\_con\_bs} := h_{con} \cdot \left(b_{flan} - 2 \cdot t_{web}\right) \cdot \gamma_{con} = 0.287 \ \frac{kip}{ft}$$

$$w_{DL\_barrier} := \frac{2 \cdot w_{barrier}}{N_b} = 0.144 \ \frac{kip}{ft}$$

$$w_{DL} := w_{DL\_slab} + w_{DL\_frp} + w_{DL\_con\_bs} + w_{DL\_barrier} = 1.098 \ \frac{kip}{ft}$$

Total DL (excluding future wearing surface)

$$w_{DL\_fws} := W_{fws} \cdot S = 0.092 \ \frac{kip}{ft}$$

Live Loads w/ Distribution Factors

$$w_{LL\_Moment} := w_{lane} \cdot DF_{Mom} = 0.336 \ \frac{kip}{ft}$$

$$w_{LL\_Shear} := w_{lane} \cdot DF_{Shear} = 0.429 \ \frac{kip}{ft}$$

These values will later be multiplied by the appropriate load factor for each limit state. The results will then serve as input for a separate shear and moment envelope generator.

$$P_{truck\_Mom} := P_{truck} \cdot DF_{Mom} = \begin{bmatrix} 4.206 \\ 16.822 \\ 16.822 \end{bmatrix} kip$$

$$P_{truck\_Shear} := P_{truck} \cdot DF_{Shear} = \begin{bmatrix} 5.367 \\ 21.468 \\ 21.468 \end{bmatrix} kip$$

$$P_{tandem\_Mom} := P_{tandem} \cdot DF_{Mom} = \begin{bmatrix} 13.143 \\ 13.143 \end{bmatrix} kip$$

$$P_{tandem\_Shear} := P_{tandem} \cdot DF_{Shear} = \begin{bmatrix} 16.772 \\ 16.772 \end{bmatrix} kip$$

Load Factors

	IM	LL-Trk/Tan	LL-Lane	DL	DL-FWS
LS-1: Concrete Compressive Stresses	1.3300	1	1	1	1
LS-2: Displacements	1.3300	1	0	0	0
LS-3: Fatigue/Creep Rupture	1.3300	0.7500	0	1	1
LS-4: Strength	1.3300	1.7500	1.7500	1.2500	1.5000

Limit State 1 - Concrete Compressive Stresses - Need factored design moment, M_u

Define Load Factors:

$IM := 1.33$	Impact
$LL_{vehicle} := 1$	Live load for truck/tandem
$LL_{lane} := 1$	Live load for lane loading
$DL := 1$	Dead load
$DL_{fws} := 1$	Dead load - future wearing surface

Factored loads (includes distribution factors for live loads):

$$w_{u\_LS1} := w_{LL\_Moment} \cdot LL_{lane} + w_{DL} \cdot DL + w_{DL\_fws} \cdot DL_{fws} = 1.527 \ \frac{kip}{ft}$$

$$w_{u\_LS1} = 0.127 \ \frac{kip}{in}$$

$$P_{u\_truck\_LS1} := P_{truck\_Mom} \cdot LL_{vehicle} \cdot IM = \begin{bmatrix} 5.593 \\ 22.374 \\ 22.374 \end{bmatrix} kip$$

$$P_{u\_tandem\_LS1} := P_{tandem\_Mom} \cdot LL_{vehicle} \cdot IM = \begin{bmatrix} 17.48 \\ 17.48 \end{bmatrix} kip$$

Shear and Moment Envelope Results:

$$M_{u\_truck\_LS1} := 10953 \ kip \cdot in = 912.75 \ kip \cdot ft \qquad M_{u\_tandem\_LS1} := 10543 \ kip \cdot in = 878.583 \ kip \cdot ft$$

$$M_{u\_LS1} := \max\left(M_{u\_truck\_LS1}, M_{u\_tandem\_LS1}\right) = 10953 \ kip \cdot in$$

V_M_Envelopes Program Output for LS-1, Concrete Compressive Stresses
Truck Loading

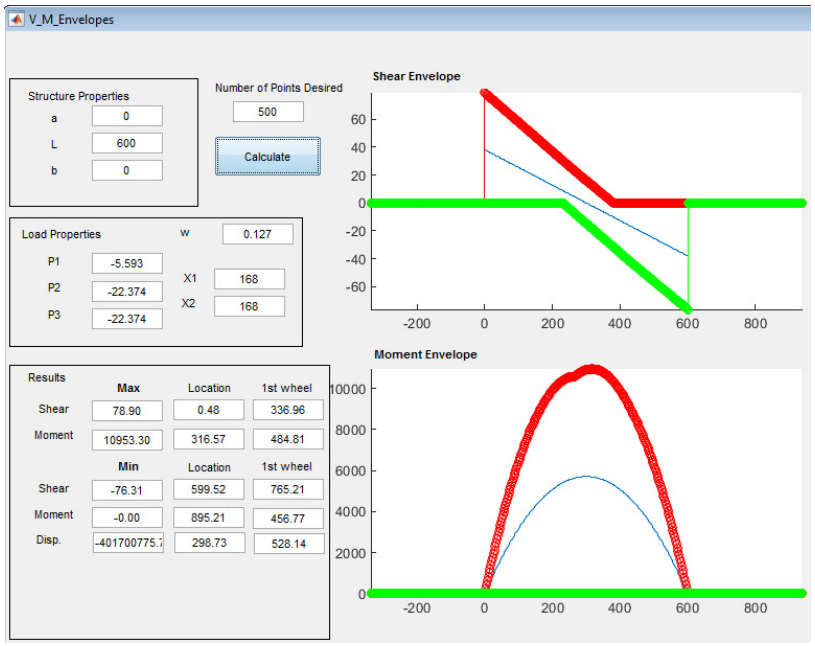

All units are kips & inches

Tandem Loading

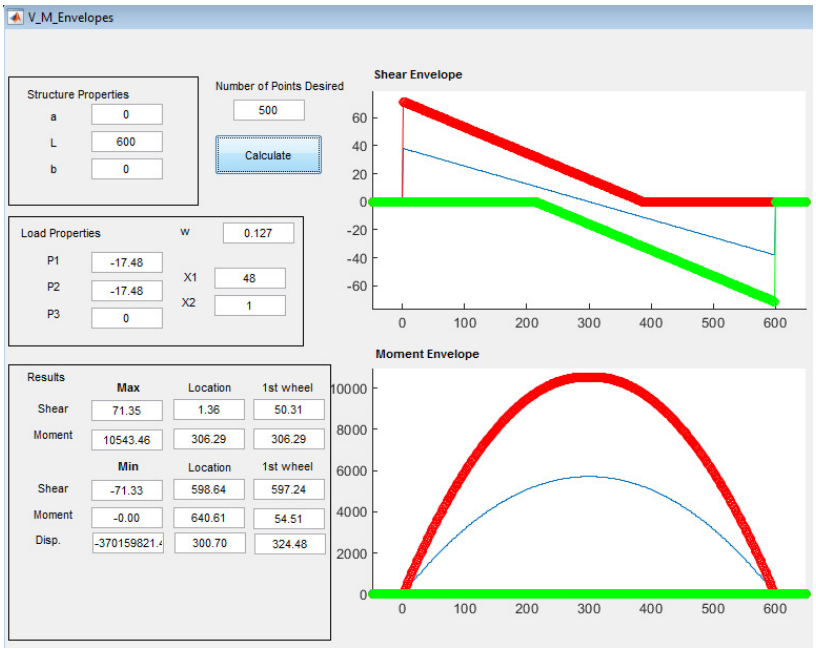

All units are kips & inches

Limit State 2 - Displacements

Generate displacement envelope for simply supported beam with EI = 1. Truck load includes impact and the number of trucks applied equals the number of lanes in the bridge.

Define Load Factors:

$IM := 1.33$	Impact
$LL_{vehicle} := 1$	Live load for truck/tandem
$LL_{lane} := 0$	Live load for lane loading
$DL := 0$	Dead load
$DL_{fws} := 0$	Dead load - future wearing surface

Factored loads (includes distribution factors for live loads):

$$w_{u\_LS2} := w_{LL\_Moment} \cdot LL_{lane} + w_{DL} \cdot DL + w_{DL\_fws} \cdot DL_{fws} = 0 \ \frac{kip}{ft}$$

$$w_{u\_LS2} = 0 \ \frac{kip}{in}$$

Multiple Presence Factor:

$$m := \begin{cases} \text{if } N_{lane} = 1 \\ \quad \text{return } 1.2 \\ \text{else if } N_{lane} = 2 \\ \quad \text{return } 1.0 \\ \text{else if } N_{lane} = 3 \\ \quad \text{return } 0.85 \\ \text{else} \\ \quad \text{return } 0.65 \end{cases} \qquad m = 1$$

$$14 \ ft = 168 \ in$$

$$P_{u\_truck\_LS2} := P_{truck} \cdot LL_{vehicle} \cdot IM \cdot N_{lane} \cdot m = \begin{bmatrix} 21.28 \\ 85.12 \\ 85.12 \end{bmatrix} kip$$

note: P_{truck} does not include distribution factor

Displacement envelope results:

$$\Delta_{max} = \frac{-712923596 \cdot kip \cdot in^3}{EI_{total}}$$

EI_{total} = total bridge flexural stiffness in $kip \cdot in^2$ assuming that all elements of the bridge deflect uniformly. EI_{total} should not include cast-in-place barriers or sidewalks-- only the bridge deck and supporting girders.

V_M_Envelopes Program Output for LS-2, Displacements

Truck Loading (for deflection calculations)

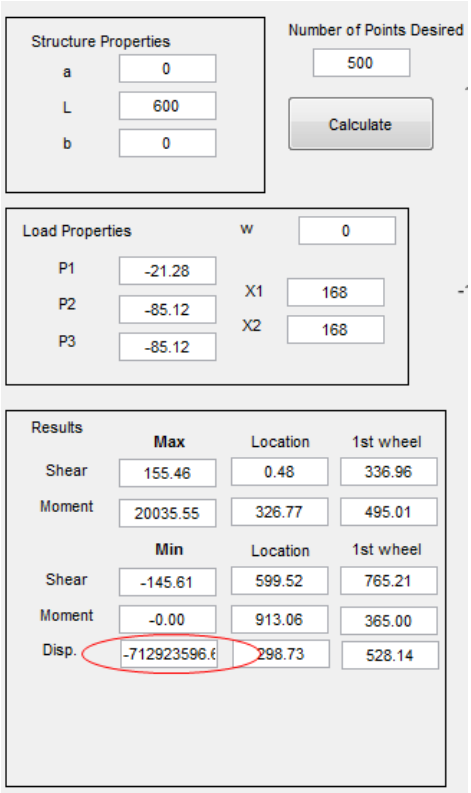

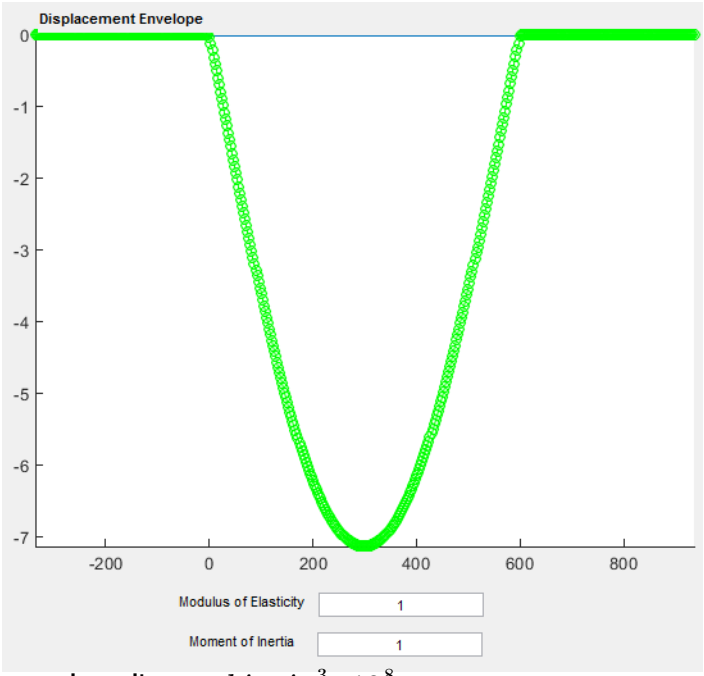

y-axis units are $kip \cdot in^3 \cdot 10^8$
x-axis units are in

Vehicle positioning to generate maximum displacement:

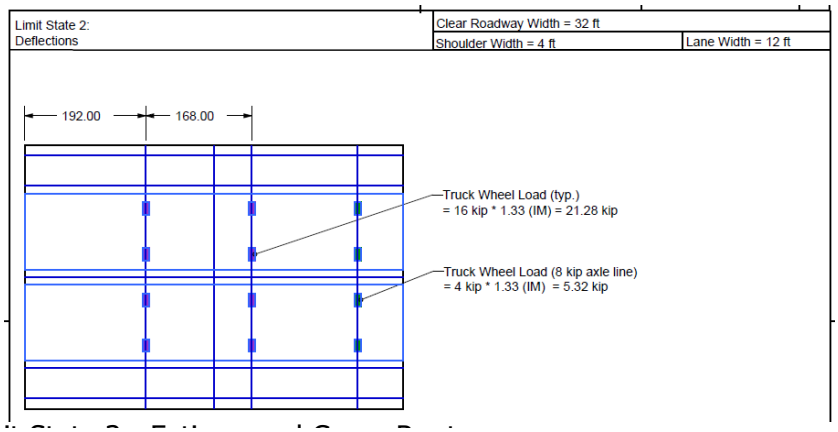

Limit State 3 - Fatigue and Creep Rupture

Require moment envelope for fatigue truck with 1.33 factor for impact and 0.75 factor for fatigue and creep rupture limit state. Also includes dead load and future wearing surface.

Define Load Factors:

$IM := 1.33$	Impact
$LL_{vehicle} := 0.75$	Live load for truck/tandem
$LL_{lane} := 0$	Live load for lane loading
$DL := 1$	Dead load
$DL_{fws} := 1$	Dead load - future wearing surface

Factored loads (includes distribution factors for live loads):

$$w_{u\_LS3} := w_{LL\_Moment} \cdot LL_{lane} + w_{DL} \cdot DL + w_{DL\_fws} \cdot DL_{fws} = 1.19 \ \frac{kip}{ft}$$

$$w_{u\_LS3} = 0.099 \ \frac{kip}{in}$$

$$P_{u\_truck\_LS3} := P_{truck\_Mom} \cdot LL_{vehicle} \cdot IM = \begin{bmatrix} 4.195 \\ 16.78 \\ 16.78 \end{bmatrix} kip$$

note: P_{truck_Mom} includes distribution factor

$$S_{truck\_fatigue} = \begin{bmatrix} 168 \\ 360 \end{bmatrix} in$$

Axle spacing for LS-3 (fatigue and creep rupture)

Shear and Moment Envelope Results:

$$M_{u\_LS3} := 7249 \ kip \cdot in = 604.083 \ kip \cdot ft$$

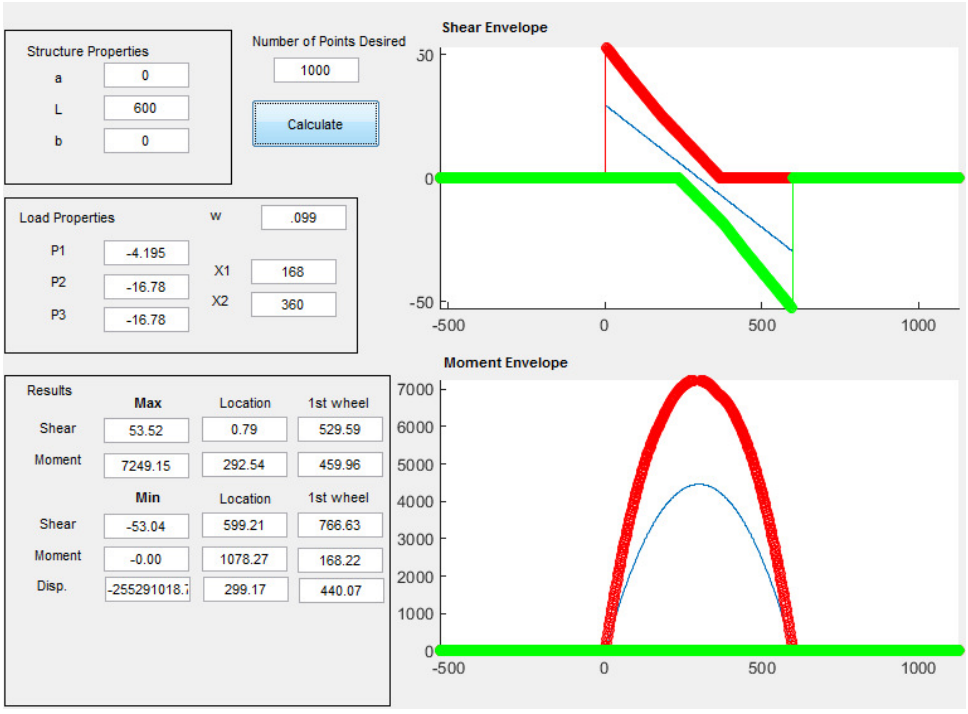

Limit State 4a - Flexural Strength

Require moment envelope for standard truck and tandem, lane loading, and dead loads.

Define Load Factors:

$S = 73.867\ in$

$IM := 1.33$	Impact
$LL_{vehicle} := 1.75$	Live load for truck/tandem
$LL_{lane} := 1.75$	Live load for lane loading
$DL := 1.25$	Dead load
$DL_{fws} := 1.5$	Dead load - future wearing surface

Factored loads (includes distribution factors for live loads):

$$w_{u\_LS4a} := w_{LL\_Moment} \cdot LL_{lane} + w_{DL} \cdot DL + w_{DL\_fws} \cdot DL_{fws} = 2.1\ \frac{kip}{ft}$$

$$w_{u\_LS4a} = 0.175\ \frac{kip}{in}$$

$18.6 \cdot DF_{Mom} = 9.778$

$$P_{u\_truck\_LS4a} := P_{truck\_Mom} \cdot LL_{vehicle} \cdot IM = \begin{bmatrix} 9.789 \\ 39.154 \\ 39.154 \end{bmatrix} kip$$

note: P_{truck_Mom} and P_{tandem_Mom} includes distribution factor

$$P_{u\_tandem\_LS4a} := P_{tandem\_Mom} \cdot LL_{vehicle} \cdot IM = \begin{bmatrix} 30.589 \\ 30.589 \end{bmatrix} kip$$

Shear and Moment Envelope Results:

$$M_{u\_truck\_LS4a} := 17048.5\ kip \cdot in = 1421\ kip \cdot ft$$

$$M_{u\_tandem\_LS4a} := 16325\ kip \cdot in = 1360\ kip \cdot ft$$

$$M_{u\_LS4a} := \max\left(M_{u\_truck\_LS4a}, M_{u\_tandem\_LS4a}\right) = 17049\ kip \cdot in$$

V and M Envelopes for truck:

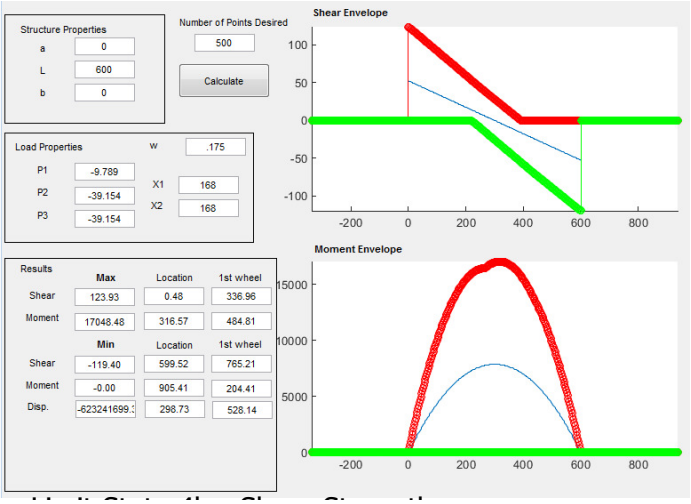

V and M Envelopes for Tandem:

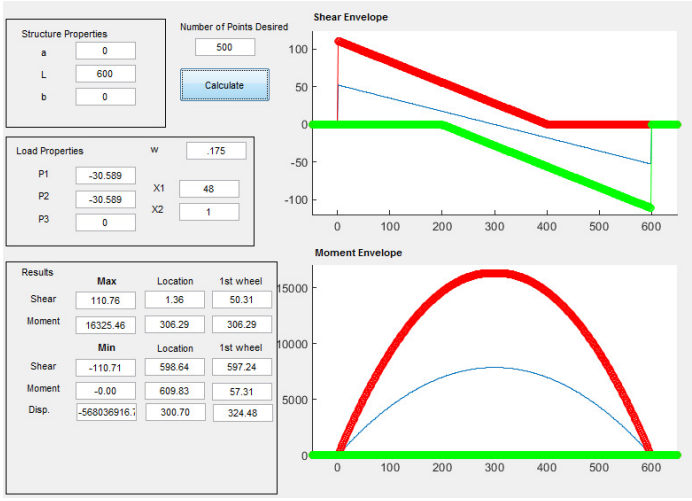

Limit State 4b - Shear Strength

Require shear envelope for standard truck and tandem, lane loading, and dead loads.

Define Load Factors:

$IM := 1.33$	Impact
$LL_{vehicle} := 1.75$	Live load for truck/tandem
$LL_{lane} := 1.75$	Live load for lane loading
$DL := 1.25$	Dead load
$DL_{fws} := 1.5$	Dead load - future wearing surface

Factored loads (includes distribution factors for live loads):

$$w_{u\_LS4b} := w_{LL\_Shear} \cdot LL_{lane} + w_{DL} \cdot DL + w_{DL\_fws} \cdot DL_{fws} = 2.262 \ \frac{kip}{ft}$$

$$w_{u\_LS4b} = 0.189 \ \frac{kip}{in}$$

$$w_{u\_LS4b} \cdot \frac{L}{2} = 56.562 \ kip$$

$$S_{truck} = \begin{bmatrix} 168 \\ 168 \end{bmatrix} in$$

$$P_{u\_truck\_LS4b} := P_{truck\_Shear} \cdot LL_{vehicle} \cdot IM = \begin{bmatrix} 12.491 \\ 49.966 \\ 49.966 \end{bmatrix} kip$$

note: P_{truck_Shear} and P_{tandem_Shear} includes distribution factor

$$P_{u\_tandem\_LS4b} := P_{tandem\_Shear} \cdot LL_{vehicle} \cdot IM = \begin{bmatrix} 39.036 \\ 39.036 \end{bmatrix} kip$$

Shear and Moment Envelope Results:

$$V_{u\_truck\_LS4b} := 147.9 \ kip$$

$$V_{u\_tandem\_LS4b} := 131.04 \ kip$$

$$V_{u\_LS4b} := \max\left(V_{u\_truck\_LS4b}, V_{u\_tandem\_LS4b}\right) = 148 \ kip$$

V and M Envelopes for truck:

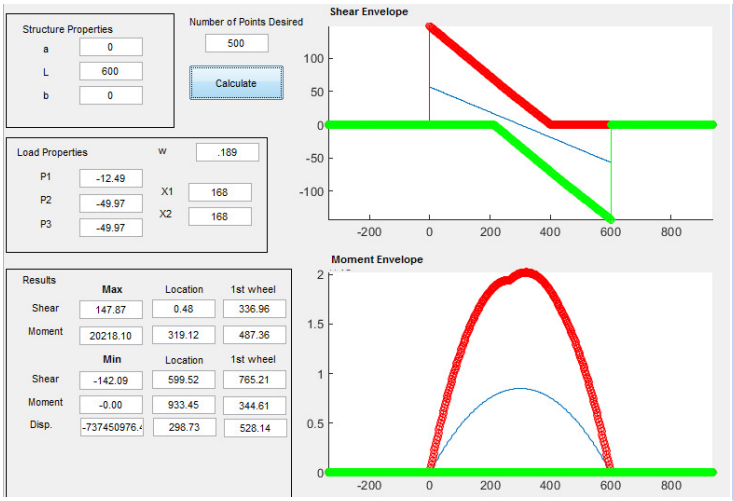

V and M Envelopes for Tandem:

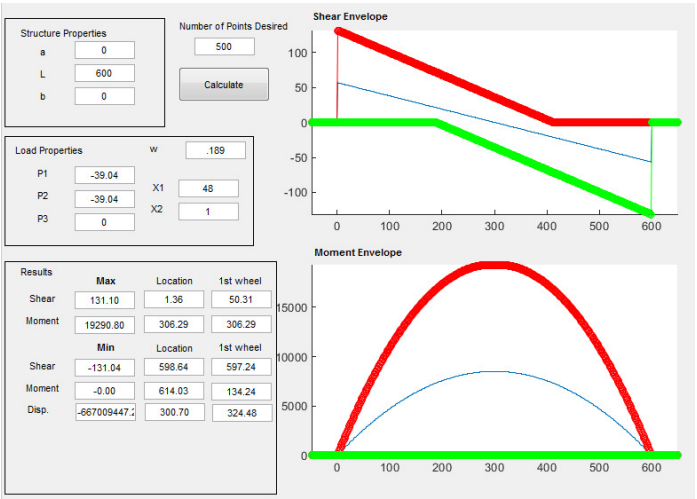

Summary of Factored Structural Demands and Limit State Criteria:

LS-1: Concrete Compressive Stresses

$M_{u\_LS1} = 10953\ kip \cdot in$

$M_{u\_LS1} = 912.8\ kip \cdot ft$

Criteria:
Maximum concrete compressive stress less than 45% of concrete compressive strength

$$f_c \le 0.45\ f'_c$$

LS-2: Displacements

$$\Delta_{max} = \frac{-712923596 \cdot kip \cdot in^3}{EI_{total}}$$

In the section on Capacity Analysis for LS-2, the EI_{total} for the entire bridge will be calculated. This value will then be used to compute the maximum displacement assuming the that all girders deflect uniformly.

Criteria:

$$\Delta_{max} \le \frac{L}{1000}$$

LS-3: Fatigue and Creep Rupture

$M_{u\_LS3} = 7249\ kip \cdot in$

$M_{u\_LS3} = 604.1\ kip \cdot ft$

Criteria:
Maximum tensile stress in FRP is limited by the following:

$$f_{frp\_max} \le f'_{fu\_flan} \cdot C_E \cdot C_{fatigue\_rupture}$$

where:
f_{frp_max} = maximum FRP stress that develops under LS-3 loading conditions
f'_{fu_flan} = manufacturer's specified tensile strength
C_E = enviromental knockdown factor
$C_{fatigue\_rupture}$ = knockdown factor for fatigue and creep rupture

LS-4a: Flexural Strength

$M_{u\_LS4a} = 17048.5\ kip \cdot in$

$M_{u\_LS4a} = 1420.708\ kip \cdot ft$

Criteria:

$$M_{u\_LS4a} \le \Phi \cdot M_n$$

LS-4b: Shear Strength

$V_{u\_LS4b} = 147.9\ kip$

Criteria:

$$V_{u\_LS4b} \le \Phi \cdot V_n$$

Establish function for concrete stress as a function of strain using Thorenfeldt, Tomaszewicz, and Jensen Model. (pg. 71 of Wight text on Reinforced Concrete)

Summary of input material properties:

$f_r = 0.469\ ksi$ Max tensile stress

$f'_c = 5.5\ ksi$ Max compressive stress

$\varepsilon_{ult} = 0.003$ Max compressive strain of concrete

$E_{con} = 4268\ ksi$ Modulus of elasticity of concrete in linear region

Other factors needed to develop function:

$\varepsilon_{ult\_tension} := \frac{-f_r}{E_{con}} = -1.099 \cdot 10^{-4}$ Ultimate tensile strain

$cf := 0.8 + \frac{f'_c}{2.5 \cdot ksi} = 3$ Curve fitting factor

$\varepsilon_o := \frac{f'_c}{E_{con}} \cdot \left(\frac{cf}{cf - 1}\right) = 0.002$ compressive strain corresponding to maximum tensile stress

Define concrete stress, f_c , as a function of concrete strain, ε_c

$f_c(\varepsilon_c) :=$ if $\varepsilon_c < \varepsilon_{ult\_tension}$ — Concrete cracked

  return $0 \cdot ksi$

else if $\varepsilon_c < 0$ — Concrete in tension

  return $\varepsilon_c \cdot E_{con}$

else if $\varepsilon_c \le \varepsilon_o$ — Concrete in compression with $\varepsilon_c \le \varepsilon_o$

  $k \leftarrow 1$

  return $f'_c \cdot \left(\frac{cf \cdot \frac{\varepsilon_c}{\varepsilon_o}}{cf - 1 + \left(\frac{\varepsilon_c}{\varepsilon_o}\right)^{cf \cdot k}}\right)$

else if $\varepsilon_c \le \varepsilon_{ult}$ — Concrete in compression with $\varepsilon_c \le \varepsilon_{ult}$

  $k \leftarrow \max\left(1, 0.67 + \frac{f'_c}{9 \cdot ksi}\right)$

  return $f'_c \cdot \left(\frac{cf \cdot \frac{\varepsilon_c}{\varepsilon_o}}{cf - 1 + \left(\frac{\varepsilon_c}{\varepsilon_o}\right)^{cf \cdot k}}\right)$

$\max\left(1, 0.67 + \frac{f'_c}{9 \cdot ksi}\right) = 1.281$

Plot of stress vs. strain for concrete

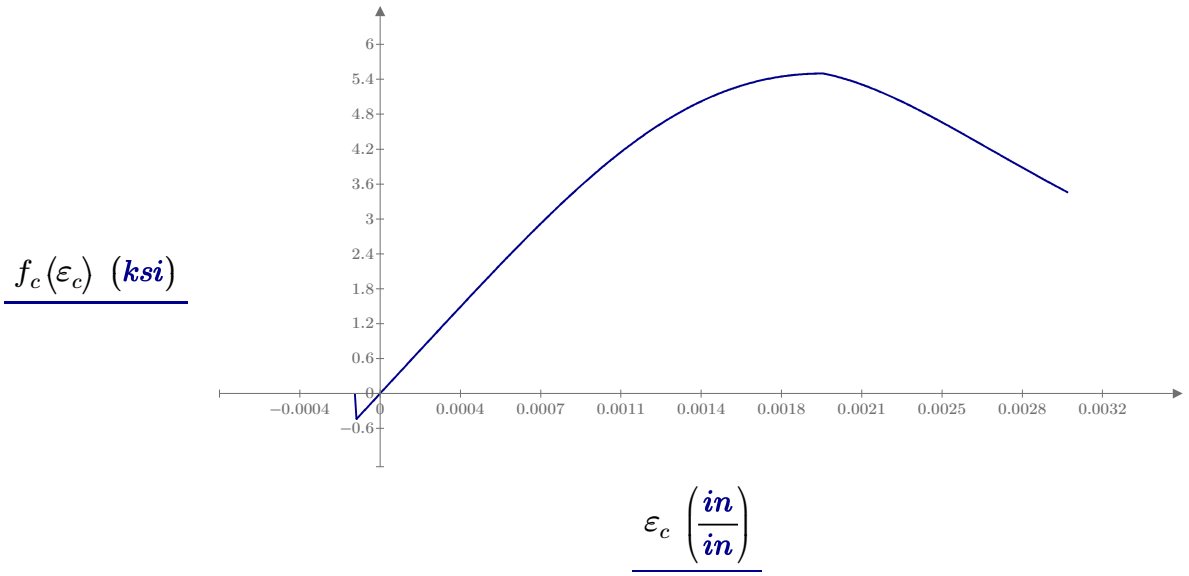

LS-1: Concrete Compressive Stress

Two methods for computing the moment capacity for LS-1 will be investigated:

Method 1: Moment-curvature analysis that incorporates non-linear stress-vs-strain relationship for concrete.

Method 2: Simplified cracked-section analysis that assumes linear stress-vs-strain relationship for concrete and transformed width properties for FRP.

Method 1 - Moment-curvature analysis

1. Find concrete strain corresponding to $0.45 \cdot f'_c$

Guess Values

$\varepsilon_{c\_max} := 0.45 \cdot \varepsilon_o$ initial guess required by solver

Constraints

$f_c(\varepsilon_{c\_max}) = 0.45\ f'_c$

Solver

$\varepsilon_{c\_max} := \text{find}(\varepsilon_{c\_max})$ $\varepsilon_{c\_max} = 5.88 \cdot 10^{-4}$ max concrete strain

$f_c(\varepsilon_{c\_max}) = 2.475$ ksi

$0.45\ f'_c = 2.475$ ksi

2. Establish strain profile as a function of known strain and depth to NA

$$\varepsilon\left(\varepsilon_{known}, y_{known}, y_{NA}, y\right) := \left\| \begin{array}{l} m \leftarrow \dfrac{\varepsilon_{known}}{y_{known} - y_{NA}} \\ \text{return } m \cdot \left(y - y_{NA}\right) \end{array} \right\|$$

$$f_{frp\_flan}\left(\varepsilon_{frp}\right) := E_{flan} \cdot \varepsilon_{frp}$$

$$f_{frp\_web}\left(\varepsilon_{frp}\right) := E_{web} \cdot \varepsilon_{frp}$$

For Limit State 1, $\varepsilon_{known} = \varepsilon_{c\_max}$
where
ε_{c_max} is the strain in concrete corresponding to $0.45\ f'_c$ (determined in Step 1)
y_{known} = 0 because this strain occurs at the top of the slab

2. Determine the depth of the neutral axis through force equilibrium. The stress profile is integrated over the depth of the section. The neutral axis occurs where the sum of the forces is equal to zero. The "solve block" feature in MathCAD is used to determine the depth of the neutral axis.

Guess Values

$y_{NA} := 4\ in$
$F_{ff} := 1\ kip$
$F_{fw} := 1\ kip$
$F_{cbs} := 1\ kip$
$F_s := 1\ kip$

Constraints

$$F_{ff} = \int_{t_s + h_{web}}^{t_s + h_{web} + t_{flan}} f_{frp\_flan}\left(\varepsilon\left(\varepsilon_{c\_max}, 0, y_{NA}, y\right)\right) \cdot \left(b_{flan}\right) \mathrm{d}y \qquad F_{ff} \text{ = force in FRP flange}$$

$$F_{fw} = \int_{t_s}^{t_s + h_{web}} f_{frp\_web}\left(\varepsilon\left(\varepsilon_{c\_max}, 0, y_{NA}, y\right)\right) \cdot \left(2 \cdot t_{web}\right) \mathrm{d}y \qquad F_{fw} \text{ = force in FRP web}$$

$$F_{cbs} = \int_{t_s}^{t_s + h_{web}} f_c\left(\varepsilon\left(\varepsilon_{c\_max}, 0, y_{NA}, y\right)\right) \cdot \left(b_{flan} - 2 \cdot t_{web}\right) \mathrm{d}y \qquad F_{cbs} \text{ = force in concrete below slab}$$

$$F_s = \int_{0\ in}^{t_s} f_c\left(\varepsilon\left(\varepsilon_{c\_max}, 0, y_{NA}, y\right)\right) \cdot \left(S\right) \mathrm{d}y \qquad F_s \text{ = force in slab}$$

$F_{ff} + F_{fw} + F_{cbs} + F_s = 0$ The sum of the forces = 0 when the correct depth to the neutral axis has been identified.

Solver

$$\begin{bmatrix} y_{NA} \\ F_{ff} \\ F_{fw} \\ F_{cbs} \\ F_s \end{bmatrix} := \text{find}\left(y_{NA}, F_{ff}, F_{fw}, F_{cbs}, F_s\right)$$

"find" is MathCAD's solve function that determines the depth to the neutral axis numerically.

$$\begin{bmatrix} \quad \\ \quad \end{bmatrix} \begin{bmatrix} \quad 0.434\ ft \quad \end{bmatrix}$$

$$\begin{bmatrix} y_{NA} \\ F_{ff} \\ F_{fw} \\ F_{cbs} \\ F_s \end{bmatrix} = \begin{bmatrix} 0.434\ ft \\ -1.765 \cdot 10^5\ lbf \\ -2.883 \cdot 10^5\ lbf \\ \left(4.704 \cdot 10^{-27}\right) lbf \\ \left(4.649 \cdot 10^5\right) lbf \end{bmatrix}$$

Note: Compression is positive, Tension is negative

$y_{NA} = 5.211\ in$ $F_s = 464.877\ kip$ $F_{ff} = -176.547\ kip$ $F_{cbs} = 0\ kip$

$F_{fw} = -288.33\ kip$

3. Determine the moment generated by each component using the depth to the neutral axis obtained in Step 2.

$$M_{ff} := \int_{t_s + h_{web}}^{t_s + h_{web} + t_{flan}} f_{frp\_flan}\left(\varepsilon\left(\varepsilon_{c\_max}, 0, y_{NA}, y\right)\right) \cdot \left(b_{flan}\right) \cdot \left(y_{NA} - y\right) \mathrm{d}y = \left(4.472 \cdot 10^3\right)\ kip \cdot in$$

$$M_{fw} := \int_{t_s}^{t_s + h_{web}} f_{frp\_web}\left(\varepsilon\left(\varepsilon_{c\_max}, 0, y_{NA}, y\right)\right) \cdot \left(2 \cdot t_{web}\right) \cdot \left(y_{NA} - y\right) \mathrm{d}y = \left(4.819 \cdot 10^3\right)\ kip \cdot in$$

$$M_{cbs} := \int_{t_s}^{t_s + h_{web}} f_c\left(\varepsilon\left(\varepsilon_{c\_max}, 0, y_{NA}, y\right)\right) \cdot \left(b_{flan} - 2 \cdot t_{web}\right) \cdot \left(y_{NA} - y\right) \mathrm{d}y = 0\ kip \cdot in$$

$$M_s := \int_{0\ in}^{t_s} f_c\left(\varepsilon\left(\varepsilon_{c\_max}, 0, y_{NA}, y\right)\right) \cdot (S) \cdot \left(y_{NA} - y\right) \mathrm{d}y = \left(1.676 \cdot 10^3\right)\ kip \cdot in$$

4. Determine the total moment capacity of the cross-section for Limit State 1 by summing the moment contributions from each component

$$M_{n\_LS1} := M_{ff} + M_{fw} + M_{cbs} + M_s = \left(1.097 \cdot 10^4\right)\ kip \cdot in$$

5. Compare the moment capacity with the factored demand for the current limit state

$$M_{u\_LS1} = \left(1.095 \cdot 10^4\right)\ kip \cdot in$$

$M_{n\_LS1} \geq M_{u\_LS1} = 1$ "ok"

Method 2 - Simplified cracked-section analysis

Step 1: Determine transformed section properties

Modulus ratio for FRP in web to concrete

$$n_{web} := \frac{E_{web}}{E_{con}} = 0.914$$

Modulus ratio for FRP in flange to concrete

$$n_{flan} := \frac{E_{flan}}{E_{con}} = 0.914$$

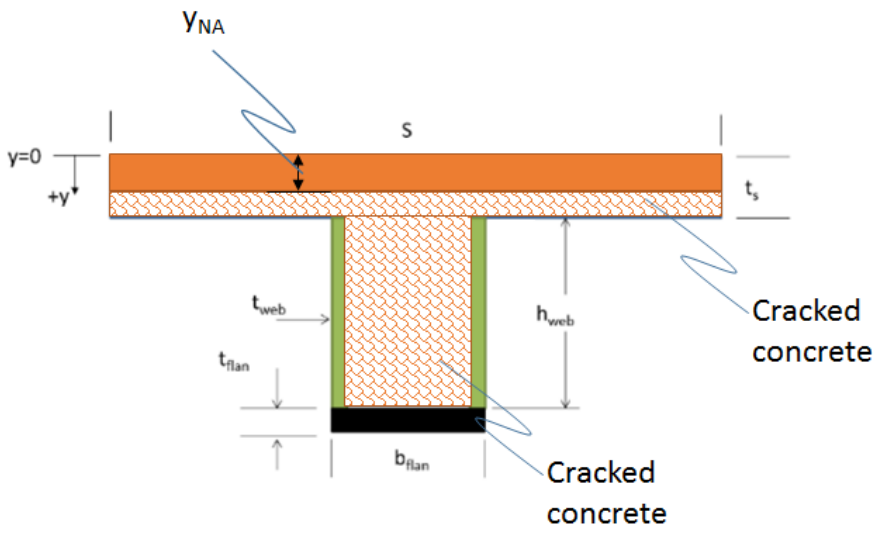

Transformed Section Dimensions:

$$t_{web\_tr} := t_{web} \cdot n_{web} = 0.987 \ in$$

$$b_{flan\_tr} := b_{flan} \cdot n_{flan} = 13.401 \ in$$

Step 2: Determine location of neutral axis

First moment of area for regions above the Neutral Axis must equal first moment of area for regions below the Neutral Axis. Use solve block to solve for y_{NA}:

Given

$y_{NA} := 4 \ in$ initial guess value required by solver

$$S \cdot y_{NA} \cdot \frac{y_{NA}}{2} = b_{flan\_tr} \cdot t_{flan} \cdot \left(\left(t_s + h_{web} + \frac{t_{flan}}{2} \right) - y_{NA} \right) + 2 \cdot t_{web\_tr} \cdot h_{web} \cdot \left(\left(t_s + \frac{h_{web}}{2} \right) - y_{NA} \right)$$

$y_{NA} := \text{find}(y_{NA})$

$y_{NA} = 5.125 \ in$ Distance to neutral axis for cracked concrete section measured from the top of slab. Note this value must be less than the slab thickness in order for the constraint equation defined above to be valid.

$y_{NA\_cr\_tr} := y_{NA}$ Use this value below for LS-3.

Step 3: Determine moment of inertia of cracked/transformed section about the neutral axis

$$b := \begin{bmatrix} S \\ 2 \cdot t_{web\_tr} \\ b_{flan\_tr} \end{bmatrix}$$

b_1 = width of concrete slab

b_2 = transformed width of FRP web

b_3 = transformed width of FRP flange

$$h := \begin{bmatrix} y_{NA} \\ h_{web} \\ t_{flan} \end{bmatrix}$$

h_1 = height of concrete slab in compression

h_2 = height of FRP web

h_3 = height of FRP flange

$$d := \begin{bmatrix} \frac{y_{NA}}{2} \\ \left(t_s + \frac{h_{web}}{2}\right) - y_{NA} \\ \left(t_s + h_{web} + \frac{t_{flan}}{2}\right) - y_{NA} \end{bmatrix}$$

d_1 = distance from NA to centroid of concrete slab in compression

d_2 = distance from NA to centroid of FRP webs

d_3 = distance from NA to centroid FRP flange

$$I_{cr\_tr} := \sum_{i=1}^{3} \left(\frac{b_i \cdot h_i^{\,3}}{12} + \left(b_i \cdot h_i\right) \cdot d_i^{\,2} \right) = \left(2.277 \cdot 10^4\right)\ in^4$$

I_{cr_tr} = cracked/transformed moment of inertia

Step 4: Determine moment that results in concrete compressive stress equal to $0.45\ f'_c$

Basic relationship for normal stress due to bending:

$$\sigma = \frac{M \cdot y}{I} \qquad \text{or} \qquad M = \frac{\sigma \cdot I}{y}$$

$$M_{n\_LS1\_simplified} := \frac{0.45\ f'_c \cdot I_{cr\_tr}}{y_{NA}} = \left(1.0997 \cdot 10^4\right)\ kip \cdot in$$

This result is almost identical to the value obtained using the complete moment-curvature formulation. This makes sense because the stress-vs-strain curve for concrete is effectively linear up to the value of $f_c = 0.45\ f'_c$.

LS-2: Displacements

For $L = 50\ ft$, the displacement envelope for $N_{lane} = 2$ results in the following relationship for Δ_{max}:

$$\Delta_{max} = \frac{-712923596 \cdot kip \cdot in^3}{EI_{total}}$$

To determine the maximum displacment due to live loading, assuming that all elements deflect equally, the total flexural stiffness of the bridge, EI_{total}, is needed. Moment of intertia calculations do not include the cast-in-place concrete barriers. The modulus of elasticity used in these calculations will be the modulus of concrete. Therefore, the FRP material needs to be transformed to concrete.

$n_{web} := \frac{E_{web}}{E_{con}} = 0.914$ Modulus ratio for FRP in web to concrete

$n_{flan} := \frac{E_{flan}}{E_{con}} = 0.914$ Modulus ratio for FRP in flange to concrete

Transformed Section Dimensions:

$t_{web\_tr} := t_{web} \cdot n_{web} = 0.987\ in$

$b_{flan\_tr} := b_{flan} \cdot n_{flan} = 13.401\ in$

Width of concrete in compression zone:

$b_w := b_{flan} - 2 \cdot t_{web} = 12.507\ in$

Define vectors for each component in bridge: Array indices:

$$b := \begin{bmatrix} W_{slab} \\ N_b \cdot b_w \\ N_b \cdot 2 \cdot t_{web\_tr} \\ N_b \cdot b_{flan\_tr} \end{bmatrix} = \begin{bmatrix} 416 \\ 75.04 \\ 11.842 \\ 80.407 \end{bmatrix} in$$

1. Concrete deck
2. Concrete below slab
3. FRP webs (transformed to concrete)
4. FRP bottom flanges (transformed to concrete)

$$h := \begin{bmatrix} t_s \\ h_{con} \\ h_{web} \\ t_{flan} \end{bmatrix} = \begin{bmatrix} 8 \\ 22 \\ 22 \\ 1.08 \end{bmatrix} in$$

Location of centroid with respect to top of slab:

$$y_{bar} := \begin{bmatrix} \frac{t_s}{2} \\ t_s + \frac{h_{con}}{2} \\ t_s + \frac{h_{web}}{2} \\ t_s + h_{web} + \frac{t_{flan}}{2} \end{bmatrix} = \begin{bmatrix} 4 \\ 19 \\ 19 \\ 30.54 \end{bmatrix} in$$

Locate centroid of transformed section

$$Y_{bar} := \frac{\sum_{i=1}^{4} b_i \cdot h_i \cdot y_{bar_i}}{\sum_{i=1}^{4} b_i \cdot h_i} = 9.816\ in$$

Distance to centroid of transformed girder measured from the top of the slab. Note: array origin == 1

Determine moment of inertia of transformed section about its own centroid

$$I_{bridge} := \sum_{i=1}^{4} \left(\frac{b_i \cdot h_i^{3}}{12} + b_i \cdot h_i \cdot \left(y_{bar_i} - Y_{bar} \right)^{2} \right) = 405938\ in^4$$

Multiply by modulus of concrete to obtain the flexural stiffness of the bridge:

$$EI_{total} := E_{con} \cdot I_{bridge} = \left(1.733 \cdot 10^{9}\right)\ kip \cdot in^2$$

Determine the maximum deflection using results from displacement envelope generated for $EI_{total} = 1$:

$$\Delta_{max} := \frac{712923596 \cdot kip \cdot in^3}{EI_{total}} = 0.411\ in$$

$$\Delta_{max\_LS2} := \frac{L}{1000} = 0.6\ in$$

LS-3: Fatigue and Creep Rupture

Similar to the calculations provided for LS-1, two methods for evaluating LS-3 will be explored:

Method 1 - Moment-curvature analysis

1. Find FRP strain corresponding to stress at fatigue and creep rupture limit.

$f'_{fu\_flan} = 73.8\ ksi$

$f_{f\_cr\_limit} := -f'_{fu\_flan} \cdot C_E \cdot C_{fatigue\_rupture} = -7.38\ ksi$

$\varepsilon_{frp\_max} := \frac{f_{f\_cr\_limit}}{E_{flan}} = -0.002$

2. Determine the depth of the neutral axis through force equilibrium. The stress profile is integrated over the depth of the section. The neutral axis occurs where the sum of the forces is equal to zero. The "solve block" feature in MathCAD is used to determine the depth of the neutral axis.

For Limit State 3, $\varepsilon_{known} = \varepsilon_{frp\_max}$

where

ε_{frp_max} is the strain in FRP corresponding to stress at fatigue and creep rupture limit (determined in Step 1)

$y_{known} = t_s + h_{web} + t_{flan}$ because this strain occurs at the bottom of the flange

Guess Values

$y_{NA} := 4\ in$

$F_{ff} := 1\ kip$

$F_{fw} := 1\ kip$

$F_{cbs} := 1\ kip$

$F_s := 1\ kip$

Constraints

$$F_{ff} = \int_{t_s + h_{web}}^{t_s + h_{web} + t_{flan}} f_{frp\_flan}\left(\varepsilon\left(\varepsilon_{frp\_max}, t_s + h_{web} + t_{flan}, y_{NA}, y\right)\right) \cdot \left(b_{flan}\right) \mathrm{d}y$$

$$F_{fw} = \int_{t_s}^{t_s + h_{web}} f_{frp\_web}\left(\varepsilon\left(\varepsilon_{frp\_max}, t_s + h_{web} + t_{flan}, y_{NA}, y\right)\right) \cdot \left(2 \cdot t_{web}\right) \mathrm{d}y$$

$$F_{cbs} = \int_{t_s}^{t_s + h_{web}} f_c\left(\varepsilon\left(\varepsilon_{frp\_max}, t_s + h_{web} + t_{flan}, y_{NA}, y\right)\right) \cdot \left(b_{flan} - 2 \cdot t_{web}\right) \mathrm{d}y$$

$$F_s = \int_{0\ in}^{t_s} f_c\left(\varepsilon\left(\varepsilon_{frp\_max}, t_s + h_{web} + t_{flan}, y_{NA}, y\right)\right) \cdot \left(S\right) \mathrm{d}y$$

$F_{ff} + F_{fw} + F_{cbs} + F_s = 0$

Solver

$$\begin{bmatrix} y_{NA} \\ F_{ff} \\ F_{fw} \\ F_{cbs} \\ F_s \end{bmatrix} := \mathbf{find}\left(y_{NA}, F_{ff}, F_{fw}, F_{cbs}, F_s\right)$$

$$\begin{bmatrix} y_{NA} \\ F_{ff} \\ F_{fw} \\ F_{cbs} \\ F_s \end{bmatrix} = \begin{bmatrix} 0.442\ ft \\ -1.144 \cdot 10^5\ lbf \\ -1.863 \cdot 10^5\ lbf \\ -3.565 \cdot 10^{-28}\ lbf \\ \left(3.008 \cdot 10^5\right)\ lbf \end{bmatrix}$$

$$y_{NA} = 5.309\ in$$

3. Determine the moment generated by each component using the depth to the neutral axis obtained in Step 2.

$$M_{ff} := \int_{t_s + h_{web}}^{t_s + h_{web} + t_{flan}} f_{frp\_flan}\left(\varepsilon\left(\varepsilon_{frp\_max}, t_s + h_{web} + t_{flan}, y_{NA}, y\right)\right) \cdot \left(b_{flan}\right) \cdot \left(y_{NA} - y\right) \mathrm{d}y = \left(2.888 \cdot 10^3\right)\ kip \cdot in$$

$$M_{fw} := \int_{t_s}^{t_s + h_{web}} f_{frp\_web}\left(\varepsilon\left(\varepsilon_{frp\_max}, t_s + h_{web} + t_{flan}, y_{NA}, y\right)\right) \cdot \left(2 \cdot t_{web}\right) \cdot \left(y_{NA} - y\right) \mathrm{d}y = \left(3.1 \cdot 10^3\right)\ kip \cdot in$$

$$M_{cbs} := \int_{t_s}^{t_s + h_{web}} f_c\left(\varepsilon\left(\varepsilon_{frp\_max}, t_s + h_{web} + t_{flan}, y_{NA}, y\right)\right) \cdot \left(b_{flan} - 2 \cdot t_{web}\right) \cdot \left(y_{NA} - y\right) \mathrm{d}y = 0\ kip \cdot in$$

$$M_s := \int_{0\ in}^{t_s} f_c\left(\varepsilon\left(\varepsilon_{frp\_max}, t_s + h_{web} + t_{flan}, y_{NA}, y\right)\right) \cdot (S) \cdot \left(y_{NA} - y\right) \mathrm{d}y = \left(1.174 \cdot 10^3\right)\ kip \cdot in$$

4. Determine the total moment capacity of the cross-section for Limit State 1 by summing the moment contributions from each component

$$M_{n\_LS3} := M_{ff} + M_{fw} + M_{cbs} + M_s = \left(7.162 \cdot 10^3\right)\ kip \cdot in$$

5. Compare the moment capacity with the factored demand for the current limit state

$$M_{u\_LS3} = \left(7.249 \cdot 10^3\right)\ kip \cdot in$$

Discussion: The moment capacity, M_{n_LS3} , is 1.2% less than the factored demand for LS-3. This is due to the fact that the moment-curvature routine used to determine the required thickness of 1.08 in for LS-3 assumes that the stress at the **centroid** of the FRP flange equals the stress at the fatigue and creep rupture limit. The value computed in the hand calculations above assumes that LS-3 is reached when the stress at the **bottom** of the FRP flange equals the stress at the fatigue and creep rupture limit. If the hand calculations are modified such that the FRP stress is evaluated at the centroid of the flange, the resulting M_{n_LS3} is $7.315 \cdot 10^3\ kip \cdot in$, which exceeds the required moment demand of $7.249 \cdot 10^3\ kip \cdot in$.

Method 2 - Simplified cracked-section analysis

The transformed section properties determined for LS-1 are applicable to LS-3 as long as the concrete has cracked and the stress-vs-strain response of the concrete is still approximately linear.

$$y_{NA\_cr\_tr} = 5.125\ in$$

$$I_{cr\_tr} = \left(2.277 \cdot 10^4\right)\ in^4$$

The equivalent stress in the transformed FRP flange is:

$$f_{frp\_tr} := \frac{-f_{f\_cr\_limit}}{n_{flan}} = 8.077\ ksi$$ negative sign has been neglected

The moment required to generate this level of stress at the bottom of the FRP flange is:

$$M_{n\_LS3\_simplified\_1} := \frac{f_{frp\_tr} \cdot I_{cr\_tr}}{\left(t_s + h_{web} + t_{flan}\right) - y_{NA\_cr\_tr}} = \left(7.087 \cdot 10^3\right)\ kip \cdot in$$

The moment required to generate this level of stress at the centroid of the FRP flange is:

$$M_{n\_LS3\_simplified\_2} := \frac{f_{frp\_tr} \cdot I_{cr\_tr}}{\left(t_s + h_{web} + \frac{t_{flan}}{2}\right) - y_{NA\_cr\_tr}} = \left(7.238 \cdot 10^3\right)\ kip \cdot in$$

Discussion: Both values for the moment capacity at Limit State 3 that were computed using the simplified method of cracked/transformed sections are in reasonable agreement with the result obtained from a complete moment-curvature analysis.

There is no appropriate/simplified closed-form solution for determining the flexural capacity at the strength limit state. The moment-curvature approach adopted below assumes that the section's capacity is reached when the stress in the FRP flange reaches the design tensile strength. This needs to be verified for each cross-section.

1. Find FRP strain corresponding to design tensile strength

$f'_{fu\_flan} = 73.8\ ksi$

$f_{f\_strength\_limit} := -f'_{fu\_flan} \cdot C_E = -36.9\ ksi$

$\varepsilon_{frp\_max} := \frac{f_{f\_strength\_limit}}{E_{flan}} = -0.009$

2. Find depth to the neutral axis. Assume maximum strain in FRP is achieved at the bottom of the FRP flange.

Guess Values

$y_{NA} := 4\ in$
$F_{ff} := 1\ kip$
$F_{fw} := 1\ kip$
$F_{cbs} := 1\ kip$
$F_s := 1\ kip$

Constraints

$$F_{ff} = \int_{t_s + h_{web}}^{t_s + h_{web} + t_{flan}} f_{frp\_flan}\left(\varepsilon\left(\varepsilon_{frp\_max}, t_s + h_{web} + t_{flan}, y_{NA}, y\right)\right) \cdot \left(b_{flan}\right) \mathrm{d}y$$

$$F_{fw} = \int_{t_s}^{t_s + h_{web}} f_{frp\_web}\left(\varepsilon\left(\varepsilon_{frp\_max}, t_s + h_{web} + t_{flan}, y_{NA}, y\right)\right) \cdot \left(2 \cdot t_{web}\right) \mathrm{d}y$$

$$F_{cbs} = \int_{t_s}^{t_s + h_{web}} f_c\left(\varepsilon\left(\varepsilon_{frp\_max}, t_s + h_{web} + t_{flan}, y_{NA}, y\right)\right) \cdot \left(b_{flan} - 2 \cdot t_{web}\right) \mathrm{d}y$$

$$F_s = \int_{0\,in}^{t_s} f_c\left(\varepsilon\left(\varepsilon_{frp\_max}, t_s + h_{web} + t_{flan}, y_{NA}, y\right)\right) \cdot \left(S\right) \mathrm{d}y$$

$$F_{ff} + F_{fw} + F_{cbs} + F_s = 0$$

Solver

$$\begin{bmatrix} y_{NA} \\ F_{ff} \\ F_{fw} \\ F_{cbs} \\ F_s \end{bmatrix} := \mathbf{find}\left(y_{NA}, F_{ff}, F_{fw}, F_{cbs}, \mathrm{F_s}\right)$$

$$\begin{bmatrix} y_{NA} \\ F_{ff} \\ F_{fw} \\ F_{cbs} \\ F_s \end{bmatrix} = \begin{bmatrix} 0.467\ ft \\ -5.721 \cdot 10^5\ lbf \\ -9.222 \cdot 10^5\ lbf \\ \left(1.116 \cdot 10^{-26}\right) lbf \\ \left(1.494 \cdot 10^6\right) lbf \end{bmatrix} \qquad y_{NA} = 5.599\ in$$

Determine if concrete crushes in compression:

$\varepsilon\left(\varepsilon_{frp\_max}, t_s + h_{web} + t_{flan}, y_{NA}, 0\right) = 0.002$ strain in concrete at top of slab (y = 0)

ε_{frp_max} = maximum strain in FRP corresponding to design tensile strength of FRP
$t_s + h_{web} + t_{flan}$ = Distance from top of slab to extreme FRP fiber in flange
y_{NA} = depth to neutral axis from the top of the slab
0 = location on cross section where strain is desired

Result:
Strain in concrete is less than .003 when FRP reaches design tensile strength, therefore FRP fails before concrete crushes. This is a tension controlled section. The strength reduction factor, Φ, is given as follows:

$\Phi := 0.55$

3. Compute factored moment capacity at strength limit state:

$$M_{ff} := \int_{t_s + h_{web}}^{t_s + h_{web} + t_{flan}} f_{frp\_flan}\left(\varepsilon\left(\varepsilon_{frp\_max}, t_s + h_{web} + t_{flan}, y_{NA}, y\right)\right) \cdot \left(b_{flan}\right) \cdot \left(y_{NA} - y\right) dy = \left(1.427 \cdot 10^4\right)\ kip \cdot in$$

$$M_{fw} := \int_{t_s}^{t_s + h_{web}} f_{frp\_web}\left(\varepsilon\left(\varepsilon_{frp\_max}, t_s + h_{web} + t_{flan}, y_{NA}, y\right)\right) \cdot \left(2 \cdot t_{web}\right) \cdot \left(y_{NA} - y\right) dy = \left(1.513 \cdot 10^4\right)\ kip \cdot in$$

$$M_{cbs} := \int_{t_s}^{t_s + h_{web}} f_c\left(\varepsilon\left(\varepsilon_{frp\_max}, t_s + h_{web} + t_{flan}, y_{NA}, y\right)\right) \cdot \left(b_{flan} - 2 \cdot t_{web}\right) \cdot \left(y_{NA} - y\right) dy = 0\ kip \cdot in$$

$$M_s := \int_{0\ in}^{t_s} f_c\left(\varepsilon\left(\varepsilon_{frp\_max}, t_s + h_{web} + t_{flan}, y_{NA}, y\right)\right) \cdot (S) \cdot \left(y_{NA} - y\right) dy = \left(5.316 \cdot 10^3\right)\ kip \cdot in$$

$M_{n\_LS4a} := M_{ff} + M_{fw} + M_{cbs} + M_s = \left(3.472 \cdot 10^4\right)\ kip \cdot in$

$\Phi \cdot M_{n\_LS4a} = \left(1.91 \cdot 10^4\right)\ kip \cdot in$

4. Compare factored resistance to factored demand

$M_{u\_LS4a} = \left(1.705 \cdot 10^4\right)\ kip \cdot in$ $\Phi \cdot M_{n\_LS4a} \geq M_{u\_LS4a} = 1$ "ok"

1. Determine depth to neutral axis for cracked concrete section

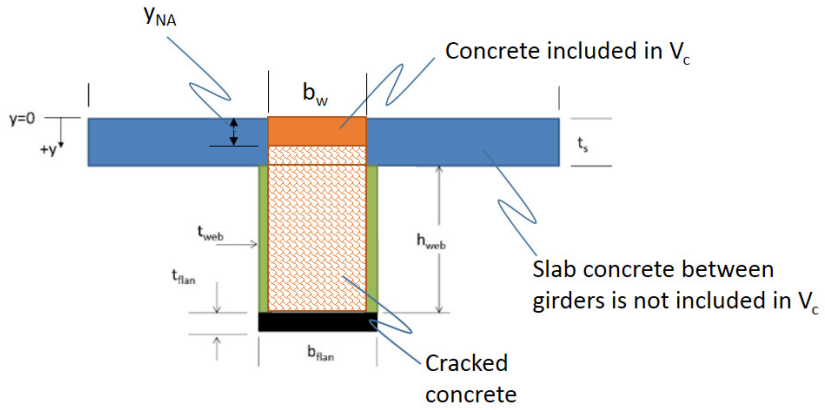

$n_{web} := \frac{E_{web}}{E_{con}} = 0.914$ Modulus ratio for FRP in web to concrete

$n_{flan} := \frac{E_{flan}}{E_{con}} = 0.914$ Modulus ratio for FRP in flange to concrete

Transformed Section Dimensions:

$t_{web\_tr} := t_{web} \cdot n_{web} = 0.987\ in$

$b_{flan\_tr} := b_{flan} \cdot n_{flan} = 13.401\ in$

Width of concrete in compression zone:

$b_w := b_{flan} - 2 \cdot t_{web} = 12.507\ in$

First moment of area for regions above the Neutral Axis must equal first moment of area for regions below the Neutral Axis. Use solve block to solve for y_{NA}:

Guess Values

$y_{NA} := 4\ in$ initial guess value required by solver

Constraints

$$b_w \cdot y_{NA} \cdot \frac{y_{NA}}{2} = b_{flan\_tr} \cdot t_{flan} \cdot \left(\left(t_s + h_{web} + \frac{t_{flan}}{2}\right) - y_{NA}\right) + 2 \cdot t_{web\_tr} \cdot h_{web} \cdot \left(\left(t_s + \frac{h_{web}}{2}\right) - y_{NA}\right)$$

Solver

$y_{NA} := \text{find}(y_{NA})$

$y_{NA} = 10.339\ in$ Distance to neutral axis for cracked concrete section measured from the top of slab

2. Determine area of concrete that participates in shear transfer

$$A_{con\_V} := b_w \cdot y_{NA} = 129.305\ in^2$$

3. Determine shear resistance provided by concrete

$$V_c := 0.158 \cdot \sqrt{\frac{f'_c}{ksi}} \cdot ksi \cdot A_{con\_V} = 47.913\ kip$$

4. Determine shear resistance provided by FRP

Basic relationship for shear stress in FRP webs:

$$\tau_{max} = \frac{3}{2} \cdot \frac{V_{FRP}}{A_{webs}}$$

$$A_{webs} := 2 \cdot t_{web} \cdot h_{web} = 47.52\ in^2$$

$$\tau_{fu} := C_E \cdot \tau'_{fu} = 5\ ksi$$

C_E = Environmental knockdown factor
τ'_{fu} = Manufacturer's specified shear strength for FRP in webs
τ_{fu} = Design shear strength for FRP in webs

Rearranging and solving for V_{FRP}

$$V_{FRP} := \frac{2}{3} \cdot \tau_{fu} \cdot A_{webs} = 158.4\ kip$$

4. Determine factored shear resistance

$$V_n := V_c + V_{FRP} = 206.313\ kip$$

$$\Phi_V := 0.75$$

$$\Phi_V \cdot V_n = 154.735\ kip$$

$$V_{u\_LS4b} = 147.9\ kip$$

5. Compare factored resistance to factored demand

$$\Phi_V \cdot V_n \geq V_{u\_LS4b} = 1 \qquad \text{"ok"}$$

Summary of Results

Limit State 1: Concrete compressive stress

$M_{n\_LS1} = 913.97\ kip \cdot ft$

$M_{u\_LS1} = 912.75\ kip \cdot ft$

Limit State 2: Displacements

$\Delta_{max} := \frac{712923596 \cdot kip \cdot in^3}{EI_{total}} = 0.411\ in$

$\Delta_{max\_LS2} := \frac{L}{1000} = 0.6\ in$

Limit State 3: Fatigue and creep rupture

$M_{n\_LS3} = 596.8\ kip \cdot ft$

$M_{u\_LS3} = 604.1\ kip \cdot ft$

Note: Discussion on why factored resistance is less than factored demand is provided on page 24.

Limit State 4a: Flexural strength

$\Phi \cdot M_{n\_LS4a} = 1591.4\ kip \cdot ft$

$M_{u\_LS4a} = 1420.7\ kip \cdot ft$

Limit State 4b: Shear strength

$\Phi_V \cdot V_n = 154.735\ kip$

$V_{u\_LS4b} = 147.9\ kip$